LBL-1247

TRANSFER REACTIONS IN THE Zr-Mo REGION INDUCED BY α PARTICLES AND HEAVY IONS

Michael Steven Zisman
(Ph. D. thesis)

RECEIVED
LAWRENCE
RADIATION LABORATORY

DEC 1 1972

LIBRARY AND
DOCUMENTS SECTION

August 1972

AEC Contract No. W-7405-eng-48

For Reference

Not to be taken from this room

LBL-1247

DISCLAIMER

This document was prepared as an account of work sponsored by the United States Government. While this document is believed to contain correct information, neither the United States Government nor any agency thereof, nor the Regents of the University of California, nor any of their employees, makes any warranty, express or implied, or assumes any legal responsibility for the accuracy, completeness, or usefulness of any information, apparatus, product, or process disclosed, or represents that its use would not infringe privately owned rights. Reference herein to any specific commercial product, process, or service by its trade name, trademark, manufacturer, or otherwise, does not necessarily constitute or imply its endorsement, recommendation, or favoring by the United States Government or any agency thereof, or the Regents of the University of California. The views and opinions of authors expressed herein do not necessarily state or reflect those of the United States Government or any agency thereof or the Regents of the University of California.

TRANSFER REACTIONS IN THE Zr-Mo REGION INDUCED BY α PARTICLES AND HEAVY IONS

Contents

Figure Captions vi

Abstract xv

I. Introduction 1

A. (α,t) Reactions 1

B. (α,d) Reactions 3

C. Heavy Ion Reactions 6

II. Experimental Equipment 8

A. α Particle Reactions 8

1. Cyclotron and Beam Optics 8

2. Scattering Chamber 10

3. Detectors and Electronics 16

4. Targets 20

B. Heavy Ion Reactions 22

1. Beam Optics 22

2. Scattering Chamber 22

3. Spectrometer 24

4. Detector and Electronics 29

5. Targets 38

III. Data Reduction 42

A. α Particle Reactions 42

B. Heavy Ion Reactions 45

IV. Experimental Results 53

A. (α,t) Reactions 53

1. Selection Rules 53

2. $^{90}Zr(\alpha,t)^{91}Nb$ 53

3. $^{92}Mo(\alpha,t)^{93}Tc$ 69

4. $^{92}Zr(\alpha,t)^{93}Nb$ 78

5. $^{94}Zr(\alpha,t)^{95}Nb$ 85

6. $^{91}Zr(\alpha,t)^{92}Nb$ 91

B. (α,d) Reactions 100

1. Selection Rules 100

2. $^{14}N(\alpha,d)^{16}O$ 100

3. $^{90}Zr(\alpha,d)^{92}Nb$ 118

4. $^{92}Mo(\alpha,d)^{94}Tc$ 122

5. $^{92}Zr(\alpha,d)^{94}Nb$ 130

6. $^{94}Zr(\alpha,d)^{96}Nb$ 135

7. $^{91}Zr(\alpha,d)^{93}Nb$ 139

C. Heavy Ion Reactions 147

1. Selection Rules 147

2. $^{90}Zr(^{16}O,^{15}N)^{91}Nb$ 149

3. $^{92}Mo(^{16}O,^{15}N)^{93}Tc$ 157

4. $^{94}Zr(^{16}O,^{15}N)^{95}Nb$ 160

5. $^{91}Zr(^{16}O,^{15}N)^{92}Nb$ 164

6. $^{93}Nb(^{16}O,^{15}N)^{94}Mo$ 167

7. $^{90}Zr(^{16}O,^{15}O)^{91}Zr$ 173

8. $^{92}Mo(^{16}O,^{15}O)^{93}Mo$ 183

9. $^{93}Nb(^{16}O,^{15}O)^{94}Nb$ 186

10. $^{94}Zr(^{16}O,^{15}O)^{95}Zr$ 190

11. $^{91}Zr(^{16}O,^{15}O)^{92}Zr$ 192

12. $(^{16}O,^{17}O)$ Reactions 196

V. Discussion 200

A. Single-nucleon Transfer 200

1. Comparison with Shell Model Predictions 200

2. Comparison Between α Particle and Heavy Ion Induced Reactions 204

B. Two-nucleon Transfer 211

1. Q-value Dependence 211

2. Shell Model Calculations 213

3. (α,d) Structure Factors 219

4. Other Evidence 221

VI. Conclusions 223

A. (α,t) Reactions 223

B. (α,d) Reactions 225

C. Heavy Ion Reactions 227

Acknowledgments 229

Appendices 231

A. Calculation of the Favored Momentum Transfer 231

B. Calculation of Shell Model Diagonal Matrix Elements 244

References 254

FIGURE CAPTIONS

Figure number	Title	Page
1.	Beam transport system for the high-resolution (Cave 4) experimental area of the Berkeley 88-inch cyclotron. Both the 36-inch scattering chamber (Cave 4A) and spectrometer (Cave 4C) layouts are shown.	9
2.	Proton yield curves at $\theta_\ell = 165°$ for the bombardment of carbon targets with beams of protons and the molecular hydrogen ions H_2^+ and H_3^+. The target thickness and integrated charge are shown for each experiment separately. (The resonance corresponds to the $J^\pi = 3/2^-$, $T = 3/2$ level in ^{13}N at $E_x = 15.066$ MeV.)	11
3.	Schematic diagram of the 36-inch scattering chamber.	12
4.	Schematic diagram of the counter holder used with liquid nitrogen cooled counters.	14
5.	Photographs of the liquid nitrogen cooled counter holder and preamp. The internal features are labelled in Fig. 4.	15
6.	Block diagram of the particle identifier electronics.	18
7.	Schematic diagram of the 24-inch scattering chamber and magnetic spectrometer.	25
8.	General view of the heavy ion focal plane detector. The operating position of the counter system is indicated in Fig. 7.	30
9.	Detail of one end of the proportional counter. The support for the quartz fiber is enlarged in the lower half of the figure.	31
10.	Block diagram of the electronics used in conjunction with the heavy ion focal plane detector system. The various delay times are indicated in the hexagonal boxes.	34

Figure number	Title	Page
11.	Time-of-flight vs. position spectrum obtained from the bombardment of ^{90}Zr with 104 MeV ^{16}O at $\theta_\ell = 25°$. The M/q value for each band of particles is indicated at the right of the figure. The lowest band is mainly $^{12}C(6+)$, the middle band is $^{15}N(7+)$ and $^{15}O(7+)$, and the upper band is mainly $^{16}O(7+)$. The slope is due to the 10% change in velocity of the ions along the focal plane. The dots are intensified on a logarithmic scale. A display threshold of 10 counts was used to clearly differentiate the various bands.	39
12.	$\Delta E/\Delta X$ vs. position spectrum obtained from the bombardment of ^{90}Zr with 104 MeV ^{16}O at $\theta_\ell = 25°$. Bands corresponding to carbon, nitrogen, and oxygen are indicated at the right of the figure. A display threshold of 10 counts was employed.	40
13.	Time-of-flight vs. $\Delta E/\Delta X$ spectrum obtained from the bombardment of ^{90}Zr with 104 MeV ^{16}O at $\theta_\ell = 25°$. The TOF signals were corrected by the computer (see Fig. 14) to remove the position dependence. Groups corresponding to various values of M/q and Z are indicated. A display threshold of 15 counts was employed.	41
14.	Corrected time-of-flight vs. position spectrum obtained from the bombardment of ^{90}Zr with 104 MeV ^{16}O at $\theta_\ell = 25°$. The method of correction is described in the text. (See caption to Fig. 11.)	46
15.	Triton energy spectrum from the $^{90}Zr(\alpha,t)^{91}Nb$ reaction at $\theta_\ell = 30°$. The peak numbers correspond to excitation energies given in Table IV.	63
16.	Angular distributions of tritons from the $^{90}Zr(\alpha,t)^{91}Nb$ reaction leading to the 0.0, 4.18, and 4.77 MeV levels.	64

Figure number	Title	Page
	Statistical errors are shown for each point. The curves have no theoretical significance.	
17.	Angular distributions of tritons from the $^{90}Zr(\alpha,t)^{91}Nb$ reaction leading to the 3.37 and 4.18 MeV levels. Statistical errors are shown for each point. The curves have no theoretical significance.	65
18.	Triton energy spectrum from the $^{92}Mo(\alpha,t)^{93}Tc$ reaction at $\theta_\ell = 15°$. The peak numbers correspond to excitation energies given in Table V.	70
19.	Angular distributions of tritons from the $^{92}Mo(\alpha,t)^{93}Tc$ reaction leading to the 0.0, 3.91, 4.37, and 4.90 MeV levels. Statistical errors are shown for each point. The curves have no theoretical significance.	75
20.	Angular distributions of tritons from the $^{92}Mo(\alpha,t)^{93}Tc$ reaction leading to the 3.36 and 3.91 MeV levels. Statistical errors are shown for each point. The curves have no theoretical significance.	76
21.	Triton energy spectrum from the $^{92}Zr(\alpha,t)^{93}Nb$ reaction at $\theta_\ell = 20°$. The peak numbers correspond to excitation energies given in Table VI.	79
22.	Angular distributions of tritons from the $^{92}Zr(\alpha,t)^{93}Nb$ reaction leading to the 0.0, 1.08, and 1.29 MeV levels. The solid line through each set of data points represents a smooth curve drawn through the experimental angular distribution of the ground state. Statistical errors are shown for each point.	80
23.	Triton energy spectrum from the $^{94}Zr(\alpha,t)^{95}Nb$ reaction at $\theta_\ell = 20°$. The peak numbers correspond to excitation energies given in Table VII.	86

Figure number	Title	Page
24.	Angular distributions of tritons from the $^{94}Zr(\alpha,t)^{95}Nb$ reaction leading to the 0.0, 1.27, 1.65, and 2.10 MeV levels. The solid line through each set of data points represents a smooth curve drawn through the experimental angular distribution of the ground state. Statistical errors are shown for each point.	92
25.	Triton energy spectrum from the $^{91}Zr(\alpha,t)^{92}Nb$ reaction at $\theta_\ell = 15°$. The peak numbers correspond to excitation energies given in Table IX.	93
26.	Angular distributions of tritons from the $^{91}Zr(\alpha,t)^{92}Nb$ reaction leading to the 0.0, 0.14, 0.28, 0.36, and (unresolved) 0.48-0.50 MeV states. The solid line through each set of data points represents a smooth curve drawn through the experimental angular distribution of the $^{90}Zr(\alpha,t)^{91}Nb$ (g.s.) reaction from Fig. 16. Statistical errors are shown for each point.	95
27.	Deuteron energy spectrum from the $^{14}N(\alpha,d)^{16}O$ reaction at $\theta_\ell = 10°$. The "14 MeV" peak contains a contribution of unknown amount from the $^{16}O(\alpha,d)^{18}F$ (1.13 MeV) reaction on a target impurity.	101
28.	Angular distributions of deuterons from the $^{14}N(\alpha,d)^{16}O$ reaction leading to the 14.40, 14.82, and 16.24 MeV levels. Statistical errors are shown for each point. The curves have no theoretical significance.	103
29.	Deuteron energy spectrum from the $^{90}Zr(\alpha,d)^{92}Nb$ reaction at $\theta_\ell = 20°$. The peak numbers correspond to excitation energies given in Table XII.	119
30.	Angular distributions of deuterons from the $^{90}Zr(\alpha,d)^{92}Nb$ reaction leading to the 0.0 and 2.58 MeV states. Statistical errors are shown for each point. The curves have no theoretical significance.	123

Figure number	Title	Page
31.	Deuteron energy spectrum from the $^{92}Mo(\alpha,d)^{94}Tc$ reaction at $\theta_\ell = 20°$. The peak numbers correspond to excitation energies given in Table XIII.	124
32.	Angular distributions of deuterons from the $^{92}Mo(\alpha,d)^{94}Tc$ reaction leading to the 0.0 and 2.68 MeV states. The solid lines through the data points represent smooth curves drawn through the experimental angular distributions of the $^{90}Zr(\alpha,d)^{92}Nb$ reaction leading to the ground and 2.58 MeV states (see Fig. 30). Statistical errors are shown for each point.	125
33.	Deuteron angular distributions from the $^{90}Zr(\alpha,d)^{92}Nb$ (0.36 MeV) and $^{92}Mo(\alpha,d)^{94}Tc$ (0.21 MeV) reactions. Statistical errors are shown for each point.	129
34.	Deuteron energy spectrum from the $^{92}Zr(\alpha,d)^{94}Nb$ reaction at $\theta_\ell = 20°$. The peak numbers correspond to excitation energies given in Table XIV.	131
35.	Angular distributions of deuterons from the $^{92}Zr(\alpha,d)^{94}Nb$ reaction leading to the 0.08 and 2.42 MeV states. The solid line through the 0.08 MeV data points represents a smooth curve drawn through the experimental angular distribution of the summed 0.0 MeV (7^+) and 0.36 MeV (5^+) levels in $^{90}Zr(\alpha,d)^{92}Nb$. The solid line through the 2.42 MeV data points is a smooth curve drawn through the experimental angular distribution of the $^{90}Zr(\alpha,d)^{92}Nb$ (2.58 MeV) reaction. Statistical errors are shown for each point.	132
36.	Deuteron energy spectrum from the $^{94}Zr(\alpha,d)^{96}Nb$ reaction at $\theta_\ell = 20°$. The peak numbers correspond to excitation energies given in Table XV.	136

Figure number	Title	Page
37.	Angular distributions of deuterons from the $^{94}Zr(\alpha,d)^{96}Nb$ reaction leading to the 0.23 and 2.38 MeV states. The solid lines through the data points represent smooth curves drawn through the experimental angular distributions of the $^{90}Zr(\alpha,d)^{92}Nb$ reaction leading to the ground and 2.58 MeV states. (See Fig. 30.) Statistical errors are shown for each point.	140
38.	Deuteron energy spectrum from the $^{91}Zr(\alpha,d)^{93}Nb$ reaction at $\theta_\ell = 20°$. The peak numbers correspond to excitation energies given in Table XVI.	141
39.	Angular distributions of deuterons from the $^{91}Zr(\alpha,d)^{93}Nb$ reaction leading to the 0.96, 1.33, and 1.48 MeV levels. The solid lines represent smooth curves drawn through experimental angular distributions from the $^{90}Zr(\alpha,d)^{92}Nb$ reaction leading to the 7^+ (g.s.) and 5^+ (0.36 MeV) with weighting factors of: 0.96 MeV $[7^+ + 5^+]$, 1.33 MeV $[7^+]$, and 1.48 MeV $[7^+ + 2 \times (5^+)]$. (See text, Sec. IV-B7.) Statistical errors are shown for each point.	144
40.	Angular distributions of deuterons from the $^{91}Zr(\alpha,d)^{93}Nb$ reaction leading to the 3.54 and 4.52 MeV states. The solid lines represent smooth curves drawn through the experimental angular distribution of the $^{90}Zr(\alpha,d)^{92}Nb$ (2.58 MeV) reaction. (See Fig. 30.) Statistical errors are shown for each point.	146
41.	^{15}N position spectrum from the $^{90}Zr(^{16}O,^{15}N)^{91}Nb$ reaction at $\theta_\ell = 25°$. The two-dimensional arrays corresponding to this spectrum are displayed in Figs. 11 to 14.	150
42.	Angular distributions of ^{15}N from the $^{90}Zr(^{16}O,^{15}N)^{91}Nb$ reaction leading to the 0.0 and 3.37 MeV states. The angular distributions for the two states have identical	151

Figure number	Title	Page
	shapes, although the ground state ($p_{1/2} \rightarrow g_{9/2}$ transition) should be L=5 and the 3.37 MeV state ($p_{1/2} \rightarrow d_{5/2}$ transition) L=3 based on the selection rules.	
43.	Position spectra from the inelastic scattering of 104 MeV ^{16}O on targets of ^{90}Zr, ^{92}Mo, and ^{93}Nb. The broad states near 6 MeV may be due to (Doppler broadened) ^{16}O excited states.	156
44.	^{15}N position spectrum from the $^{92}Mo(^{16}O,^{15}N)^{93}Tc$ reaction at $\theta_\ell = 20°$.	158
45.	^{15}N position spectrum from the $^{94}Zr(^{16}O,^{15}N)^{95}Nb$ reaction at $\theta_\ell = 25°$.	161
46.	^{15}N position spectrum from the $^{91}Zr(^{16}O,^{15}N)^{92}Nb$ reaction at $\theta_\ell = 25°$. The peak near channel 50 is due to leak-through of an intense ^{17}O peak from the $^{15}O(7+)$ gate (see Fig. 54).	165
47.	^{15}N position spectrum from the $^{93}Nb(^{16}O,^{15}N)^{94}Mo$ reaction at $\theta_\ell = 20°$.	168
48.	^{15}O position spectrum from the $^{90}Zr(^{16}O,^{15}O)^{91}Zr$ reaction at $\theta_\ell = 25°$. A $^{90}Zr(\alpha,^{3}He)^{91}Zr$ spectrum at $\theta_\ell = 25°$ is shown for comparison.	174
49.	$^{15}O(7+)$ position spectrum from the $^{90}Zr(^{16}O,^{15}O)^{91}Zr$ reaction at $\theta_\ell = 25°$. The small peaks near channel 50 are due to the $(^{16}O,^{17}O)$ reaction on isotopic impurities in the target leading to the final states indicated above the peaks.	175
50.	^{15}O angular distributions from the $^{90}Zr(^{16}O,^{15}O)^{91}Zr$ reaction leading to the 0.0 and 2.16 MeV states. According to the selection rules, the ground state transition is L=3 and the 2.16 MeV transition is L=6.	176

Figure number	Title	Page
51.	^{15}O position spectrum from the $^{92}Mo(^{16}O,^{15}O)^{93}Mo$ reaction at $\theta_\ell = 20°$. A $^{92}Mo(\alpha,^{3}He)^{93}Mo$ spectrum at $\theta_\ell = 25°$ is shown for comparison.	184
52.	^{15}O position spectrum from the $^{93}Nb(^{16}O,^{15}O)^{94}Nb$ reaction at $\theta_\ell = 20°$. Due to difficulty with the calibration, the energy of the $[\pi g_{9/2},(\nu d_{5/2})^{3}_{5/2}]$ multiplet was found to be -0.05 MeV. The excitation energies for all three states are believed to be low by about 110 keV. (See text, Sec. IV-C9.)	187
53.	$^{15}O(7+)$ position spectrum from the $^{94}Zr(^{16}O,^{15}O)^{95}Zr$ reaction at $\theta_\ell = 25°$. The large peak at the bottom of the spectrum is due to the $^{94}Zr(^{16}O,^{17}O)^{93}Zr$ (g.s.) reaction.	191
54.	$^{15}O(7+)$ position spectrum from the $^{91}Zr(^{16}O,^{15}O)^{92}Zr$ reaction at $\theta_\ell = 25°$. The peaks at the bottom of the spectrum are due to the $^{91}Zr(^{16}O,^{17}O)^{90}Zr$(g.s.) reaction, with the larger one being due to ^{17}O in its ground state and the smaller one to ^{17}O in its 0.87 MeV ($s_{1/2}$) first excited state.	193
55.	Comparison between the calculated and experimental spectra for the $(\pi g_{9/2},\nu d_{5/2})$ multiplet in ^{92}Nb.	215
56.	(a) Momentum vector diagram illustrating the angular momentum transfer in the plane wave picture of a nuclear reaction. (b) Momentum vector triangle corresponding to the reaction shown in (a).	232
57.	Trajectories for a nuclear reaction in the presence of the Coulomb force. The reaction is assumed to occur at the distance of closest approach, D, of both the incoming (solid curve) and outgoing (dashed curve) Coulomb orbits. The actual path of the particles is indicated by the	236

Figure number	Title	Page
	arrows. Note that in this picture the observed scattering angle does not correspond to the scattering angles associated with the individual Coulomb orbits.	
58.	Diagram of the coordinate system for heavy ion induced transfer reactions. The relationships between the various vectors are indicated below the diagram.	239

TRANSFER REACTIONS IN THE Zr-Mo REGION INDUCED BY α PARTICLES AND HEAVY IONS

Michael Steven Zisman

Lawrence Berkeley Laboratory
University of California
Berkeley, California 94720

August 1972

ABSTRACT

The (α,d) and (α,t) reactions on targets of ^{90,91,92,94}Zr and ^{92}Mo have been investigated with 50 and 65 MeV α-particle beams from the Berkeley 88-inch cyclotron. High-spin proton states observed in the (α,t) reaction, based on comparisons with (^{3}He,d) data on the same targets, include: ^{91}Nb [2.39, 2.53, 2.61, 2.77, 2.90, 3.01, 4.18, 4.77, 4.89, and (5.14) MeV], ^{93}Tc [0.68, (3.58), 3.91, 4.37, (4.47), (4.67), 4.77, 4.90, 6.01 (multiplet), 6.17, and 6.44 MeV], ^{92}Nb [≈ 5 MeV multiplet], ^{93}Nb [1.08, 1.29, and ≈ 4.5 MeV], and ^{95}Nb [1.27, 1.65, (2.10), and ≈ 4.5 MeV]. A difference in Q-values for the ^{90}Zr(α,t)^{91}Nb and ^{91}Zr(α,t)^{92}Nb reactions of 680 ± 25 keV yields a new Q-value, -14.643 ± 0.027 MeV, for the ^{90}Zr(α,t) reaction. This corresponds to a change in the ^{91}Nb mass excess of +98 keV, in agreement with other recent determinations of this quantity.

Two groups of strongly excited states appear in the (α,d) data. Members of the lower group [^{92}Nb (g.s.), ^{94}Nb (0.08 MeV), and ^{96}Nb (0.23 MeV)] have been previously identified as $(\pi g_{9/2}, \nu d_{5/2})_{7^+}$ states. From the ^{92}Mo(α,d)^{94}Tc results, the ^{94}Tc ground state can also be assigned

$J^{\pi} = 7^{+}$. The higher levels [^{92}Nb (2.58 MeV), ^{94}Nb (2.42 MeV), ^{96}Nb (2.38 MeV), and ^{94}Tc (2.68 MeV)] are believed to be either $(\pi g_{9/2}, \nu h_{11/2})_{10-}$ or $(\pi g_{9/2}, \nu g_{7/2})_{8^+}$ states, based on the results of shell model matrix element calculations and the (α,d) structure factors of Glendenning. As an example of the systematics of the (α,d) reaction, results from the ^{14}N(α,d)^{16}O reaction at 40 MeV are also included here. Accurate excitation energies and widths for the previously observed $\left[^{14}\text{N}\ (1^{+}) + (d_{5/2})^{2}_{5^{+}}\right]$ triplet in ^{16}O have been determined to be: 14.40 ± 0.03 MeV ($\Gamma_{c.m.}$ = 30 ± 30 keV), 14.82 ± 0.03 MeV ($\Gamma_{c.m.}$ = 69 ± 30 keV), and 16.24 ± 0.04 MeV ($\Gamma_{c.m.}$ = 125 ± 50 keV).

The (^{16}O,^{15}N) and (^{16}O,^{15}O) reactions on targets of ^{90,91,94}Zr, ^{92}Mo, and ^{93}Nb were also investigated with a 104 MeV ^{16}O (4+) beam from the Berkeley 88-inch cyclotron. Outgoing heavy ions were detected in the focal plane of a magnetic spectrometer with a Borkowski-Kopp type position sensitive proportional counter backed by a plastic scintillator and phototube. The (^{16}O,^{15}N) and (^{16}O,^{15}O) data indicate a preference for high angular momentum transfer similar to (but less pronounced than) that shown by the (α,t) and (α,^{3}He) reactions on the same targets. Contrary to a suggestion by Nickles et al., no strong evidence for a multi-step excitation of core-excited states is apparent from the present data.

I. INTRODUCTION

A. (α,t) Reactions

In recent years there have been many studies of proton configurations in the Zr-Mo region using the (^{3}He,d) reaction.[1-6] Most of this work concentrated on the N=50 nuclei ^{90}Zr and ^{92}Mo, although (^{3}He,d) data on all of the Zr isotopes was reported in one case.[4] A general feature of these (^{3}He,d) experiments is that very few high angular momentum transfers were observed except for the ground states ($g_{9/2}$). The shell model states expected in this region are $1g_{9/2}$, $1g_{7/2}$, $2d_{5/2}$, $2d_{3/2}$, $3s_{1/2}$, and $1h_{11/2}$ (hereafter radial quantum numbers will be suppressed), which should give rise to both ℓ=4 and ℓ=5 transitions to various excited states.

The locations of these ℓ=4 and ℓ=5 proton states are of interest for comparison with the detailed shell model calculations[7-9] which have been performed for this region. These calculations predict the existence of many high-spin levels at low excitation energies. Some of these levels have been observed in β-decay studies (e.g., ^{91}Mo $\longrightarrow$ ^{91}Nb (Ref. 10) and ^{95}Zr $\longrightarrow$ ^{95}Nb (Ref. 11)) and Coulomb excitation (e.g., ^{93}Nb (p,p'γ)[12]) but few have been seen in proton transfer.[1-6] Of course, some of these states have spins which cannot mix with the available single-proton states in this region, but others are expected[7-9] to be $9/2^+$ or $7/2^+$ and might mix with the $g_{9/2}$ or $g_{7/2}$ states and be observable in proton stripping.

The lack of such high angular momentum transitions in (^{3}He,d) is not surprising, since the semi-classical angular momentum transfer is rather low, $\vec{q} \times \vec{R} \approx 2$. (See Appendix A). In contrast, the expected

momentum transfer in (α,t) at 50 MeV is much larger due to the large negative Q-value associated with the reaction $(\vec{q} \times \vec{R} \approx 6)$. These numbers indicate that high angular momentum transitions are unfavorable in $(^3He,d)$ since the momentum mismatch is large, while for (α,t) the opposite is true and the low momentum transfers are unfavorable. Thus, a comparison of the relative strengths of states seen in both $(^3He,d)$ and (α,t) should give information on the locations of high angular momentum (ℓ = 4 or 5) proton states in this region. The targets used in this series of experiments are $^{90,91,92,94}Zr$ and ^{92}Mo. On all of these targets results from the two-nucleon transfer (α,d) reaction were obtained simultaneously.

B. (α,d) Reactions

Previous studies of (α,d) reactions on light and medium mass nuclei have shown that, in general, a few levels of the residual nucleus are preferentially populated.[13-18] The nature of these states has been shown to be [15-17]

$$\left[J_t + (j_1, j_2)_J\right] J_f \qquad (1)$$

where J_t is the target spin, j_1 and j_2 are the spins of the shell model states into which the two transferred nucleons are captured, and J_f is the spin of the final state formed from vector coupling J_t and J. This sort of configuration is consistent with the standard picture[19] of the reaction mechanism: a one step grazing collision in which the nucleons are transferred with no rearrangement of the core.

The configuration (1) is general to all two-nucleon stripping reactions such as (t,p), (^{3}He,p), and (α,d), although selection rules do, of course, limit the possibilities for the captured nucleons $(j_1, j_2)_J$. It has been shown[19] that two-nucleon transfer reactions are extremely sensitive to the details of the nuclear wave function, since the cross sections depend upon the degree to which the transferred nucleons are correlated in the final state. The (α,d) reaction evidences this form of selectivity but, in addition, there is a preference for large momentum transfer due to the very negative Q-value associated with the reaction. (See Appendix A.)

In all previous (α,d) experiments the strongest state was one in which $j_1=j_2=j$ (referred to as a "j^2" configuration) and $J=j_1+j_2=2j$

(referred to as a "stretched" configuration). For example in $^{12}C(\alpha,d)^{14}N$ the 9.0 MeV state was assigned the configuration $\left[^{12}C(0^+) + (d_{5/2})^2_{5^+}\right]_{5^+}$ and in $^{40}Ca(\alpha,d)^{42}Sc$ the 0.6 MeV state was assigned the configuration $\left[^{40}Ca(0^+) + (f_{7/2})^2_{7^+}\right]_{7^+}$ by Rivet et al.[15] Similarly the states in the Fe-Ni region have been associated with the $\left[\text{Target core} + (g_{9/2})^2_{9^+}\right]_{9^+}$ configuration.[16,17]

The high spin levels formed preferentially in the (α,d) reaction are expected to have relatively simple configurations, since there are no other nearby two-particle shell model states which can give the same spin. The $(f_{7/2})^2_{7^+}$ state in ^{42}Sc observed by Rivet et al.,[15] for example, cannot contain any other shell model configurations below $(g_{9/2})^2_{7^+}$ (which is far away in energy and thus unlikely to mix appreciably). The actual wave function of the strong (α,d) state may be rather complicated in nuclei some distance from closed shells, but as long as the complicated structure is due to J_t, that is, as long as the initial and final states differ only in that there is an additional pair of nucleons in the state $(j_1,j_2)_J$, we can still hope to learn something about the residual interaction of a specific shell model configuration. The observed[17] constancy of the empirical neutron-proton residual interaction in the large (α,d) state over a range of masses appears consistent with such an assumption.

The targets chosen for the present study are in the Zr-Mo region, since this region appears to be well-described by the shell model.[7-9] There are many possible high-spin shell model states which might be populated in (α,d) on these targets, e.g., $(\pi g_{9/2},\nu d_{5/2})_{7^+}$, $(\pi g_{9/2}, \nu g_{7/2})_{8^+}$, $(\pi g_{9/2},\nu h_{11/2})_{10^-}$, etc. All of these are approximately consistent

with the kinematic preference of the (α,d) reaction. For a 50 MeV α-particle beam the (α,d) reaction has a favored momentum transfer $\vec{q} \times \vec{R} \approx 8$. The technique employed here is the same as in previous searches: Systematic trends have been sought which can, with the aid of shell model predictions, indicate which possibility is most reasonable. (The assignments based on previous (α,d) systematics, summarized in Ref. 17, have been verified in many cases by spin assignments determined by other work.)[20-23]

At about the time this project was undertaken a new beam analysis system[24] was installed at the 88-in. cyclotron. The possibility for improved resolution made it attractive to repeat the earlier $^{14}N(\alpha,d)^{16}O$ experiment.[13,15] The interpretation of this experiment had been hampered by the fact that the ground state spin of ^{14}N is 1^+ and, according to equation (1), the expected $(d_{5/2})^2_{5^+}$ configuration splits into a 4^+, 5^+, 6^+ multiplet. Since a 6^+ state was known[25] to lie near one of the strong (α,d) states, it was important to obtain accurate widths and excitation energies for these states. With the 250 keV resolution attained previously,[13,15] this had not been possible. This reaction, while clearly outside the stated scope of this paper, is an interesting illustration of the systematics involved in (α,d) work and as such it will be included here.

C. Heavy Ion Reactions

There is presently a great deal of interest in the spectroscopic information obtainable from heavy ion induced transfer reactions.[26] In particular, the (^{16}O,^{15}N) reaction at 60 MeV on all of the even Zr isotopes has been reported.[27] This reaction was observed to strongly favor the capture of a $g_{9/2}$ proton by an undisturbed Zr core. (The ground state was in all cases a factor of 3 stronger than any other state.) This result suggests a preference for large angular momentum transfer similar to that shown by the (α,t) reaction. The preference for high angular momentum transfer can be understood qualitatively by estimating the favored momentum transfer as illustrated in Appendix A. In the case of a heavy ion beam the momentum transfer at the distance of closest approach is the relevant quantity to consider. If we use the estimate for the barrier height given by Becchetti et al.[28] we obtain a value of $\Delta L \approx 3$ at the maximum in the angular distribution ($\theta_{c.m.} = 70°$). Similar calculations for (α,t) at 50 MeV and (^3He,d) at 31 MeV (both at the grazing angle) give expected momentum transfers of about 4 and 0, respectively.

The Zr(^{16}O,^{15}N) results[27] were compared with the (^3He,d) data of Cates, Ball, and Newman[4] in order to determine which levels were populated by single-particle transitions. Several other states, not seen or seen weakly in (^3He,d) were interpreted as possible core-excited levels of the type $\left[Zr(2^+) \otimes \pi g_{9/2}\right]$ or $\left[Zr(3^-) \otimes \pi g_{9/2}\right]$. However, essentially all of the levels seen in the heavy ion work were also visible in the (α,t) reactions on the same targets.[29,30] To see whether the

apparent similarity of the (^{16}O,^{15}N) and (α,t) reactions held true at an energy somewhat further above the Coulomb barrier, spectra of the (^{16}O,^{15}N) reaction on targets of $^{90,91,94}Zr$, ^{92}Mo, and ^{93}Nb were obtained at a beam energy of 104 MeV. Data on the neutron transfer reaction (^{16}O,^{15}O) were obtained simultaneously. Since the angular distributions of all the states seen in the heavy ion experiment were expected[28] to be similar, an angular distribution was obtained only for the ^{90}Zr target. For the other targets spectra for both (^{16}O,^{15}N) and (^{16}O,^{15}O) were taken near the maximum of the angular distribution.

II. EXPERIMENTAL EQUIPMENT

A. α Particle Reactions

1. Cyclotron and Beam Optics

The experiments described here were done with the 40, 50, and 65 MeV α-particle beams of the Berkeley 88-inch sector-focused cyclotron. The transport system is shown in Fig. 1. The extracted cyclotron beam is made parallel with a quadrupole doublet (QS1), bent 20° by a switching magnet (M_s) and focused by a second quadrupole doublet (Q31) at the entrance slit (AS3A1) of the high-resolution analyzing magnets.[24] These magnets are operated so that the first magnet is the energy analyzer and the second magnet serves to remove any slit-scattered particles which are created at the analyzing slit (AS41). Object and image slit widths of 1 mm were typically employed. The beam transmitted through these slits, when measured with the second magnet, was found to have a resolution, $\Delta E/E$, of 0.04%. The final analyzing slit (AS42) was always left open (≈ 1 inch) during experiments. After energy analysis the beam was bent 7 1/2° (M43) and brought to a double focus at the target position by means of two quadrupole doublets (Q4A1 and Q4A2). The current was monitored by a split Faraday cup which was connected to a current integrator in the counting area. Equal currents were maintained on each side of the Faraday cup to insure a constant beam angle. Typical currents on target ranged from about 0.25 to 1 μA. At each focus it was possible to view the beam on Al_2O_3 plates via a closed circuit television system.

Energy calibration of the analyzing magnets was done by measuring[31] the position of the 14.232 MeV, T = 3/2 resonance in $^{12}C(p,p)$ using beams of protons, H_2^+, and H_3^+. This calibrated the magnets up to the maximum

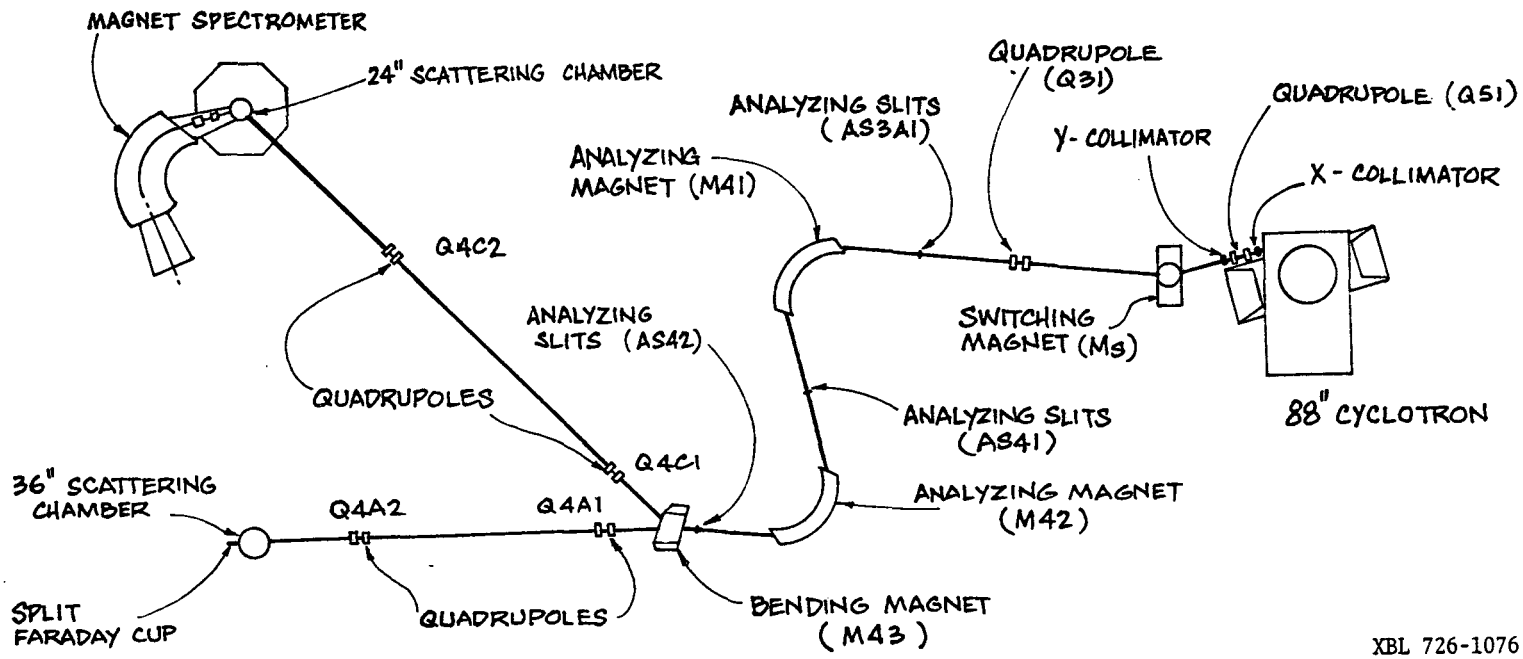

Fig. 1. Beam transport system for the high-resolution (Cave 4) experimental area of the Berkeley 88-inch cyclotron. Both the 36-inch scattering chamber (Cave 4A) and spectrometer (Cave 4C) layouts are shown.

$B\rho$ of the cyclotron. (The magnetic rigidity of 42.7 MeV H_3^+ corresponds to 128 MeV protons or α particles.) Yield curves for the three beams are shown in Fig. 2. The reproducibility of these measurements was about 0.5 keV in proton energy. Since the beams used here are close to the H_2^+ calibration point, the absolute beam energies are expected to be correct to better than 10 keV.

2. Scattering Chamber

A schematic diagram of the 36" scattering chamber is shown in Fig. 3. Since this apparatus has been described in detail previously,[32] only a brief outline will be given here. Recent modifications of the scattering chamber will be discussed more carefully. The solid targets were mounted on aluminum frames with a 3/4" hole in the center. Up to six frames could be placed in a target ladder at the center of the scattering chamber, but one of these positions was always used for an aluminum oxide TV target. Controls from the counting area allowed both the vertical height and rotation of the targets to be set remotely. The detector holders were clamped on a movable hub which was also controlled remotely from the counting area. Positions of all remotely controlled devices in the scattering chamber were determined by a digital voltmeter. The precision in setting the counter angle by this method was about 0.1°.

Cooling of the detectors was provided by thermoelectric coolers attached to the back of the counter mounts. These coolers, along with their water-cooled heat sinks, allowed the counters to be run at about -25°C. A convenient feature of this technique is that the coolers are reversible. Thus, by changing the polarity of the power supply, it was possible to warm the detectors back to room temperature in about 15 minutes.

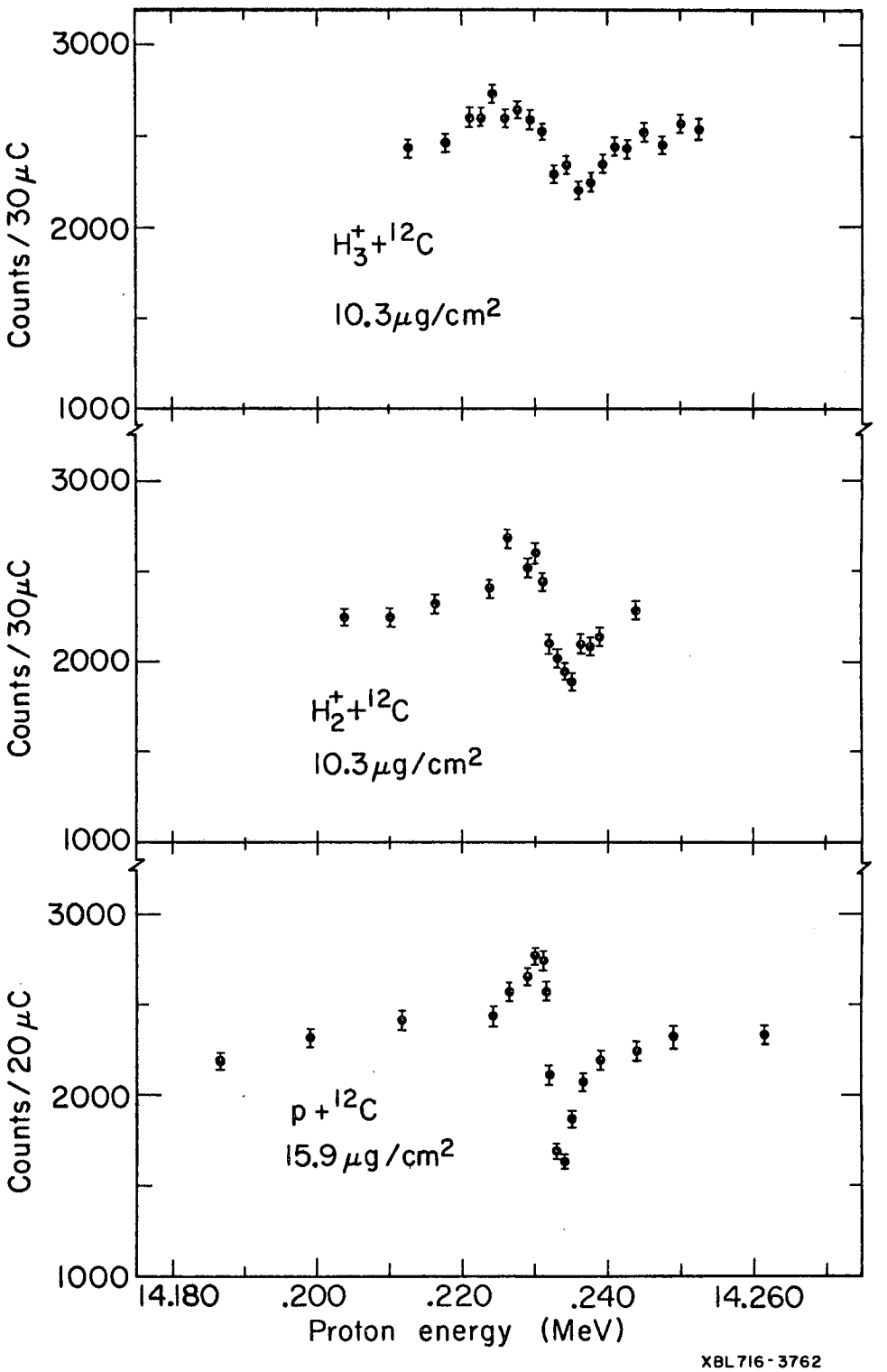

Fig. 2. Proton yield curves at $\theta_\ell = 165°$ for the bombardment of carbon targets with beams of protons and the molecular hydrogen ions H_2^+ and H_3^+. The target thickness and integrated charge are shown for each experiment separately. (The resonance corresponds to the $J^\pi = 3/2^-$, $T = 3/2$ level in ^{13}N at $E_x = 15.066$ MeV.)

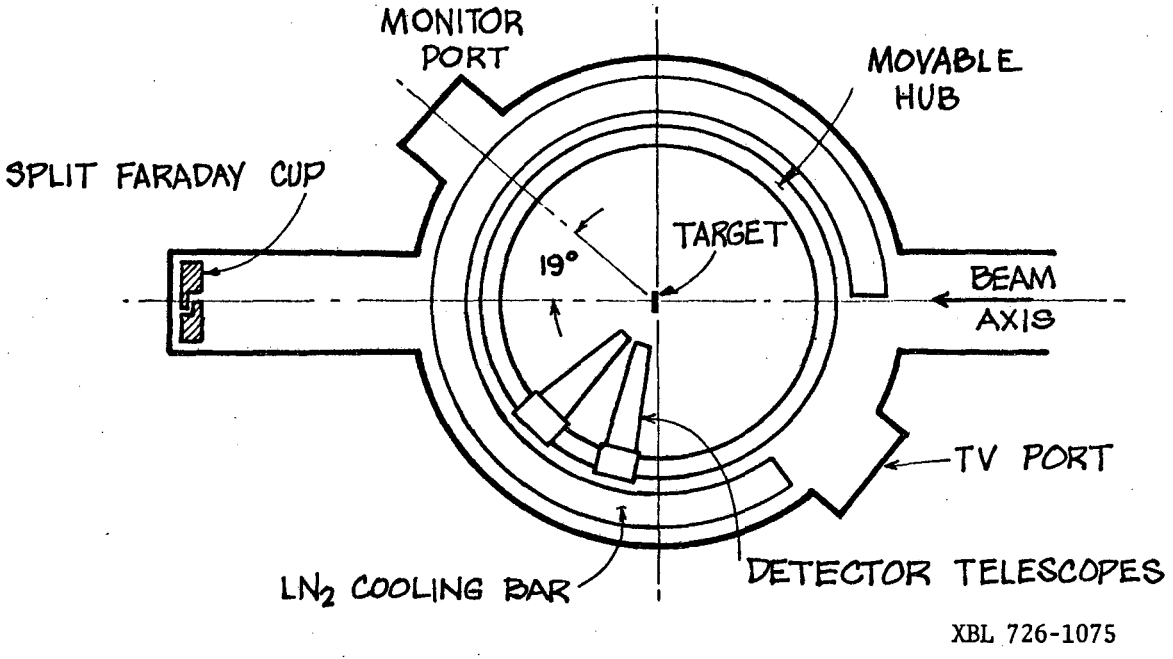

Fig. 3. Schematic diagram of the 36-inch scattering chamber.

For the $^{14}N(\alpha,d)$ experiment a gas target was used. This target was mounted in place of the solid-target ladder at the center of the chamber. The shaft on which it was mounted was hollow and terminated in an external vacuum fitting to which the gas handling apparatus was attached. The gas cell used was a modified version of that described in Ref. 32. It consisted of a stainless steel cylinder 7.6 cm in diameter and 2.5 cm high with an exit foil of 2.1 mg/cm^2 Havar covering 315°. The remaining solid section of the cell was bored out and fitted with a hollow brass plug on the end of which a 0.22 mg/cm^2 Ni entrance foil was epoxied. A circular tantalum collimator 3.8 mm in diameter was used to define the beam entering the target. This collimator was electrically insulated from the rest of the cell in order to monitor the untransmitted beam. By careful attention to the beam optics it was possible to keep the beam loss below 1% during the course of the run. Several antiscattering slits were also employed to further define the beam and to protect the edge of the thin entrance foil.

A modification of the chamber not described in Ref. 32 was the addition of a liquid nitrogen cooling bar (see Fig. 3). This modification was made specifically for the purpose of testing Ge(Li) counters[33] for use in charged particle spectroscopy. However, the holder designed for use with the Ge(Li) system was also employed for a 65 MeV α-particle run in conjunction with an experimental 1 cm thick Si(Li) detector fabricated at this laboratory. This special counter holder, shown in Figs. 4 and 5, could be clamped to the cold bar by means of a stainless steel bellows which was expanded with compressed air. The holder itself was mounted

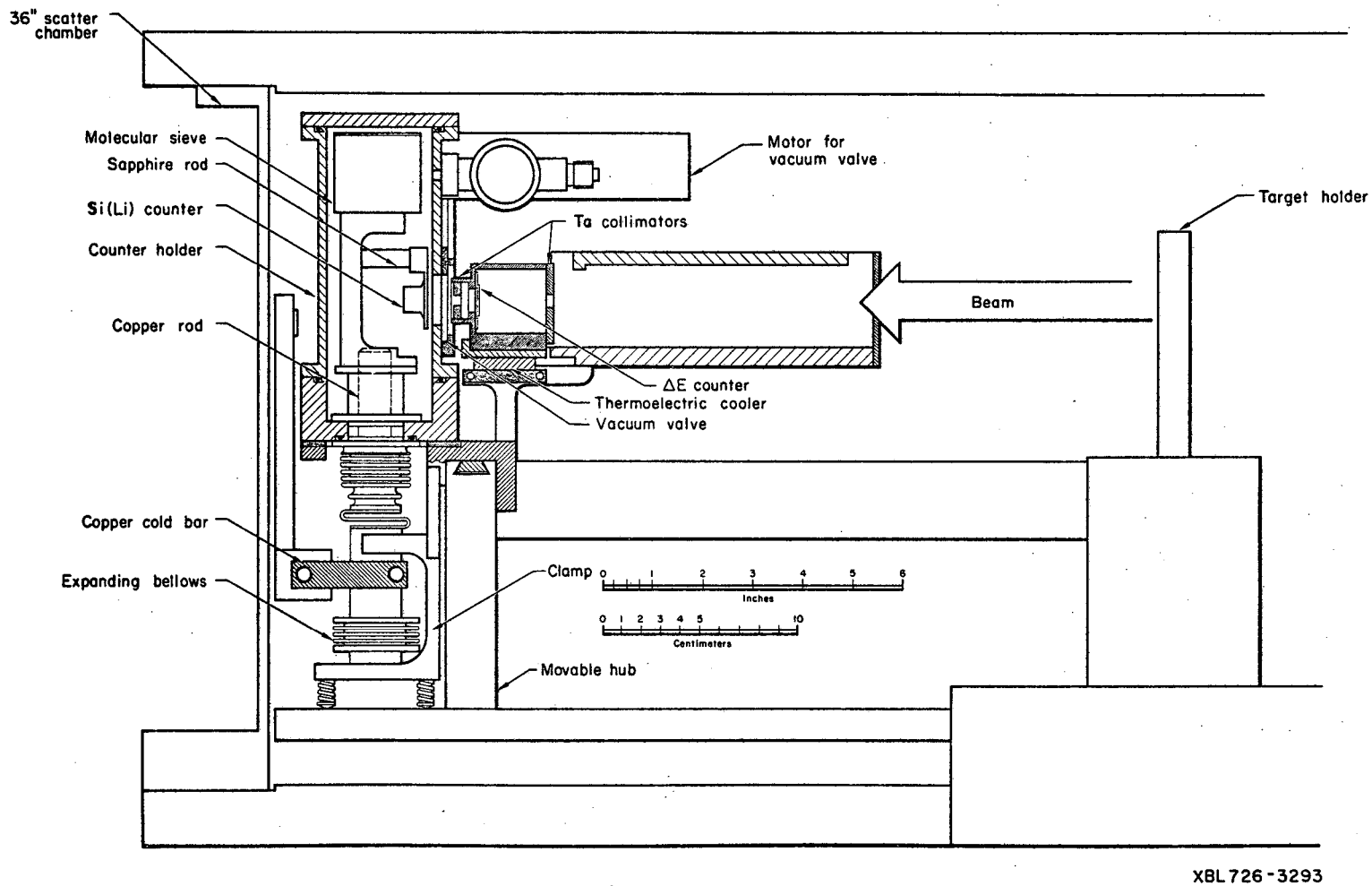

Fig. 4. Schematic diagram of the counter holder used with liquid nitrogen cooled counters.

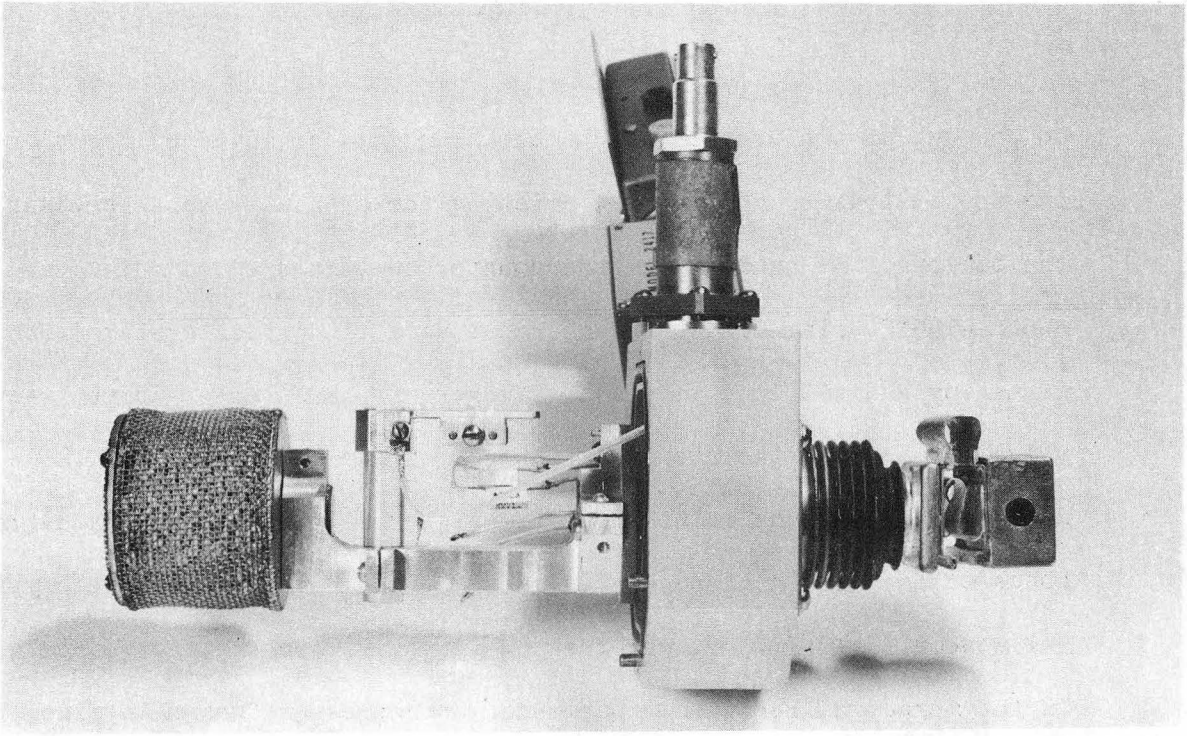

XBB 6812-7636

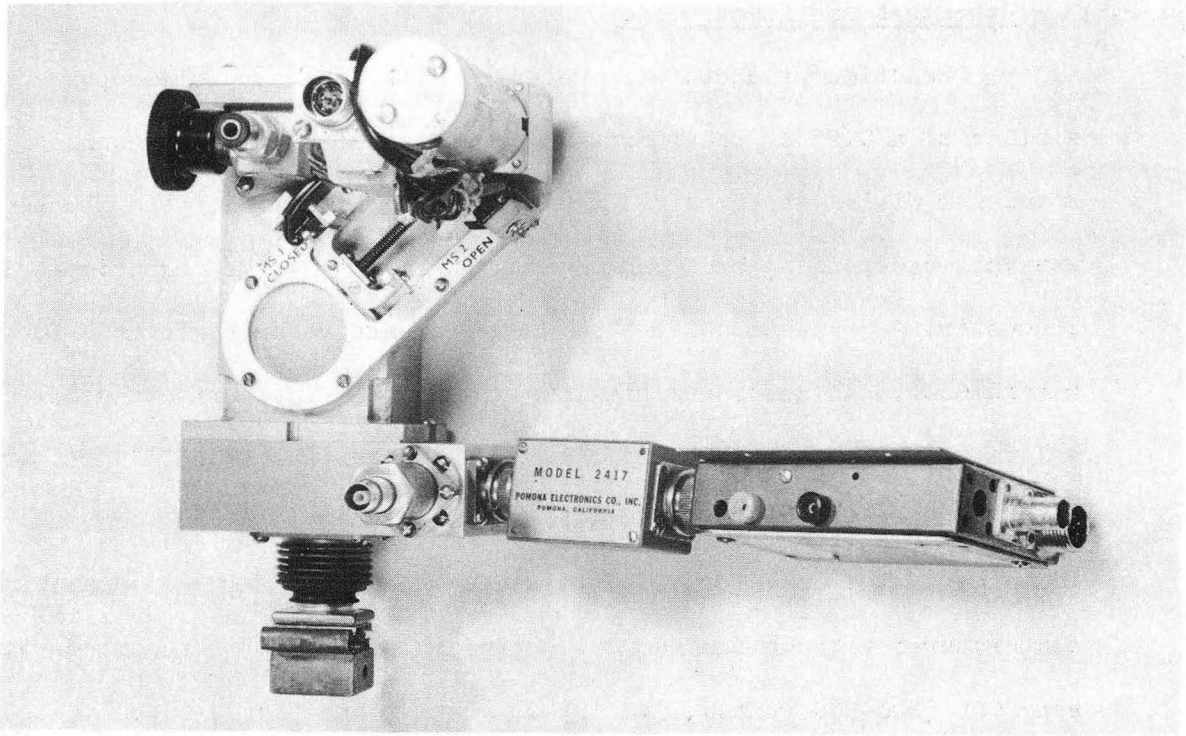

XBB 6812-7634

Fig. 5. Photographs of the liquid nitrogen cooled counter holder and preamp. The internal features are labelled in Fig. 4.

on the hub of the scattering chamber and could be moved by first evacuating the bellows to unclamp it, rotating the hub, and then repressurizing the bellows. At equilibrium the counter temperature was maintained at about -150°C. The holder was operated as a windowless system (both for germanium and silicon systems). However, it had a motor-driven vacuum valve which could isolate the counter from the chamber vacuum while the molecular sieve pump maintained a low internal pressure. An additional bonus of the liquid nitrogen bar was that the chamber pressure, typically about 5×10^{-6} Torr, was greatly improved when the bar was cold. In the magnet calibration experiment[31] the pressure was maintained at about 7×10^{-7} Torr by this method.

3. Detectors and Electronics

Reaction products were detected with detector telescopes consisting of a 0.25 mm phosphorus-diffused transmission (ΔE) counter and a thicker Si(Li) stopping (E) counter. The thickness of the E detector was varied depending on the beam energy. For the 40 MeV experiment 3 mm E counters were used, while 5 mm counters were required for the 50 MeV experiments. As mentioned previously, the 65 MeV experiment utilized a 1 cm Si(Li) counter. This latter counter was run at -150°C rather than the standard -25°C because the bias voltage required for best performance of the detector, 2750 volts, could not be maintained at higher temperatures without breakdowns. Standard voltages for the other detectors are: ΔE (200-300 volts), 3mm E (400 volts), and 5mm E (1,000 volts). In all cases the leakage currents of the cooled detectors were about 0.1 μA or less. Normally two telescopes were mounted on the hub of the

scattering chamber with a fixed angular increment (usually 20°) between them. For the 65 MeV experiment only one telescope was available. The solid angle of each telescope was defined by a rectangular collimator located in front of the ΔE counter, at a distance of about 13 inches from the target. A second rectangular collimator, about 3 inches from the center of the target, was required to adequately define the target thickness for the gas target run. A discussion of the geometrical considerations involved in the gas target case has been given by Maples.[34] A typical solid angle for the solid target experiments was about 1×10^{-4} sr.

In addition to these systems a monitor counter, which was mounted in a special port in the scattering chamber (see Fig. 3), was also employed. This counter allowed a check on the constancy of the product of beam current × target thickness and precluded any difficulties due to disintegration of the target by the beam. It was also utilized in determing the dead time of the system as will be described below.

The block diagram of the electronics, shown in Fig. 6 for a single ΔE-E system, is a modified version of the system used previously.[32] The important changes are the use of the newer high-rate amplifier systems[35] and the inclusion of a pile-up rejector. The amplifier produces two output signals. The "fast" output is a singly differentiated signal. It is not integrated and thus exhibits the fast rise time (≈ 50 ns) of the preamp signal. In our system the fast output is used for timing and is inspected by the pile-up rejector to determine whether the event is "valid." The requirements for a valid output from the pile-up rejector are, (1) that a signal must not have been preceded by another signal within the

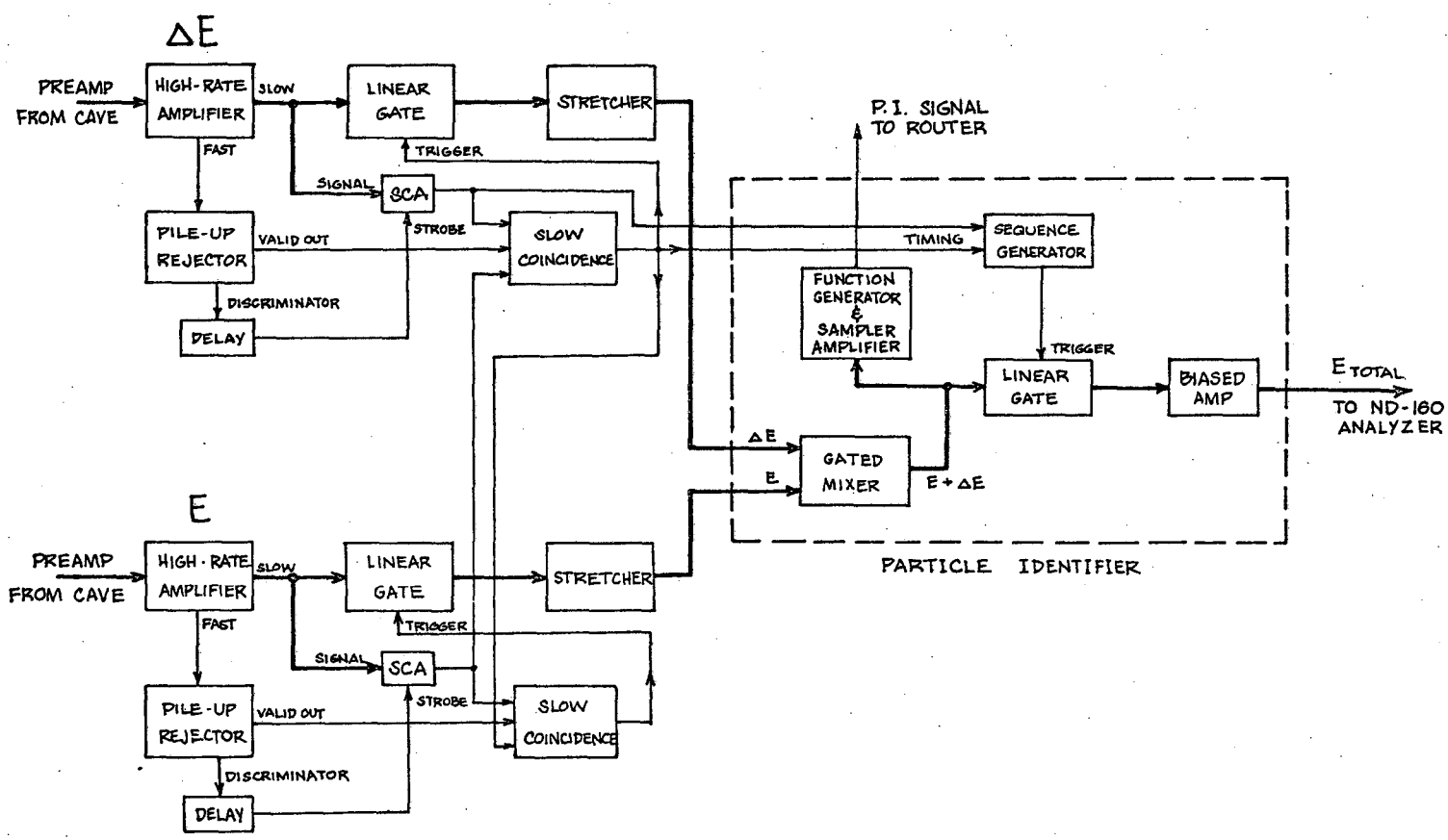

XBL 726-1079

Fig. 6. Block diagram of the particle identifier electronics.

inspection time (variable from 5 to 25 μs), and (2) that a second pulse must not have occurred during the rise time and for 0.5 μs after the peak of the signal being considered. For these experiments an inspection time of 20 μs was standard. The "slow" output, after differentiation, is shaped by an active integrator which is roughly a series of RC integrations, all with the same time constant. The system used here resulted in a semi-Gaussian pulse with a peaking time of 2 μs. It is this signal which is used for energy analysis. The high-rate aspects of this amplifier are not particularly relevant for this application and will not be discussed here. The choice of these amplifiers was based on their improved noise characteristics compared to previous systems.

A Goulding-Landis particle identifier[36] was used to generate a signal approximately proportional to MZ^2 of the detected particle. This signal was then used to route the total energy signals into different 1024-channel groups of a Nuclear Data analyzer. After each run the analyzer memory was dumped onto magnetic tape by a PDP-5 computer. Final data analysis was done using the SCC-660 and CDC-6600 computers.

The overall dead time of the system was conveniently measured by using a pulse generator which injects charge directly into the preamp. By appropriate choices of ΔE and E pulser gains it was possible to simulate a particle of a given type so that the pulser signal could be stored in the analyzer. (The energy of the pulser was generally chosen to put it above the ground state peak of whatever reaction it was simulating.) If the pulser is triggered by a signal from the monitor counter (generally scaled down by a factor of 10 or 100) then it goes into the preamp at a rate proportional to the actual beam intensity, the same as the real

signals do. Thus, it suffers the same probability for getting "lost" as the real signals. The dead time correction can be easily obtained by comparing the total number of pulser triggers (recorded in a scaler) with the number of pulser counts actually stored in the analyzer:

$$C = \frac{\Sigma \text{ pulser triggers}}{\Sigma \text{ pulser signals stored}}$$

This factor multiplies the observed number of events stored in the analyzer to give the actual number of events required for cross section calculations.

4. Targets

The solid targets used in these experiments were self-supporting metal foils which were prepared by evaporation. The materials were obtained from the Stable Isotopes Division of Oak Ridge National Laboratory. Target compositions are summarized in Table I. The ^{14}N target consisted of natural nitrogen (99.6% ^{14}N) at a pressure of about 30 Torr. This rather low pressure was dictated by the fact that only a single thin entrance foil was available and its breaking pressure was completely unknown.

Table I. Target Composition

Target	Nominal Thickness (mg/cm^2)	Isotopic Abundance (At. %)				
		Zr Targets				
		^{90}Zr	^{91}Zr	^{92}Zr	^{94}Zr	^{96}Zr
^{90}Zr	0.20	97.8	0.95	0.65	0.49	<0.1
^{91}Zr	0.30	4.95	91.85	2.51	0.62	0.07
^{92}Zr	0.40	2.86	1.29	94.57	1.15	0.14
^{94}Zr	0.25	2.08	0.69	0.92	96.07	0.24
		Mo Target				
		^{92}Mo	^{94}Mo	^{95}Mo	^{96}Mo	^{97}Mo	^{98}Mo	^{100}Mo
^{92}Mo	0.30	98.27	0.46	0.37	0.26	0.13	0.27	0.25

B. Heavy Ion Reactions

1. Beam Optics

The heavy ion experiments described in this paper made use of the new magnetic spectrometer system at the 88-inch cyclotron.[37] The optics layout described in Sec. II-A1 is essentially the same as the one used here up to the last bending magnet (see Fig. 1). For the spectrometer experiments the beam is bent 42° (M43) and then focused at the target position by two quadrupole doublets (Q4C1 and Q4C2). The beam is stopped in a split Faraday cup located inside the 24" scattering chamber. This arrangement allows data to be taken at very forward angles ($\theta_\ell \approx 10°$). The object and image slit widths of the beam analysis system were 2.5 mm for these experiments. (This was required in order to transmit a maximum amount of beam to the target, since the cyclotron produces appreciably lower currents of heavy ions than α particles.) The beam resolution, $\Delta E/E$, is thus expected to be about 0.1%. Typical currents of ^{16}O in the Faraday cup (measured in the 8^+ charge state after passing through the target) ranged from 0.1 - 0.5 μA.

Due to the fact that the analyzing slits AS3A1 and AS41 were replaced subsequent to the light ion experiments, the validity of the previously mentioned energy calibration[31] is uncertain. The beam energy measurement based on the old calibration gives $E(^{16}O) = 104$ MeV. The error in this value is not known with certainty, but should be less than 100-200 keV.

2. Scattering Chamber

The design of the 24" scattering chamber is similar to that of the 36" scattering chamber (Sec. II-A2). The target ladder holds up to

six target frames, one of which contains an Al_2O_3 plate for viewing the beam. Two monitor counters were employed during experiments. One was mounted in a fixed position (about 20°) while the other was mounted on the movable floor of the chamber. Due to space limitations this latter monitor was generally at a rather back angle (40-50°) and thus had a very low counting rate. The targets and monitor counter could be positioned remotely and their positions read by means of a digital voltmeter in the counting area.

The most noteworthy feature of the scattering chamber is the sliding spring-steel band which forms the vacuum connection to the spectrometer. This band allows a continuous range of scattering angles spanning 110° to be covered. By rotating the scattering chamber itself it is easy to change the angular range. The ranges normally used are 15 to 125° or -30 to +80°, with positive angles defined as being to the left of the beam line looking downstream. At each end the band is attached to a shaft which is driven by an electric motor. The commands to the motors are given by various microswitches which are connected mechanically to the motion of the spectrometer. With a system of this type there is a strong tendency for the band to leak while it is being moved. (This is probably caused by the band dragging the O-ring slightly.) For this reason certain precautions, such as closing valves and removing bias from the monitor counters, were normally followed when changing spectrometer angles. Fortunately, it was almost always possible to regain a good vacuum once the new spectrometer position had been reached.

3. Spectrometer

A schematic drawing of the spectrometer and the 24" scattering chamber is shown in Fig. 7. The uniform field sector magnet has a central radius of 1.775 m and a bending angle of 114.5°. Table II lists the general properties of the system. The spectrometer is rotated by inflating air pads under the structure so that it can be moved with a small motor near the outside edge. As mentioned above, after the magnet moves a short distance it mechanically activates one of the two motors connected to the sliding metal band. The band then moves to catch up. Due to the vacuum problems associated with changing angles the controls for this motion are located only in the cave area, although the digital voltmeter position readout is available in the counting room. When set at a scattering angle the magnet rests on two flat steel rails, with the scattering chamber mounted at the center of rotation.

There are several unusual features of the spectrometer which deserve special mention. For example, the sector magnet has a non-normal entry angle of 37° in order to achieve vertical focusing. This technique is similar to that used in the design of the beam analysis magnets,[24] which have a non-normal exit as well as entry angle. The effects of edge-focusing have been discussed by Enge.[38]

The original design of the spectrometer[39] was made with a view toward a live detection system rather than, for example, nuclear emulsions. For this reason it was desirable to have a focal plane located normal to the particle trajectories rather than at a steep angle as is more common with plates. (If a particle enters a live focal plane detector at an

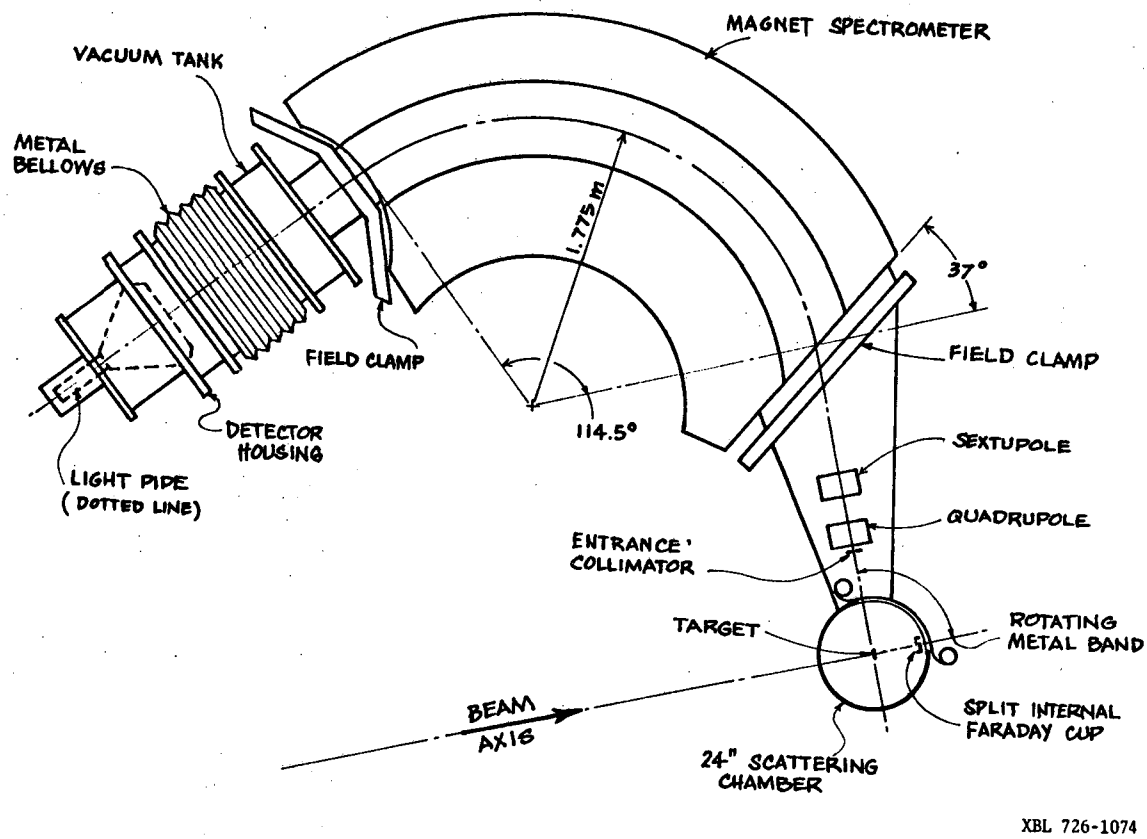

Fig. 7. Schematic diagram of the 24-inch scattering chamber and magnetic spectrometer.

Table II. Parameters of the 88-inch cyclotron magnetic spectrometer.

Magnet gap	10.95 cm
Radius	1.65 - 1.90 m
Focal plane length	55 cm
Vertical acceptance	100 mrad
Radial acceptance	20 mrad
Solid angle (maximum)	2 msr
Energy range	30%
Mass-energy product	270 MeV - amu
Dispersion	3.3 - 4.2 m
Radial magnification	0.33 - 0.40
Vertical magnification	4.7
Angular range (total)	+125 to -180°
Angular range (ext. Faraday cup)	+15 to 125° -55 to -165°
Angle of incidence on focal plane	-11 to +10°
Resolving power $\frac{E}{\Delta E}$ at $\Delta\Omega$ = 1 msr	3,000
Maximum resolving power	10,000

angle θ with respect to normal entry, the width of the position signal is broadened roughly by an amount t × tan θ, where t is the counter thickness. For large angles this might easily be the limiting factor in the position resolution.) To accomplish this "rotation" of the focal surface a negative radius of curvature (r = -0.8 m) was used at the exit of the sector magnet.

There are several advantages of the spectrometer over solid-state detectors. One is that it has a relatively large solid angle. This is important for heavy ion reactions because the available beam intensity is low. The solid angle used here was about 0.9 msr, compared with 0.1 msr for the detector experiments described above (Sec. II-A3). However, at high beam energies the slopes of angular distributions are often quite steep. This makes a large acceptance angle in the scattering plane undesirable. The problem is avoided here by using a large vertical acceptance angle while keeping the angle in the scattering plane small. The angles are defined by horizontal and vertical slits located about 63 cm from the target. During these experiments a horizontal gap of 0.7 cm and a vertical gap of 5.1 cm were used, corresponding to horizontal and vertical acceptance angles of about 0.6° and 4.6°, respectively. The use of a large vertical angle is facilitated by using a single quadrupole lens just after the defining collimators. The quadrupole is vertically focusing and "collects" the scattered particles to keep them from hitting the magnet poles. (The vertical focus in the focal plane is still provided mainly by the edge focusing of the sector magnet.) Of course, there must be some loss of solid angle in the horizontal plane due to

the defocusing of the quadrupole lens, but the overall gain is still substantial. The idea is similar to one proposed by Enge[40] except that here the quadrupole is not the only vertically focusing element. One drawback in this technique is that the large vertical size of the beam makes 2nd-order effects important to the resolution. In this case the calculations indicate[39] that the most important 2nd-order term is connected with the angular divergence $(y_0')^2$. The sextupole, which has no first-order properties[41] (i.e., it is a drift space in first order), is adjusted to correct for this term.

Another advantage of the spectrometer is that it can be used in such a way as to compensate for the energy spread in the incident beam ("dispersion matching"). This was convenient for these experiments since the low heavy ion currents available from the cyclotron make it impractical to use a well-analyzed beam. Also, by moving the focal surface it is possible to eliminate the resolution contribution due to the kinematics of the reaction, i.e., due to the change in outgoing energy as a function of scattering angle ("kinematic compensation"). These compensation techniques have been discussed in detail by Hendrie.[42] The change in focal length required for kinematic compensation is given approximately by:

$$\Delta L = -KMD$$

where M and D are the magnification and dispersion of the spectrometer and K is a kinematic factor which describes the amount of Doppler broadening. Specifically,

$$K = \left| \frac{1}{p} \frac{dp}{d\theta} \right|$$

For the $^{90}Zr(^{16}O,^{15}N)^{91}Nb$ (g.s.) reaction at 104 MeV, K=0.08 at 25° and (using average parameters from Table II)

$$\Delta L = -(0.08)\ (-0.365)\ (3.75\times10^{2})$$
$$= 11 \text{ cm.}$$

The kinematic compensation will introduce a rotation as well as a displacement of the focal plane since ΔL depends on p, but the former effect is much smaller and can generally be ignored.

The capability of performing these compensations, which are unavailable to counters, makes the spectrometer a very powerful means of studying heavy ion reactions. As will be discussed below, the ability to identify different heavy ion species is also an area where the spectrometer compares favorably to present solid-state counter techniques.

4. Detector and Electronics

The position-sensitive detector used in conjunction with the spectrometer is of the Borkowski-Kopp design.[43] It consists of a proportional counter 1 cm deep with anodes made from high-resistance carbon-coated quartz wires.[44] The vertical magnification of our spectrometer (see Table II) dictated a rather large vertical height for the focal plane detector in order to take full advantage of the increased solid angle of the system. Similarly, the dispersion of the magnet implies a total focal plane length (assuming a 30% energy range) of nearly 60 cm. With these facts in mind, the counter was designed with 6 resistive wires, 45 cm long, mounted vertically in the focal plane 1 cm apart. The detector, shown in Figs. 8 and 9, is mounted on a movable table with a bellows connecting it to the spectrometer vacuum chamber. In this way it can be

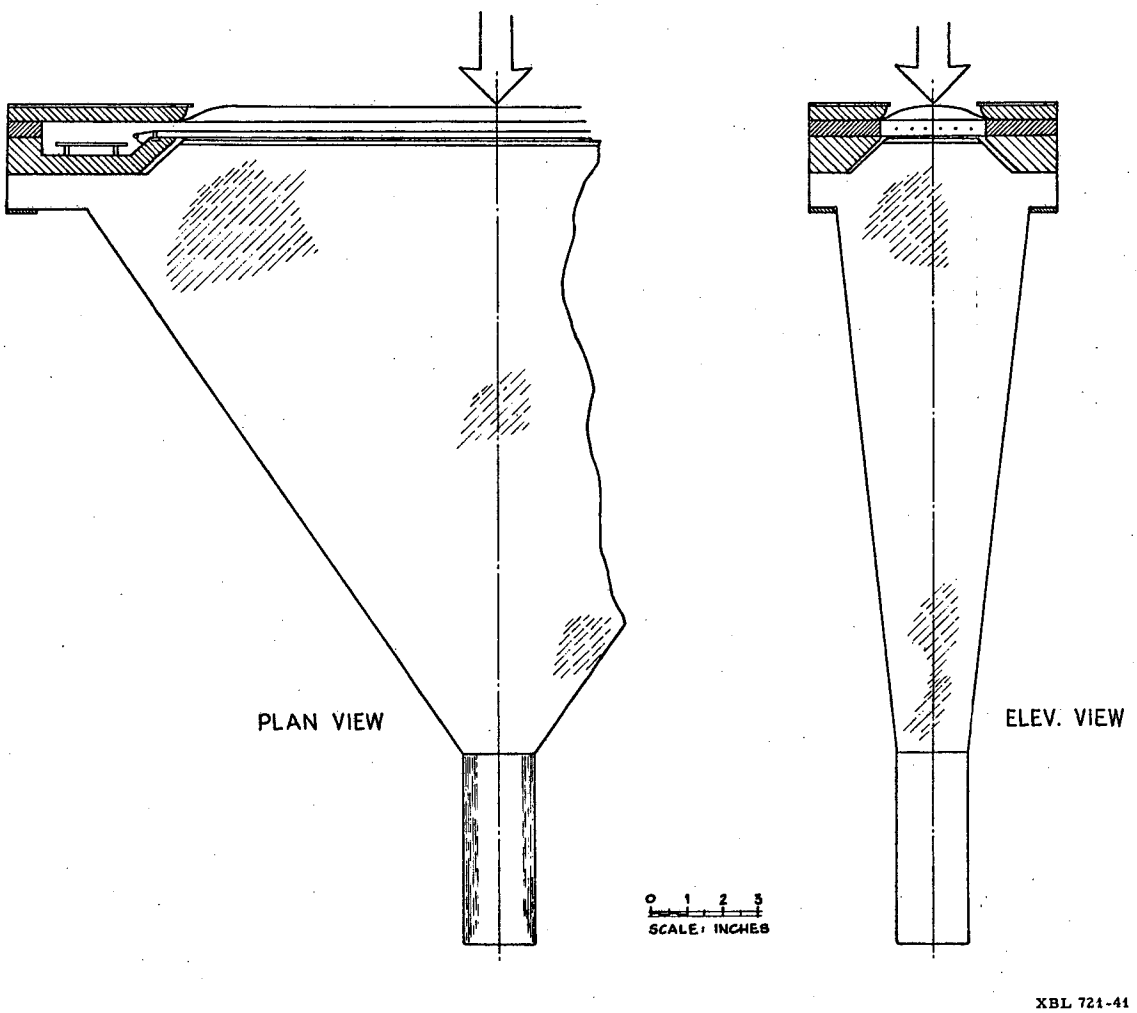

Fig. 8. General view of the heavy ion focal plane detector. The operating position of the counter system is indicated in Fig. 7.

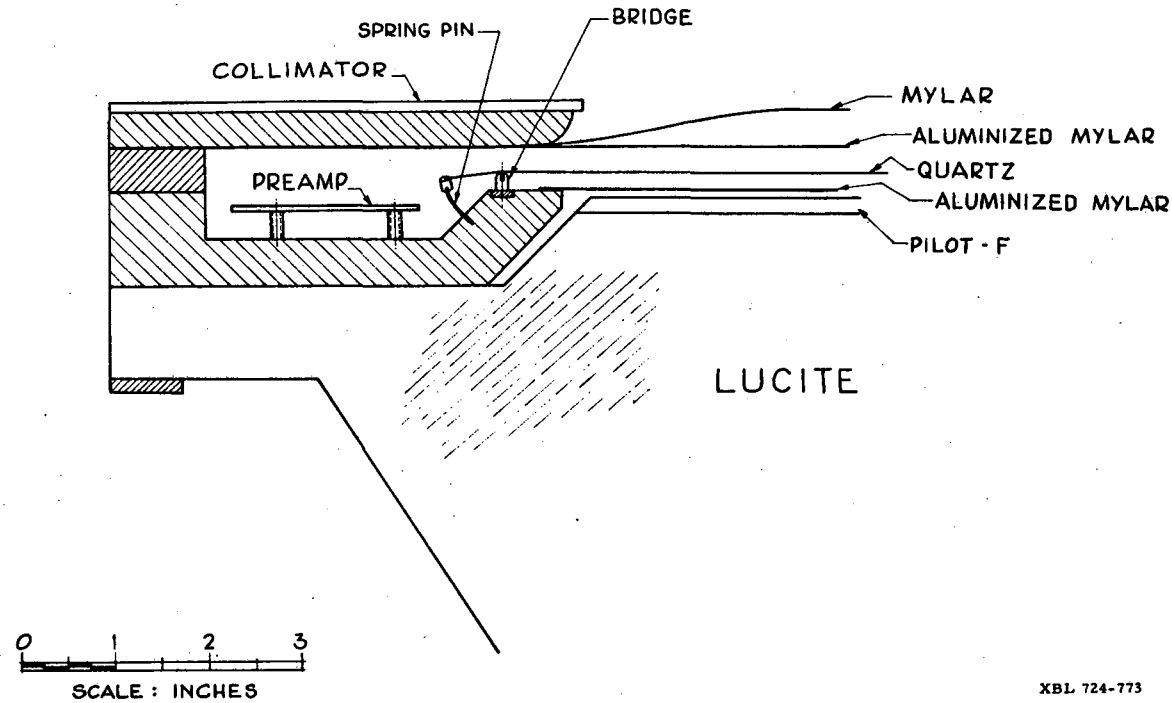

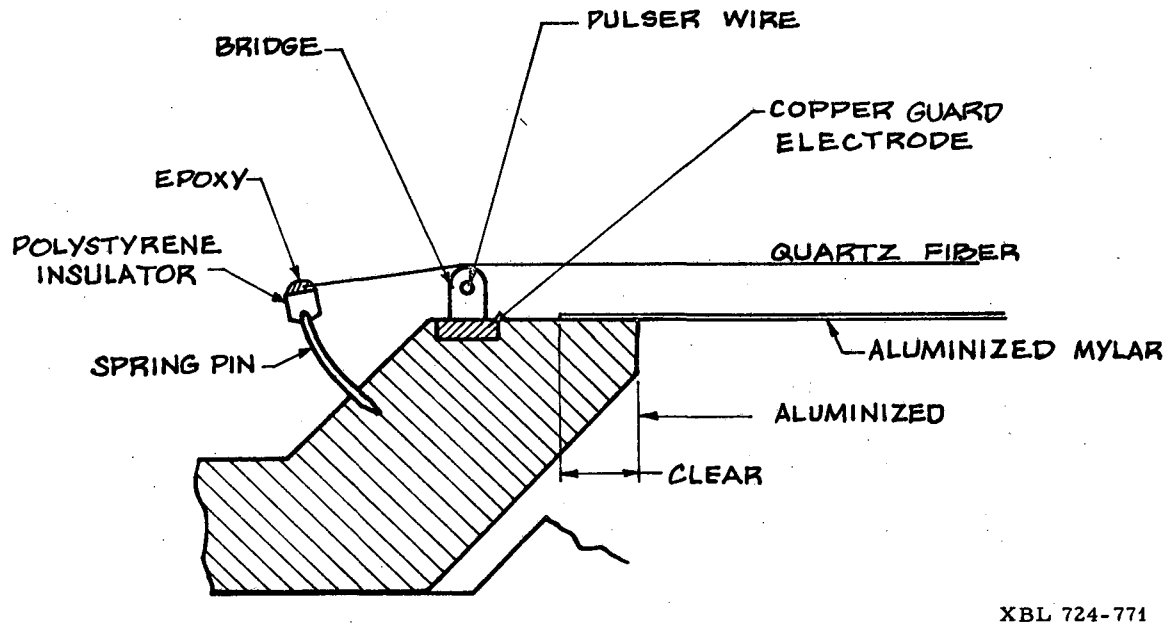

Fig. 9. Detail of one end of the proportional counter. The support for the quartz fiber is enlarged in the lower half of the figure.

moved to the appropriate kinematically compensated focal plane. The total movable range of the bellows is about 30 cm. If more range is required for the compensation, spacers can be added to extend the distance between the bellows and the magnet exit.

The counter was normally run at a pressure of 0.2 atm with a mixture of 93% Ar and 7% CH_4. Gas flows through the counter continuously and is evacuated by a small mechanical pump on the exit side. The gas pressure is controlled by a regulator on the inlet side. Both sides of the detector have pressure-interlocked solenoid valves which isolate it from the gas inlet and relief pump in case of an accident. The front and back high-voltage electrodes are formed from 0.006 mm aluminized mylar. For this experiment the counter was run at 620 volts. In order to insure a parallel sensitive area for the detector (which is essential for $\Delta E/\Delta X$ measurement), the pressure is contained by a separate mylar window 0.012 mm thick which lies in front of the first electrode.

Each of the 6 wires has a voltage-sensitive preamp at both ends, making a total of 12 preamps required for the detector. As has been noted by other groups working with detectors of this type, it is necessary to have the preamps close to the wires to minimize the extra capacitance.[45,46] For this reason the first stage of each preamp is located inside the detector housing, where it is connected directly to the wire. Details of the construction of the counter and preamps as well as recent improvements in their operation may be found in Ref. 47.

The counter system used here has an additional feature not found on other versions of the device.[43,45,46] Behind the rear aluminized-mylar

electrode there is a plastic scintillator which covers the whole active area of the proportional counter. The output of the scintillator is transmitted via a lucite light pipe (see Figs. 7 and 8) to a phototube (RCA 8575) operated at about 2 kV. Signals from the phototube provide time-of-flight information which is used for particle identification. Altogether, four signals are obtained from the detector system: right and left proportional counter preamps, phototube dynode, and phototube anode.

A block diagram of the electronics is shown in Fig. 10. In order to simplify the connections between the cave and the counting area, some of the logic is done at the detector. The signals from the right and left preamps go through (separate) mixers so that only two proportional counter signals ("right" and "left") need be sent to the counting room. Additionally, a routing signal is coded which provides information on which wire detected the event. A routing output is not generated unless the sum of the two preamp pulses exceeds a threshold which is set remotely from the counting room. The routing signal is given as a 3-digit binary number (i.e., three signals, "1", "2", and "4" are sent to the counting area) which corresponds to a number from 0 to 7. If a single wire detects an event the routing signal corresponds to the wire number (from 1 to 6). A route 7 corresponds to an event detected by two or more wires simultaneously and, as mentioned, a 0 route corresponds to a signal below threshold. The routing signal thus generated is used both for the ND-160 analyzer and for the computer so that the information from individual wires can be stored separately. Routes 0 and 7 are not stored by the computer but

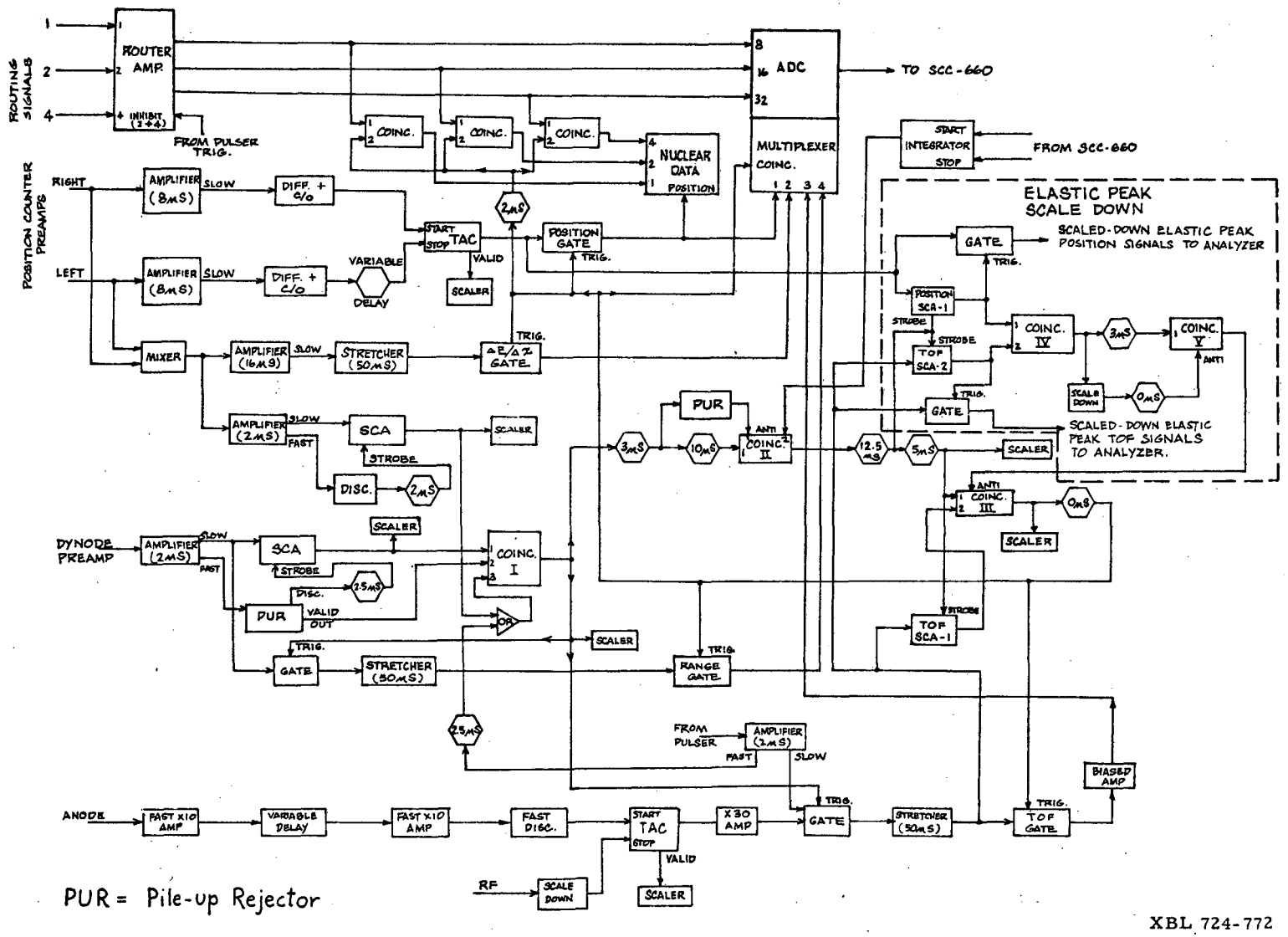

XBL 724-772

Fig. 10. Block diagram of the electronics used in conjunction with the heavy ion focal plane detector system. The various delay times are indicated in the hexagonal boxes.

they are in the analyzer, which is run in an 8 x 512 routing mode with no coincidence requirement, thus allowing unrouted events to be stored in the first 512-channel group.

The electronic logic illustrated in Fig. 10 is basically straightforward. Most of the complications arise due to the widely different timing of the four signals. (The signals must all arrive at the multiplexer simultaneously.) This aspect will not be discussed in detail here. The right and left preamp signals from the proportional counter are used both for position and $\Delta E/\Delta X$ information. The position information comes from a measurement of the risetime difference between the signals at the two ends of a wire. The difference in risetime is due to the fact that the counter can be viewed as a distributed RC integrator.[43] (The resistance is that of the central wire and the capacitance is between the wire and the high-voltage electrodes. In our case we have $R = 8k\Omega/mm$ and $C \approx 10^{-2}$pf/mm.) The risetime measurement is performed by first shaping the preamp signals with high-rate amplifiers (see Sec. II-A3) having 8 μs peaking times, and then differentiating the amplifier outputs. The bi-polar signals thus generated are sent to cross-over discriminators whose outputs are used to start and stop a time-to-amplitude converter (TAC). An additional delay of about 9 μs is used for the stop signal to insure that it is always preceded by a start signal. For the system illustrated in Fig. 10, the TAC output is proportional to $B\rho$, i.e., a large $B\rho$ gives a large TAC signal and vice versa. Typical resolution for the $(^{16}O,^{15}N)$ data was about 4 mm or 200 keV.

The $\Delta E/\Delta X$ signal is obtained by summing the right and left preamp outputs and then shaping the signal with a high-rate amplifier having a 16 μs peaking time. The purpose of the long time-constant is to obtain a signal which is essentially independent of position. Typical $\Delta E/\Delta X$ resolution was about 10%.

The signal from the last dynode of the phototube serves to define a real event when in coincidence with the signal from the proportional counter (Coinc. I). Originally, it was hoped to obtain energy information from this signal. For highly ionizing particles, it was expected that the light output from the scintillator would be saturated and that a signal depending on path length (or range) would result. However, it turns out that the response is actually reasonably linear with energy for ^{12}C and ^{16}O ions.[48] Unfortunately, the resolution obtained for ^{16}O ions ($\gtrsim$ 20%) was insufficient to resolve different peaks in the spectrum. Thus, the "range" signal, while stored in the computer, has not been utilized for particle identification. (The name "range" was retained for the signal in order to avoid confusion with the $\Delta E/\Delta X$ signal, which is often referred to loosely as "energy".)

The anode signal of the phototube goes directly to the counting area where it is used for a time-of-flight measurement. Since a stop pulse for the time-of-flight TAC is generated by the cyclotron RF, the TAC output is actually related to T modulo τ, where T is the true time of flight and τ is the cyclotron period. In principle this introduces some ambiguities, but, for the experiments discussed here, the cyclotron period (160 ns) was long enough to eliminate any problems. Since the

anode signals were used as start pulses for the TAC, the output is inverted, i.e., it corresponds to "1-TOF". This was modified in the computer by storing the signal as C' = 4095-C, where "C" is the channel number obtained from the 4096-channel ADC. The resolution of the TOF signal was generally about 5 ns. This was completely dependent on the cyclotron tuning since a second phototube looking at γ rays from the target always gave identical results. Moreover, on lower energy beams accelerated in the 3rd-harmonic mode, time resolution as low as 2 ns has been obtained.

The problem of the relative timing of the four signals is solved by stretching them to about 50 μs and putting them into linear gates. The gates are opened simultaneously after all coincidence requirements are satisfied (Coinc. III) and the signals are sent to the multiplexer and ADC. The lengths of the stretched signals are chosen such that all of them are still present when the master coincidence is made. However, this introduces a "dead time" problem in the electronics since each event is processed for a long time. Similarly, there is a pile-up problem due to the long time-constants of the position and $\Delta E/\Delta X$ amplifiers. These count-rate problems, coupled with the computer writing-time requirements (see below), effectively limit the counting rate to 50-100 counts/second in order to be free of pile-up and excessive computer losses. Since it is often necessary, or at least desirable, to run with the elastic peak on the detector, a scale-down system based on a coincidence between position and time-of-flight is available. (Scale-down factors of from 2 to 100 are provided.) This at least minimizes the writing time of the computer and eliminates unnecessary sections of data tapes having nearly 100%

elastic events. Of course, this does nothing to improve the pile-up effects which determine the basic limitation.

During a run, data are taken on-line by the SCC-660 computer. The raw data are written on a binary magnetic tape for final data analysis. At the same time, singles spectra of position, TOF, $\Delta E/\Delta X$, and range, and 2-dimensional spectra of range vs. position, TOF vs. position, $\Delta E/\Delta X$ vs. position, and TOF vs. $\Delta E/\Delta X$ are accumulated, and can be individually displayed on a Tektronix 611 storage scope. While the computer is writing on tape it is unable to store data. For this reason a gating signal is generated which turns off the ADC, analyzers, and scalers while the tape is being written. The monitor counters, however, are connected to duplicate scalers, one gated and one ungated. The ratio of these two scalers gives the writing dead time of the system and is used to correct the stored spectra for this effect. Position spectra of the 6 individual wires are also stored in the computer. This is necessary because the wire spectra are slightly non-linear and the non-linearities of different wire spectra are not identical. (This non-linearity problem has been observed previously.[46]) Sample two-dimensional spectra are shown in Figs. 11-13.

5. Targets

The targets used for these experiments are the same as those listed in Table I, with two exceptions: A natural ^{93}Nb target 150 $\mu g/cm^2$ thick was used in the heavy ion work and a new, thinner ^{92}Mo target, 150 $\mu g/cm^2$, having the same isotopic composition as the ^{92}Mo target listed in Table I, was also employed.

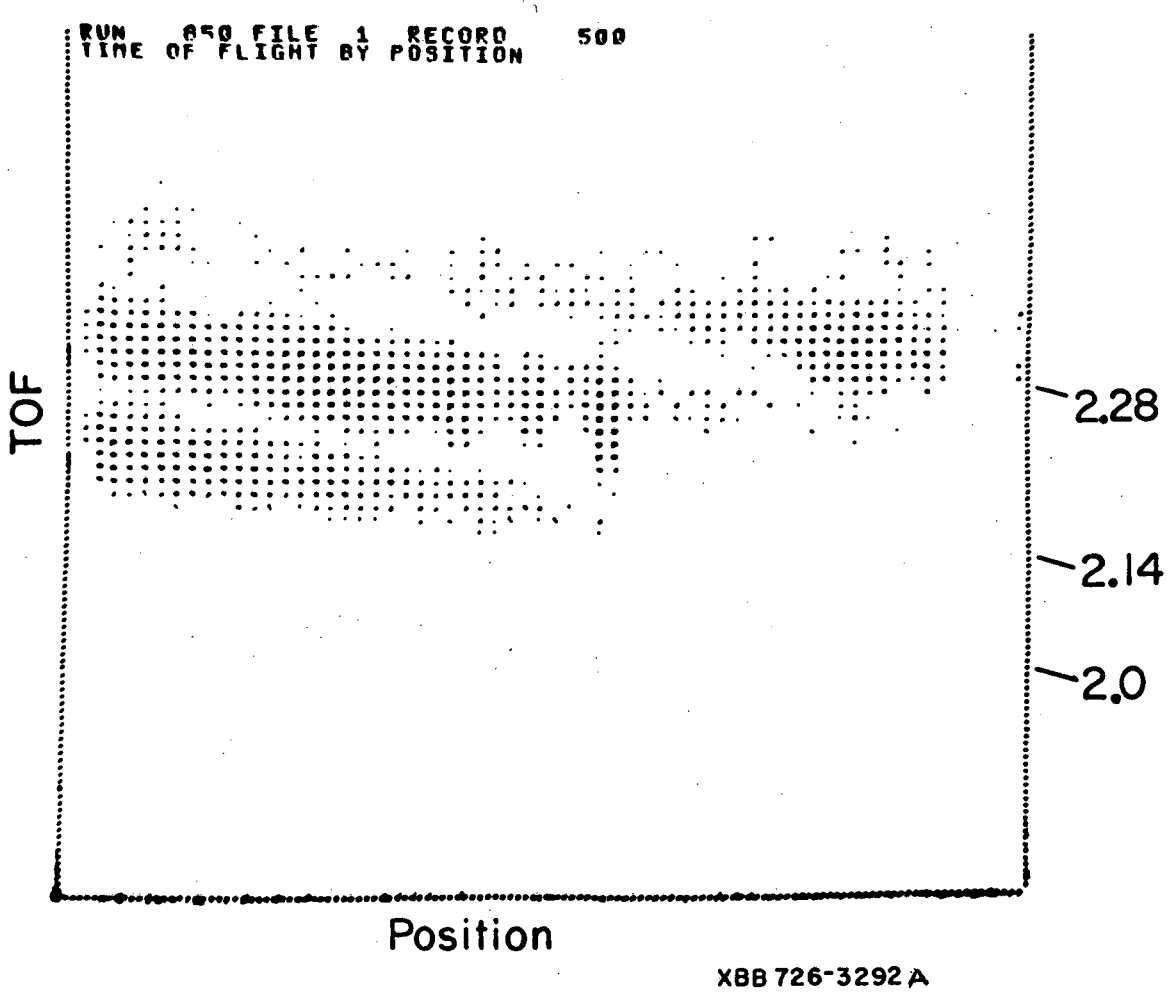

Fig. 11. Time-of-flight vs. position spectrum obtained from the bombardment of ^{90}Zr with 104 MeV ^{16}O at $\theta_\ell = 25°$. The M/q value for each band of particles is indicated at the right of the figure. The lowest band is mainly $^{12}C(6+)$, the middle band is $^{15}N(7+)$ and $^{15}O(7+)$, and the upper band is mainly $^{16}O(7+)$. The slope is due to the 10% change in velocity of the ions along the focal plane. The dots are intensified on a logarithmic scale. A display threshold of 10 counts was used to clearly differentiate the various bands.

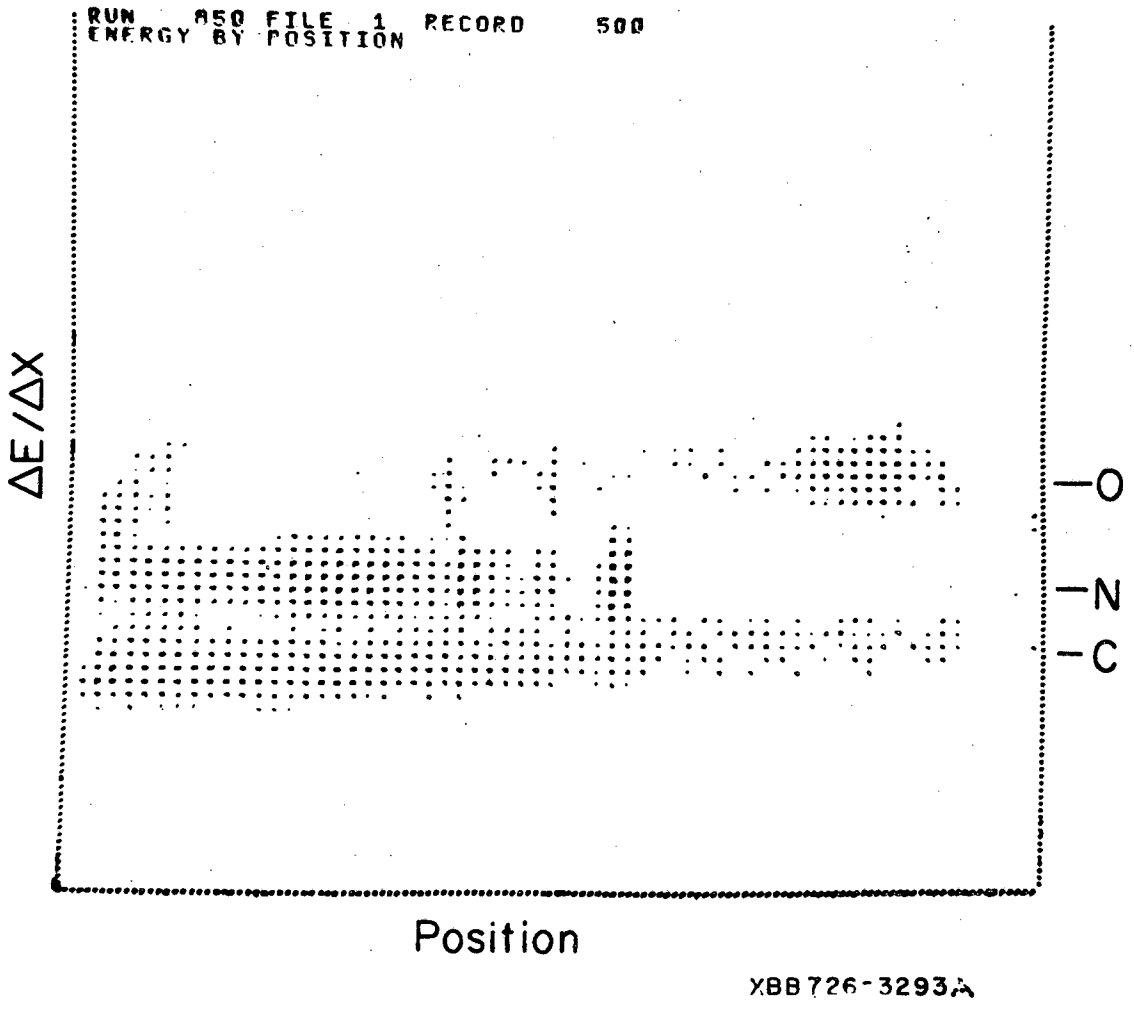

Fig. 12. $\Delta E/\Delta X$ vs. position spectrum obtained from the bombardment of ^{90}Zr with 104 MeV ^{16}O at $\theta_\ell = 25°$. Bands corresponding to carbon, nitrogen, and oxygen are indicated at the right of the figure. A display threshold of 10 counts was employed.

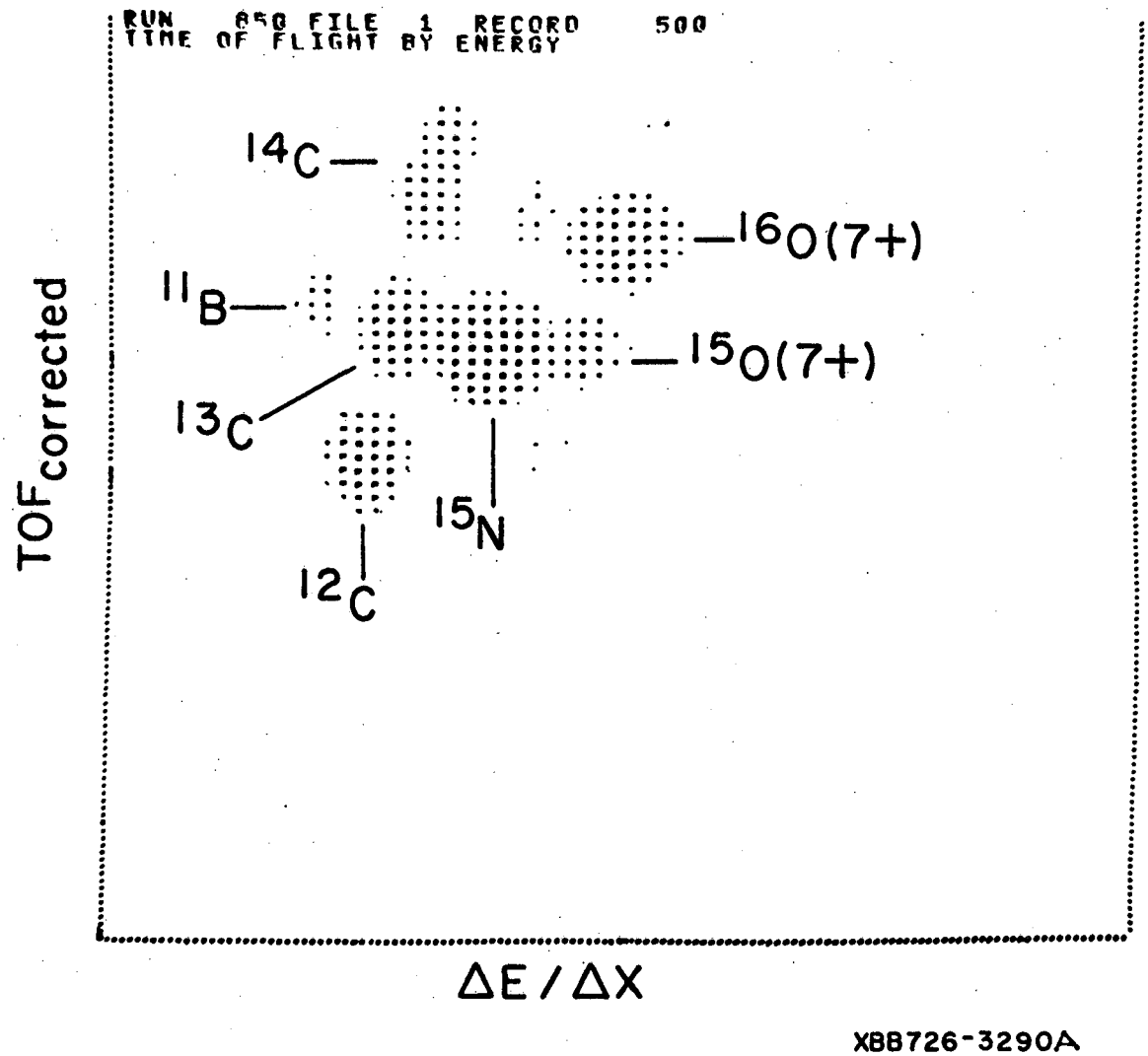

XBB726-3290A

Fig. 13. Time-of-flight vs. $\Delta E/\Delta X$ spectrum obtained from the bombardment of ^{90}Zr with 104 MeV ^{16}O at $\theta_\ell = 25°$. The TOF signals were corrected by the computer (see Fig. 14) to remove the position dependence. Groups corresponding to various values of M/q and Z are indicated. A display threshold of 15 counts was employed.

III. DATA REDUCTION

A. α Particle Reactions

After transfer from the micro-tapes of the PDP-5 computer to a standard IBM tape, the data were analyzed on the SCC-660 computer with the program DERTAG.[34] This program does a least-squares fit to both single and multiple peaks with either Gaussian or asymmetric (Gaussian + exponential tail) peak shapes. The program is also capable of removing a smooth background from the spectrum. All of the actions of the program are displayed on a scope so that the user can easily determine whether or not the results are satisfactory. The output from this program consists of centroids, integrals, and widths for the fitted peaks.

The centroids and sums are then used in the CDC-6600 program LORNA.[34] This program generates a calibration curve based on the centroids of known input peaks, taking into account energy losses in the target or other absorbers and also possible shifts between data taken in different runs. The program then examines unknown peaks and obtains excitation energies for them based on relativistic kinematics. At all stages of the program statistical criteria are applied to reject any points, either known or unknown, which are inconsistent with the rest of the data. Finally, this program also calculates differential cross sections for any states for which counts have been entered. The integrated cross sections are obtained from a third program, FISH,[34] which also generates plots of the angular distributions.

The center of mass differential cross section (in mb/sr) is calculated according to the formula

$$\frac{d\sigma}{d\Omega} = G \times J \times \frac{N}{B} \tag{1}$$

For a solid target, the geometry factor is

$$G = 2.660 \times 10^{-7} \left[\frac{Z \cdot M}{\Delta\Omega \cdot t}\right] \cos\theta_t \tag{2}$$

For a gas target, the target thickness, t, is a function of the scattering angle. Geometrical considerations give:[34]

$$t = \rho \times \tau \times 10^3 \tag{3a}$$

$$= \frac{P \cdot M}{R_0 \cdot (T+273)} \times \frac{W_1 \cdot (1 + L_1/L_2)}{\sin\theta} \times 10^3 \tag{3b}$$

where we have assumed an ideal gas to obtain the density, ρ. Replacing "t" in eq. (2) by eq. (3b) we obtain the geometry factor for a gas target:

$$G = 2.660 \times 10^{-7} \left[\frac{Z \times (T + 273) \times \sin\theta}{\Delta\Omega \cdot P \cdot W_1 \cdot (1 + L_1/L_2)} \times \frac{R_0}{10^3}\right] \tag{4}$$

where R_0 is the ideal gas constant.

For P in Torr,

$$R_0 = 6.2365 \times 10^4 \ \frac{cm^3 \cdot Torr}{mole \cdot deg} \tag{5}$$

and

$$G = 1.659 \times 10^{-5} \left[\frac{Z \cdot (T + 273) \sin\theta}{\Delta\Omega \cdot P \cdot W_1 \cdot (1 + L_1/L_2)}\right] \tag{6}$$

The symbols used above and their units are:

J = Jacobian for laboratory to center of mass transformation

N = Number of counts

B = Number of μCoulombs

θ = Laboratory scattering angle (deg.)

θ_t = Target angle (deg.)

M = Atomic weight of target (g/mole)

Z = Charge state of incident beam after passing through the target

t = Target thickness (mg/cm^2)

$\Delta\Omega = A/R^2$ = Detector solid angle

ρ = Gas target density (g/cm^3)

τ = Effective length of gas target (cm)

L_1 = Distance from gas target center to target thickness defining slit (cm)

$L_2 = R - L_1$ = Distance from L_1 to detector collimator (cm)

W_1 = Width of target thickness defining slit (cm)

P = Gas target pressure (Torr)

R_0 = Ideal gas constant = 6.2365×10^4 (cm^3. Torr/mole · deg.)

T = Gas target temperature (°C)

R = Distance of detector collimator from target (cm)

A = Area of detector collimator (cm^2)

B. Heavy Ion Reactions

Data analysis of the heavy ion experiments is done off-line on the SCC-660 computer by "replaying" the data tapes obtained during a run. In order to set gates in the two-dimensional arrays it is necessary to apply correction factors to the raw data which remove the position dependence. The corrections are of the form

$$TOF_{corrected} = TOF + \alpha P$$

and

$$\Delta E/\Delta X_{corrected} = \Delta E/\Delta X + \beta P$$

where "P" is the position signal. For the data reported here a correction factor $\alpha = 0.165$ was used. Normally $\beta = 0$ was sufficient to set gates in $\Delta E/\Delta X$ spectra. A corrected time-of-flight vs. position spectrum is shown in Fig. 14.

Measurement of the four signals (position, TOF, $\Delta E/\Delta X$, range) makes it possible, at least in principle, to completely specify the identity of a heavy ion. As it turns out, however, three of these pieces of information (the range signal has insufficient resolution to be useful) are generally enough for particle identification. The identification scheme relies on two-dimensional plots of various parameters. Non-relativistically we have

$$\text{Position} \propto B\rho \propto \frac{MV}{q} \tag{1}$$

$$TOF \propto \frac{1}{V} \tag{2}$$

and

$$\Delta E/\Delta X \propto Z^2 \left(\frac{M}{E}\right)^n \propto \frac{Z^2}{V^{2n}} \tag{3}$$

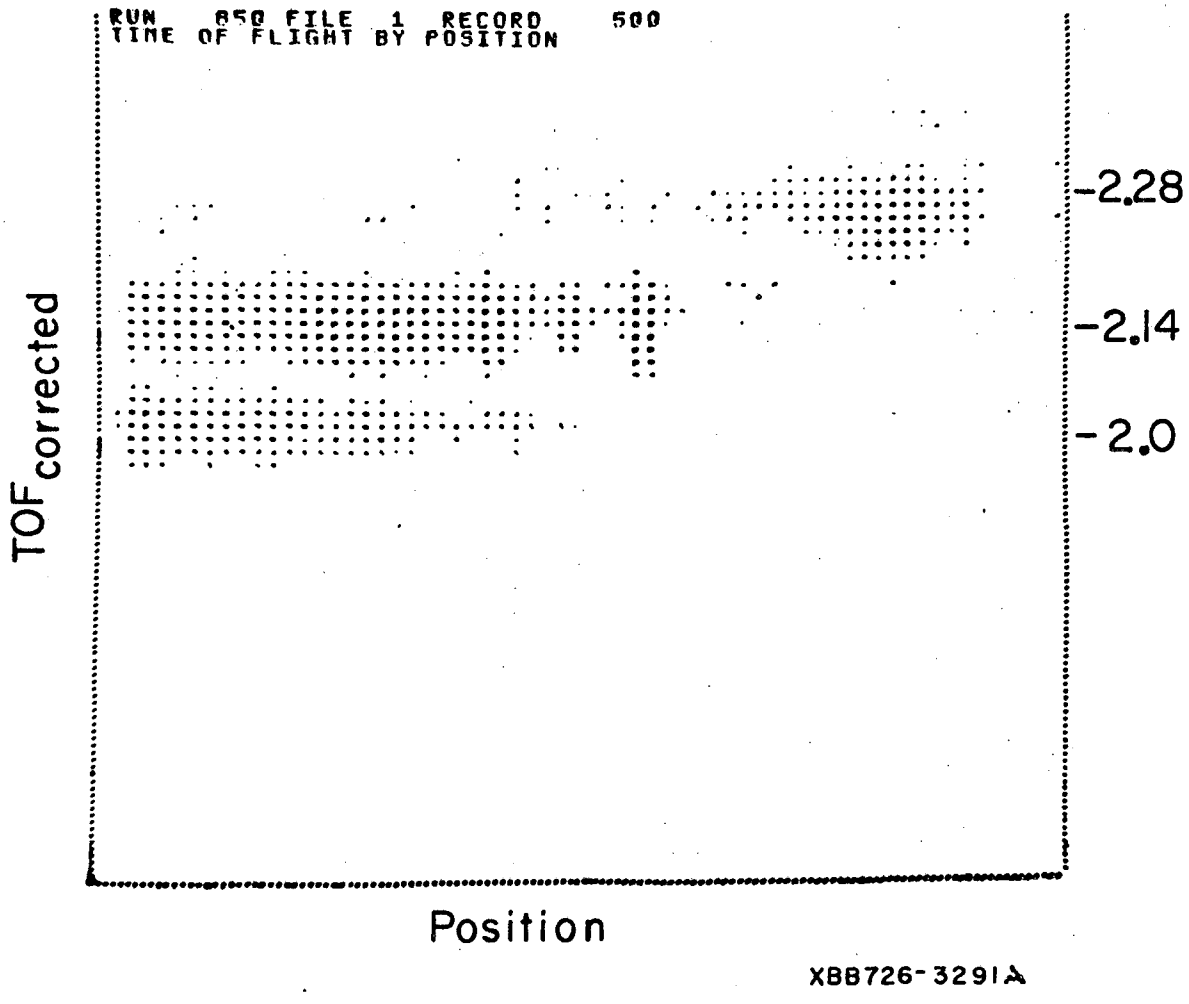

Fig. 14. Corrected time-of-flight vs. position spectrum obtained from the bombardment of ^{90}Zr with 104 MeV ^{16}O at $\theta_\ell = 25°$. The method of correction is described in the text. (See caption to Fig. 11.)

where, for heavy ions in this energy range, $n \approx 1/2$. Thus, a plot of TOF vs. position gives bands of particles corresponding to different values of M/q. (This may be more obvious if we think of the position axis as the independent variable "P". Then the TOF axis is just $(M/q) \times (1/P)$ and, at constant values of P, the groups clearly separate according to their M/q ratio.) Now, having selected a group of particles with a given M/q value, consider a plot of $\Delta E/\Delta X$ vs. position. This separates particles according to Z^2. (Again, think of P as the independent variable and $\Delta E/\Delta X$ becomes $(M/q) \times (Z^2/P)$. For a given value of M/q this gives, at constant P, groups which differ in Z^2.)

In analyzing the data, gates are first set in the (corrected) TOF vs. position spectrum. The data tape is then read in again, but only events falling within the gate are stored in the two-dimensional spectra. This allows the "Z" gate to be set easily in either the $\Delta E/\Delta X$ vs. position or TOF vs. $\Delta E/\Delta X$ spectrum. Finally, the data tape is read in a third time and the gated singles position spectra (of the separate wires) can be transferred to a magnetic tape. Interpretation of the two-dimensional arrays is aided by the use of a computer program which predicts what will appear. Basically the program does kinematics for all reactions (up to 5 nucleon transfer) in energy steps up to 10 MeV of excitation energy. It calculates $B\rho$, $\Delta E/\Delta X$, and TOF for the outgoing particles from which "sample" two-dimensional plots can be drawn. In practice, the predicted plots are extremely similar to what is observed on the scope and the identification of a specific heavy ion is generally quite straightforward.

Having obtained a set of 6 gated individual wire spectra, there remains the problem of merging them. The technique adopted makes use of a calibration done with a well-collimated α-source. The calibration was obtained by moving the source across the detector in 1 cm steps. This method measures position along the wire unambiguously, since it is independent of any possible line-shape abnormalities at the focal surface. The results of this calibration were fit with least-squares polynomials which give "true position" on each wire as a function of ADC channel number (see Ref. 47). A second calibration, obtained by moving the elastic peak across the detector by changing the magnetic field, yielded calibration curves with shapes similar to those found with the α-source. However, it was found that a constant shift was required because corresponding curves were often displaced from one another. (This is due to a curved line shape at the focal surface caused by aberrations in the magnetic field.) For this reason the merging routine first converts each of the gated individual wire spectra to absolute position by means of the α-source calibration and then (optionally) shifts them to conform to the absolute position of a specific peak in one wire. Then the wires can be added with essentially no loss in resolution. After being merged, the runs are written on magnetic tape for further analysis with the program DERTAG described above.

Cross sections were obtained from the merged spectra as ratios to the elastic scattering cross section at the same angle, based on a short elastic "normalization" run. The elastic cross sections were obtained from optical model predictions.[49] (A separate normalization of

the elastic scattering runs yielded a curve in good agreement with the calculated angular distribution.) The normalizations were based on the monitor counter since there was some doubt as to the reliability of the Faraday cup measurements. The G-factors [Sec. III-A, eq. (2)] were calculated using nominal values for the spectrometer solid angle and the target thicknesses. From the observed elastic scattering charge state ratio (see below) the charge of the incident beam was taken to be 7.8, corresponding to about 85% 8+ and 15% 7+ after passing through the target. The observed number of elastic events from a normalization run, corrected for computer writing dead time, was then used to calculate an "effective" charge B^* which reproduced the correct elastic scattering cross section.

$$B^* = \frac{J \cdot G \cdot N'}{d\sigma} \qquad (4)$$

where N' is the corrected number of counts and $d\sigma$ is the elastic scattering cross section. This effective charge was then applied to other runs at the same angle by correcting it according to the ratio of ungated monitor counts. Generally there were three or four data runs corresponding to a given normalization run and it was found that the ratio of effective charge to observed μC (from the current integrator) was quite constant for the set. However, the ratio did change somewhat from angle to angle, which suggests that either the efficiency of the Faraday cup or the target thickness was not constant. Since the ratio did not appear to change in a systematic manner, the former explanation seems more likely. After approximately correcting for the charge state ratio of the elastically scattered ^{16}O ions, the discrepancy between the effective charge and

the integrator was about 30%. Since absolute target thicknesses were not measured, this could be partly due to the targets being thinner than expected. However, the 30% discrepancy appeared with all targets and is probably related to the beam "halo" in the scattering chamber.

In calculating cross sections it is necessary to know the relative charge state intensities of the heavy ions. During these experiments, the ratio $^{16}O(8+)/^{16}O(7+)$ was measured on one target (^{93}Nb) and the ratio $^{15}O(8+)/^{15}O(7+)$ was obtained for ^{93}Nb, ^{92}Mo, and ^{90}Zr. (The $^{15}N(7+)/^{15}N(6+)$ ratio was not directly measured.) In most of these cases the results agree rather well with the simple expressions given by Northcliffe:[50]

$$\varepsilon = 137\ \beta/Z = 137\ V/cZ \tag{5a}$$

$$\begin{aligned} R_{Z/Z-1} &= 0.365\ \varepsilon^{4} \qquad (\varepsilon \lesssim 2) \\ &= 0.3\ \varepsilon^{4.35} \qquad (\varepsilon \gtrsim 2) \end{aligned} \tag{5b}$$

$$R_{Z-1/Z-2} = 1.6\ \varepsilon^{4} \tag{5c}$$

$$R_{Z-2/Z-3} = 12\ \varepsilon^{4} \tag{5d}$$

where V is the ion velocity and Z is its atomic number. For example, the elastic scattering on ^{93}Nb gives $\varepsilon = 1.99$ and, from eq. (5b), $R_{8/7} = 5.8$, while the observed ratio is 5.9. Similarly, for $^{93}Nb(^{16}O,^{15}O)$ at 25° the predicted ratio is almost the same as for the elastic since the velocity is essentially identical ($\varepsilon = 1.96$). The observed ratio, 5.5, again agrees with eq. (5b). The $^{92}Mo(^{16}O,^{15}O)$ results are also given approximately by eq. (5b), but for the $^{90}Zr(^{16}O,^{15}O)$ data at 25° a substantial disagreement exists because the observed ratio ($\gtrsim 8$) is larger than expected. Since the <u>integrated</u> cross section ratio for the

$^{90}Zr(^{16}O,^{15}O)^{91}Zr$ (g.s.) reaction, about 6.4, agrees reasonably with eq. (5b), it is likely that some ^{15}O was lost in setting the computer gates (see above) for the 25° run.

If $d\sigma_u$ are the ("uncorrected") cross sections for the $(^{16}O,^{15}N)$ and $(^{16}O,^{15}O)$ reactions, calculated by ignoring charge state corrections both in the normalization and data runs, then the corrected cross sections are

$$d\sigma(^{15}N) = \frac{\chi(^{16}O)}{\chi(^{15}N)} \, d\sigma\,(^{15}N) \tag{7a}$$

and

$$d\sigma(^{15}O) = \frac{\chi(^{16}O)}{\chi(^{15}O)} \, d\sigma_u\,(^{15}O) \tag{7b}$$

where χ is the fraction of particles in the highest charge state. For heavy ions of the velocities encountered here,

$$\chi \approx \frac{R_{Z/Z-1}}{1 + R_{Z/Z-1}} \tag{8}$$

since the probability for a charge state Z-2 is less than 1%. From eq. (5b) we obtain (for an equilibrium charge distribution)

$$R_{8/7}(^{16}O) = 1.04\, R_{8/7}(^{15}O) \tag{9a}$$

and

$$R_{7/6}(^{15}N) = 1.89\, R_{8/7}(^{15}O) \tag{9b}$$

If we assume that eqs. (9a) and (9b) are valid for all targets we obtain

$$d\sigma(^{15}N) = 0.94\, d\sigma_u(^{15}N) \tag{10a}$$

and

$$d\sigma(^{15}O) = d\sigma_u(^{15}O) \tag{10b}$$

The heavy ion cross sections reported in this paper have all been corrected in this manner. As long as only the highest charge state is considered in determining the cross section, the ambiguities discussed here introduce only a few percent uncertainty into the correction.

The position calibration of the focal plane has not yet been determined. For this reason an internal calibration for each run was obtained by using various known peaks to obtain ρ as a function of channel number. The known ρ's were calculated by assuming B was given from the NMR frequency by

$$B = 0.234885\ \nu_{NMR} \tag{11}$$

where ν is in MHz and B is in kilogauss. This procedure is not highly accurate and so the excitation energies quoted for the heavy ion data generally have rather large uncertainties.

IV. EXPERIMENTAL RESULTS

A. (α,t) Reactions

1. Selection Rules

The general assumptions made in dealing with single-nucleon transfer reactions are that the states formed are those in which one particle is coupled to the undisturbed target ground state,[19] and that the transfer occurs in a single step. These lead to the selection rules

$$J_{tgt} + J_f \geqslant j \geqslant \left| J_{tgt} - J_f \right| \tag{1}$$

and

$$\pi_f = (-)^{\ell}\, \pi_i \tag{2}$$

where

$$\vec{j} = \vec{\ell} + \vec{1/2} \tag{3}$$

Generally the targets studied are even-even and have $J^{\pi}_{tgt} = 0^+$. In this case the selection rules can be simplified to

$$J_f = j \tag{4}$$

and

$$\pi_f = (-)^{\ell} \tag{5}$$

2. $^{90}Zr(\alpha,t)^{91}Nb$

Since the previously reported level energies from $^{90}Zr(^3He,d)^{91}Nb$ experiments[1,2,4,6] indicate substantial discrepancies, they were remeasured. The energies reported in Refs. 1 and 6 are systematically higher than those found in Ref. 2 and the differences appear to increase with excitation energy. For example, the strongest peak in $^{90}Zr(^3He,d)^{91}Nb$ is assigned excitation energies of 3.360 ± 0.010,[2] 3.395 ± 0.015,[1] and 3.410 ± 0.010[6] MeV. The data reported here were calibrated with the ^{17}F(g.s.) impurity

peak and the ^{91}Nb(g.s.) peak as a function of angle. The Q-value for the ^{16}O(α,t)^{17}F reaction, -19.2136 MeV, was taken from published tables.[51] However, recent results from various reactions leading to ^{91}Nb give conflicting values for the mass excess of that nucleus.

A ^{90}Zr(^{3}He,d)^{91}Nb experiment[6] gives a Q-value of -0.227 ± 0.020 MeV, which agrees with the value obtained from the Mass Table of Mattauch, Thiele, and Wapstra.[52] On the other hand, two recent measurements of the ^{91}Zr(p,n)^{91}Nb reaction give Q = -2.045 ± 0.006 MeV[53] and Q = -2.0388 ± 0.0034 MeV,[54] which correspond to a ^{91}Nb mass excess differing from the previous value[52] by about +120 keV. The mass excess of ^{91}Nb determined here comes from the relative Q-values of the ^{90}Zr(α,t)^{91}Nb and ^{91}Zr(α,t)^{92}Nb reactions, which were observed simultaneously (see Sec. IV-A6) with a ^{91}Zr target containing about 5% ^{90}Zr impurity. The energy calibration of the ^{91}Zr(α,t) data (using the ^{17}F(g.s.) and the ^{92}Nb(g.s.) as a function of angle, with Q-values from Ref. 51) gives a difference in Q-values of 680 ± 25 keV between the ^{90}Zr(α,t)^{91}Nb and ^{91}Zr(α,t)^{92}Nb reactions. In a similar measurement Ball and Cates[55] found a difference in (^{3}He,d) Q-values for the two isotopes of 677 ± 7 keV, which agrees very well with the (α,t) result.

The change in the ^{91}Nb mass excess indicated by the (α,t) data (and the (^{3}He,d) data of Ball and Cates[55]) is about +98 keV, which is slightly less than the value of +120 keV required by the ^{91}Zr(p,n)^{91}Nb data.[53,54] This discrepancy could be due to errors in the ^{91}Zr(α,t) and ^{91}Zr(^{3}He,d) Q-values[51] since the results from the ^{91}Zr target are

measured relative to these. However, the (α,t) calibration is also consistent with the position of the $^{92}Zr(\alpha,t)^{93}Nb$(g.s.) peak, which would mean that this Q-value[51] must also be in error in order to obtain agreement with the results of Refs. 53 and 54. A recent measurement of the Q-value of the $^{90}Zr(p,\gamma)^{91}Nb$ reaction[56] yielded Q = 5.167 ± 0.005 MeV, which gives a ^{91}Nb mass excess in agreement with the (α,t) results. Thus while there still appears to be a small inconsistency, it seems clear that the $^{90}Zr(^{3}He,d)^{91}Nb$ Q-value measured by Knöpfle et al.[6] is incorrect. A summary of the relevant Q-values is given in Table III.

The $^{90}Zr(\alpha,t)^{91}Nb$ Q-value used in this analysis is -14.643 MeV. This corresponds to the relative difference in (α,t) Q-values of 680 keV discussed above, and is slightly less negative than the value of -14.665 MeV which would be inferred from the $^{91}Zr(p,n)^{91}Nb$ results.[53] The excitation energies of ^{91}Nb states observed in this work are given in Table IV. The results agree, in general, with those of Vourvopoulos et al.,[2] and indicate that the excitation energies reported by Picard and Bassani[1] and Knöpfle et al.[6] are somewhat too high. Since the method of calibration used here gives excitation energies that depend on the choice of $^{90}Zr(\alpha,t)^{91}Nb$ Q-value, the errors quoted in Table IV reflect an uncertainty of ± 27 keV in the Q-value used in the analysis. Due to the high level density in ^{91}Nb it is difficult to compare the results of experiments where γ rays are observed with those from charged-particle studies. However, the strong (^{3}He,d) level referred to above, while unobserved in $^{91}Zr(p,n\gamma)$,[57] may correspond to a state observed by Rauch[56] at

Table III. Summary of Q-values for Reactions Relating to ^{91}Nb.

Reaction	Measured Q-value (MeV)	Published Q-value[a] (MeV)	^{91}Nb mass excess[b] (MeV)
^{91}Zr(^{3}He,d)^{92}Nb	---	0.358 ± 0.011	---
^{91}Zr(α,t)^{92}Nb	---	-13.963 ± 0.011	---
^{91}Zr(p,n)^{91}Nb	-2.045 ± 0.006[c]	-1.925 ± 0.060	-86.630 ± 0.008
"	-2.0388 ± 0.0034[d]	"	-86.636 ± 0.006
^{90}Zr(p,γ)^{91}Nb	5.167 ± 0.005[e]	5.269 ± 0.060	-86.648 ± 0.006
^{90}Zr(^{3}He,d)^{91}Nb	-0.227 ± 0.020[f]	-0.225 ± 0.060	-86.748 ± 0.020
"	-0.319 ± 0.013[g]	"	-86.656 ± 0.014
^{90}Zr(α,t)^{91}Nb	-14.643 ± 0.027[h]	-14.545 ± 0.060	-86.652 ± 0.027

[a]Taken from Ref. 51, which uses a mass excess for ^{91}Nb (from Ref. 52) of -86.750 ± 0.060 MeV.

[b]Calculated from the difference between the measured and published Q-values.

[c]Ref. 53. [d]Ref. 54. [e]Ref. 56. [f]Ref. 6.

[g]Relative to the ^{91}Zr(^{3}He,d)^{92}Nb Q-value listed above. The Q-value difference is from Ref. 55 (see text).

[h]Relative to the ^{91}Zr(α,t)^{92}Nb Q-value listed above (see text).

Table IV. Levels Observed in the $^{90}Zr(\alpha,t)^{91}Nb$ Reaction at 50 MeV.

	(α,t)		(^{3}He,d)			^{91}Mo (g.s.) Decay
No.	Levels Observed[a] (MeV)	Intensity[b] (mb)	Levels Observed[c,d] (MeV)	ℓ_p[d]	C^2S[d]	Levels Observed[e] (MeV)
1	0.0	3.441	0.0	4	0.918	---
2	(0.103)[f]	0.144	0.103	1	0.430	
3	1.29	0.038[g]	1.31	1	0.048[h]	
						1.581
4	1.60	0.073	1.60	1	0.078[h]	1.637
						1.791
5	1.82	0.069[g]	1.84	3	0.058[h]	
6	1.95 ± .04	Weak	1.96	2[h]	0.014[h]	
7	2.30	0.043[i]	2.34	1	0.017[h]	
8	2.39 ± .03	Weak				(2.391)[j]
9	2.53	0.032[i]				2.531
10	2.61	0.023[k]	2.62[ℓ]		Weak[ℓ]	2.631
11	2.77	0.012[k]				2.792
12	2.90	0.074	2.92[ℓ]		Weak[ℓ]	

(continued)

Table IV (continued)

	(α,t)		(^{3}He,d)			^{91}Mo (g.s.) Decay
No.	Levels Observed[a] (MeV)	Intensity[b] (mb)	Levels Observed[c,d] (MeV)	ℓ_p[d]	C^2S[d]	Levels Observed[e] (MeV)
13	3.01	0.036[m]				3.028
			3.07 }	2	0.035	
14	3.12 ± .04	Weak	3.11 }			3.149
						3.187
15	3.37	0.218	3.36	2	0.388	
16	3.65 ± .04	0.027[k]	3.66	2[h]	0.023[h]	
						3.837
						3.886
			3.92[n]		Weak[n]	3.916
			3.95 }			
			3.99 }			
			4.11	0	0.055	
17	4.18	0.107	4.18	(2)	0.020	4.179
			4.23	(2)	0.008	

(continued)

Table IV (continued)

	(α,t)		(^{3}He,d)			^{91}Mo (g.s.) Decay
No.	Levels Observed[a] (MeV)	Intensity[b] (mb)	Levels Observed[c,d] (MeV)	ℓ_p[d]	C^2S[d]	Levels Observed[e] (MeV)
			4.30	2	0.023	
			4.39	0	0.160	
			4.49	2	0.043	
			4.61	2	0.013	
			4.70	2	0.033	
18	4.77 ± .03	0.232[g]	4.77 } 4.80 }	4	0.343	
			4.85			
19	4.89 ± .03	0.096[g]	4.90			
			4.95 } 4.99 }	(0)	0.055	
20	5.02 ± .03	Weak	5.04	0	0.040	
21	5.14 ± .03	0.067[i]	5.17	(0)	0.080	
			5.24	2	0.133	

(continued)

Table IV (continued)

	(α,t)		(^{3}He,d)			^{91}Mo (g.s.) Decay
No.	Levels Observed[a] (MeV)	Intensity[b] (mb)	Levels Observed[c,d] (MeV)	ℓ_p[d]	C^2S[d]	Levels Observed[e] (MeV)
22	5.34 ± .03	Weak	5.33	0	0.090	
			5.44	2	0.165	
			5.57	(0)	0.035	
			5.64	0	0.060	
			5.74	0	0.020	
			5.80	0	0.120	
			5.86	0	0.045	
23	5.95 ± .05	(0.1)°	6.01	4	0.500	
24	6.09 ± .05	Weak	6.09	2	0.075	
			6.17	2	0.103	
			6.215[n]	(4)[n]	Weak[n]	

[a]Excitation energy ± 20 keV except as noted. The Q-value for the reaction was assumed to be -14.643 MeV. (See text.)

[b]Integrated from $\theta_{c.m.}$ = 12.5 to 57° except as noted.

(continued)

Table IV (continued)

[c]Excitation energy ± 15 keV.

[d]Taken from Ref. 2 except as noted. All $\ell = 2$ levels up to 5.44 MeV are assumed $d_{5/2}$. All $\ell = 4$ levels except g.s. are assumed $g_{7/2}$.

[e]Taken from Ref. 10. Only those levels believed to be populated in the g.s. ($9/2^+$) decay are included. All energies ± 1 keV or less. The upper limit for the decay is about 4.4 MeV.

[f]Not resolved.

[g]Integrated from $\theta_{c.m.} = 12.5$ to 52°.

[h]Taken from Ref. 4. All $\ell = 1$ levels except 0.103 MeV are assumed $p_{3/2}$. The 1.85 MeV level is assumed $f_{5/2}$.

[i]Integrated from $\theta_{c.m.} = 12.5$ to 36.5°.

[j]The existence of this level was uncertain.

[k]Integrated from $\theta_{c.m.} = 12.5$ to 32°.

[ℓ]Taken from Ref. 1.

[m]Integrated from $\theta_{c.m.} = 12.5$ to 42°.

[n]Taken from Ref. 6.

[o]Observed at only 3 angles. The average differential cross section ratio to the 4.179 MeV level (~ 0.9) was used in obtaining the intensity.

3.365 ± 0.010 MeV in the $^{90}Zr(p,\gamma)$ reaction. If so, this would confirm the result of Vourvopoulos et al.[2] and the (α,t) calibration obtained here.

A triton spectrum of the $^{90}Zr(\alpha,t)^{91}Nb$ reaction at 50 MeV and $\theta_\ell = 30°$ is shown in Fig. 15. The resolution is 50 keV, full width at half maximum (FWHM). [This reaction was also studied at 65 MeV. In the higher energy experiment data were taken at only three angles and the resolution was worse, ≈ 100 keV (FWHM). Since, within the limitations of the poorer resolution, the 65 MeV data are very similar to the data obtained at 50 MeV, only the lower energy results will be discussed in detail.] The $g_{9/2}$ ground state is a factor of 15 more intense than any other single level in the spectrum. In the $^{90}Zr(^3He,d)^{91}Nb$ data at 30.9 MeV[4] the ground state has only about half the intensity of the 3.36 MeV $\ell = 2$ level. Based on $(^3He,d)$ spectroscopic factors,[2,6] the strength of the ground state indicates that $\sigma_{9/2^+}/\sigma_{7/2^+} \approx 5$ for the (α,t) reaction.

Figures 16 and 17 show angular distributions of tritons leading to some of the stronger final states. The angular distributions of all strong triton groups show very little structure. One observable difference between the $\ell = 4$ (g.s.) and $\ell = 2$ (3.37 MeV) curves, displayed in Figs. 16 and 17, respectively, is the forward-angle behavior: The $\ell = 2$ curve tends to flatten out near 10°, while the $\ell = 4$ curve is much steeper. The 4.77 MeV level, assigned $\ell = 4$ by the $(^3He,d)$ reaction,[2,6] also shows a very steep angular distribution at forward angles (see Fig. 16). The 4.18 MeV level, whose angular distribution is shown in both Figs. 16 and 17, has been assigned[2,6] $\ell = 2$ (the ℓ value is bracketed in Ref. 2). The

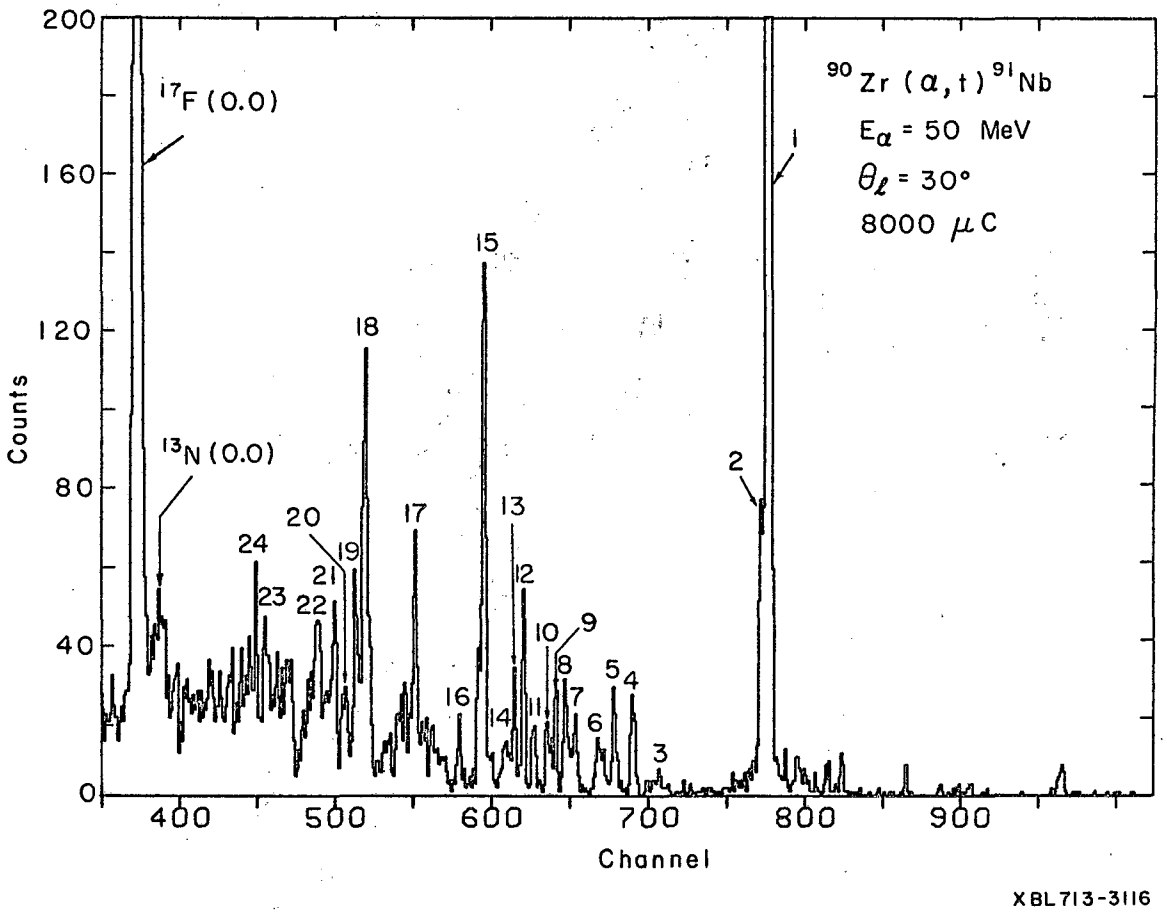

Fig. 15. Triton energy spectrum from the $^{90}Zr(\alpha,t)^{91}Nb$ reaction at $\theta_\ell = 30°$. The peak numbers correspond to excitation energies given in Table IV.

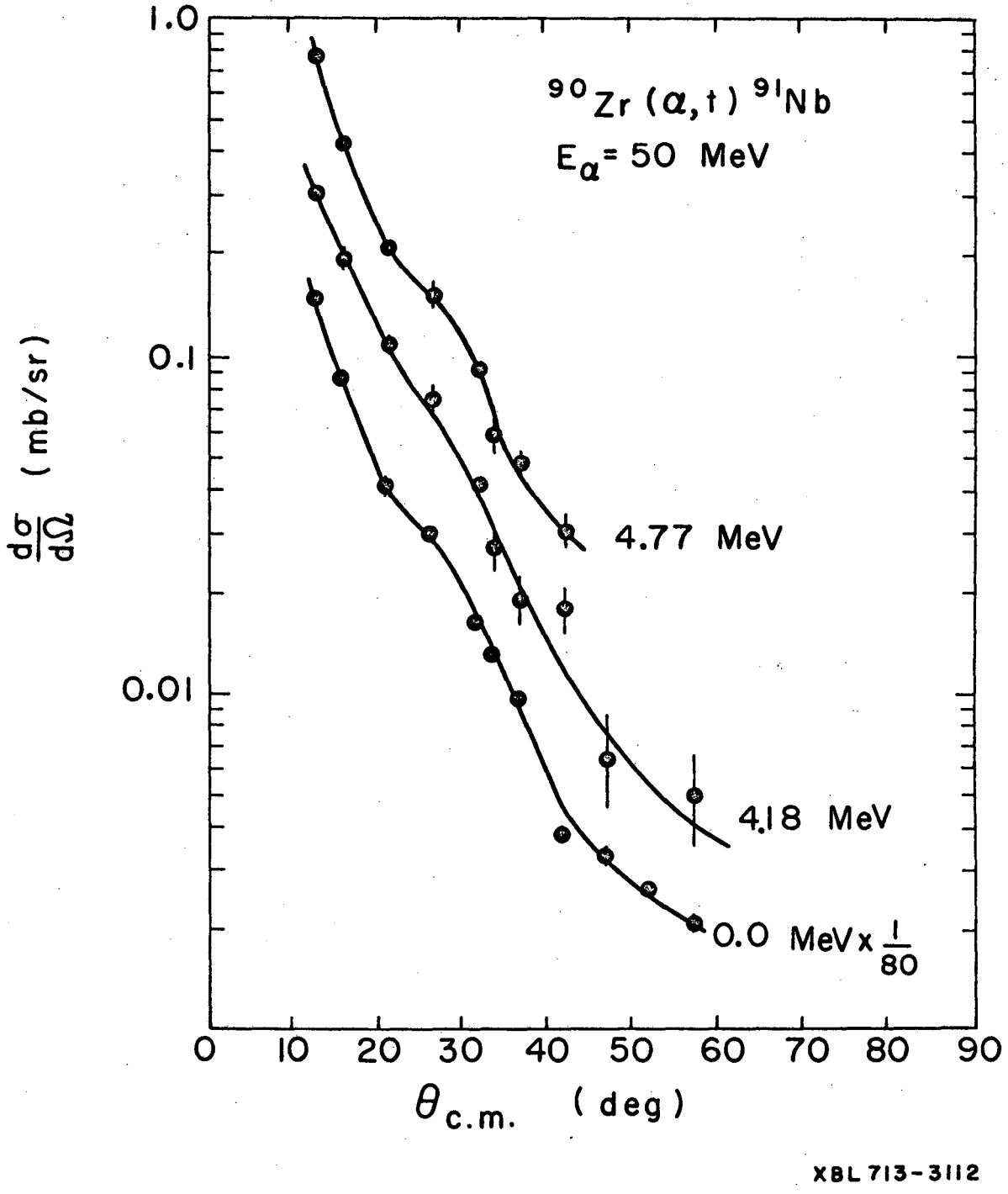

Fig. 16. Angular distributions of tritons from the $^{90}Zr(\alpha,t)^{91}Nb$ reaction leading to the 0.0, 4.18, and 4.77 MeV levels. Statistical errors are shown for each point. The curves have no theoretical significance.

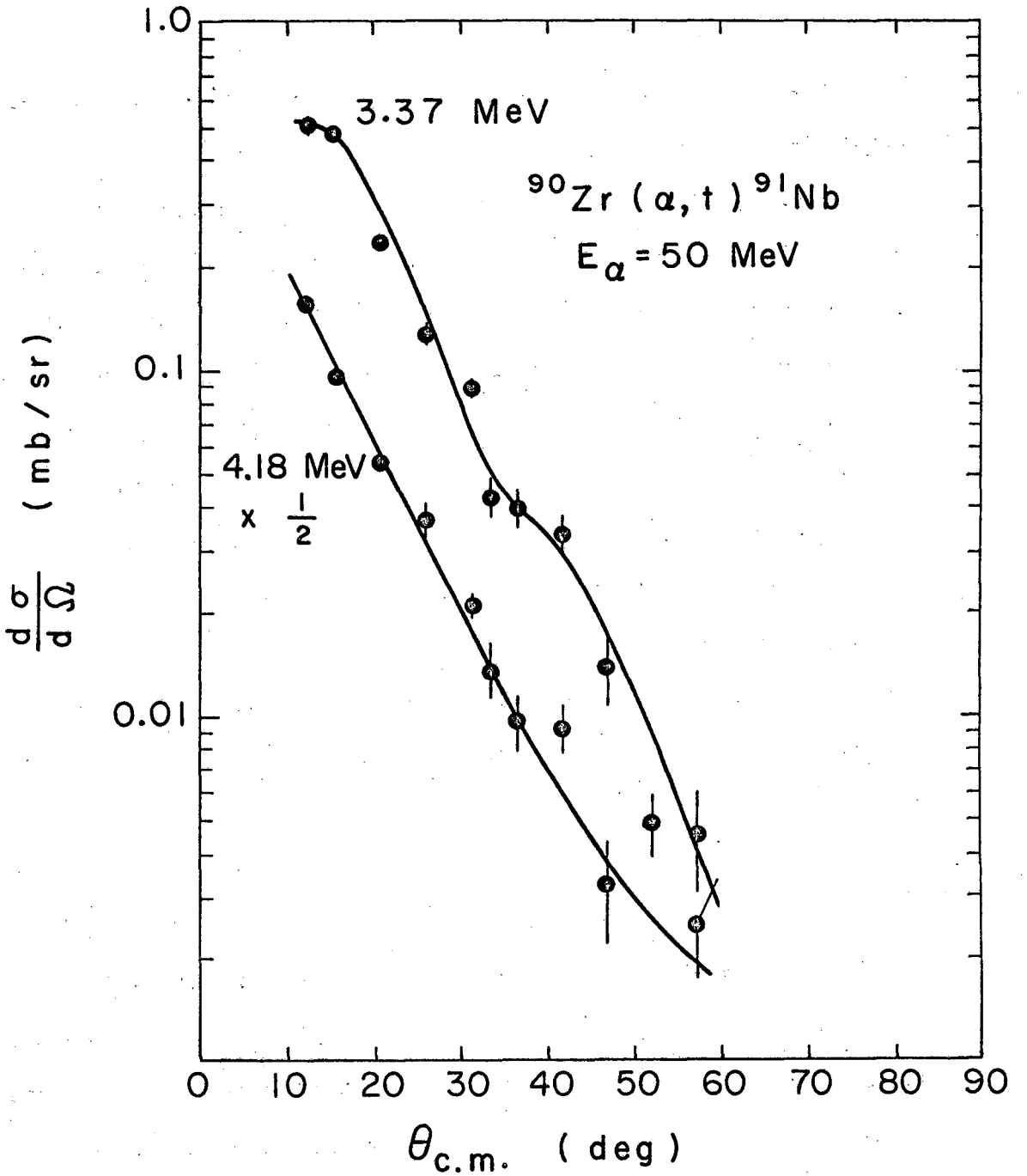

XBL713-3113

Fig. 17. Angular distributions of tritons from the $^{90}Zr(\alpha,t)^{91}Nb$ reaction leading to the 3.37 and 4.18 MeV levels. Statistical errors are shown for each point. The curves have no theoretical significance.

(α,t) angular distribution agrees better with the $\ell = 4$ curves, although the differences are very slight.

Also in contradiction with the $\ell = 2$ assignment of the 4.18 MeV level is the strength of the state in the (α,t) reaction. The spectroscopic factors given for this level predict it to be weaker than the 3.37 MeV state by a factor of between 14 (Ref. 6) and 20 (Ref. 2), while the relative cross sections of the levels seen in the (α,t) data (see Table IV) differ only by a factor of 2. (This is also true of the 65 MeV data, where $\sigma(3.37)/\sigma(4.18)$ is again about 2.) Thus, the 4.18 MeV level is between 7 and 10 times too strong to be consistent with the $\ell = 2$ spectroscopic factors of previous work.[2,6] This discrepancy seems rather large since it has been verified[58] that (α,t) spectroscopic factors are generally the same as those obtained from (^{3}He,d) experiments (within about a factor of 2).

Additional evidence for the existence of a high-spin state in this region comes from a recent study of the β decay of ^{91}Mo,[10] which indicates a weak level at 4.179 ± 0.001 MeV. A summary of the levels observed in the β decay is included in Table IV. Since no intensity was measured for the γ decay of the 4.179 MeV level, it is not possible to distinguish between an allowed and a first-forbidden electron capture decay. For an allowed decay, final spins of $7/2^+$, $9/2^+$, and $11/2^+$ are possible, while for a first-forbidden transition $5/2^-$, $7/2^-$, $9/2^-$, $11/2^-$, or $13/2^-$ states are permitted. Shell model considerations rule out the $11/2^+$, $9/2^-$, and $13/2^-$ possibilities, since the level is strongly populated in proton transfer. A $5/2^-$ assignment seems unlikely because the 4.179

MeV state is observed to decay only to the $9/2^+$ ground state.[10] There are at least two $5/2^-$ levels and a number of $3/2^-$ levels which should be fed from the decay of a $5/2^-$ state, while none are observed. (A second decay branch of the 4.179 MeV level has, however, been tentatively assigned to a level at 2.992 MeV by Matthews et al.[57]) A $7/2^-$ level strongly populated with the (α,t) reaction would presumably be an $f_{7/2}$ proton-hole state. However, in the available (d,^{3}He) experiments in this mass region[3,59] no $f_{7/2}$ hole states were observed. The remaining choices, $7/2^+$, $9/2^+$, and $11/2^-$ are all equally consistent with the β-decay results.

In the excitation energy region between 2.5 and 3 MeV there are several levels observed in (α,t) which appear either weakly[1,6] or not at all[2,4] in the (^{3}He,d) data. The many levels which are populated by both reactions make it seem likely that these "new" proton levels, e.g., 2.30, 2.39, 2.53, 2.61, 2.77, 2.90, and 3.01 MeV, appear in the ^{90}Zr(α,t)^{91}Nb spectra because they are high angular momentum transitions. States containing small amplitudes of, say, $g_{9/2}$, $g_{7/2}$, or $h_{11/2}$ strength would have larger cross sections in (α,t) than (^{3}He,d) because the (α,t) reaction has the best momentum matching for $\ell = 4$ and 5 transitions. Of the seven levels seen in the (α,t) data between 2.30 and 3.01 MeV, only the 2.90 MeV level was not observed in the ^{91}Mo($9/2^+$) β decay.[10] This supports the contention that these levels are high-spin states having at least some single-particle amplitude.

The 4.89 MeV level observed in the (α,t) experiment corresponds to an unassigned doublet at 4.85 and 4.90 MeV in Ref. 2. A level at 4.912 MeV was observed in a lower-energy experiment[6] and assigned $\ell = 2$. The (α,t)

angular distribution of the 4.89 MeV level (not shown) corresponds more closely to the $\ell = 4$ shape and the strength of the state relative to the 3.37 MeV level is too large by a significant factor. The spectroscopic factor for this level would correspond to a cross section relative to the 3.37 MeV level of 1/16 instead of the observed intensity ratio of 1/2.3. Thus, the 4.89 MeV level is about 7 times stronger than its $\ell = 2$ assignment[6] would indicate. The ^{91}Mo(g.s.) β decay can only populate ^{91}Nb levels up to about 4.4 MeV so it provides no additional information about the 4.89 MeV state.

The intensity of the (α,t) level at 5.14 MeV, relative to the 3.37 MeV level, is about 1/3. Of the reported[2,6] levels in this region, only that at 5.24 MeV has a spectroscopic factor consistent with the observed intensity. However, the discrepancy in excitation energies is larger than the expected uncertainties if both reactions are populating the same state. (The state at 5.14 MeV was also observed in the 65 MeV experiment, with an intensity about half that of the 3.37 MeV state.)

It is interesting that the intensity of the ℓ=4 level near 6 MeV in the (α,t) data is rather low compared with the spectroscopic factors from (^{3}He,d).[2,6] Knöpfle <u>et al.</u>[6] show a cross section ratio $\sigma(6.04)/\sigma(4.82) \approx 2$, while the data reported here give $\sigma(5.95)/\sigma(4.77) \approx 1/2$. Unfortunately, the 6 MeV region of the (α,t) spectrum is obscured at forward angles by the ^{17}F(g.s.) impurity peak, so the measured intensity of the 5.95 MeV level is only approximate. This level was not observed in the 65 MeV data, again due to impurity problems. Whether the apparent difference in strength is related to the fact that the upper level is unbound cannot be determined without DWBA (Distorted Wave Born Approximation) calculations.

3. $^{92}Mo(\alpha,t)^{93}Tc$

A triton spectrum of the $^{92}Mo(\alpha,t)^{93}Tc$ reaction at 50 MeV and $\theta_\ell = 15°$ is shown in Fig. 18. The resolution is 55 keV (FWHM). The intensity of the ground state ($g_{9/2}$) is again much greater than that of any other level in the spectrum. A summary of the levels observed in the $^{92}Mo(\alpha,t)^{93}Tc$ reaction, compared with the $^{92}Mo(^3He,d)$ results[1,5] is given in Table V. The spectra were calibrated using the ^{17}F(g.s.) and ^{93}Tc(g.s.) peaks as a function of angle, with Q-values obtained from Ref. 51. As can be seen from Table V, the excitation energies determined here agree well with those found previously,[1,5] with very few exceptions.

The largest energy discrepancy occurs for the (α,t) level at 3.10 ± 0.02 MeV, which may correspond to the (^{3}He,d) state observed at 3.17 ± 0.02[1] and 3.147 ± 0.015[5] MeV. Two recent studies of the ^{92}Mo(d,n) reaction have also indicated a state in this region at 3.21 ± 0.02[60] and 3.17 MeV.[61] This level has been assigned[5,61] $\ell = 2$. However, the $\ell = 2$ spectroscopic factor for the 3.147 MeV level is only 1/23 that of the 3.343 MeV level,[5] while the (α,t) intensity ratio, $\sigma(3.10)/\sigma(3.36)$, is about 1/4. Thus, the different values for the excitation energy may be due to population in (α,t), but not in (^{3}He,d) or (d,n), of a high-spin state near the 3.15 MeV level. Both the excitation energy and the strength of the 3.10 MeV state are confirmed by the 65 MeV (α,t) data.

The 0.68 and 2.14 MeV levels, both weakly populated in (^{3}He,d) are relatively stronger in (α,t), which indicates high spin assignments. Neither of these states was observed in the ^{92}Mo(d,n) experiments.[60,61] The 2.13 MeV level was assigned $\ell = 3$ ($f_{5/2}$) in Ref. 5, in agreement with

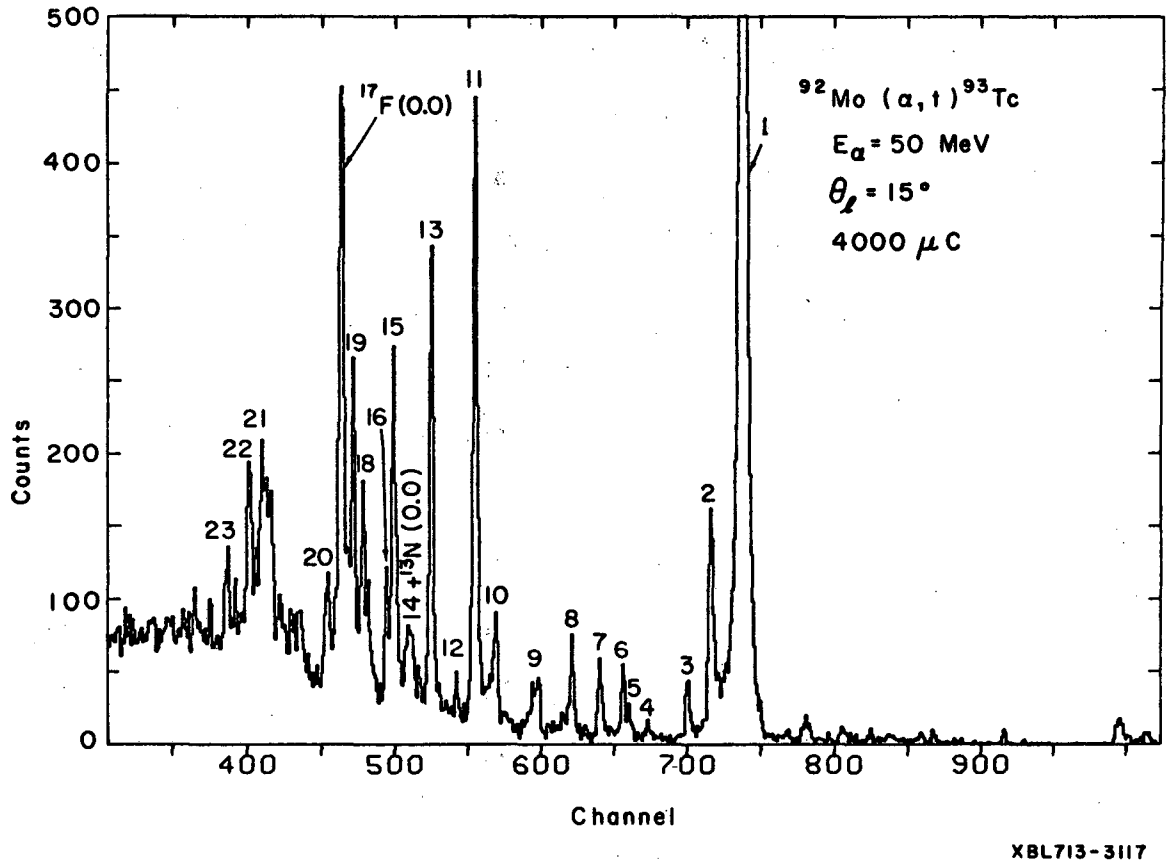

Fig. 18. Triton energy spectrum from the $^{92}Mo(\alpha,t)^{93}Tc$ reaction at $\theta_\ell = 15°$. The peak numbers correspond to excitation energies given in Table V.

Table V. Levels Observed in the $^{92}Mo(\alpha,t)^{93}Tc$ Reaction at 50 MeV.

	(α,t)		$(^3He,d)^a$			$(^3He,d)^b$		
No.	Levels Observed[c] (MeV)	Intensity[d] (mb)	Levels Observed (MeV)	ℓ_p	C^2S [e]	Levels Observed (MeV)	ℓ_p	C^2S [e]
1	0.0	3.709	0.0	4	0.67	0.0	4	0.50
2	0.39	0.118	0.390±.010	1	0.30	0.396±.005	1	0.28
3	0.68	0.040	0.660±.020		Weak	(0.66)		Weak
4	1.18	0.019	1.190±.015	1	0.03,0.01	1.21 ±.020	1	0.034,0.015
5	1.42±.03	0.037						
6	1.51	0.044	1.500±.015	1	0.10,0.04	1.500±.010	1	0.12, 0.052
7	1.78	0.055[f]	1.780±.020	1	0.12,0.05	1.788±.010	1	0.11, 0.048
8	2.14	0.097	2.130±.020		Weak	2.134±.015	3	0.045[g]
9	2.59±.04	0.082	2.565±.020	2	0.04,0.02	2.556±.015	2	0.037,0.019
10	3.10	0.091						
			3.170±.020	(2)		3.147±.015	2	0.034,0.018
11	3.36	0.390	3.360±.020	2	0.78,0.38	3.343±.015	2	0.78, 0.41
12	3.58	0.064						
13	3.91	0.245	3.910±.020	2	0.09,0.05	3.89 ±.020	(2)	(0.11, 0.06)

(continued)

Table V (continued)

	(α,t)		(^{3}He,d)[a]			(^{3}He,d)[b]		
No.	Levels Observed[c] (MeV)	Intensity[d] (mb)	Levels Observed (MeV)	ℓ_p	C^2S[e]	Levels Observed (MeV)	ℓ_p	C^2S[e]
			4.110±.020	(0)	(0.15)	4.09 ±.030	0	0.23
14	4.15±.04	0.059[f]						
15	4.37	0.192[f]	4.43			4.39 ±.040		
16	4.47	0.066[h]						
17	4.67±.03	0.07[i]						
18	4.77±.03	0.087[i]	4.79			4.76 ±.030		
19	4.90	0.166[i]	4.92			4.88 ±.030		
			5.02					
20	5.20±.03	0.097[h]	5.18			5.170±.015	1	0.23, 0.083
			5.33			5.302±.015	2	0.059,0.032
			5.49			5.50 ±.040	(2)	(0.051,0.028)
			5.65			5.64 ±.040	2	0.035,0.019
21	6.01±.03	0.16[h]				5.98 ±.040	(5)	(0.079)[j]
22	6.17±.03	0.17[h]				6.24 ±.040		

(continued)

Table V (continued)

	(α,t)		$(^3He,d)^a$			$(^3He,d)^b$		
No.	Levels Observed[c] (MeV)	Intensity[d] (mb)	Levels Observed (MeV)	ℓ_p	C^2S[e]	Levels Observed (MeV)	ℓ_p	C^2S[e]
23	6.44±.04	0.11[h]						

[a]Taken from Ref. 1. No spectroscopic information is given for levels above 4.110 MeV.

[b]Taken from Ref. 5.

[c]Excitation energy ± 20 keV, except as noted.

[d]Integrated from $\theta_{c.m.}$ = 12.5 to 57° except as noted.

[e]When two values are listed the first corresponds to $j = \ell - 1/2$, the second to $j = \ell + 1/2$.

[f]Integrated from $\theta_{c.m.}$ = 12.5 to 52°.

[g]Assumed $f_{5/2}$.

[h]Integrated from $\theta_{c.m.}$ = 12.5 to 36.5°.

[i]Integrated from $\theta_{c.m.}$ = 15.5 to 52°.

[j]Assumed $h_{11/2}$.

0 0 0 0 8 0 1 7 4

its stronger population in (α,t). The 0.68 MeV level, which is quite weak even in (α,t), might correspond to a $7/2^+$ level calculated to lie at about 0.7 MeV in ^{93}Tc.[7-9] Population of this level, which is mainly a $(\pi g_{9/2})^3_{7/2^+}$ configuration, would indicate some mixing with the $\pi g_{7/2}$ single-particle state.

In the ^{92}Mo(α,t)^{93}Tc data, as was the case for ^{90}Zr(α,t)^{91}Nb (see Sec. IV-A2), there is one level, at 3.91 MeV, whose strength is inconsistent with the ℓ = 2 assignment from the (^{3}He,d) reaction.[1] [The 3.89 MeV level is also given a tentative ℓ = 2 assignment in Ref. 5, although it does not have a typical ℓ = 2 angular distribution. This may be an indication that there exist two closely spaced levels at this energy, but Kozub and Youngblood[5] found no combination of two ℓ values which would yield the observed shape.] The angular distribution of the 3.91 MeV level (Figs. 19 and 20) shows a forward angle behavior similar to that of the ground state (ℓ = 4); it does not appear to flatten out at forward angles as does the 3.36 MeV level in ^{93}Tc (and the 3.37 MeV level in ^{91}Nb). As mentioned above, this difference in angular distributions is very slight and would certainly not allow a determination of the ℓ transfer by itself. The spectroscopic factors for this level from the (^{3}He,d) experiments[1,5] predict it to be weaker than the 3.36 MeV level by a factor of about 7, while the ratio of (α,t) cross sections is about 1.6. The 3.91 MeV level observed in the ^{92}Mo(α,t) data is, therefore, about 4 times too strong to be consistent with the ℓ = 2 assignment of previous work. A level in this region was also observed in the ^{92}Mo(d,n) experiments. The 3.95 MeV level reported by Bommer et al.[60]

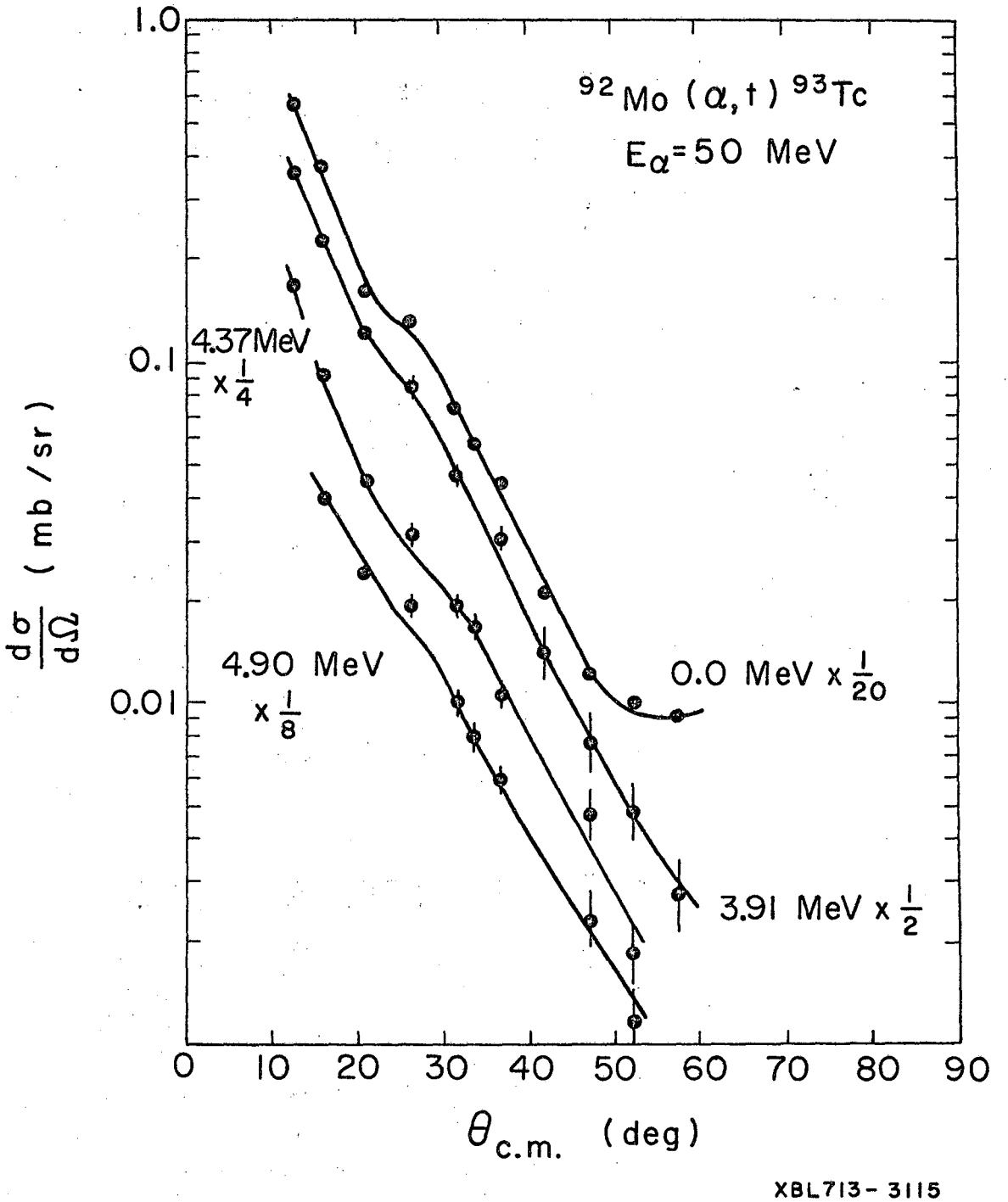

Fig. 19. Angular distributions of tritons from the $^{92}Mo(\alpha,t)^{93}Tc$ reaction leading to the 0.0, 3.91, 4.37, and 4.90 MeV levels. Statistical errors are shown for each point. The curves have no theoretical significance.

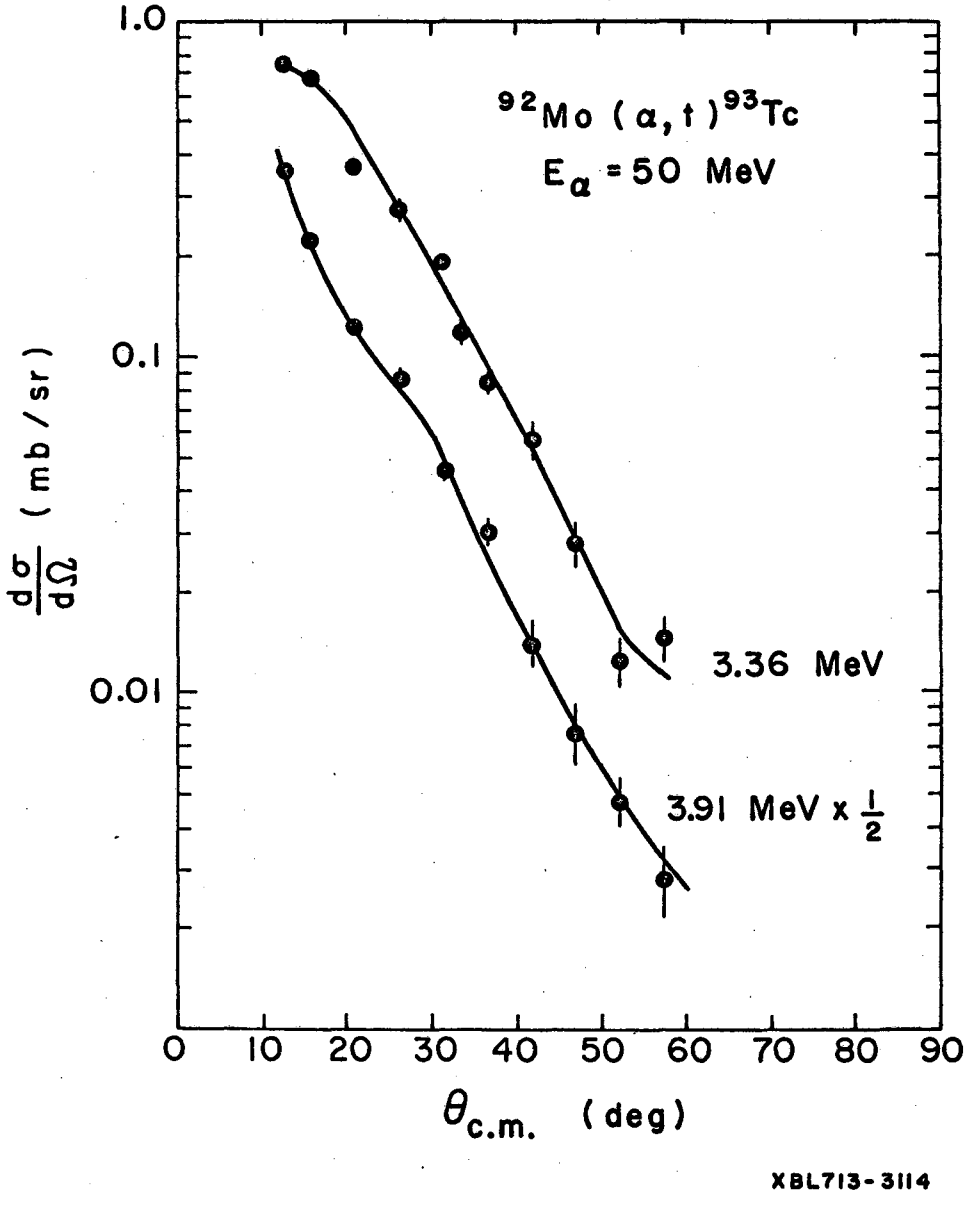

Fig. 20. Angular distributions of tritons from the $^{92}Mo(\alpha,t)^{93}Tc$ reaction leading to the 3.36 and 3.91 MeV levels. Statistical errors are shown for each point. The curves have no theoretical significance.

was assigned $\ell = 3$, while the 3.90 MeV level seen by Riley et al.[61] was given an $\ell = 0$ assignment. It seems clear, therefore, that the $\ell = 2$ assignment from (^{3}He,d) must be regarded as uncertain.

Around 4.5 MeV there are several levels (mostly doublets) which are more strongly excited by (α,t) than (^{3}He,d).[1,5] Thus, they may be populated by $\ell > 2$ transfers. The angular distributions of the 4.37 and 4.90 MeV states (Fig. 19) are similar to that of the $\ell = 4$ ground state transition. Moreover, Vourvopoulos et al.[2] found $\ell = 4$ levels at about this energy in ^{91}Nb.

The 5.98 MeV level seen in Ref. 5 probably corresponds to the multiplet at 6.01 MeV in the (α,t) data. The tentative $\ell = 5$ assignment made by Kozub and Youngblood[5] for the 5.98 MeV level is in qualitative agreement with the observed strength of the 6.01 MeV multiplet in (α,t) (level 21 in Fig. 18). The (^{3}He,d) experiment finds the $d_{5/2}$ analog state at 8.4 MeV, which corresponds to a splitting between $T_>$ and $T_<$ centroids of about 4.7 MeV for the $d_{5/2}$ configuration. Recent ^{92}Mo(d,p)^{93}Mo experiments[62,63] show the existence of an $h_{11/2}$ neutron level at 2.30 MeV. Assuming the same splitting between $T_>$ and $T_<$ states for the $h_{11/2}$ configuration would then give 6.0 MeV as the expected location of the $T_<$ $\ell = 5$ levels. The predicted $g_{7/2}$ centroid (based on the neutron single-particle centroid from Ref. 62) would be about 5.2 MeV, but this is somewhat higher than the strong levels observed in these data. The data of Vourvopoulos et al.[2] indicate that the $T_> - T_<$ splitting is about 1 MeV larger for the $g_{7/2}$ states than it is for the $d_{5/2}$ states in ^{91}Nb and a similar difference in ^{93}Tc would predict a

$g_{7/2}$ centroid in reasonable agreement with the observed strong levels in ^{93}Tc between 3.9 and 4.9 MeV.

4. ^{92}Zr(α,t)^{93}Nb

A triton spectrum of the ^{92}Zr(α,t)^{93}Nb reaction is shown in Fig. 21. The resolution is 50 keV full width at half maximum (FWHM). As was true for the ^{90}Zr(α,t)^{91}Nb reaction (Sec. IV-A2), the spectrum is dominated by the $g_{9/2}$ ground state (level 1). (Based on the ^{90}Zr(α,t) data, the unresolved $p_{1/2}$ level at 0.029 MeV is expected to contribute no more than about 5% to the ground state intensity.) A summary of the ^{93}Nb levels observed in this work is given in Table VI, along with the results obtained from ^{92}Zr(^{3}He,d)[4] and Coulomb excitation.[12] The excitation energies from (α,t) agree, in general, with those from the (^{3}He,d) reaction.[4]

The 1.08 MeV $\ell = 4$ level is populated about 1/20 as strongly as the ground state, in agreement with the spectroscopic factors measured by Cates, Ball, and Newman.[4] The 1.29 MeV level, however, is too strong to be the $\ell = 1$ level assigned in Ref. 4. Rogers et al.[12] observed a level at 1.295 MeV which agreed equally well with either a $7/2^+$ or $9/2^-$ assignment. More recently, Stelson et al.[64] investigated the Coulomb excitation of ^{93}Nb with α particles and ^{16}O ions and obtained a tentative $9/2^+$ state at 1.297 MeV. The strength of the (α,t) state seen here tends to confirm the Coulomb excitation assignments[12,64] of a high-spin state at 1.29 MeV in ^{93}Nb. The angular distributions of the 0.0, 1.08, and 1.29 MeV levels are shown in Fig. 22. The shapes of the three curves are all quite similar but, as was indicated in Sec. IV-A2, the ℓ-dependence of (α,t) angular distributions is not very pronounced.

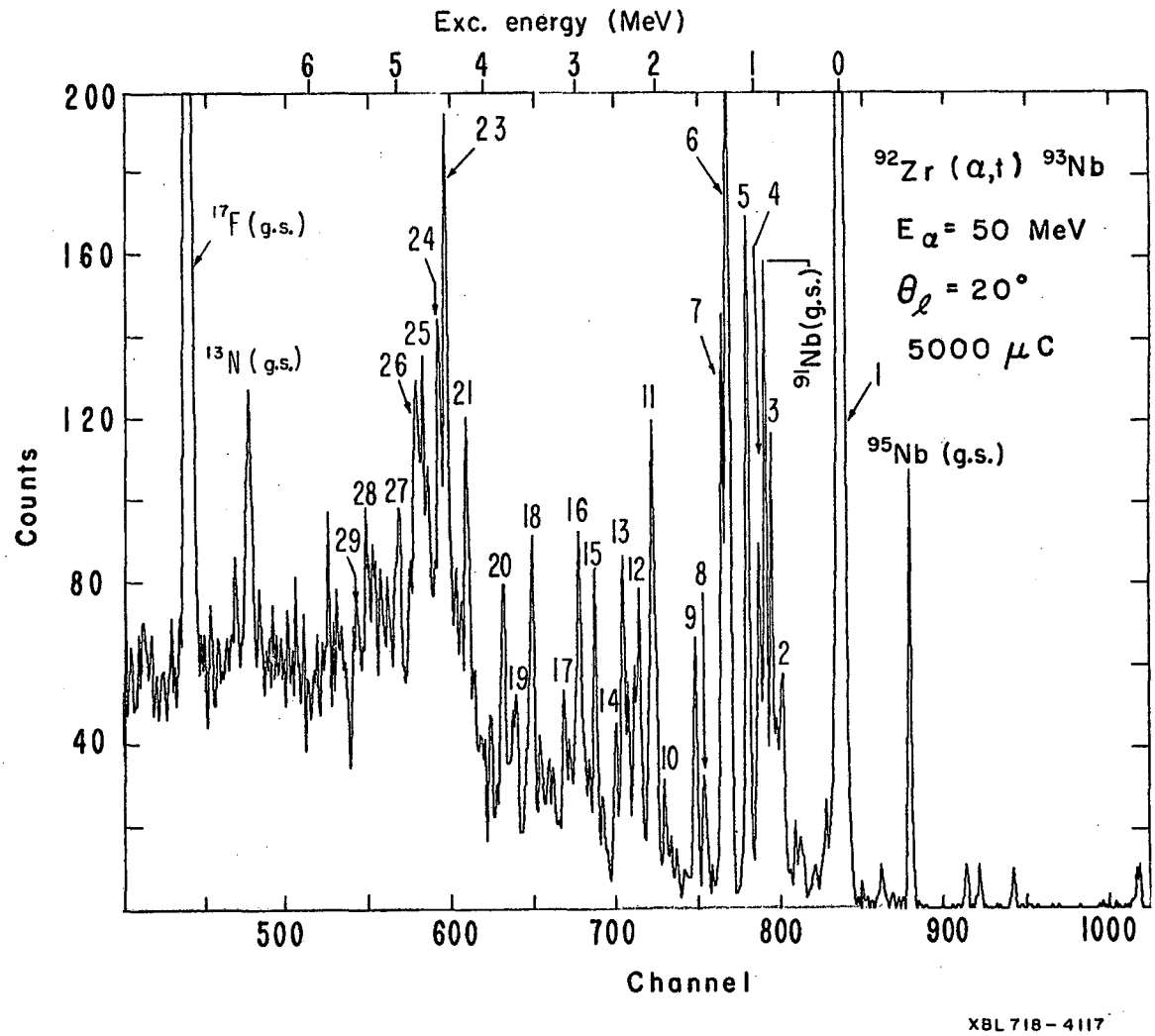

Fig. 21. Triton energy spectrum from the $^{92}Zr(\alpha,t)^{93}Nb$ reaction at $\theta_\ell = 20°$. The peak numbers correspond to excitation energies given in Table VI.

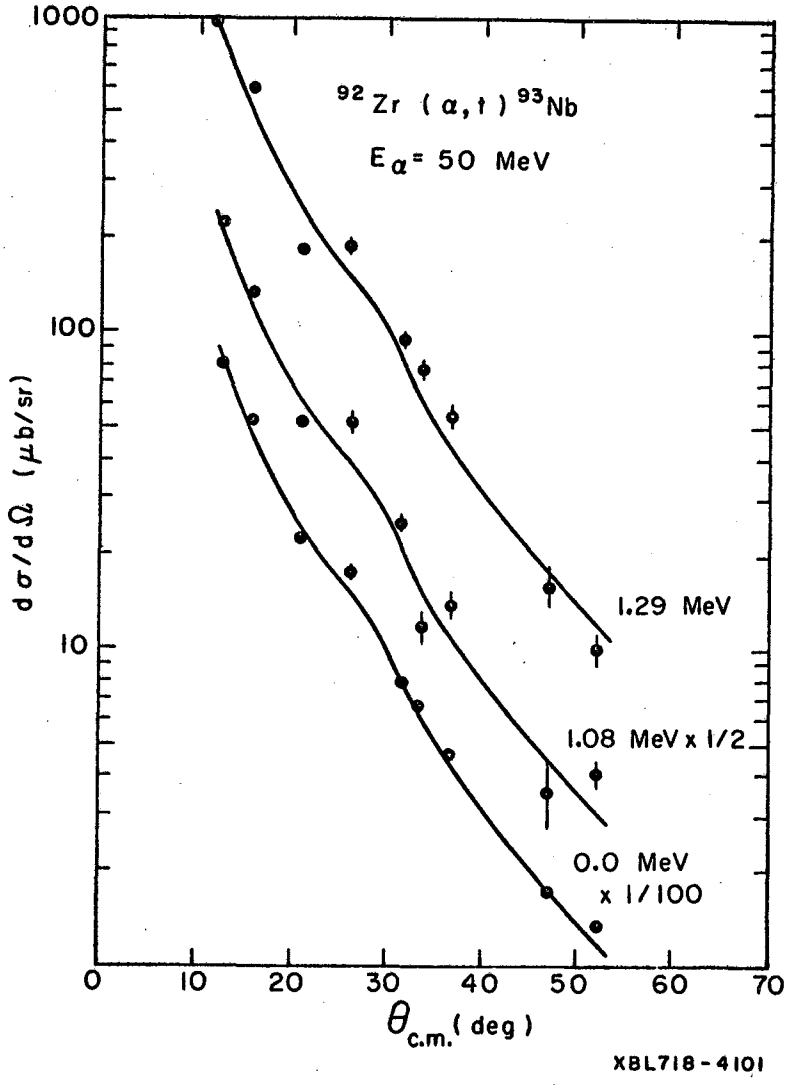

Fig. 22. Angular distributions of tritons from the $^{92}Zr(\alpha,t)^{93}Nb$ reaction leading to the 0.0, 1.08, and 1.29 MeV levels. The solid line through each set of data points represents a smooth curve drawn through the experimental angular distribution of the ground state. Statistical errors are shown for each point.

Table VI. Levels Observed in the $^{92}Zr(\alpha,t)^{93}Nb$ Reaction at 50 MeV.

	(α,t)		(^{3}He,d)[a]			Coulomb Excitation[b]	
No.	Levels Observed[c] (MeV)	Intensity[d] (mb)	Levels Observed[e] (MeV)	ℓ_p[f]	C^2S	Levels Observed[g] (MeV)	J^π
1	0.0	2.672	0.0	4	0.79	0.0	$9/2^+$
			0.029±0.005	1	0.53	0.028	$1/2^-$
2	0.69	0.079	0.685	1	0.07		
						0.742	$7/2^+$
						0.808	$3/2^-$
3	0.80±0.03	0.070	0.807	2	0.06	0.809	$5/2^+$
4	0.95	0.064[h]				0.952	$13/2^+$
			0.97 ±0.01	1	0.006	0.980	$9/2^+$
5	1.08	0.144	1.08	4	0.04	1.080	$7/2^+$
6	1.29	0.304	1.29	1	0.05	1.295	$(7/2^+,9/2^-)$
			1.33	(2)	(0.04)	1.337	$(17/2^+)$
7	1.37±0.03	Weak					
						1.465	$(3/2^+,5/2^-)$
						1.492	$(9/2^+,11/2^+,13/2^+)$

(continued)

0 0 0 0 5 8 0 1 / 5 / 8

Table VI (continued)

	(α,t)		(^{3}He,d)[a]			Coulomb Excitation[b]	
No.	Levels Observed[c] (MeV)	Intensity[d] (mb)	Levels Observed[e] (MeV)	ℓ_p[f]	C^2S	Levels Observed[g] (MeV)	J^π
						1.507	$(9/2^+,11/2^+,13/2^+)$
						1.528	
8	1.57±0.03	0.028	1.57	1	0.02		
9	1.67	0.055	1.66	2	0.008		
			1.71	2	0.006		
10	2.00±0.03	0.021[i]					
11	2.15±0.03	0.125	2.18	2	0.03		
12	2.30 2.36	0.087	2.32	2	0.03		
13	2.48±0.03	0.089	2.52	(0)			
14	2.59±0.03	0.038	2.59	2	0.02		
15	2.81	0.067					
16	2.98	0.091[j]					
17	3.15	0.054					

(continued)

Table VI (continued)

	(α,t)		(^{3}He,d)[a]			Coulomb Excitation[b]	
No.	Levels Observed[c] (MeV)	Intensity[d] (mb)	Levels Observed[e] (MeV)	ℓ_p[f]	C^2S	Levels Observed[g] (MeV)	J^π
18	3.50	0.066[i]					
19	3.72±0.03	0.038[i]					
20	3.84±0.03	0.044[i]					
21	4.23	0.072[i]					
22	4.34	0.043[i]					
23	4.46	0.120[i]					
24	4.56	0.080[i]					
	(4.65)	--					
25	4.70±0.03	0.067[i]					
26	4.81±0.03	0.084[i]					
27	5.00±0.03	0.066[i]					
28	5.34±0.04	0.071[i]					
29	5.49±0.04	--					

(continued)

Table VI (continued)

[a]Ref. 4.

[b]Ref. 12.

[c]Excitation energy ± 20 keV except as noted.

[d]Integrated from $\theta_{c.m.} = 12.5$ to $52.2°$ except as noted.

[e]Excitation energy ± 15 keV except as noted.

[f]All $\ell = 1$ transitions assumed $p_{3/2}$ except for 0.029 MeV. All $\ell = 2$ transitions assumed $d_{5/2}$. All $\ell = 4$ transitions assumed $g_{9/2}$.

[g]Excitation energy ± 2 keV.

[h]Integrated from $\theta_{c.m.} = 15.7$ to $52.2°$.

[i]Integrated from $\theta_{c.m.} = 12.5$ to $36.7°$.

[j]Integrated from $\theta_{c.m.} = 12.5$ to $47.1°$.

In the $^{92}Mo(\alpha,t)^{93}Tc$ experiment (Sec. IV-A3) a group of strong levels was observed at an excitation energy of about 6 MeV. A $^{92}Mo(^{3}He,d)$ experiment[5] indicated a possible $\ell = 5$ assignment for one of these levels. A similar group of levels occurs in the $^{92}Zr(\alpha,t)^{93}Nb$ data at about 4.5 MeV (see Fig. 21). The appearance of rather strong levels at this excitation energy suggests a high angular momentum assignment, but it is not possible to assign ℓ values from these data.

5. $^{94}Zr(\alpha,t)^{95}Nb$

A triton spectrum of the $^{94}Zr(\alpha,t)^{95}Nb$ reaction is shown in Fig. 23. The resolution is 50 keV FWHM. A summary of the ^{95}Nb levels observed in this work is given in Table VII, along with the results of the β-decay[11] and $^{94}Zr(^{3}He,d)^{4}$ experiments. The excitation energies obtained here agree well with those reported by Cates, Ball, and Newman.[4]

Information on the pair of $7/2^{+}$ states at 724.23 and 756.74 keV observed by Brahmavar and Hamilton[11] was, unfortunately, impossible to obtain from the data. The 0.74 and 0.82 MeV levels (both assigned $\ell = 1$ in Ref. 4) are not adequately resolved in the spectra (see Fig. 23) and the doublet also contains a contribution from the $^{92}Zr(\alpha,t)^{93}Nb(g.s.)$ peak due to an isotopic impurity in the target. The existence of an $\ell = 1$ level at 0.77 MeV was also reported in the $^{96}Mo(d,^{3}He)$ experiment of Ohnuma and Yntèma,[3] in agreement with the $^{94}Zr(^{3}He,d)$ results.[4] The intensities of both the 0.74 and 0.82 MeV levels appear somewhat large compared to the 0.25 MeV state based on the $\ell = 1$ spectroscopic factors of Ref. 4. However, in view of the experimental problems it is difficult to know whether this discrepancy is real.

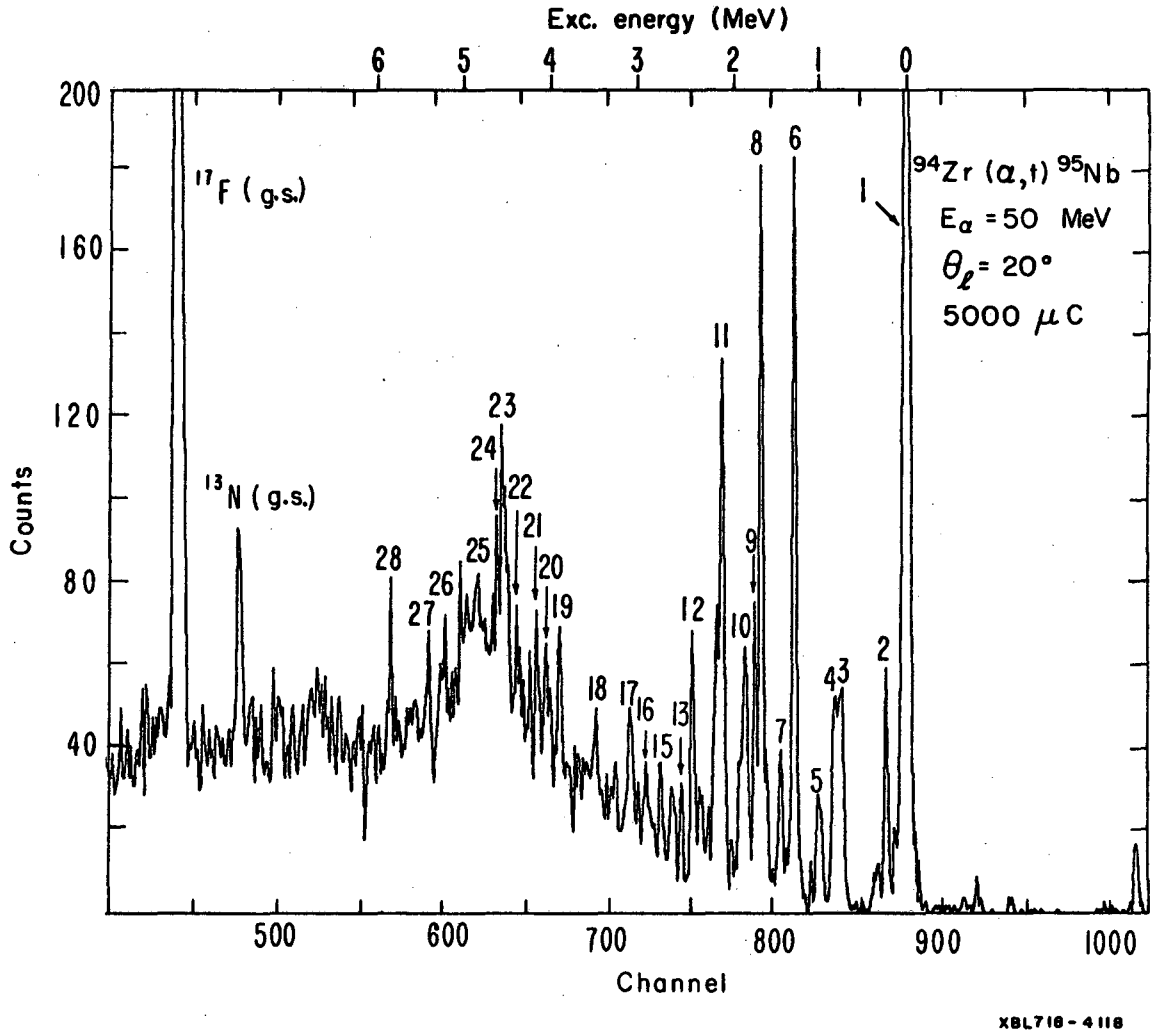

Fig. 23. Triton energy spectrum from the $^{94}Zr(\alpha,t)^{95}Nb$ reaction at $\theta_\ell = 20°$. The peak numbers correspond to excitation energies given in Table VII.

Table VII. Levels Observed in the $^{94}Zr(\alpha,t)^{95}Nb$ Reaction at 50 MeV.

	(α,t)		$(^3He,d)$[a]			^{95}Zr Decay[b]	
No.	Levels Observed[c] (MeV)	Intensity[d] (mb)	Levels Observed[e] (MeV)	ℓ_p[f]	C^2S	Levels Observed[g] (MeV)	J^π
1	0.0	2.540	0.0	4	0.86	0.0	$9/2^+$
2	0.25	0.081	0.26	1	0.34	0.23470	$1/2^-$
3	0.74	0.104	0.73	1	0.045	0.72423	$(7/2)^+$
						0.75674	$(7/2)^+$
4	0.82	0.103	0.80	1	0.077		
5	1.00	0.038	0.99	3	0.030		
			1.20	1	0.022		
6	1.27	0.198	1.26	(3,4)			
7	1.43	0.054					
8	1.65	0.139[h]					
9	1.72	0.079[i]					
10	1.81	0.15					
	1.90						
11	2.10	0.212					

(continued)

Table VII (continued)

	(α,t)		(^{3}He,d)[a]			^{95}Zr Decay[b]	
No.	Levels Observed[c] (MeV)	Intensity[d] (mb)	Levels Observed[e] (MeV)	ℓ_p[f]	C^2S	Levels Observed[g] (MeV)	J^π
12	2.42	0.090					
13	2.54	0.023[j]					
14	2.66	0.032[j]					
15	2.79	0.030[j]					
16	2.92	0.036[j]					
17	3.11	0.062[j]					
18	3.51	0.035[k]					
19	3.90	0.073[j]					
20	4.05	0.041[j]					
21	4.16	0.057[j]					
22	4.36	0.125[j]					
23	4.52	0.147[j]					
24	4.61	0.060[j]					
25	4.83	0.102[j]					

(continued)

Table VII (continued)

	(α,t)		(^{3}He,d)[a]			^{95}Zr Decay[b]	
No.	Levels Observed[c] (MeV)	Intensity[d] (mb)	Levels Observed[e] (MeV)	ℓ_p[f]	C^2S	Levels Observed[g] (MeV)	J^π
26	5.20	0.068[ℓ]					
27	5.36	--					
28	5.77	--					

[a]Ref. 4.

[b]Ref. 11.

[c]Excitation energy ± 20 keV except as noted.

[d]Integrated from $\theta_{c.m.}$ = 12.5 to 52.1° except as noted.

[e]Excitation energy ± 15 keV.

[f]All ℓ = 1 levels except 0.26 MeV assumed $p_{3/2}$. The 0.99 MeV level assumed $f_{5/2}$.

[g]Excitation energy ± 0.2 keV or less.

[h]Corrected for ^{90}Zr(α,t)^{91}Nb (g.s.) impurity.

[i]Integrated from $\theta_{c.m.}$ = 15.7 to 52.1°.

[j]Integrated from $\theta_{c.m.}$ = 12.5 to 33.6°.

(continued)

Table VII (continued)

[k] Integrated from $\theta_{c.m.} = 12.5$ to $26.1°$.

[ℓ] Integrated from $\theta_{c.m.} = 12.5$ to $31.4°$.

The level observed in the data at 1.00 MeV appears to be populated relatively more strongly than was true for the (^{3}He,d) experiment, which is consistent with the $\ell = 3$ assignments made in Refs. 3 and 4.

The highest level reported in the ^{94}Zr(^{3}He,d) data,[4] at 1.26 MeV, was believed to be a high angular momentum ($\ell = 3, 4$) state. As can be seen from Fig. 23, this state (level 6), at 1.27 MeV in these data, is strongly excited in the (α,t) reaction. Similarly, the levels 8 and 11, at 1.65 and 2.10 MeV, are also strongly populated. The 1.65 MeV level contains a contribution from the ^{90}Zr(α,t)^{91}Nb(g.s.) impurity peak amounting to about 1/3 of the total intensity. The 2.10 MeV level appears broad at all angles and is probably a doublet. Angular distributions for the 0.0, 1.27, 1.65, and 2.10 MeV levels (Fig. 24) are all very similar. The angular distribution of the 1.65 MeV level has been corrected for the presence of ^{91}Nb(g.s.) tritons.

Figure 23 shows a group of fairly strong excited states at about 4.5 MeV in ^{95}Nb. The strength of these levels in the (α,t) reaction suggests a high angular momentum assignment, although no definite ℓ value can be assigned from these data.

6. <u>^{91}Zr(α,t)^{92}Nb</u>

This data corresponds to that mentioned in Sec. IV-A2. A triton spectrum of the ^{91}Zr(α,t)^{92}Nb reaction at $\theta_\ell = 15°$ is shown in Fig. 25. The resolution is 65 keV FWHM. The spectrum is dominated by the multiplet of levels whose configuration is predominantly[65] $(\pi g_{9/2}, \nu d_{5/2})_{2^+} \longrightarrow 7^+$, i.e., by the capture of a $g_{9/2}$ proton. Insofar as this simple picture is correct, two results are required: the cross sections of the states

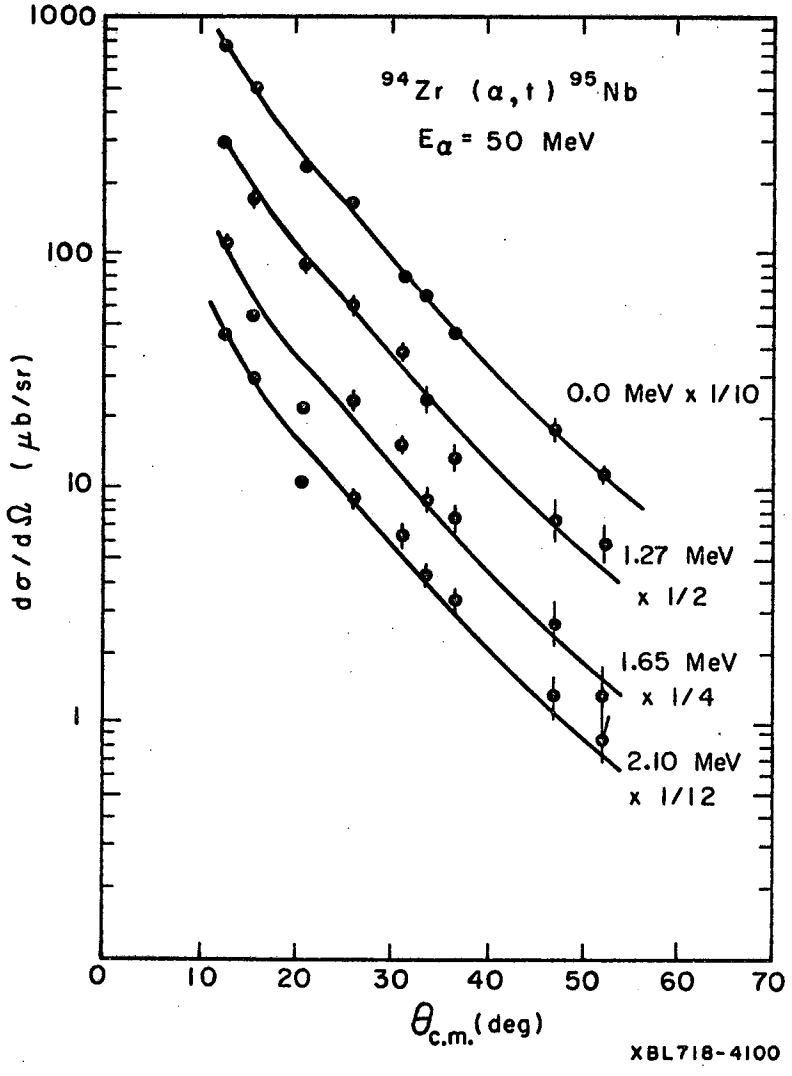

Fig. 24. Angular distributions of tritons from the $^{94}Zr(\alpha,t)^{95}Nb$ reaction leading to the 0.0, 1.27, 1.65, and 2.10 MeV levels. The solid line through each set of data points represents a smooth curve drawn through the experimental angular distribution of the ground state. Statistical errors are shown for each point.

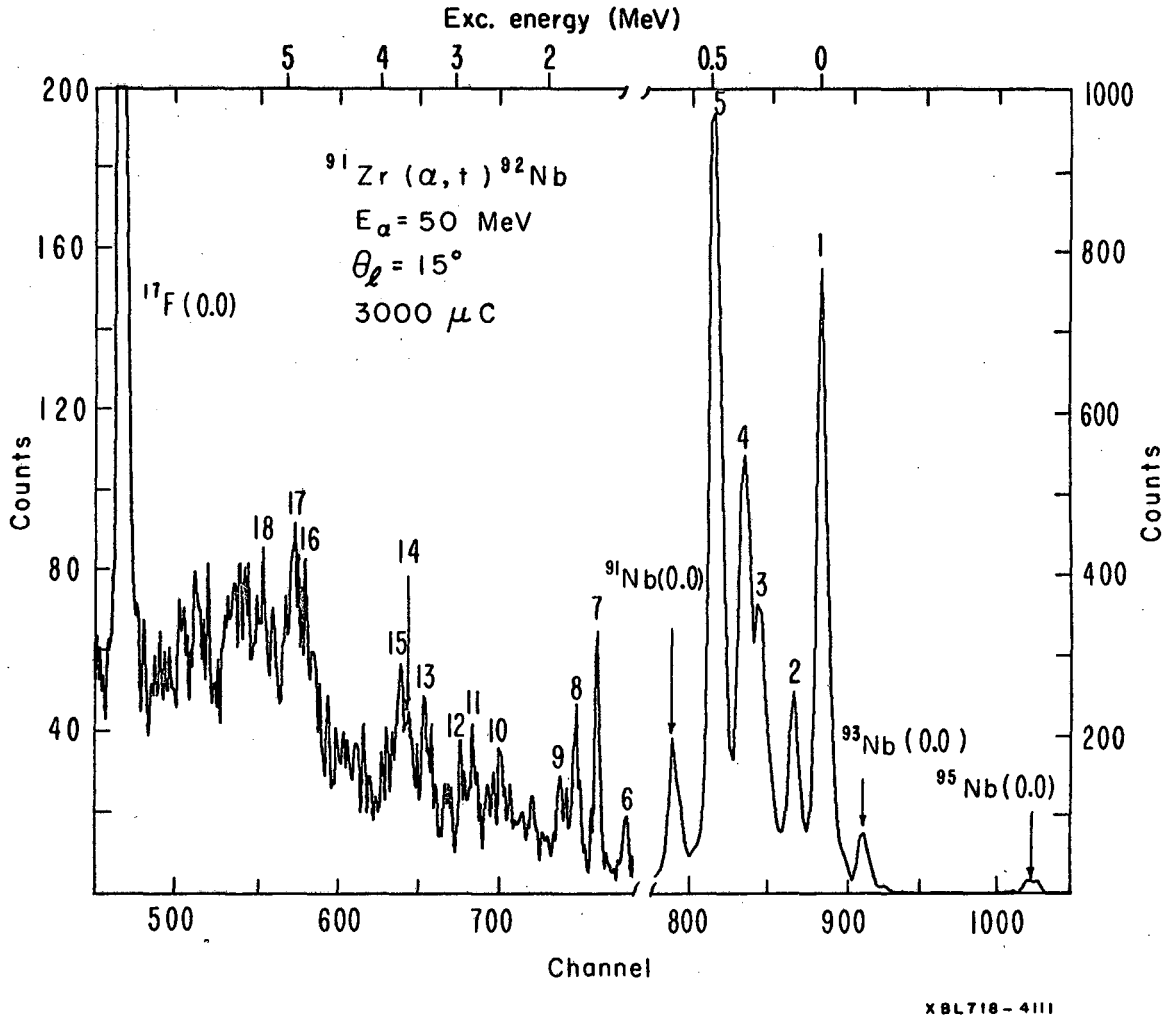

Fig. 25. Triton energy spectrum from the $^{91}Zr(\alpha,t)^{92}Nb$ reaction at $\theta_\ell = 15°$. The peak numbers correspond to excitation energies given in Table IX.

should be proportional to $(2J_f + 1)$ and the total (α,t) strength of the multiplet should be the same as that for the $g_{9/2}$ ground state of ^{91}Nb. The angular distributions of the five strong levels (the 0.478 and 0.498 MeV states were not resolved in the data) are shown in Fig. 26. The 0.27 and 0.36 MeV levels were separated by means of a Gaussian peak fitting program (Sec. III-A). The similarity to the ^{90}Zr$(\alpha,t)^{91}$Nb (g.s.) angular distribution is clear. The $(2J_f + 1)$ dependence of the integrated cross sections is given in Table VIII. The results are consistent with the recent ^{93}Nb$(d,t\gamma)^{92}$Nb experiment of Bhatia, Daehnick, and Canada[65] and the ^{91}Zr$(^3$He$,d)$ results of Ball and Cates.[55]

The absolute target thicknesses (and therefore absolute cross sections) are not well known, but a check on the <u>relative</u> thicknesses of the ^{90}Zr and ^{91}Zr targets is possible due to the appearance of the ^{90}Zr$(\alpha,t)^{91}$Nb (g.s.) peak as an impurity in the ^{91}Zr(α,t) spectra. Since the integrated cross section for this impurity peak is only about 6% higher than that obtained from the ^{90}Zr target (using the nominal target thicknesses given in Table I), it is possible to compare the ^{90}Zr(α,t) and ^{91}Zr(α,t) cross sections directly. The total integrated cross section of the five levels (from $\theta_{c.m.} = 15.7$ to $57.4°$) is 2.4 mb. The cross section for the ^{90}Zr$(\alpha,t)^{91}$Nb (g.s.) reaction (with the ^{90}Zr target) over the same angular range is 2.7 mb. The agreement indicates that this multiplet does, in fact, contain most of the $\pi g_{9/2}$ strength.

A list of the levels observed in the ^{91}Zr$(\alpha,t)^{92}$Nb reaction is given in Table IX, along with the ^{91}Zr$(^3$He$,d)^{92}$Nb results.[4] As can be seen in Fig. 25, there are few strong excited states except for the 1.40 and 1.63 MeV levels, both of which are assigned $\ell = 1$ in the $(^3$He$,d)$

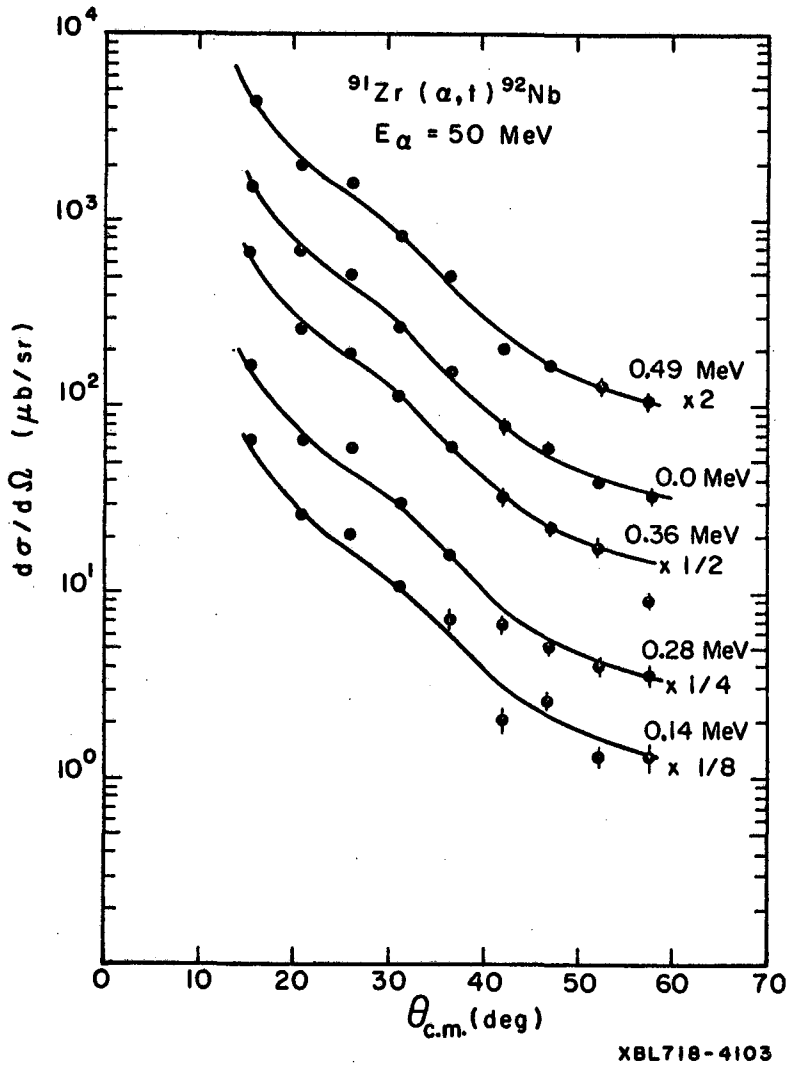

Fig. 26. Angular distributions of tritons from the $^{91}Zr(\alpha,t)^{92}Nb$ reaction leading to the 0.0, 0.14, 0.28, 0.36, and (unresolved) 0.48-0.50 MeV states. The solid line through each set of data points represents a smooth curve drawn through the experimental angular distribution of the $^{90}Zr(\alpha,t)^{91}Nb$ (g.s.) reaction from Fig. 16. Statistical errors are shown for each point.

Table VIII. $(2J_f + 1)$ Dependence of the $(\pi g_{9/2}, \nu d_{5/2})$ Multiplet in the $^{91}Zr(\alpha,t)^{92}Nb$ Reaction.

Level[a] (MeV)	J_f^{π} [a]	σ[b] (mb)	σ_R[c] (mb)	Ratio[d]
0.0	7^+	0.590	0.236	1.00
0.135	2^+	0.190	0.228	0.97
0.285	3^+	0.255	0.219	0.93
0.356	5^+	0.492	0.269	1.14
0.478 }	4^+	0.899	0.245	1.04
0.498 }	6^+			

[a]Taken from Ref. 65.

[b]Integrated from $\theta_{c.m.} = 15.7$ to $57.4°$.

[c]
$$\sigma_R = \frac{(2J_i + 1)}{(2J_f + 1)} \times \sigma = \frac{6\sigma}{(2J_f + 1)}$$

[d]Relative to ground state reduced cross section.

Table IX. Levels Observed in the $^{91}Zr(\alpha,t)^{92}Nb$ Reaction at 50 MeV.

No.	(α,t) Levels Observed[b] (MeV)	Intensity[c] (mb)	(^{3}He,d)[a] Levels Observed (MeV)	ℓ_p	C^2S
1	0.0	0.590	0.0	4	0.75
2	0.14	0.190	0.130 ± 0.005	4	0.74
			0.225	1	0.40
3	0.28	0.255	0.285	4	0.81
4	0.36	0.492	0.350	4	0.67
			0.388	1	0.34
5	0.49	0.899	0.478	4	1.00
			0.503	4	0.91
6	1.10	0.017[d]	1.09 ± 0.01	1	
			1.32	1	
7	1.40	0.059	1.42	1	
8	1.63	0.055	1.64	1	
			1.67	1	
			1.72	1	
9	1.83	0.048[e]			
10	2.49	0.044[f]			
11	2.80	0.038[e]			
12	2.94	0.032[f]			
13	3.36	--			
14	3.53	0.025[g]			
15	3.66	0.060[f]			
16	4.83 ± 0.10	--			

(continued)

Table IX (continued)

No.	(α,t) Levels Observed[b] (MeV)	Intensity[c] (mb)	(^{3}He,d)[a] Levels Observed (MeV)	ℓ_p	C^2S
17	4.93 ± 0.10	--			
18	5.21 ± 0.10	--			

[a]Ref. 4.

[b]Excitation energies ± 20 keV except as noted.

[c]Integrated from $\theta_{c.m.}$ = 15.7 to 57.4° except as noted.

[d]Integrated from $\theta_{c.m.}$ = 15.7 to 36.5°.

[e]Integrated from $\theta_{c.m.}$ = 15.7 to 52.3°.

[f]Integrated from $\theta_{c.m.}$ = 15.7 to 47.1°.

[g]Integrated from $\theta_{c.m.}$ = 15.7 to 31.4°.

work.[4] Weak levels at these energies were also reported in the ^{93}Nb(d,t) reaction,[65] but both were assigned $\ell = 0$ transitions. Since the neutron pickup and proton stripping reactions would not, in general, be expected to populate the same levels, the discrepancy is probably due to the formation of different states.

A weak group of levels appears at about 3.5 MeV in both the (α,t) and (^{3}He,d) data, which would be consistent with the formation of a $\left[^{91}\text{Nb}(3.37\text{ MeV}) \otimes \nu d_{5/2}\right]$ multiplet at this energy. A similar group of levels at about 5 MeV which is populated rather strongly in (α,t) might be associated with a $\left[^{91}\text{Nb}(4.77\text{ MeV}) \otimes \nu d_{5/2}\right]$ multiplet. Both multiplets would be expected based on the strong states observed in the ^{90}Zr(α,t)^{91}Nb reaction (see Sec. IV-A2).

B. (α,d) Reactions

1. Selection Rules

The general selection rules for two-nucleon stripping reactions are:[19]

$$J_{tgt} + J_f \geqslant J \geqslant \left| J_{tgt} - J_f \right| \tag{1}$$

and

$$\pi_f = (-)^{\ell_1 + \ell_2} \pi_i = (-)^{L + \ell} \pi_i \tag{2}$$

where

$$\vec{J} = \vec{j}_1 + \vec{j}_2 = \vec{L} + \vec{S} \tag{3}$$

For light projectiles the relative motion is assumed to be pure s-state (i.e., $\ell = 0$), in which case

$$\pi_f = (-)^L \pi_i \tag{4}$$

In the case of the (α,d) reaction, the overlap integral between the α particle and deuteron requires that the transferred pair have S = 1 and T = 0 and equation (3) becomes

$$\vec{J} = \vec{L} + \vec{1} \tag{5}$$

For (α,d) reactions on even-even targets, where $J^{\pi}_{tgt} = 0^+$, eqs. (1) and (2) can be further simplified to

$$\vec{J}_f = \vec{L} + \vec{1} \tag{6}$$

and

$$\pi_f = (-)^L \tag{7}$$

2. $^{14}N(\alpha,d)^{16}O$

A deuteron spectrum of the $^{14}N(\alpha,d)^{16}O$ reaction at 40 MeV and $\theta_\ell = 10°$ is shown in Fig. 27. The resolution is 66 keV (FWHM) for the narrow states of ^{16}O. Since a biased amplifier was used to look selectively at the high

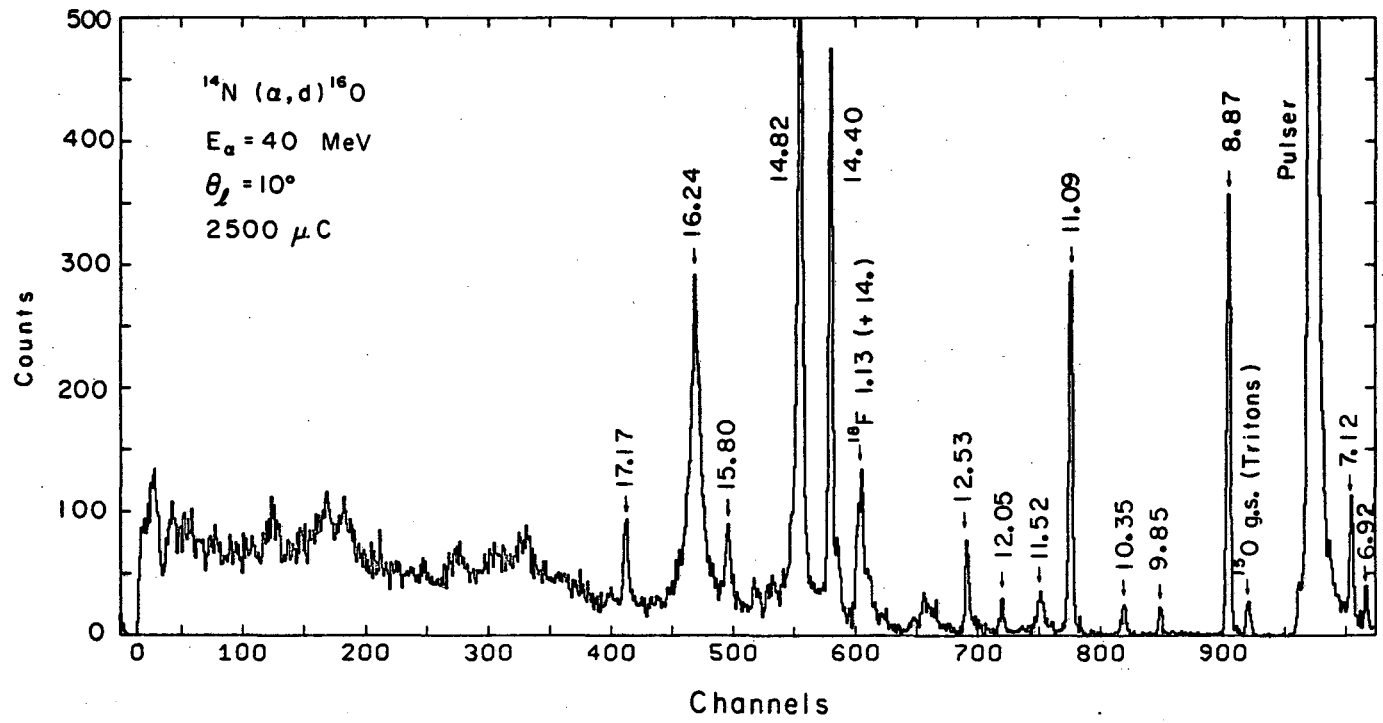

Fig. 27. Deuteron energy spectrum from the $^{14}N(\alpha,d)^{16}O$ reaction at $\theta_\ell = 10°$. The "14 MeV" peak contains a contribution of unknown amount from the $^{16}O(\alpha,d)^{18}F$ (1.13 MeV) reaction on a target impurity.

excitation energy region of ^{16}O, the ground state does not appear at any angle and the first two excited states, at 6.05 and 6.13 MeV, are visible only at the more backward angles. It can be seen that even with this improved experimental resolution the three members of the previously observed[15] triplet still appear as single states. However, a new state at 15.80 MeV, which was unresolved in the earlier work,[15] is now visible. The excitation energies determined from this work for the strongest states are 14.40 ± 0.03, 14.82 ± 0.03, and 16.24 ± 0.04 MeV.

Angular distributions for the triplet from $\theta_{c.m.}$ = 12.9 to 57.7° are shown in Fig. 28. As was observed in the earlier work,[14,15,17] the angular distributions are rather structureless and decrease almost exponentially with angle. The integrated cross sections for these states (from $\theta_{c.m.}$ = 12.9 to 57.7°), after background subtraction, are 1.52, 2.90, and 1.91 mb. In Ref. 15, the cross section of the 15.8 MeV state was contributing to that of the 16.16 MeV level. This amounts to a correction of about 13% to the cross section reported[15] for the 16.16 MeV state. The uncertainty in the absolute cross sections is estimated to be about 10%.

Widths were obtained for all three states based on an average of seven runs at five angles. The values for $\Gamma_{c.m.}$ (with the experimental resolution subtracted in quadrature) as well as previously measured widths for nearby T = 0 levels are given in Table X. The difficulty in obtaining accurate widths for the states was due to uncertainties in the background subtraction and to the experimental resolution. The latter was particularly important for the 14.40 MeV state, whose width is small compared with the

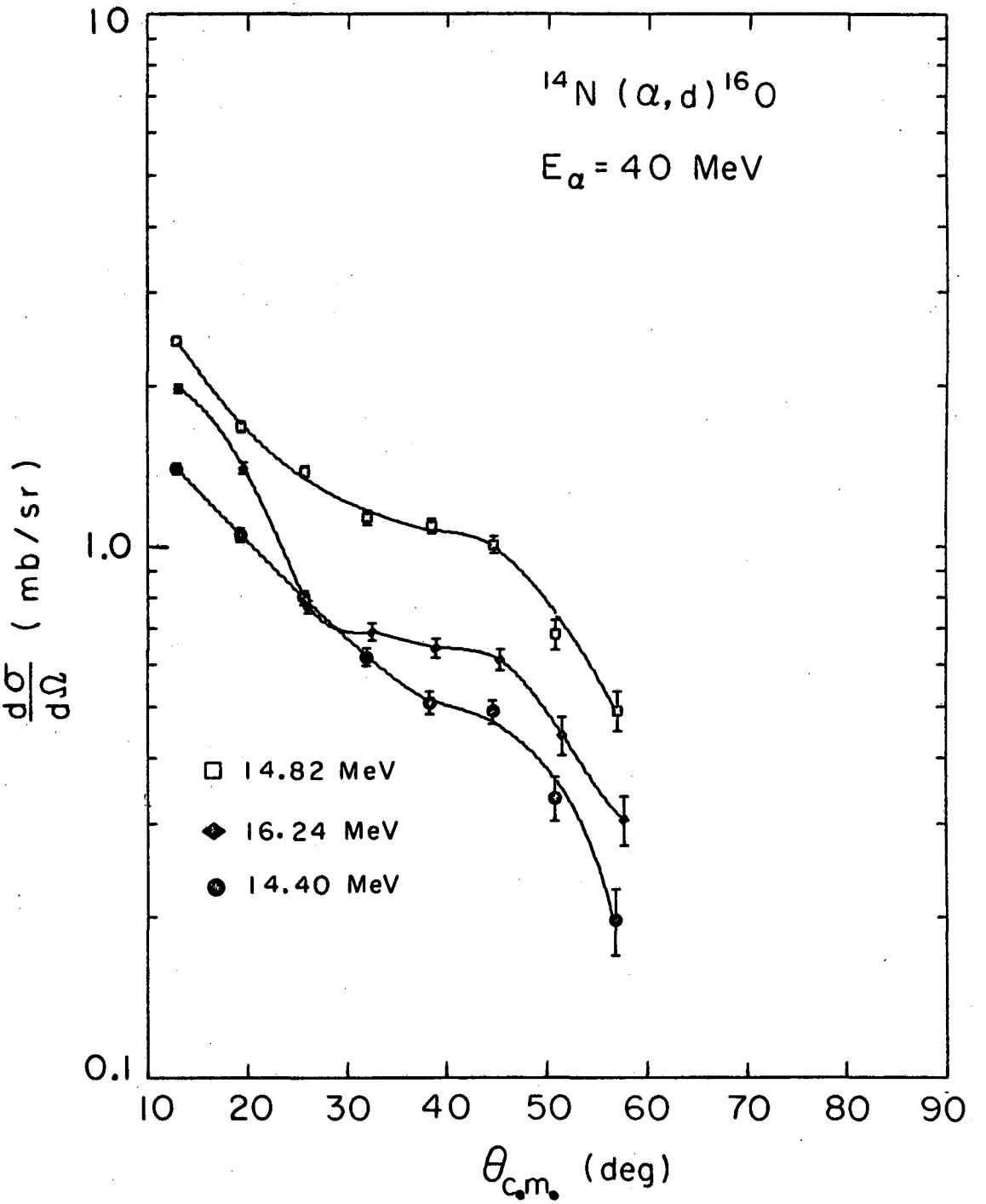

XBL706-3086

Fig. 28. Angular distributions of deuterons from the $^{14}N(\alpha,d)^{16}O$ reaction leading to the 14.40, 14.82, and 16.24 MeV levels. Statistical errors are shown for each point. The curves have no theoretical significance.

Table X. Widths of Levels Observed in $^{14}N(\alpha,d)^{16}O$ Compared with Previously Measured Nearby T=0 Level Widths.

This Work		Previously Measured[a]	
E_x (MeV)	Γ_{cm}[b] (keV)	E_x (MeV)	Γ_{cm} (keV)
14.40 ± 0.03	30 ± 30	14.40	<30[c]
		14.72	400
14.82 ± 0.03	69 ± 30	14.81	40-60, 60[c], 67[d], 53[e]
		14.85	75
		15.42	60
		15.7	525
15.80 ± 0.04	(60)	15.8	300-400, ≈ 40[f], <80[c]
16.24 ± 0.04	125 ± 50	16.2	320[g]
		16.30	360[h]
		16.41	60
		17.10	110
17.17 ± 0.04	(70)	17.14	≈ 80[f,i]

[a]Taken from Ref. 25 unless otherwise noted.

[b]With experimental resolution (≈ 75 keV) subtracted in quadrature.

[c]Ref. 81. [d]Ref. 82. [e]Ref. 83. [f]Ref. 95.

[g]This value was changed from that in Ref. 25 by Ref. 73.

[h]Ref. 76

[i]This state is possibly a T=1 analog to the ^{16}N(4.32 MeV) level.

resolution. In fact, in two of the seven runs the observed width (after background subtraction) was consistent with those of the lower energy, sharp states in ^{16}O. The problem of background subtraction was most severe for the 16.24 MeV state, since it has a large width and, at backward angles, the peak shape was poorly defined.

The selectivity of the (α,d) reaction in populating the various final states in ^{16}O is indicated by Fig. 27. Aside from the triplet of states at 14.40, 14.82, and 16.24 MeV, the only other strongly populated states are those at 8.87 and 11.09 MeV. At backward angles where the 6.13 MeV level was observed, it too was found to be populated strongly. (A summary of the states observed in this experiment and their intensities is given in Table XI.) In part, this selectivity is based on the kinematics of the reaction, i.e., on the fact that the favored momentum transfer (see Appendix A) is large. However, due to the 1^+ spin of the target nucleus, the number of possible L values for a given transition is increased, with the result that selection rules allow $L \geqslant 2$ for all values of J_f^π except 0^-. Since the maximum angular momentum transfer for placing two nucleons in the sd shell is L = 4, this form of selectivity is somewhat reduced.

The other reason for selective population of certain final states is based on the sensitivity of two-nucleon transfer reactions to the details of nuclear structure. In the notation of Glendenning,[19] the states which can be strongly populated are those with a large "structure factor," i.e., those whose wave functions are predominantly of the form [target core + "deuteron"] for the (α,d) reaction. This implies that the final states in ^{16}O which are preferentially populated should be those described as 1p-1h

Table XI. Comparison of ^{16}O (T=0) Levels Observed in $^{14}N(\alpha,d)^{16}O$ with Those Reported Previously.

Levels Observed[a] (MeV ± keV)	T=0 Levels Previously Reported[b] (MeV)	J^{π} [b]	Intensity[c] (mb)
---[d]	0.0	0^+	
	6.050	0^+	
6.13	6.131	3^-	0.78[e]
6.92	6.919	2^+	Weak
7.12	7.119	1^-	Weak
8.87	8.872	2^-	0.62
	9.597	1^-	
9.85	9.847	2^+	0.10
10.35	10.353	4^+	0.16
	10.952	0^-	
	11.080	3^+	
11.09	11.096	4^+	1.01
	11.26	0^+	
11.52	11.521	2^+	0.24
	11.63	3^-	
12.05 ± 30	12.053	0^+[f]	0.08[g]
	12.441	1^-	
12.53	12.528	2^-	0.27
	[Mainly T=1]		

(continued)

Table XI (continued)

Levels Observed[a] (MeV ± keV)	T=0 Levels Previously Reported[b] (MeV)	J^{π}[b]	Intensity[c] (mb)
	13.869	4^+	
(14.0)[h]	13.978	2^-	
14.40 ± 30	14.39		1.52
	14.6[i]	even[i]	
	14.78[i]	$(0^+,1^-)$[i]	
14.82 ± 30	14.81	6^+	2.90
	14.85[i]		
	14.922	4^+	
	15.22	2^-	
	15.26	2^+	
	15.42	$3^-,1^-$	
	15.7[i]	3^-[i]	
15.80 ± 40	15.792		0.25[j]
16.24 ± 40	16.23	6^+	1.91
	16.3	(0^-)	
	16.407	2^+	
	17.10[i]	$(1^-,2^+,0^+)$[i]	
17.17 ± 40	17.17	2^+	0.45
	17.30	1^-	

(continued)

Table XI (continued)

[a]All energies ± 15 keV unless otherwise specified.

[b]Information is taken from F. Ajzenberg-Selove, Energy Levels of Light Nuclei, Nucl. Phys. A166, 1 (1971) and Ref. 74 unless otherwise noted.

[c]Integrated cross section from $\theta_{c.m.}$ = 12.9 to 57.7° except as noted.

[d]The ground state was not observed due to the experimental conditions.

[e]Integrated from $\theta_{c.m.}$ = 30.5 to 54.3°.

[f]Ref. 72.

[g]Integrated from $\theta_{c.m.}$ = 12.7 to 49.9°.

[h]Contains contaminant peak due to the $^{16}O(\alpha,d)^{18}F$ reaction.

[i]Ref. 25.

[j]Integrated from $\theta_{c.m.}$ = 13.0 to 45.1°.

or 2p-2h with respect to the ^{16}O core, since the target wave function[66] is about 93% $(p_{1/2}^{-2})_{1^+}$. It has been suggested for some time that certain states in ^{16}O exhibit a rotational band structure[25,67] based on the 6.05 MeV 0^+ state. This result has been reproduced with various calculations[68-71] involving a mixture of 4p-4h and 2p-2h configurations in a deformed basis. The nature of the lowest even-parity band is believed to be mainly 4p-4h.[70,71] Clearly such states should not be strongly populated in a two-nucleon transfer reaction on a target having only about a 7% mixture of 2p-4h configurations in its ground state.[66]

These data are consistent with the interpretation that the ^{16}O states assigned to the rotational band have a dominant 4p-4h configuration. As can be seen in Fig. 27, the 6.92 and 10.35 MeV states, 2^+ and 4^+, respectively, are both populated rather weakly. The angular distribution for the 10.35 MeV level is quite different from those of the strong states, being relatively flat as opposed to the rather steep envelope typical of the strongly populated levels. This result has been observed previously[14,17] in (α,d) reactions leading to weakly populated final states. The angular distribution of the 6.92 MeV level could not be extracted since it was obscured by the pulser at most angles. At those angles where the 6.13 MeV level appeared it had a width (and peak position) consistent with only a single state being populated. However, assuming the 6.05 MeV state has a cross section similar to those of the other 4p-4h states (or to that of the other excited 0^+ state[72] at 12.05 MeV), it would probably not be visible next to the much stronger 3^- level. On this basis, strong population of the 4p-4h 6^+ state observed in the α-^{12}C resonance work[25] seems highly unlikely.

The α-^{12}C resonance experiment[25,73] yields a width for the 16.2 MeV 6^+ state of $\Gamma_{c.m.} = 320 \pm 90$ keV. This is to be compared with a value from this work of $\Gamma_{c.m.} = 125 \pm 50$ keV for the 16.24 MeV level. In contrast to the large width quoted for the 16.2 MeV 4p-4h 6^+ level, it is worth noting that there are other natural parity levels in ^{16}O which, although unbound by a large amount, have very small α widths. For example, the 12.05 MeV 0^+ level is unbound by nearly 5 MeV and yet it shows up as a very weak α resonance with a measured width of only 1.5 ± 0.5 keV,[72] while the 10.35 MeV 4^+ state, which is a member of the 4p-4h rotational band, has a width of 27 ± 8 keV[74] for a lower energy $L = 4$ α decay. The 0^+ level, however, is believed to be the predominantly 2p-2h member of the triplet of 0^+ states arising from a mixture of 0p-0h, 2p-2h, and 4p-4h states,[71] and thus has a configuration which overlaps poorly with $\left[^{12}C + \alpha\right]$. This interpretation is consistent with the data reported here inasmuch as the integrated cross section for the 12.05 MeV state is about half that for the 10.35 MeV state. Thus, the reduced cross section of the 0^+ state in (α,d) is about 4 times larger than that of the 4^+ state, in spite of the expected preference for the 4^+ state based on the kinematics argument given above. It would seem, therefore, that the large width and the strong α resonance characteristic of the 16.2 MeV level observed by Carter, Mitchell, and Davis[25] do suggest a dominant 4p-4h configuration for that state.

Another way of comparing the large states observed in the $^{14}N(\alpha,d)^{16}O$ reaction with levels of 4p-4h configuration is to look at the results of the four-nucleon transfer reactions leading to ^{16}O. These

should preferentially populate 4p-4h states if the reaction mechanism corresponds to a direct α-particle transfer. The $^{12}C(^{6}Li,d)^{16}O$,[75-78] $^{12}C(^{7}Li,t)^{16}O$,[77-79] and $^{12}C(^{12}C,^{8}Be)^{16}O$,[80] reactions have all been reported by various groups. The $^{12}C(^{6}Li,d)$ reaction[75,76] shows strong population of the 10.35 MeV 4^{+} level as well as large cross sections for states at about 14.4, 14.8, and 16.3 MeV. The $^{12}C(^{7}Li,t)$ results are essentially identical,[78,79] showing strong population of the 10.35 MeV state and broad structure at 14-15 and 16.2 MeV. The $^{12}C(^{12}C,^{8}Be)$ data, while hampered by poor resolution, give results in agreement with those of the lithium-induced reactions, the strongest states appearing at 10.34, 14.67, 16.27 MeV.[80]

The interpretation of these results, of course, requires some knowledge of the reaction mechanism. In the case of α-particle transfer the final states expected would be only natural parity, T = 0 levels, although in either reaction the selection rules allow formation of unnatural parity states, and in the $(^{7}Li,t)$ reaction T = 1 levels are also allowed. Bethge et al.[77] have made a careful comparison of both reactions and conclude that, while the $(^{6}Li,d)$ reaction seems to have some compound-nucleus contributions, the $^{12}C(^{7}Li,t)$ reaction, at least at 20 MeV, can be interpreted as an α-particle transfer reaction. It appears that the strongest states observed in both reactions can be understood in terms of α-particle transfer. This allows population of np-nh states in ^{16}O, where $0 \leqslant n \leqslant 4$, assuming the ^{12}C ground state is mainly 0p-4h.

A comparison of the $^{14}N(\alpha,d)^{16}O$ data with the above results indicates that both the four- and two-particle transfer reactions show strength for states at about 14.5 and 16.3 MeV. The level near 16.3 MeV

appears broad in the four-nucleon transfer data. A precise measurement of the excitation energy and width of this state made by Bassani et al.[76] yielded $E_x = 16.304 \pm 0.02$ MeV and $\Gamma_{c.m.} = 360 \pm 40$ keV. These values agree with the original α-^{12}C resonance measurement of Carter, Mitchell, and Davis,[25,73] and disagree with the values obtained from the $^{14}N(\alpha,d)$ data reported here. Recently the $^{14}N(\alpha,d)$ experiment was repeated at 30 MeV by Lowe and Barnett.[81] Their results for the triplet of strong states are: 14.400 ± 0.003 MeV ($\Gamma_{c.m.} \leqslant 30$ keV), 14.815 ± 0.002 MeV ($\Gamma_{c.m.} = 60 \pm 12$ keV), and 16.214 ± 0.015 MeV ($\Gamma_{c.m.} = 96 \pm 16$ keV). This latter value tends to confirm the belief that there are two distinct states in this region, one of which is the broad state of 4p-4h nature,[25,75-80] and the other of which is a 2p-2h state whose dominant configuration is $\left[{}^{14}N(1^+) + (d_{5/2})^2_{5^+}\right]$.

The fact that the four-nucleon transfer reactions appear to populate the states at 14.4 and 14.8 MeV which are observed in the (α,d) reaction may indicate that four-nucleon transfer reactions can populate both states in the 16.2 MeV region, while the $^{14}N(\alpha,d)$ reaction is able to strongly populate only the 2p-2h level. The 14.82 MeV state, which is the strongest state in the $^{14}N(\alpha,d)$ data, has been observed recently in the α-^{12}C resonance reaction and assigned[82,83] a spin of 6^+. Both the excitation energy and width of the state seen in the resonance experiments agree with the $^{14}N(\alpha,d)^{16}O$ results[18,81] (see Table X). The state which appears to be "missing" in the α-^{12}C resonance data is the one at 14.40 MeV in the (α,d) data. Evidence for an unnatural parity assignment was obtained by Artemov et al.[84] who studied the α decay of the strong states formed in $^{14}N(\alpha,d)$. They

observed no decay of the 14.40 MeV state to the ^{12}C (g.s.) while the 14.82 and 16.24 MeV states were seen to decay with equal probability to both the ground and first excited state of ^{12}C. The absence of a ground state α decay argues strongly for the assignment of $\left[^{14}N(1^+) + (d_{5/2})^2_{5^+}\right]_{5^+}$ to the 14.40 MeV state. It is interesting that the $^{12}C(^6Li,d)$ reaction[75,76] appears to strongly populate this state, since an unnatural parity state would be forbidden in a direct α-transfer reaction.

The expectation of a triplet of ^{16}O states with the configuration $\left[^{14}N(1^+) + (d_{5/2})^2_{5^+}\right]_{4^+,5^+,6^+}$ is based on the systematics of the (α,d) reaction in this mass region. On even-even targets such as ^{12}C and ^{16}O the $(d_{5/2})^2_{5^+}$ state was always the most strongly populated in the (α,d) data.[14,15] Additional support for interpreting the 14.40, 14.82, and 16.24 MeV states as members of this triplet comes from the shell model calculations of Zuker, Buck, and McGrory[85] (referred to hereafter as ZBM). ZBM perform a complete diagonalization in the space of up to four particles in the $1p_{1/2}$, $1d_{5/2}$, and $2s_{1/2}$ orbitals and predict the existence of very pure ($\gtrsim$95%) 6^+ and 5^+ states of the above configuration which essentially do not mix with the 4p-4h levels. The purity of these states is very insensitive to changes in either the matrix elements or the single-particle energies used in the calculation. Based on the matrix element set B in Ref. 85, the states are predicted at 13.4 and 14.4 MeV, with the 6^+ being lower. This ordering is also more or less independent of the choice of matrix elements and single-particle energies, although adjustments in these quantities do alter the predicted excitation energies and splitting somewhat. The existence of a nearby 4p-4h 6^+ state, containing less than 1% admixture of

2p-2h configuration, is also predicted by this model. The fact that the 4p-4h state is calculated to lie at 16.9 MeV (again using matrix element set B) is consistent with the interpretation by Carter, Mitchell, and Davis[25] that the 16.2 MeV 6^+ resonance is a 4p-4h state.

The situation for the 4^+ state is, unfortunately, not so clearcut. The ZBM results predict appreciable mixing of this state, both with 4p-4h components and with other 2p-2h configurations. There are two 4^+ states (referred to as 4^+_3 and 4^+_4 in ZBM) expected to carry the major part of the $(d_{5/2})^2_{5+}$ strength. The results from matrix element set B indicate that the (α,d) strength would go mainly to the upper, 4^+_4, state at an excitation energy of 15.8 MeV. However, this prediction <u>is</u> sensitive to the choice of matrix elements, since the wave functions for 4^+_3 and 4^+_4 essentially interchange in going to matrix element set A1, with the result that the lower 4^+ level now becomes the (expected) stronger (α,d) transition. The results for the 4^+ level would also be less certain than those for the 5^+ and 6^+ levels if there are any effects due to the omission of the $d_{3/2}$ orbital, since a small amount of $(d_{3/2})^2_{3+}$ could alter the expected strengths of the various 4^+ levels.

The reduced cross sections for the 14.40, 14.82, and 16.24 MeV states, after dividing by $[(2J_f+1)/(2J_{tgt}+1)]$, are 0.51, 0.67, and 0.52 mb, respectively. This is based on a spin sequence 4^+, 6^+, 5^+, since the observed cross sections are $\sigma_{14.82} > \sigma_{16.24} > \sigma_{14.40}$. The spin sequence predicted from the ZBM model[85] for the $\left[{}^{14}N(1^+) + (d_{5/2})^2_{5+}\right]$ triplet is 6^+, 5^+, 4^+, in order of increasing excitation energy. However, the evidence presented above implies that the 14.82 MeV level is a 6^+ state[82,83] and the 14.40 MeV level is an unnatural parity (and presumably, therefore,

5^+) state.[84] Thus, the 16.24 MeV level should be a 4^+ state if the strong (α,d) states are interpreted as a $(d_{5/2})^2$ triplet. The "experimental" ordering is in disagreement both with the $2J_f+1$ sequence and the ZBM predictions. The former discrepancy is perhaps not surprising since there can be coherent effects in the two-nucleon transfer process which change the observed cross sections by significant amounts. Within the framework of the ZBM calculation, however, it is difficult to change the ordering of the 6^+ and 5^+ states, since, as mentioned above, the purity and ordering of the levels are essentially independent of the adjustable parameters in the model. As yet there is no explanation for this anomaly, unless the identification of the strong $^{14}N(\alpha,d)$ states as a $\left[^{14}N(1^+)+(d_{5/2})^2_{5^+}\right]_{4^+,5^+,6^+}$ triplet is itself incorrect.

The other strong positive parity peak observed in this reaction is the 11.09 MeV doublet. These states, at 11.080 and 11.094 MeV, were both observed in the $^{14}N(^3He,p)$ reaction,[74] and the lower member was assigned $J^\pi = 3^+$ in the $^{14}N(^3He,p\gamma\gamma)$ reaction.[86] The upper member was seen in the $^{12}C(\alpha,\alpha_0)^{12}C$ reaction[72] and assigned $J^\pi = 4^+$ with a width $\Gamma_{c.m.} = 0.3 \pm 0.1$ keV. A peak at this energy has also been observed in almost all other stripping reactions leading to ^{16}O, including $^{15}N(^3He,d)$,[87] $^{15}N(\alpha,t)$,[88] $^{14}N(^3He,p)$,[89] $^{13}C(^6Li,t)$,[90] $^{12}C(^6Li,d)$,[75] $^{12}C(^7Li,t)$,[91] and $^{12}C(^{12}C,^8Be)$.[80] The $^{14}N(\alpha,d)$ results, as well as those from $^{12}C(^6Li,d)$, $^{12}C(^7Li,t)$, and $^{13}C(^6Li,t)$, indicate that it is mainly the upper member of the doublet which is being populated (based on the observed peak energy). A precise measurement of the energy of this state by Lowe and Barnett,[81] also using the $^{14}N(\alpha,d)$ reaction, gives $E_x = 11.094 \pm 0.003$ MeV which confirms that it is the 4^+ which appears in the (α,d) data.

The ZBM calculations predict a pair of levels with $J^{\pi} = 3^+, 4^+$ which appear rather close together [$E(3^+) = 13.39$ MeV, $E(4^+) = 13.02$ MeV] although the order is inverted and the energies are too high. These states both contain large amplitudes of the 2p-2h configurations $(d_{5/2}s_{1/2})_{3^+}$ and $(d_{5/2})^2_{3^+}$ which have fairly large L = 2 structure factors[92] for formation in the $^{14}N(\alpha,d)^{16}O$ reaction. If the association of these levels with the observed doublet at 11.09 MeV were correct, the peak should contain comparable contributions from both levels, but the data of Ref. 81 indicate that this is not true. The relatively weak population of this level in $^{12}C(^7Li,t)$[91] and the small α width[72] argue against a dominant 4p-4h configuration. This is consistent with the very strong population of this state in the $^{14}N(\alpha,d)$ and $^{13}C(^6Li,t)$ reactions. The $^{14}N(^3He,p)$ data of Weibezahn et al.,[89] however, showed only 1/5 of the 2p-2h strength for this state expected from the ZBM wave functions, and suggested that this state might be due mainly to configurations with an excited ^{12}C core. The appearance of this state in so many different reactions would seem to imply a great deal of configuration mixing, some of which, e.g., ^{12}C core-excited states, is not included in the ZBM model.

The negative parity ^{16}O levels which are strongly populated in the $^{14}N(\alpha,d)$ reaction should be those with a 1p-1h configuration. The 6.13 and 8.87 MeV levels, 3^- and 2^-, respectively, are both described as having large amplitudes of the $(p^{-1}_{1/2}d_{5/2})$ configuration[85,93] which overlaps well with the [target core + deuteron] structure expected for the strongly populated levels in the (α,d) reaction. Both levels were excited with an $\ell = 2$ transition in the $^{15}N(^3He,d)^{16}O$ reaction,[87,94] in agreement

with this picture. The other negative parity state excited in $^{14}N(\alpha,d)$, at 12.53 MeV, was also observed in the $^{15}N(^{3}He,d)$ experiments and is described as being mainly a $(p^{-1}_{1/2}d_{3/2})_{2-}$ level.[94] This state would also be expected in the (α,d) reaction based on Glendenning's structure factors.[92]

The spin and parity of the 15.80 MeV level have not been established. It was observed by Comfort, Baglin, and Thompson[95] in the $^{14}N(^{3}He,p)^{16}O$ reaction and was suggested to be a T = 0 state, since no analog in ^{16}N is known. A preliminary analysis of the $^{14}N(^{3}He,p)$ data yielded a width of about 40 keV for the 15.80 MeV level, but no L value was assigned. The appearance of this state in the $^{14}N(\alpha,d)^{16}O$ reaction confirms that it is a T = 0 level. The width obtained here for the 15.80 MeV level is approximately 60 keV, but the low cross section and the position of the peak preclude anything but a rough estimate of this quantity. A peak at 15.78 ± 0.05 MeV with a width of $\leqslant$ 80 keV was also reported in the lower energy $^{14}N(\alpha,d)$ data.[81]

The highest sharp state observed in this work is at 17.17 ± 0.04 MeV. States in this region have also been observed in the α-^{12}C and p-^{15}N resonance reactions[25,96] at 17.10 and 17.14 ± 0.015 MeV, respectively, in the $^{14}N(^{3}He,p)^{16}O$ reaction[95] at 17.14 ± 0.02 MeV, in the $^{14}N(\alpha,d)^{16}O$ reaction[81] at 17.18 ± 0.05 MeV, and in the $^{15}N(^{3}He,d)^{16}O$ reaction[94] at 17.12 MeV. The state observed in the p-^{15}N resonance was assigned J = 1 and has $\Gamma_{c.m.}$ = 33 ± 5 keV.[96] It is assumed to be the T = 1 analog of the 4.32 MeV 1^{+} level in ^{16}N, based on the fact that its observed width is much less than that of the T = 0 resonance observed by Carter, Mitchell, and Davis[25] at 17.10 MeV with $\Gamma_{c.m.}$ = 110 keV and J^{π}= $(1^{-}, 0^{+}, 2^{+})$. The

$^{14}N(^{3}He,p)$ data[95] yield a value of $\Gamma_{c.m.} \approx 80$ keV for the 17.14 MeV level. It would appear, therefore, that this state has a much larger width than that of the known T = 1 resonance.[96] The data obtained here indicate a width of approximately 70 keV for the 17.17 MeV state, but this is uncertain due to problems with background subtraction. If the 17.17 MeV level seen here is identical to that at 17.14 MeV observed by Comfort, Baglin, and Thompson,[95] then a T = 0 assignment is required. The 17.12 MeV level observed by Fulbright et al.[94] in the $^{15}N(^{3}He,d)$ reaction is believed to be a negative parity state, since its strength would be inconsistent with a positive parity assignment. However, no ℓ value was determined in that work.

3. $^{90}Zr(\alpha,d)^{92}Nb$

A spectrum of the $^{90}Zr(\alpha,d)^{92}Nb$ reaction at $\theta_\ell = 20°$ is shown in Fig. 29. The resolution is 50 keV (FWHM). A summary of the levels observed in this work is given in Table XII. Except for the low-lying $(\pi g_{9/2},\nu d_{5/2})$ multiplet in ^{92}Nb, very few levels are populated in both the $^{91}Zr(\alpha,t)$ and $^{90}Zr(\alpha,d)$ reactions. This implies that most of the states observed in (α,d) do not contain appreciable $\nu d_{5/2}$ strength. The 1.08 MeV level appears (weakly) in all reactions leading to ^{92}Nb, including the $^{93}Nb(d,t)$ experiment;[65] thus, it probably has a rather complicated structure. The level density is too high to make detailed comparisons between the $^{91}Zr(\alpha,t)$ and $^{90}Zr(\alpha,d)$ data, but the (α,d) levels at 2.46, 2.81, and 4.83 MeV may correspond to levels seen in the single-nucleon transfer (cf. Table IX).

The selectivity of the (α,d) reaction is evident from the relative intensities of the levels belonging to the $(\pi g_{9/2},\nu d_{5/2})$ multiplet (see

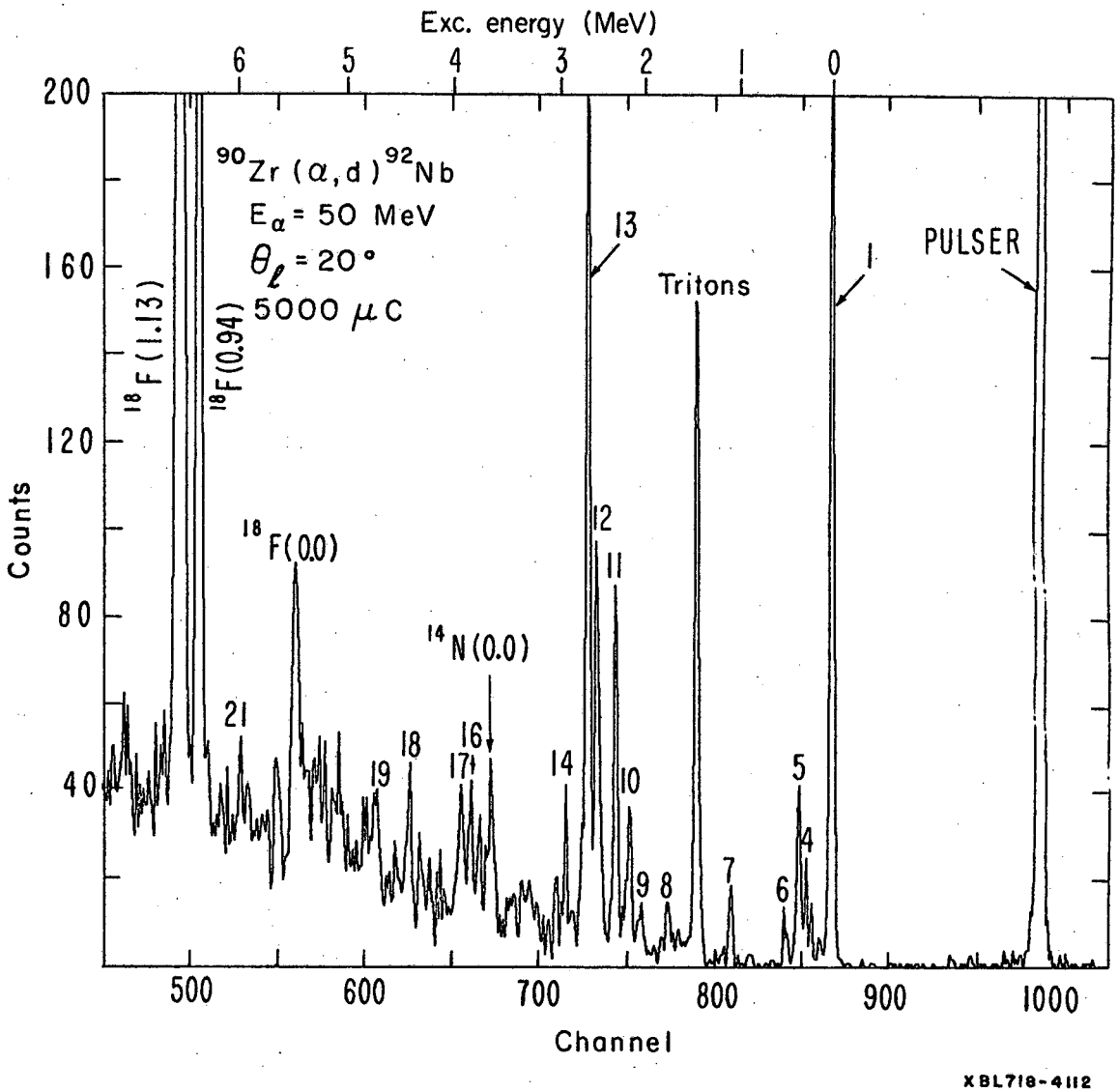

Fig. 29. Deuteron energy spectrum from the $^{90}Zr(\alpha,d)^{92}Nb$ reaction at $\theta_\ell = 20°$. The peak numbers correspond to excitation energies given in Table XII.

Table XII. Levels Observed in the $^{90}Zr(\alpha,d)^{92}Nb$ Reaction at 50 MeV.

No.	Levels Observed[a] (MeV)	Intensity[b] (mb)
1	0.0	0.278
2	0.13	Weak
3	0.21	Weak
4	0.28	0.025
5	0.36	0.069
6	0.49	0.01
7	1.08	0.022
8	1.75	0.03
9	2.03	0.019
10	2.15	0.051
11	2.28	0.097
12	2.47	0.166[c]
13	2.58	0.345
14	2.81	0.047[c]
15	3.72	0.057
16	3.81	0.040
17	3.92	0.053
18	4.45	0.04[d]
19	4.83	0.05[d]
20	5.62	0.124
21	(6.0 ± 0.1)	--

(continued)

Table XII (continued)

[a]Excitation energy ± 30 keV except as noted.

[b]Integrated from $\theta_{c.m.}$ = 12.4 to 56.8° except as noted.

[c]Integrated from $\theta_{c.m.}$ = 12.4 to 51.7°.

[d]Integrated from $\theta_{c.m.}$ = 12.4 to 31.1°.

Sec. IV-A6). The 7^+ (g.s.) is populated much more strongly than the other states in the multiplet; it is about 20 times stronger than the 4^+, 6^+ doublet at 0.50 MeV. The only level populated as strongly as the ground state (7^+) is No. 13, at 2.58 MeV. Angular distributions for the ground and 2.58 MeV states are shown in Fig. 30. The higher excited states tend to have rather structureless angular distributions, differing from one another only in slope. The ground state (7^+), however, does exhibit some oscillatory behavior. Similar structure was reported[15] for the $0^+ \longrightarrow 7^+$ transition in the $^{40}Ca(\alpha,d)^{42}Sc$ reaction although the oscillations were attributed to the presence of a nearby 1^+ level in that case. This $0^+ \longrightarrow 7^+$ (L = 6) pattern (Fig. 30) does appear to reproduce in the other examples studied in this work (see below).

4. $^{92}Mo(\alpha,d)^{94}Tc$

A spectrum of the $^{92}Mo(\alpha,d)^{94}Tc$ reaction at $\theta_\ell = 20°$ is shown in Fig. 31. The resolution is 65 keV (FWHM). The spectrum is quite similar to that of the $^{90}Zr(\alpha,d)^{92}Nb$ reaction (Fig. 29): only two levels are strongly excited, the ground and 2.68 MeV states. A summary of the levels observed in this work is given in Table XIII.

Relatively little is known about the ^{94}Tc level scheme. The ground state is known to be a 6^+ or 7^+ based on the observed isomeric transition from the 107 keV 2^+ level and the allowed β decay of ^{94g}Tc to the 2.4232 MeV 6^+ level in ^{94}Mo.[97] The observed strength of the ground state in (α,d) is inconsistent with a 6^+ assignment since the 6^+ should be at least 20 times weaker than the 7^+ based on the $^{90}Zr(\alpha,d)^{92}Nb$ results (Sec. IV-B3). Also, the angular distribution of the ground state (Fig. 32) is identical

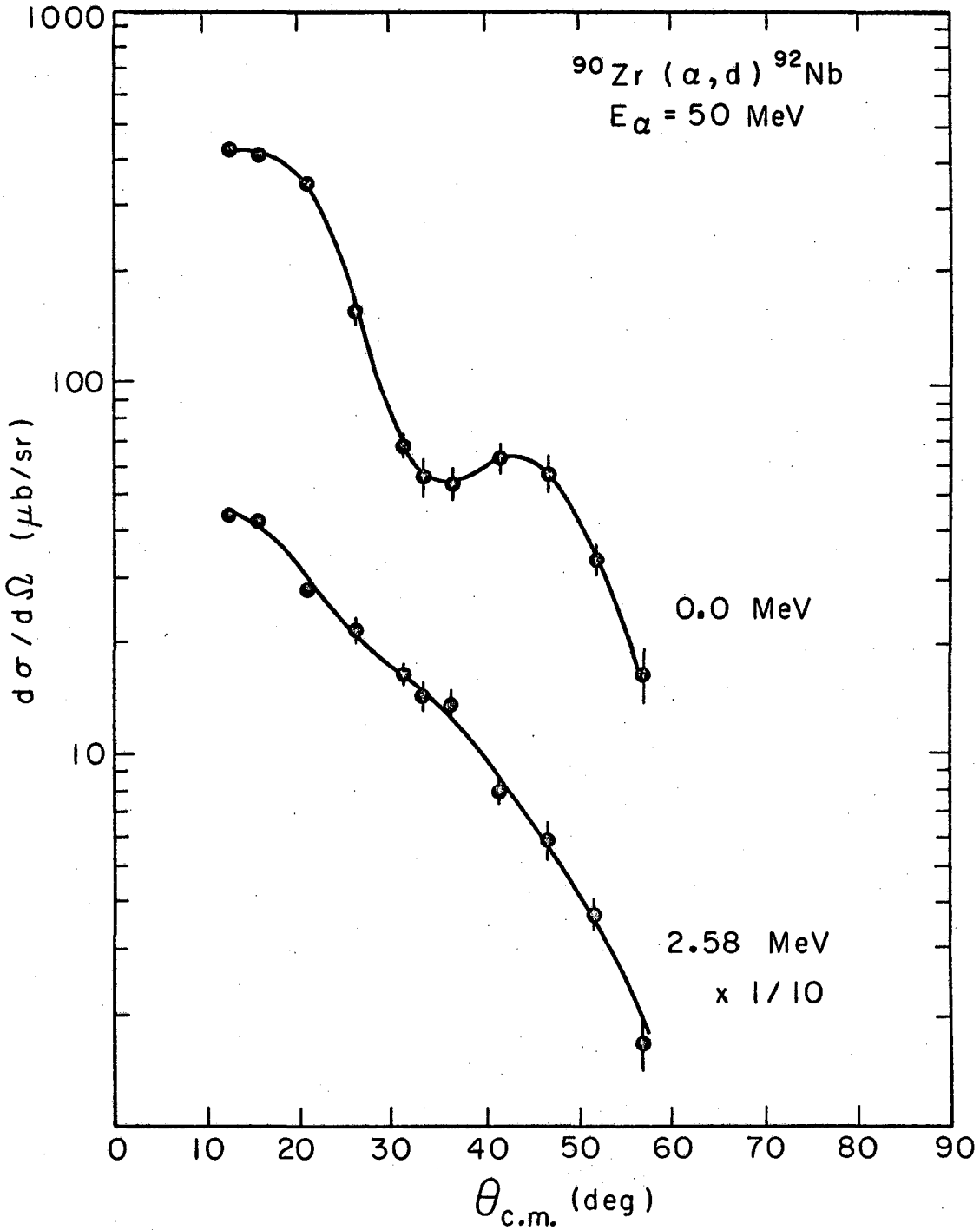

XBL718-4102

Fig. 30. Angular distributions of deuterons from the $^{90}Zr(\alpha,d)^{92}Nb$ reaction leading to the 0.0 and 2.58 MeV states. Statistical errors are shown for each point. The curves have no theoretical significance.

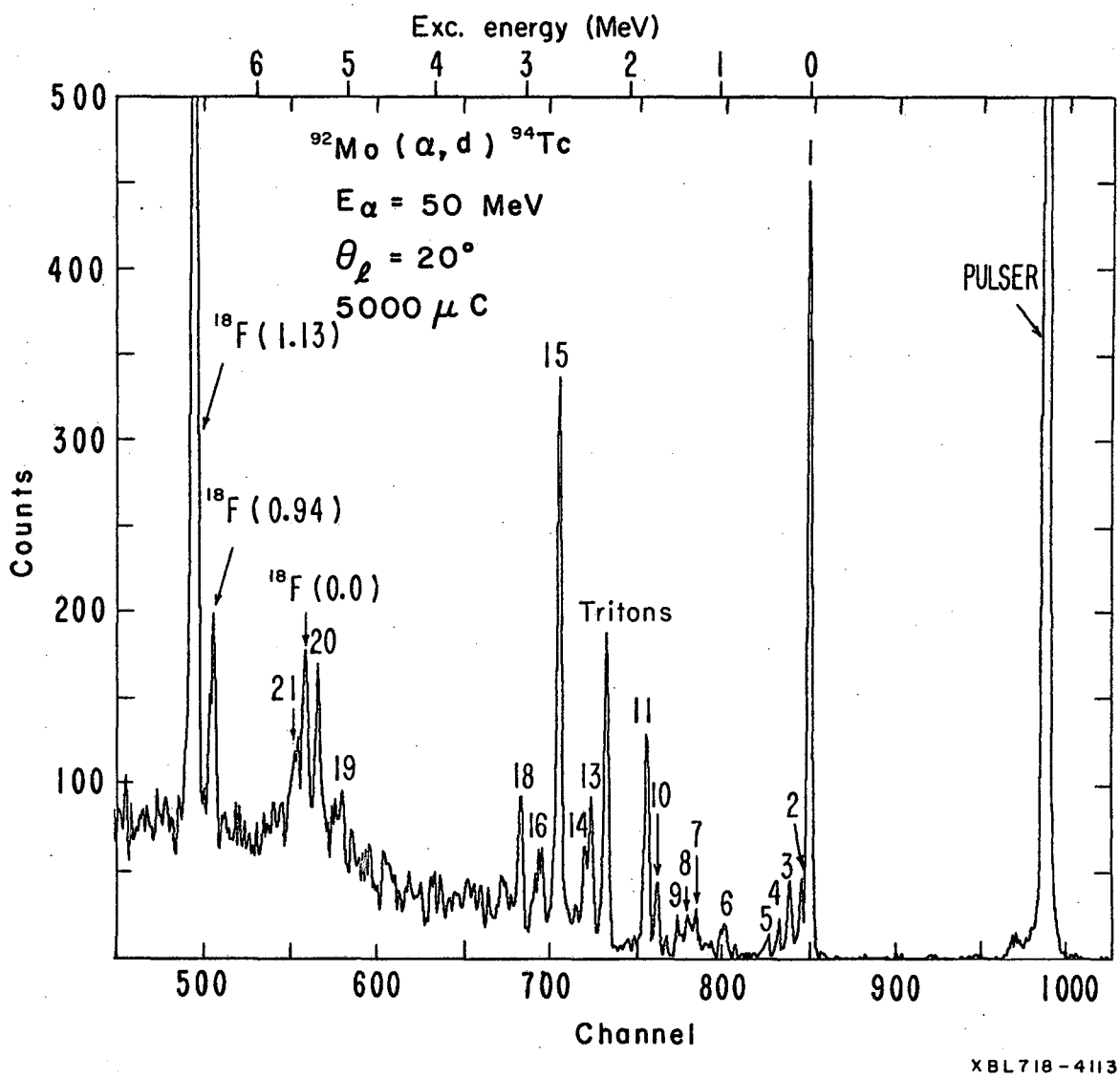

Fig. 31. Deuteron energy spectrum from the $^{92}Mo(\alpha,d)^{94}Tc$ reaction at $\theta_\ell = 20°$. The peak numbers correspond to excitation energies given in Table XIII.

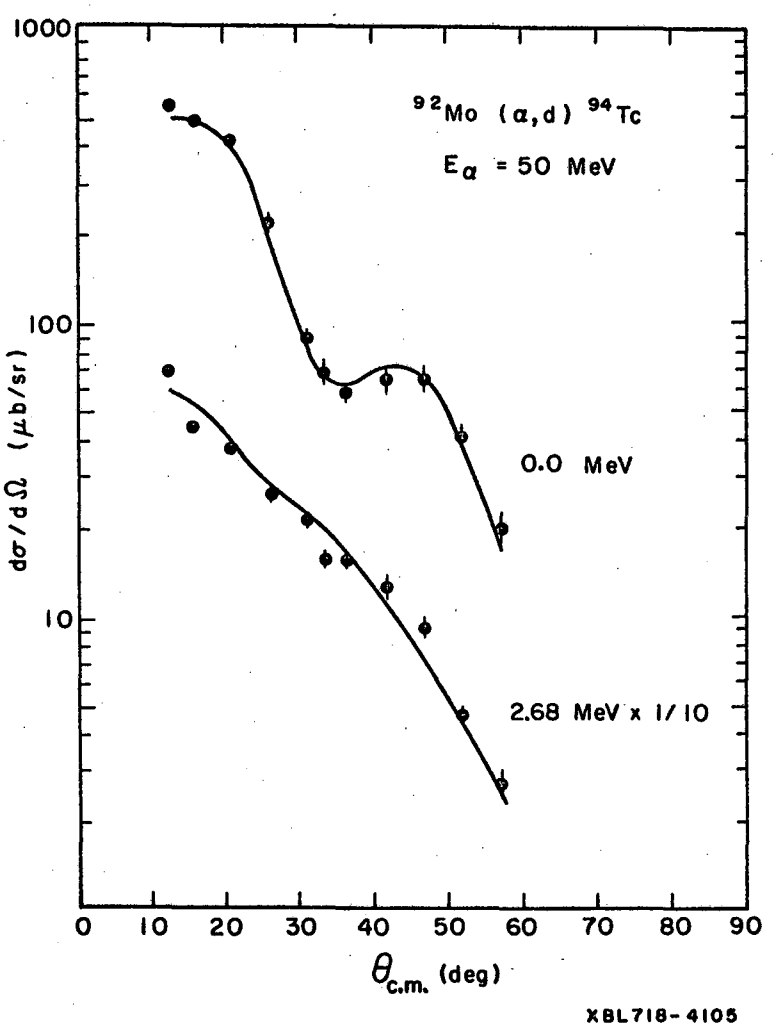

Fig. 32. Angular distributions of deuterons from the $^{92}Mo(\alpha,d)^{94}Tc$ reaction leading to the 0.0 and 2.68 MeV states. The solid lines through the data points represent smooth curves drawn through the experimental angular distributions of the $^{90}Zr(\alpha,d)^{92}Nb$ reaction leading to the ground and 2.58 MeV states (see Fig. 30). Statistical errors are shown for each point.

Table XIII. Levels Observed in the $^{92}Mo(\alpha,d)^{94}Tc$ Reaction at 50 MeV.

No.	Levels Observed[a] (MeV)	Intensity[b] (mb)
1	0.0	0.336
2	0.10	0.040
3	0.21	0.083
4	0.34	Weak
5	0.45	0.027
6	0.93	0.040
7	1.22	0.039
8	1.30	0.042
9	1.41	0.040
10	1.64	0.045
11	1.74	0.139
12	2.14	Weak
13	2.35	0.109[c]
14	2.43	0.04[d]
15	2.68	0.446
16	2.86	0.083
17	2.95	0.06
18	3.08	0.117
19	5.07	0.09[e]
20	5.24	0.183
21	5.38	0.197

(continued)

Table XIII (continued)

[a]Excitation energy ± 30 keV.

[b]Integrated from $\theta_{c.m.}$ = 12.5 to 56.9° except as noted.

[c]Integrated from $\theta_{c.m.}$ = 12.5 to 41.6°.

[d]Integrated from $\theta_{c.m.}$ = 12.5 to 36.2°.

[e]Integrated from $\theta_{c.m.}$ = 12.5 to 51.9°.

with that of the 7^+ ^{92}Nb (g.s.). Thus, the (α,d) results indicate clearly that 7^+ is the correct assignment for the ^{94}Tc ground state, in agreement with the predictions of Bhatt and Ball[7] and Vervier.[9]

The only other member of the $\left[(\pi g_{9/2})^3_{9/2}, \nu d_{5/2}\right]$ multiplet expected in (α,d) is the 5^+, which is predicted[7,9] at an excitation energy of about 0.2 MeV. The most reasonable possibility for the 5^+ state in ^{94}Tc is the (α,d) level at 0.21 MeV. The intensity of this state relative to the ground state is 0.25, in agreement with the value of $\sigma(5^+)/\sigma(7^+) = 0.25$ from the ^{90}Zr(α,d) results. The angular distribution of the 0.21 MeV level (Fig. 33) is similar to that of the 0.36 MeV 5^+ level in ^{92}Nb. The ^{94}Mo(p,n) experiment[98] indicates two closely spaced levels, at 209 and 216 keV, either (or both) of which could be responsible for the observed (α,d) strength of the 0.21 MeV state. However, the ^{90}Zr(α,d) results (Table XII) indicate that only the 5^+ and possibly the 3^+ levels will give strong (α,d) transitions.

In previous (α,d) studies[15-17] preferential population of a level in a given mass region was shown to be due to capture of a proton-neutron pair into one specific shell-model configuration (e.g., $(d_{5/2})^2_{5^+}$ or $(g_{9/2})^2_{9^+}$). The identification of the level in various final nuclei was made on the basis of: (a) strong population in (α,d), (b) similar angular distribution, and (c) regular dependence of the Q-value for forming the level on mass number. In this case the strongest (α,d) states are those at 2.58 MeV in ^{92}Nb and 2.68 MeV in ^{94}Tc. The strengths of these states (relative to their 7^+ ground states) are almost identical. Moreover, the angular distribution of the ^{94}Tc 2.68 MeV level (Fig. 32) is

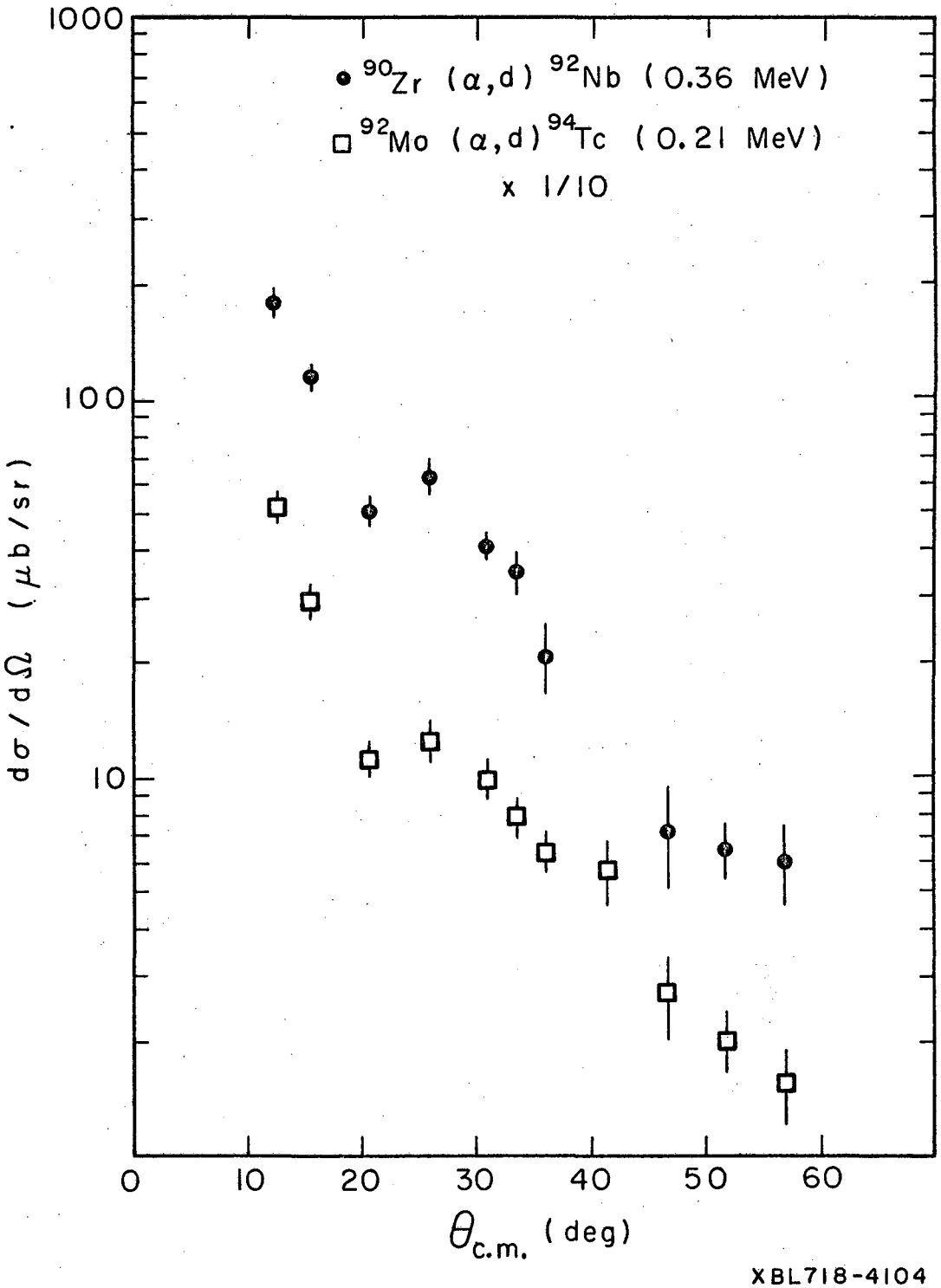

Fig. 33. Deuteron angular distributions from the $^{90}Zr(\alpha,d)^{92}Nb$(0.36 MeV) and $^{92}Mo(\alpha,d)^{94}Tc$(0.21 MeV) reactions. Statistical errors are shown for each point.

very similar to that of the ^{92}Nb 2.58 MeV level. Possible shell-model configurations for these levels will be discussed below.

5. ^{92}Zr(α,d)^{94}Nb

A spectrum of the ^{92}Zr(α,d)^{94}Nb reaction at $\theta_\ell = 20°$ is shown in Fig. 34. The resolution is 50 keV (FWHM). As with the ^{90}Zr and ^{92}Mo targets (Figs. 29 and 31) only two levels, at 0.08 and 2.42 MeV, are strongly populated. A summary of the levels observed in this work is given in Table XIV.

In contrast to the situation for ^{94}Tc, the levels in ^{94}Nb have been studied extensively, both by ^{93}Nb(n,γ)[99,100] and ^{93}Nb(d,p).[62,101] The 79 keV level is believed to be the 7^+ state based on its relative intensity in (d,p)[101] and its weak decay to the ground state.[99] [The ground state was given a tentative 7^+ assignment by Moorhead and Moyer,[62] but the excitation energy determined here of 0.08 ± 0.03 MeV argues against this assignment. Calculations of the ^{94}Nb level scheme[7,9,99-101] all give 6^+ as the lowest level.] The 5^+ level of the $\left[\pi g_{9/2}, (\nu d_{5/2})^3_{5/2}\right]$ multiplet, at 0.113 MeV,[62,99] was not resolved from the 7^+ in the data. The angular distribution of the 0.08 MeV level in (α,d) is less structured than those of the 7^+ levels in ^{92}Nb or ^{94}Tc (Figs. 30 and 32) but is accounted for rather well (Fig. 35) by assuming a $7^+ + 5^+$ doublet with relative intensities the same as those observed in ^{90}Zr(α,d).

The 2.42 MeV state has an angular distribution (Fig. 35) similar to that of the ^{92}Nb 2.58 MeV level. Its strength relative to the 7^+ level is consistent with those obtained for the strong states in ^{92}Nb and ^{94}Tc. Based on (α,d) systematics this level should have the same configuration as the ^{92}Nb 2.58 MeV and ^{94}Tc 2.68 MeV states.

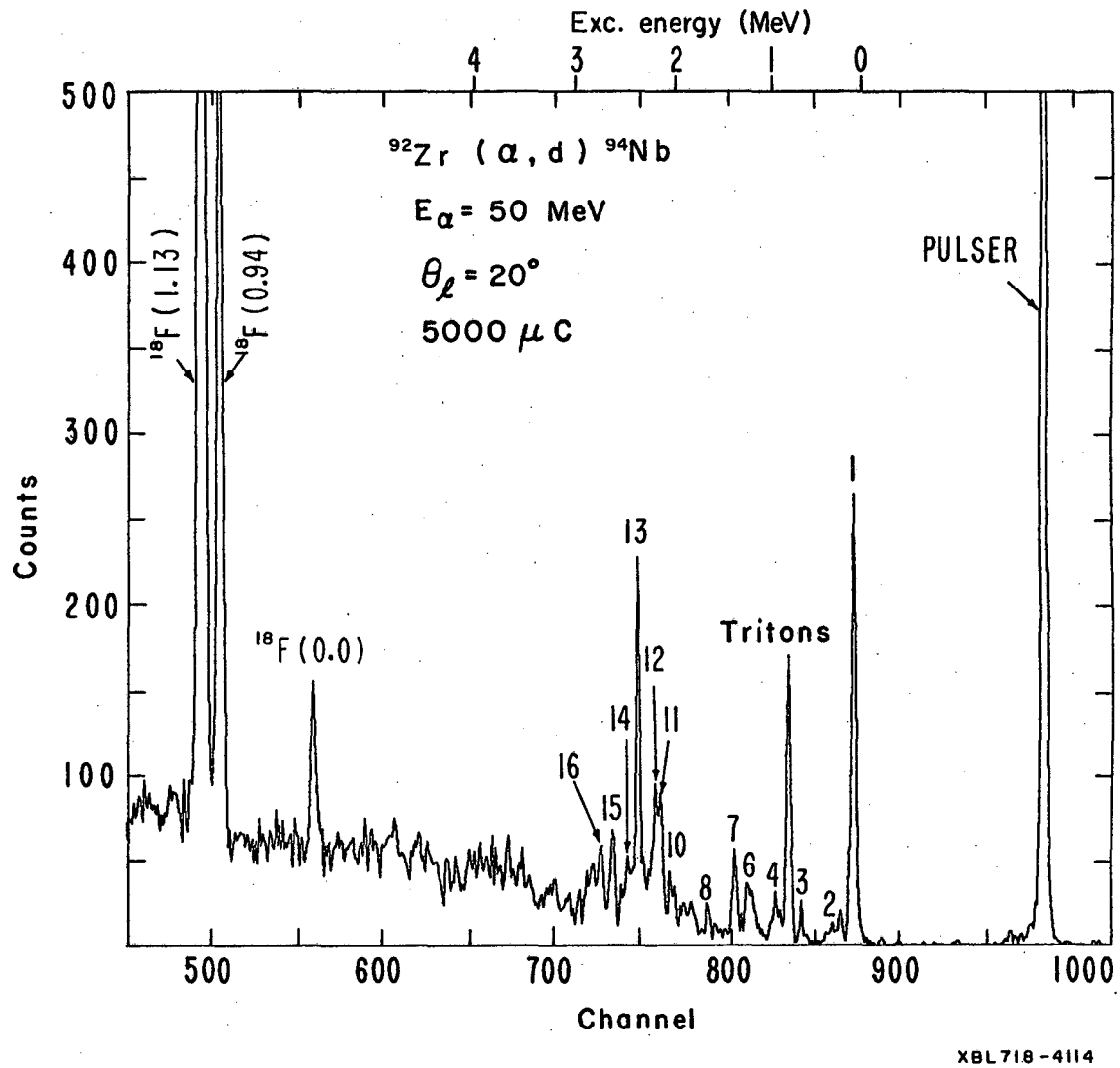

Fig. 34. Deuteron energy spectrum from the $^{92}Zr(\alpha,d)^{94}Nb$ reaction at $\theta_\ell = 20°$. The peak numbers correspond to excitation energies given in Table XIV.

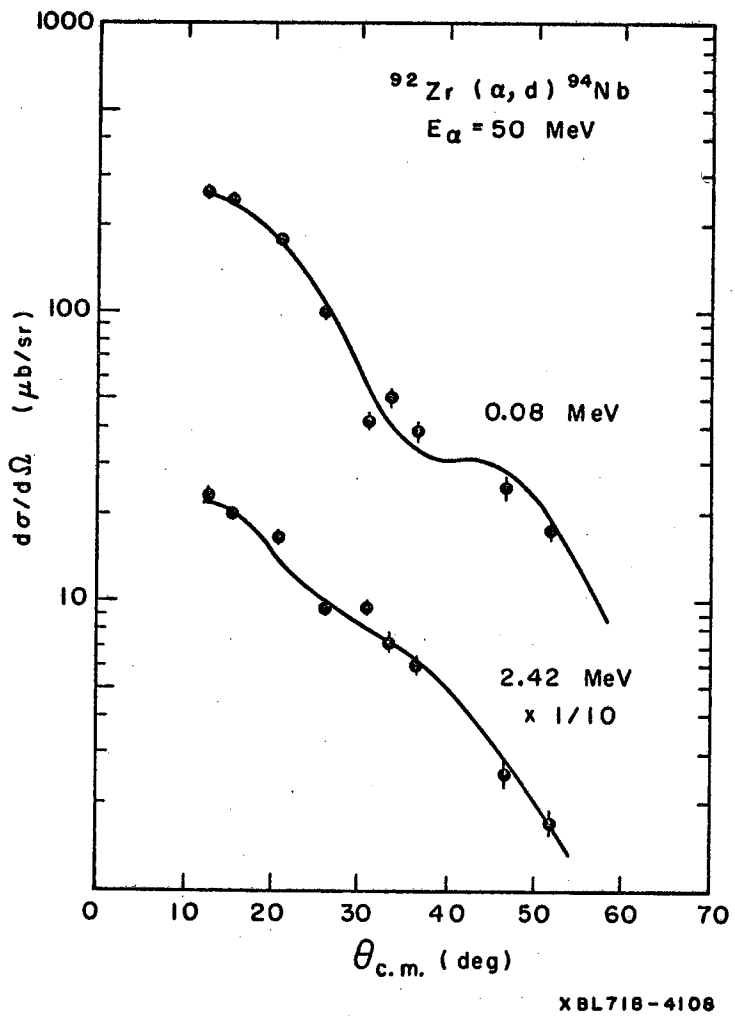

Fig. 35. Angular distributions of deuterons from the $^{92}Zr(\alpha,d)^{94}Nb$ reaction leading to the 0.08 and 2.42 MeV states. The solid line through the 0.08 MeV data points represents a smooth curve drawn through the experimental angular distribution of the summed 0.0 MeV (7^+) and 0.36 MeV (5^+) levels in $^{90}Zr(\alpha,d)^{92}Nb$. The solid line through the 2.42 MeV data points is a smooth curve drawn through the experimental angular distribution of the $^{90}Zr(\alpha,d)^{92}Nb$ (2.58 MeV) reaction. Statistical errors are shown for each point.

Table XIV. Levels Observed in the $^{92}Zr(\alpha,d)^{94}Nb$ Reaction at 50 MeV.

No.	Levels Observed[a] (MeV)	Intensity[b] (mb)
1	0.08[c]	0.178[c]
2	0.32	0.01
3	0.65	0.01
4	0.95	0.04[d]
5	1.19	Weak
6	1.25	0.049
7	1.39	0.044
8	1.65	0.027
9	1.84	0.02[d]
10	2.05	0.059
11	2.18	0.098
12	2.25	0.095
13	2.42	0.166
14	2.53	0.03[d]
15	2.69	0.060
16	2.84	0.051[e]
17	2.95	0.02[d]
18	3.7 ± 0.10	Weak

[a]Excitation energy ± 30 keV except as noted.

[b]Integrated from $\theta_{c.m.}$ = 12.4 to 51.8° except as noted.

(continued)

Table XIV (continued)

[c]This level is a doublet made up of the 0.078 and 0.113 MeV states. About 80% of the observed intensity should be due to the 0.078 MeV state. See text.

[d]Integrated from $\theta_{c.m.} = 12.4$ to $36.4°$.

[e]Integrated from $\theta_{c.m.} = 12.4$ to $46.7°$.

6. $^{94}Zr(\alpha,d)^{96}Nb$

A spectrum of the $^{94}Zr(\alpha,d)^{96}Nb$ reaction at $\theta_\ell = 20°$ is shown in Fig. 36. The resolution is 50 keV (FWHM). The low-lying levels in ^{96}Nb were studied with the $^{96}Zr(^3He,t)^{96}Nb$ reaction by Comfort et al.[102] They obtained excellent agreement with the predictions of the Pandya transformation, which relates the energies of the $\left[\pi g_{9/2},(\nu d_{5/2})^{-1}\right]$ particle-hole multiplet in ^{96}Nb to those of the $\left[\pi g_{9/2},\nu d_{5/2}\right]$ particle-particle multiplet in ^{92}Nb. In particular the 7^+ level, which should be strong in (α,d), was observed[102] at 233 ± 5 keV in ^{96}Nb. Results from the $^{96}Zr(p,n\gamma)^{96}Nb$ reaction[103] are in agreement with those from $(^3He,t)$.

Since recent measurements[104,105] of the $^{96}Nb \longrightarrow {}^{96}Mo$ β decay indicate a mass excess for ^{96}Nb different from that in the published Q-value tables,[51] an energy scale obtained by fitting (α,d) data on the ^{90}Zr, ^{92}Zr, and ^{92}Mo targets (along with light impurities) was used to determine the energy of the 7^+ level. An excitation energy of 0.26 ± 0.03 MeV was obtained using the Q-value consistent with the β-decay data[104] while the published[51] Q-value, -12.3342 MeV, gives an excitation energy of about 0.30 MeV. Thus, based on these data, the mass excess of ^{96}Nb obtained from the β decay, which is 37 keV more positive than that from Ref. 51, seems preferred. In order to minimize the effect of shifts between the various targets, the final calibration was done using a $^{94}Zr(\alpha,d)^{96}Nb$ Q-value of -12.371 MeV (inferred from Ref. 104) and assuming an excitation energy for the 7^+ level of 0.233 MeV as given by Comfort et al.[102] The excitation energies determined in this manner are given in Table XV along with the $^{96}Zr(^3He,t)^{96}Nb$ results. These energies depend

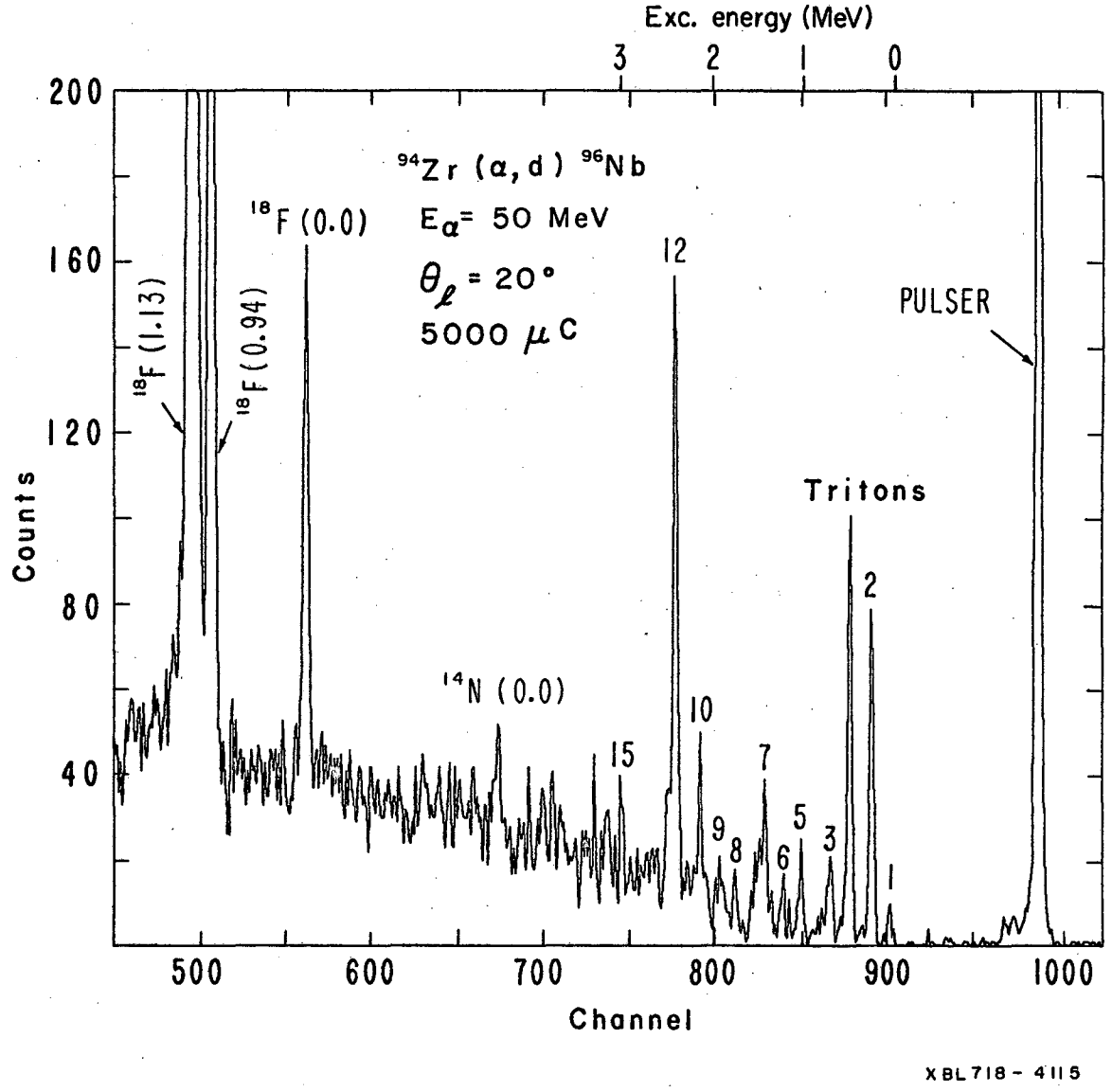

Fig. 36. Deuteron energy spectrum from the $^{94}Zr(\alpha,d)^{96}Nb$ reaction at θ_ℓ= 20°. The peak numbers correspond to excitation energies given in Table XV.

Table XV. Levels Observed in the $^{94}Zr(\alpha,d)^{96}Nb$ Reaction at 50 MeV.

	(α,d)		$(^3He,t)^a$	
No.	Levels Observed[b] (MeV)	Intensity[c] (mb)	Levels Observed[d] (MeV)	J^π
			0.0	6^+
1	0.05	0.014[e]	0.045	5^+
			0.152	4^+
			0.191	3^+
2	0.23[f]	0.071[e]	0.233	7^+
			0.515	
			0.632	2^+
3	0.70	0.02	0.685	
4	0.83	Weak		
			0.865	
5	1.01	0.02		
6	1.21	0.01		
7	1.41	0.07		
8	1.71	0.02		
9	1.89	0.02		
10	2.10	0.06		
11	2.24	0.04		
12	2.38	0.212[e]		
13	2.47	0.04		
14	2.73 ± 0.04	0.02		
15	2.96 ± 0.04	0.04		

(continued)

Table XV (continued)

[a]Ref. 102.

[b]Excitation energy ± 30 keV except as noted.

[c]Integrated from $\theta_{c.m.}$ = 12.4 to 33.2° except as noted.

[d]Relative energies ± 5 keV.

[e]Integrated from $\theta_{c.m.}$ = 12.4 to 51.8°.

[f]Used as a calibration point. The excitation energy of the 7^+ was obtained from Ref. 102 and the ground state Q-value, -12.371 MeV, was inferred from the β-decay Q-value of Ref. 104 (See text.)

on the choice of Q-value and may have a systematic error if the Q-value of the calibration state is incorrect, but this causes only small errors ($\lesssim$ 20 keV) over the energy range covered in Table XV.

As with the other Zr isotopes only two levels are strongly populated. Angular distributions of these levels, at 0.23 and 2.38 MeV, are shown in Fig. 37. The 0.23 MeV level has a shape consistent with the 7^+ assignment made by Comfort et al.[102] and the 2.38 MeV level is similar in shape to the ^{92}Nb 2.58 MeV state.

7. ^{91}Zr(α,d)^{93}Nb

A spectrum of the ^{91}Zr(α,d)^{93}Nb reaction at $\theta_\ell = 20°$ is shown in Fig. 38. The resolution is 65 keV (FWHM). A summary of the levels seen in this work is given in Table XVI.

It is interesting to compare the low-lying levels seen in the ^{91}Zr(α,d)^{93}Nb data with those seen in ^{92}Zr(α,t)^{93}Nb (Sec. IV-A4 and Table VI) and Coulomb excitation.[12] The ground state ($9/2^+$) is populated quite weakly in (α,d) compared with the dominant $\pi g_{9/2}$ capture in (α,t). A stronger group of levels appears at about 1.3 MeV in the (α,d) data. These levels have been assigned[12] spins of: 0.952 MeV ($13/2^+$), 1.337 MeV ($17/2^+$), 1.492 MeV ($9/2^+$, $11/2^+$, $13/2^+$), and 1.507 MeV ($9/2^+$, $11/2^+$, $13/2^+$). Shell model calculations of the ^{93}Nb level scheme[7,9] predict low-lying $11/2^+$, $13/2^+$, $15/2^+$, and $17/2^+$ levels whose wave functions are of the type $\left[\pi g_{9/2}, (\nu d_{5/2})^2_{J_n}\right]_J$. From the ^{90}Zr(α,d)^{92}Nb results (Sec. IV-B3) it seems clear that only those levels having appreciable amplitudes of the type $\left[(\pi g_{9/2}, \nu d_{5/2})_{7^+}, \nu d_{5/2}\right]$ and $\left[(\pi g_{9/2}, \nu d_{5/2})_{5^+}, \nu d_{5/2}\right]$ will be populated strongly, since the 7^+ and 5^+ have the most favorable structure

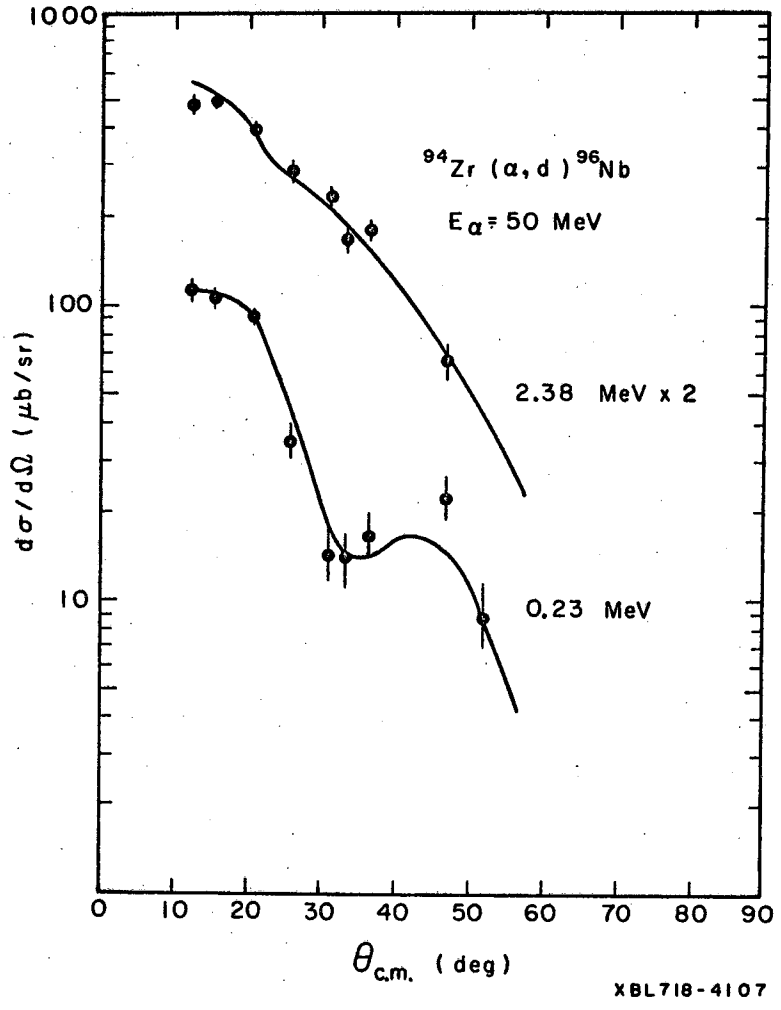

Fig. 37. Angular distributions of deuterons from the $^{94}Zr(\alpha,d)^{96}Nb$ reaction leading to the 0.23 and 2.38 MeV states. The solid lines through the data points represent smooth curves drawn through the experimental angular distributions of the $^{90}Zr(\alpha,d)^{92}Nb$ reaction leading to the ground and 2.58 MeV states. (See Fig. 30.) Statistical errors are shown for each point.

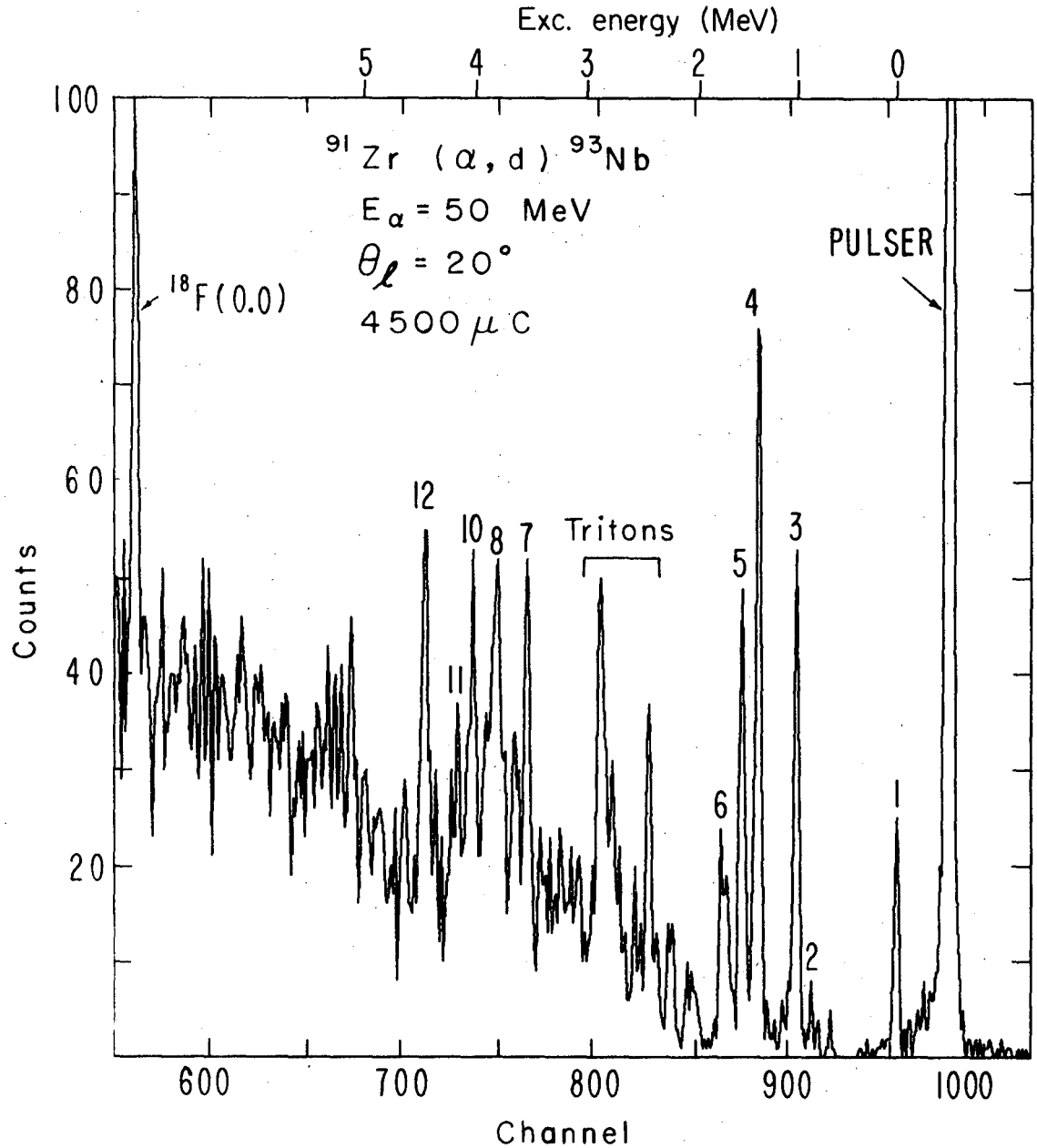

XBL 718-4116

Fig. 38. Deuteron energy spectrum from the $^{91}Zr(\alpha,d)^{93}Nb$ reaction at $\theta_\ell = 20°$. The peak numbers correspond to excitation energies given in Table XVI.

Table XVI. Levels Observed in the $^{91}Zr(\alpha,d)^{93}Nb$ Reaction at 50 MeV.

No.	Levels Observed[a] (MeV)	Intensity[b] (mb)
1	0.0	0.020[c]
2	0.80	0.010
3	0.96	0.056
4	1.33	0.077
5	1.48	0.052
6	1.66	0.039
7	3.54	0.078
8	3.84	0.094[c]
9	3.93	0.050[c]
10	4.06	0.080[d]
11	4.21	0.052[d]
12	4.52	0.100

[a]Excitation energy ± 30 keV.

[b]Integrated from $\theta_{c.m.}$ = 15.5 to 56.7° except as noted.

[c]Integrated from $\theta_{c.m.}$ = 15.5 to 46.5°.

[d]Integrated from $\theta_{c.m.}$ = 15.5 to 51.7°.

for the (α,d) reaction. The strongest levels, then, should be the $17/2^+$ and $15/2^+$ since these must contain only 5^+, 6^+, or 7^+ couplings of the transferred $(\pi g_{9/2}, \nu d_{5/2})$ pair. The $17/2^+$ state, which is the "stretched" configuration of the $\left[\pi g_{9/2}, (\nu d_{5/2})^2\right]$ multiplet, should be populated only through the 7^+ coupling, i.e., it should be the same transfer as that for the $^{90}Zr(\alpha,d)^{92}Nb$ (g.s.) reaction. (The 6^+ is not expected to contribute appreciably to the cross section either experimentally (Sec. IV-B3) or theoretically.[92]) This prediction is borne out by the angular distribution of the 1.33 MeV level (Fig. 39) which has the same shape as that from the $^{90}Zr(\alpha,d)^{92}Nb$ (g.s.) reaction. Also, the 1.33 MeV level is the strongest of the low-lying levels seen in $^{91}Zr(\alpha,d)$. Thus, the data tend to substantiate the identification of the $17/2^+$ level at 1.337 MeV made in Ref. 12.

The $15/2^+$ level is predicted[7,9] to lie slightly higher than the $17/2^+$ level. Based on these data the 1.48 MeV level would seem to be a reasonable candidate, although Rogers et al.[12] assigned ($9/2^+$, $11/2^+$, $13/2^+$,) to both the 1.492 and 1.507 MeV levels. Both the 1.48 MeV and 0.96 MeV levels have angular distributions (Fig. 39) which can be "fit" with the assumption of $7^+ + 5^+$ contributions similar to those from the ground and 0.36 MeV states of ^{92}Nb.

At about 4 MeV a second strong group of states appears in the $^{91}Zr(\alpha,d)$ data (Fig. 38). The angular distributions of these levels, at 3.54, 3.84, 3.93, 4.06, 4.21, and 4.52 MeV, are all similar to that of the 2.58 MeV level in ^{92}Nb and probably correspond to the same proton-neutron transfer. Angular distributions of two of these levels (3.54

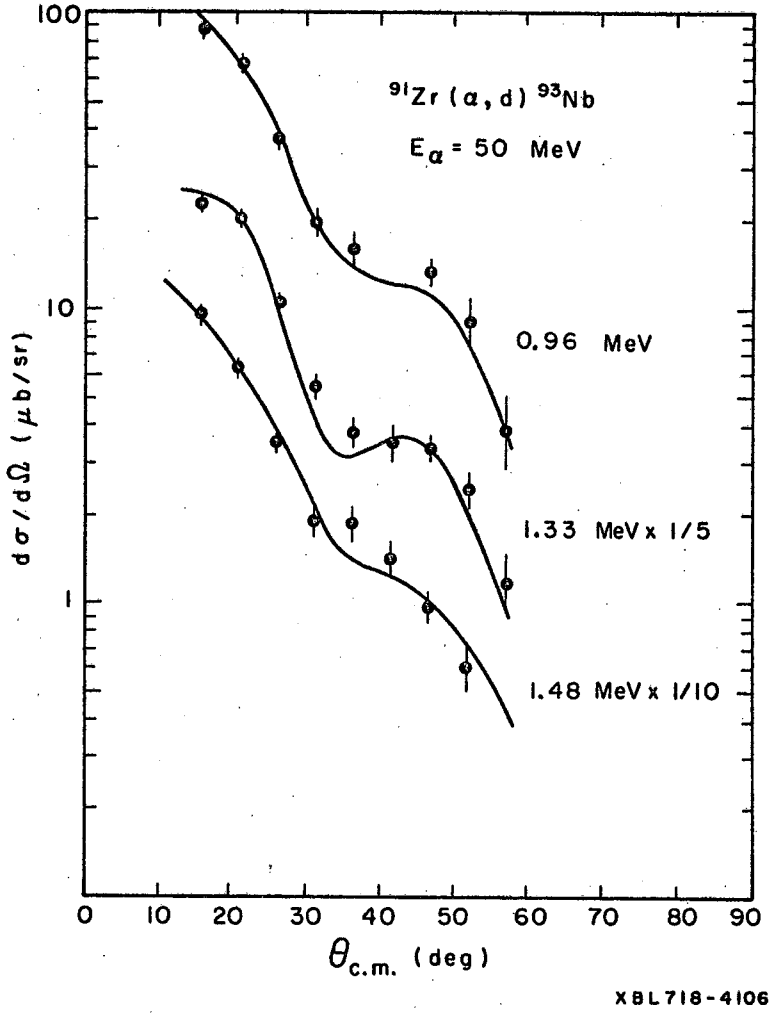

Fig. 39. Angular distributions of deuterons from the $^{91}Zr(\alpha,d)^{93}Nb$ reaction leading to the 0.96, 1.33, and 1.48 MeV levels. The solid lines represent smooth curves drawn through experimental angular distributions from the $^{90}Zr(\alpha,d)^{92}Nb$ reaction leading to the 7^+ (g.s.) and 5^+ (0.36 MeV) with weighting factors of: 0.96 MeV [$7^+ + 5^+$], 1.33 MeV [7^+], and 1.48 MeV [$7^+ + 2 \times (5^+)$]. (See text, Sec. IV-B7.) Statistical errors are shown for each point.

and 4.52 MeV) are shown in Fig. 40. The splitting between the two multiplets is about 2.7 MeV. This is consistent with a simple "weak coupling" picture of these groups of states, although it is very unlikely that the levels do not mix with other available configurations in ^{93}Nb.

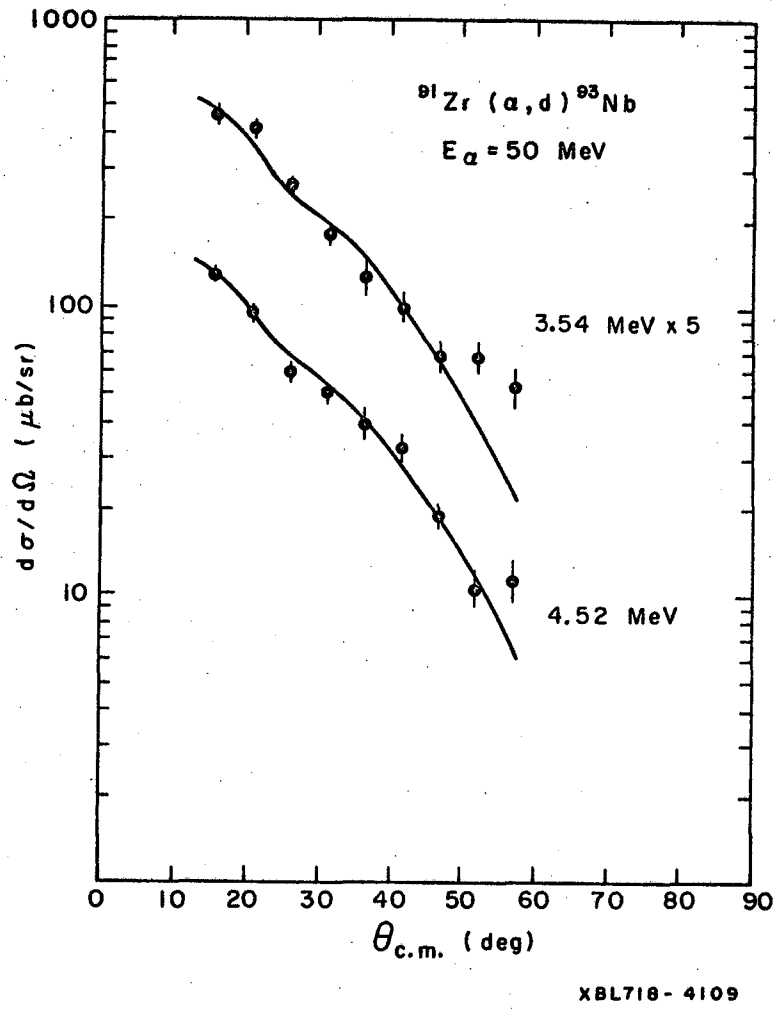

Fig. 40. Angular distributions of deuterons from the $^{91}Zr(\alpha,d)^{93}Nb$ reaction leading to the 3.54 and 4.52 MeV states. The solid lines represent smooth curves drawn through the experimental angular distribution of the $^{90}Zr(\alpha,d)^{92}Nb$ (2.58 MeV) reaction. (See Fig. 30.) Statistical errors are shown for each point.

C. Heavy Ion Reactions

1. Selection Rules

The selection rules for heavy ion induced single-nucleon transfer reactions have been obtained by several authors within the DWBA framework.[106,107] They are:

$$\ell_i + \ell_f \geq L \geq |\ell_i - \ell_f| \tag{1}$$

$$j_i + j_f \geq L \geq |j_i - j_f| \tag{2}$$

and

$$\ell_i + \ell_f + L = \text{even} \tag{3}$$

where ℓ_i, j_i and ℓ_f, j_f are the orbital and total angular momenta of the captured nucleon in the projectile and final nucleus, respectively, and L is the transferred angular momentum. For both the (^{16}O,^{15}N) and (^{16}O,^{15}O) reactions reported here, $\ell_i = 1$ and $j_i = 1/2$ (i.e., the transferred nucleon in the projectile is in a $1p_{1/2}$ state), and equations (1) to (3) become

$$\ell_f + 1 \geq L \geq |\ell_f - 1| \tag{4}$$

$$j_f + 1/2 \geq L \geq |j_f - 1/2| \tag{5}$$

and

$$L + \ell_f = \text{odd} \tag{6}$$

A consequence of the above selection rules is that <u>different</u> L values are required for stripping to states with $j_f = \ell_f + 1/2$ and $j_f = \ell_f - 1/2$. This can be seen by substituting into eq. (5). For $j_f = \ell_f + 1/2$,

$$\ell_f + 1 \geq L \geq \ell_f \tag{7}$$

and, for $j_f = \ell_f - 1/2$,

$$\ell_f \geqslant L \geqslant \ell_f - 1 \tag{8}$$

The parity selection rule, eq. (6), then further restricts these values so that, for (^{16}O,^{15}N) and (^{16}O,^{15}O) reactions,

$$L = \ell_f + 1 \qquad \text{for } j_f = \ell_f + 1/2 \tag{9}$$

or

$$L = \ell_f - 1 \qquad \text{for } j_f = \ell_f - 1/2 \tag{10}$$

This result is in contrast with the light ion selection rules (see Sec. IV-A1) where, because $\ell_i = 0$, a single L value, $L = \ell_f$, is allowed for both $j_f = \ell_f + 1/2$ and $j_f = \ell_f - 1/2$ transfers.

It has been pointed out[108] that the parity selection rule, eq. (3), is only approximate, since it results from ignoring "recoil effects" (see Appendix A) in obtaining the DWBA expression for the transition amplitude. At present, very little is known about the consequences of ignoring the recoil terms. These terms are important in DWBA calculations insofar as ignoring them leads to differences of several orders of magnitude in predicted cross sections obtained by using the (formally equivalent) post or prior form of the DWBA transition amplitude.[109] Since the predicted DWBA cross sections depend very strongly on L, ($\sigma_{L+2} \approx 10\sigma_L$),[49] an implication of the above selection rules is that a very strong j-dependence is expected in the (^{16}O,^{15}N) and (^{16}O,^{15}O) reactions. However, the experimental evidence[110] indicates a j-dependence which is considerably weaker than would be obtained from the DWBA predictions. Possibly, this can be traced back to the neglect of the recoil terms. In any case, it must be remarked

that the degree of validity of the approximate parity selection rule above has not been investigated.

2. $^{90}Zr(^{16}O,^{15}N)^{91}Nb$

A ^{15}N spectrum from the $^{90}Zr(^{16}O,^{15}N)^{91}Nb$ reaction at $\theta_\ell = 25°$ is shown in Fig. 41. The resolution is about 200 keV (FWHM). This reaction has been observed previously by Nickles et al.[27] at 60 MeV. Table XVII summarizes the states observed in this work and their intensities. An interesting feature of these data, compared with those of Nickles et al.,[27] is that the cross sections are much larger at the higher beam energy used here. The peak cross section for the ground state is about 6 times that reported at 60 MeV, and the 3.37 MeV state is stronger by a factor of 16.

Angular distributions for the ground and 3.37 MeV states are shown in Fig. 42. Based on the selection rules (Sec. IV-C1) the ground state corresponds to an L = 5 transition while the 3.37 MeV $d_{5/2}$ state requires L = 3. It can be seen from Fig. 42 that the $^{90}Zr(^{16}O,^{15}N)$ reaction shows essentially no L-dependence in the angular distributions, in agreement with the results of other $(^{16}O,^{15}N)$ studies.[27,111] The observed angular distributions can apparently be understood in terms of a semi-classical picture (see Appendix A) even at energies much greater than the Coulomb barrier (which is about 39 MeV for the ^{16}O- ^{90}Zr system). At backward angles (small impact parameters) the transfer reaction cross sections decrease due to absorption, i.e., compound nucleus formation, and at forward angles (large impact parameters) the cross sections decrease because the projectile and target nuclei are outside the range of the nuclear force which is responsible for the transfer. The peak of the

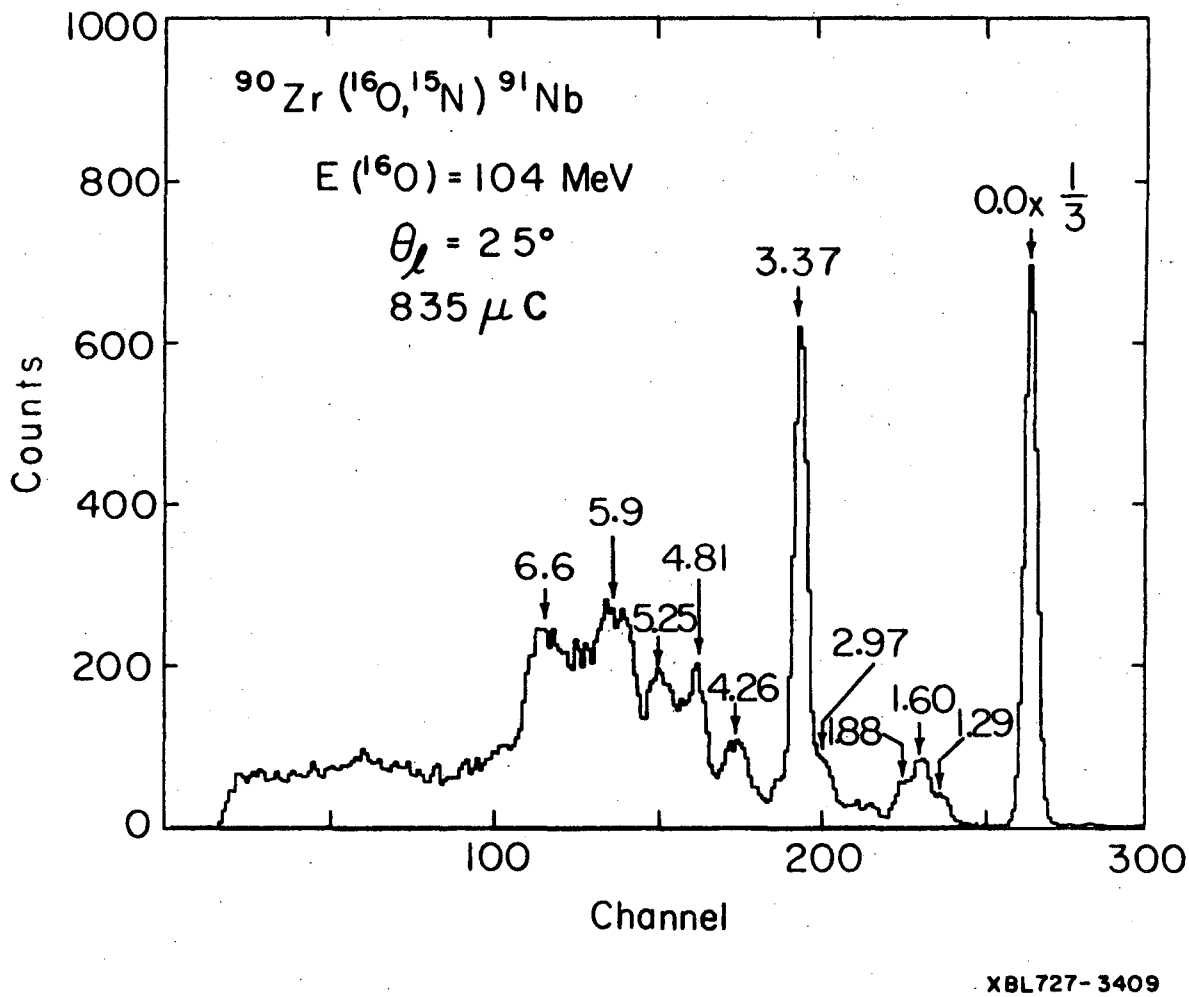

Fig. 41. ^{15}N position spectrum from the ^{90}Zr(^{16}O,^{15}N)^{91}Nb reaction at θ_ℓ= 25°. The two-dimensional arrays corresponding to this spectrum are displayed in Figs. 11 to 14.

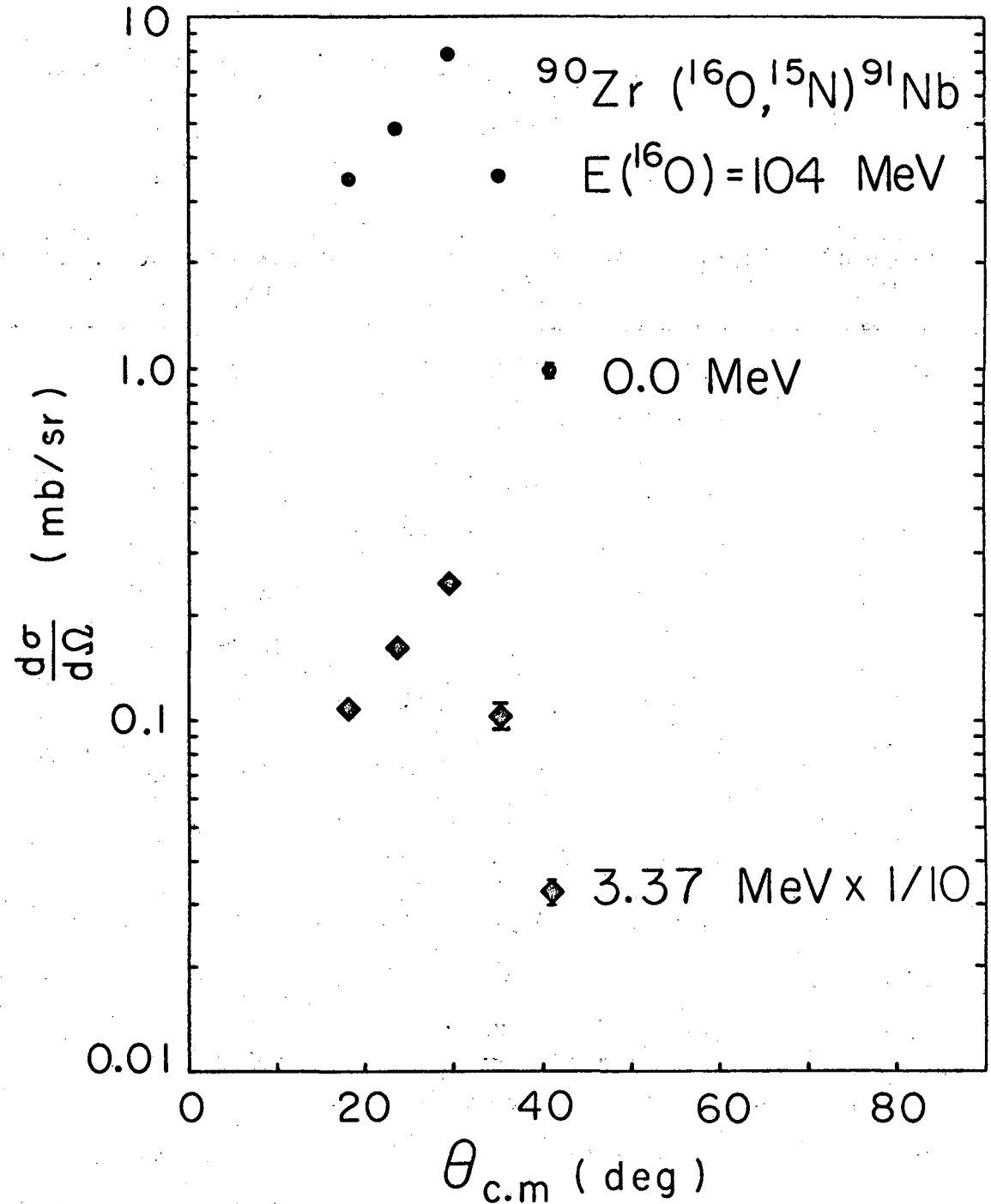

XBL727-3407

Fig. 42. Angular distributions of ^{15}N from the $^{90}Zr(^{16}O,^{15}N)^{91}Nb$ reaction leading to the 0.0 and 3.37 MeV states. The angular distributions for the two states have identical shapes, although the ground state ($p_{1/2} \longrightarrow g_{9/2}$ transition) should be L=5 and the 3.37 MeV state ($p_{1/2} \longrightarrow d_{5/2}$ transition) L=3 based on the selection rules.

Table XVII. Levels Observed in the $^{90}Zr(^{16}O,^{15}N)^{91}Nb$ Reaction at 104 MeV Compared with Previous Results.

This work			Ref. 27	
Levels Observed[a] (MeV)	Intensity[b] (mb)	Peak Cross Section[c] (mb/sr)	Levels Observed (MeV)	Peak Cross section[d] (mb/sr)
0.0[e]	5.30[f]	7.83 ± 0.08[f]	0.0	1.39
1.29	0.20	0.22 ± 0.01		
1.60	0.24	0.34 ± 0.02	1.61	0.03
1.88	0.31	0.29 ± 0.02		
			2.18	0.04
			2.75	0.08
2.97	0.24	0.34 ± 0.02		
3.37[e]	1.66	2.43 ± 0.04	3.36	0.15
4.26	0.32[g]	0.47 ± 0.02		
4.81	0.47[g]	0.59 ± 0.02		
5.25	0.66[g]	0.94 ± 0.03		
5.9 ± 0.15	1.35	1.89 ± 0.04		
6.6 ± 0.15	1.40	2.07 ± 0.04		

[a]Excitation energy ± 100 keV except as noted.

[b]Integrated from $\theta_{c.m.}$ = 18 to 41° except as noted. The cross sections have been corrected for charge state as described in the text (Sec. III-B).

[c]Differential cross section at θ_ℓ = 25°. The error shown is only that due to counting statistics. The cross section has been corrected for charge state as described in the text (Sec. III-B).

(continued)

Table XVII (continued)

[d]Differential cross section at $\theta_\ell = 60°$.

[e]Used as a calibration point.

[f]Contains a contribution of about 15% from the unresolved 0.10 MeV level.

[g]Integrated from $\theta_{c.m.} = 18$ to 35°.

angular distribution comes at the grazing angle, where σ/σ_R deviates from unity. For these data the grazing angle is about 25° (lab).

In the low energy ($^{16}O,^{15}N$) data[27] the spectrum cuts off at about 4 MeV excitation energy due to the Coulomb barrier, so only states below 3.37 MeV can be compared. In both ($^{16}O,^{15}N$) experiments the ground and 3.37 MeV states are the strongest, with the ground state being stronger by a factor of 4 in these data and by a factor of 9 in the 60 MeV experiment. (The weaker population of the 3.37 MeV state at 60 MeV might be due to the nearness of the ^{15}N to the Coulomb barrier.) Near the 1.61 MeV state reported in Ref. 27 there are three states seen here, at 1.29, 1.60 and 1.88 MeV. The 2.18 MeV state reported by Nickles et al.,[27] whose intensity was somewhat larger than that of their 1.61 MeV state, does not appear here (see Fig. 41). This state and the state at 2.75 MeV were tentatively suggested to be core-excited states of the type $\left[^{90}Zr(2^+) \otimes \pi g_{9/2}\right]$ and $\left[^{90}Zr(3^-) \otimes \pi g_{9/2}\right]$, respectively, in Ref. 27, based mainly on their excitation energies. The 2.75 MeV state is also absent in the ($^{16}O,^{15}N$) data obtained here, unless it corresponds to the level at 2.97 MeV. A 200 keV error in the excitation energy of the 2.97 MeV level seen here is unlikely, however, since it is so close to the 3.37 MeV state, which was used as a calibration point at all angles.

Above the 3.37 MeV state there are several levels seen in the $^{90}Zr(^{16}O,^{15}N)$ data which were not observed in the previous experiment. These states extend up to 6.6 MeV of excitation energy, above which no states were observed. The highest of these states, at 5.9 and 6.6 MeV are very broad (see Fig. 41). This could be due to population of unbound

states in ^{91}Nb at these energies but, since similar groups at high excitation energies appear in the ^{15}N spectra of the other targets studied, it seems reasonable to also consider the possibility of (Doppler broadened) ^{15}N excited states. Such "shadow peaks" have been observed in some heavy ion reactions,[112] but not in (^{16}O,^{15}N) specifically.

The first excited states of ^{15}N occur at 5.27 and 5.30 MeV. However, these states are $5/2^+$ and $1/2^+$ levels and cannot be reached directly from the ^{16}O ground state except through admixtures of 2p-2h, etc., components. The third excited state in ^{15}N, at 6.33 MeV, is a $p^{-1}_{3/2}$ level and thus can be reached from the major (closed shell) component of the ^{16}O ground state. [The ^{16}O(d,^{3}He)^{15}N reaction,[113] for example, yields a cross section for the 5.27-5.30 MeV doublet about 10 times smaller than those for the ground and 6.33 MeV states.] Obviously neither of the observed excited states has exactly the right energy to be the 6.33 MeV state in ^{15}N, but the average of the two energies (6.25 MeV) agrees quite well.

A similar result was observed in the inelastic scattering data, which was obtained simultaneously with the (^{16}O,^{15}O) results reported later. In all of the inelastic ^{16}O spectra (Fig. 43) a broad doublet appears at excitation energies of 5.7 and 6.4 MeV. The appearance of these states at the same excitation energies and with the same cross sections (within about 20%) in the ^{90}Zr, ^{92}Mo, and ^{93}Nb targets suggests a similar transition is involved. Here too, neither of the peaks corresponds in energy to an ^{16}O excited state, but the average energy, 6.05 MeV, could be explained by population of the 6.13 MeV 3^- state in ^{16}O. (The 6.05 MeV 0^+ state in ^{16}O is unlikely to be populated by inelastic

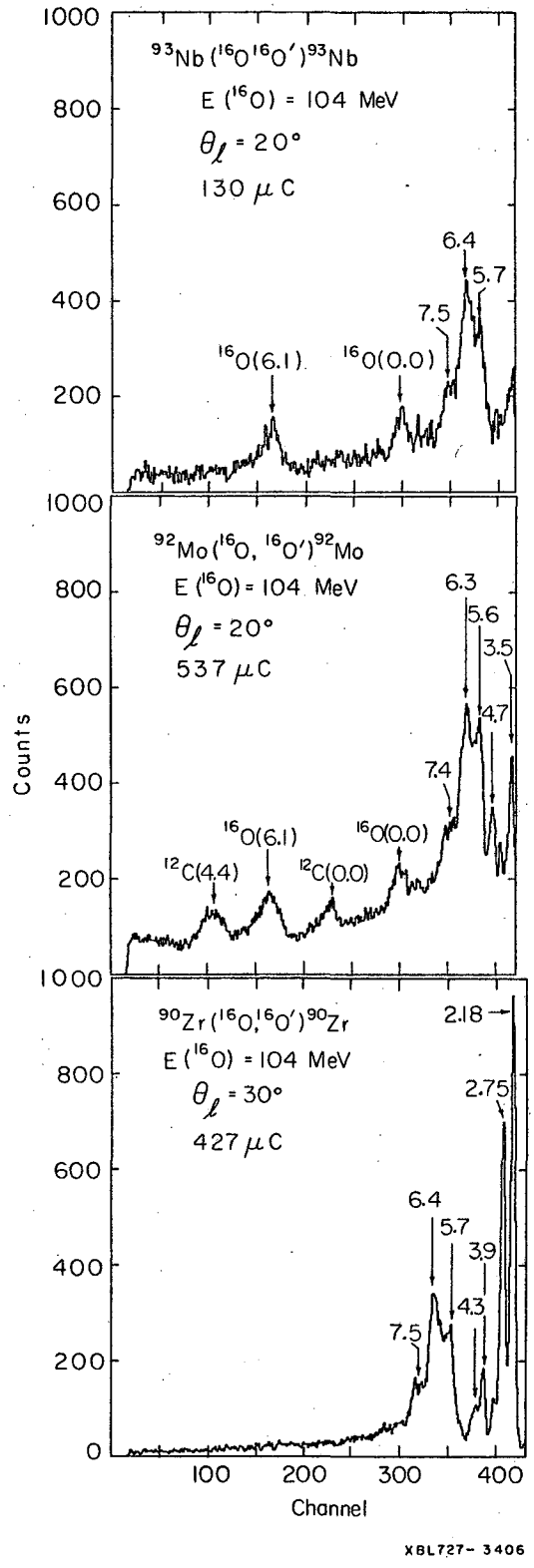

Fig. 43. Position spectra from the inelastic scattering of 104 MeV ^{16}O on targets of ^{90}Zr, ^{92}Mo, and ^{93}Nb. The broad states near 6 MeV may be due to (Doppler broadened) ^{16}O excited states.

scattering since it is orthogonal to the ^{16}O ground state and is believed to be mainly a 4p-4h level.)

The reason for the appearance of a double peak in these two cases is not clear. However, such an effect could presumably occur if the excited states are aligned with respect to the outgoing particle direction. From the results obtained here it is not possible to unambiguously interpret the highest excited states in the ^{15}N spectrum. All that can be said is that the levels above 5.27 MeV may be due to ^{15}N excited states.

3. $^{92}Mo(^{16}O,^{15}N)^{93}Tc$

The $^{92}Mo(^{16}O,^{15}N)^{93}Tc$ reaction was studied only at $\theta_\ell = 20$ and $25°$. As can be seen from Fig. 44, the spectra look very similar to those from the $^{90}Zr(^{16}O,^{15}N)^{91}Nb$ reaction (Fig. 41). A summary of the levels identified in the $^{92}Mo(^{16}O,^{15}N)$ reaction is given in Table XVIII, along with the cross sections for the ground and 3.36 MeV states seen by Christensen *et al.*[114] at 66 MeV. As was true for the $^{90}Zr(^{16}O,^{15}N)$ data (Sec. IV-C2), the cross sections observed at 104 MeV are significantly higher than those reported at 66 MeV. The cross section ratio of the ground and 3.36 MeV states in ^{93}Tc is about the same as that observed for the corresponding ^{91}Nb levels. The low-lying $p_{1/2}$ state, at 0.39 MeV in ^{93}Tc, is resolved from the ground state in these data, and has a cross section about 1/6 of the latter. The 0.10 MeV $p_{1/2}$ state in ^{91}Nb was not resolved from the ground state in $^{90}Zr(^{16}O,^{15}N)$. Therefore, assuming the same relative strengths as in ^{93}Tc, the ^{91}Nb ground state cross section quoted in Table XVII is too large by about 15 to 20%.

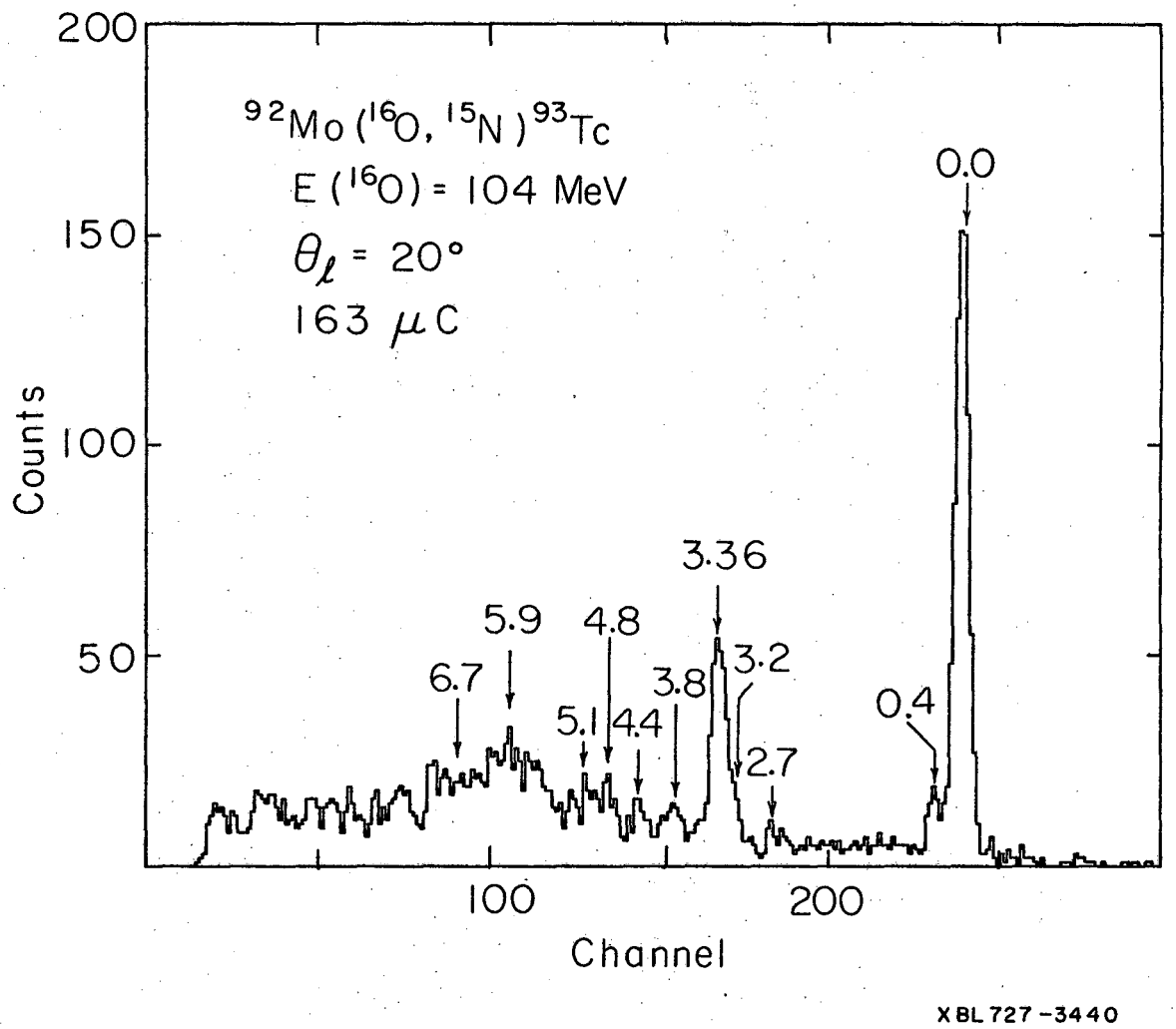

Fig. 44. ^{15}N position spectrum from the ^{92}Mo(^{16}O,^{15}N)^{93}Tc reaction at θ_ℓ= 20°.

Table XVIII. Levels Observed in the $^{92}Mo(^{16}O,^{15}N)^{93}Tc$ Reaction at 104 MeV Compared with Previous Results.

This work		Ref. 114	
Levels Observed[a] (MeV)	Peak Cross Section[b] (mb/sr)	Levels Observed (MeV)	Peak Cross Section[c] (mb/sr)
0.0[d]	4.70 ± 0.19	0.0	0.47 ± 0.05
0.4	0.75 ± 0.08		
2.7	0.23 ± 0.04		
3.2	0.37 ± 0.05		
3.36[d]	1.39 ± 0.10	3.36	(0.12)
3.8	0.26 ± 0.04		
4.4	0.42 ± 0.06		
4.8	0.43 ± 0.06		
5.1	0.29 ± 0.05		
5.9	1.39 ± 0.10		
6.7	1.61 ± 0.11		

[a]Excitation energy ± 200 keV.

[b]Differential cross section at $\theta_\ell = 25°$. The error shown is only that due to counting statistics. The cross sections have been corrected for charge state as described in the text (Sec. III-B).

[c]Differential cross section at $\theta_\ell = 50°$. The excited state has about 1/4 of the ground state intensity.

[d]Used as a calibration point.

Near 6 MeV in ^{93}Tc there are broad states in the ^{15}N spectrum similar to those found in ^{90}Zr(^{16}O,^{15}N). If the ^{91}Nb ground state cross section is corrected for the presence of the unresolved $p_{1/2}$ level, then the cross sections (relative to the ground states) of the 5.9 and 6.7 MeV states seen in the two reactions differ by less than 10%. This is consistent with the hypothesis that these states are due to excited ^{15}N levels, but clearly it is not conclusive evidence.

4. ^{94}Zr(^{16}O,^{15}N)^{95}Nb

This reaction was observed at θ_ℓ= 25 and 30°. A summary of the levels observed here, compared with those seen in the 60 MeV ^{94}Zr(^{16}O,^{15}N) data of Nickles et al.,[27] is given in Table XIX. A spectrum of the ^{94}Zr(^{16}O,^{15}N)^{95}Nb reaction at θ_ℓ= 25° is shown in Fig. 45. The resolution is 300 keV (FWHM). Here too the cross sections are larger than those observed in the 60 MeV experiment, although by much less than was true for the ^{90}Zr(^{16}O,^{15}N) data (see Sec. IV-C2). The strong low-lying states at 0.75, 1.6, and 2.05 MeV seen by Nickles et al.[27] are also the strongest states seen at 104 MeV. The cross section listed in Table XIX for the $p_{1/2}$ state at 0.26 MeV was obtained from the Gaussian peak fitting program DERTAG mentioned above (Sec. III-A). The contribution of the upper level to the ground state peak is about 16%, in agreement with the ratio obtained from the (resolved) 0.39 MeV level in ^{93}Tc. Since the spectroscopic factors for the low-lying $p_{1/2}$ levels in ^{91}Nb, ^{93}Tc, and ^{95}Nb are all quite similar, a correction of about 15% to the ^{91}Nb ground state cross section listed in Table XVII seems to be a reasonable estimate.

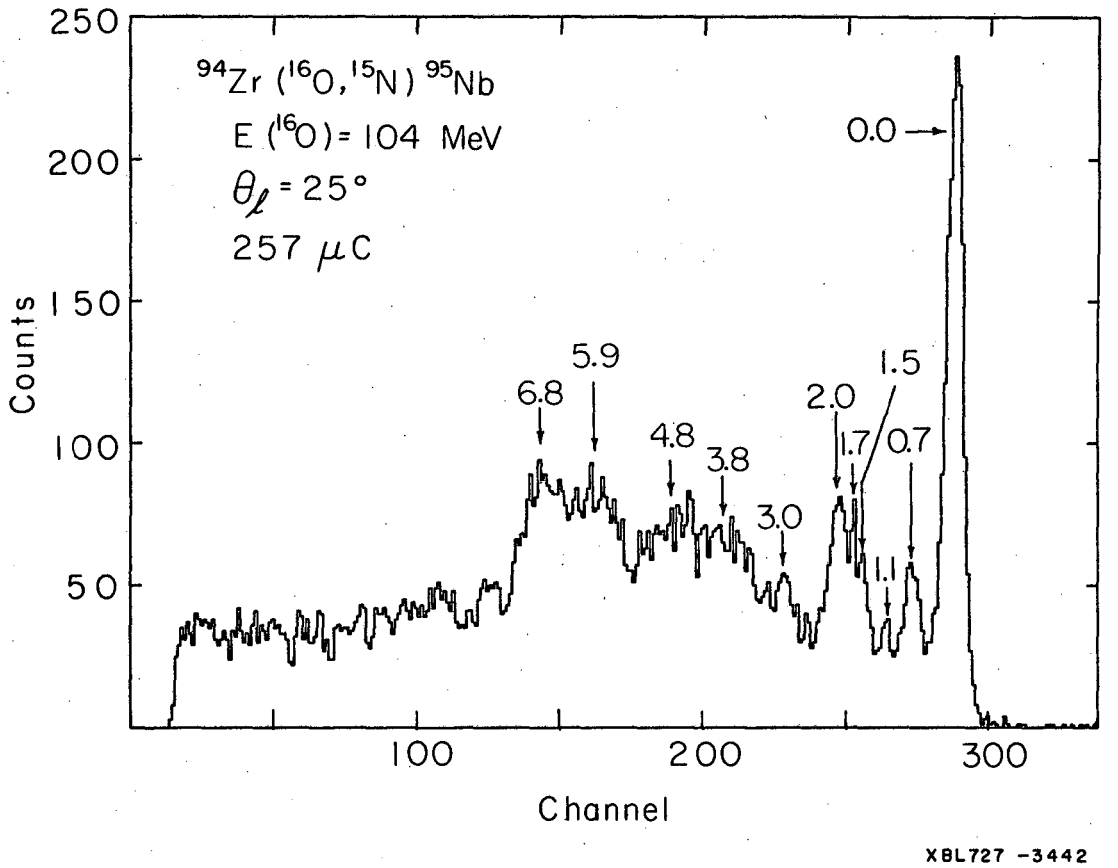

Fig. 45. ^{15}N position spectrum from the ^{94}Zr(^{16}O,^{15}N)^{95}Nb reaction at θ_ℓ = 25°.

Table XIX. Levels Observed in the $^{94}Zr(^{16}O,^{15}N)^{95}Nb$ Reaction at 104 MeV Compared with Previous Results.

This work		Ref. 27	
Levels Observed[a] (MeV)	Peak Cross Section[b] (mb/sr)	Levels Observed (MeV)	Peak Cross Section[c] (mb/sr)
0.0[d]	3.24 ± 0.09	0.0	1.43
0.3	0.64 ± 0.04		
0.7	1.12 ± 0.05	0.75 } 0.92 }	0.34
1.1	0.17 ± 0.02		
1.5	0.24 ± 0.02		
1.7	0.31 ± 0.03[e]	1.6	0.41
2.0	0.94 ± 0.05	2.05	0.52
3.0	0.40 ± 0.03		
3.2	0.21 ± 0.02		
3.8[f]	1.48 ± 0.06		
4.8[f]	1.56 ± 0.06		
5.9[f]	1.86 ± 0.07		
6.8[f]	1.46 ± 0.06		

[a]Excitation energy ± 200 keV.

[b]Differential cross section at $\theta_\ell = 25°$. The error shown is only that due to counting statistics. The cross sections have been corrected for charge state as described in the text (Sec. III-B).

[c]Differential cross section at $\theta_\ell = 60°$.

[d]Used as a calibration point.

(continued)

Table XIX (continued)

[e]Corrected for $^{90}Zr(^{16}O,^{15}N)^{91}Nb$ (g.s.) impurity by about 30%.

[f]Centroids and cross sections are for broad structures (see Fig. 45). Individual levels were not separated.

At higher excitation energies there appear four broad groups in the ^{15}N spectrum (see Fig. 45). The upper groups, at 5.9 and 6.8 MeV, are similar to those seen in the $^{90}Zr(^{16}O,^{15}N)$ and $^{92}Mo(^{16}O,^{15}N)$ reactions and are possibly due to an ^{15}N excited state. The other two groups, at 3.8 and 4.8 MeV, must be ^{95}Nb levels since they are well below the first excited state in ^{15}N. However, with data at only two angles, it was not possible to obtain any meaningful information about individual levels in these groups. The energies and cross sections for these "states" refer to the whole multiplet, rather than to any single level, as is indicated by the arrows in Fig. 45.

5. $^{91}Zr(^{16}O,^{15}N)^{92}Nb$

The $^{91}Zr(^{16}O,^{15}N)^{92}Nb$ reaction was studied only at $\theta_\ell = 25°$. The spectrum is shown in Fig. 46. Due to the fact that the target ground state has $J^\pi = 5/2^+$, each single-proton state forms a multiplet of levels. The $\pi g_{9/2}$ state, for example, forms a $(\pi g_{9/2}, \nu d_{5/2})_{2^+} \rightarrow {}_{7^+}$ multiplet in ^{92}Nb which spans 500 keV of excitation energy (cf. Table VIII). As can be seen from Fig. 46, the largest peak has a centroid (0.4 MeV) and width ($\approx$ 500 keV FWHM) consistent with populating all of the states of this multiplet. A summary of the levels observed in the $^{91}Zr(^{16}O,^{15}N)^{92}Nb$ reaction is given in Table XX. A comparison of the cross section of the 0.4 MeV "state" in ^{92}Nb with that of the ground state of ^{91}Nb (Table XVII) indicates that about 90% of the $\pi g_{9/2}$ strength can be accounted for in this multiplet. This result agrees very well with the corresponding measurement made with the (α,t) reaction (Sec. IV-A6). The other strong group in the spectrum, at 3.6 MeV, is expected to be a $\left[^{91}Nb(3.37\ \text{MeV}) \otimes \nu d_{5/2}\right]$

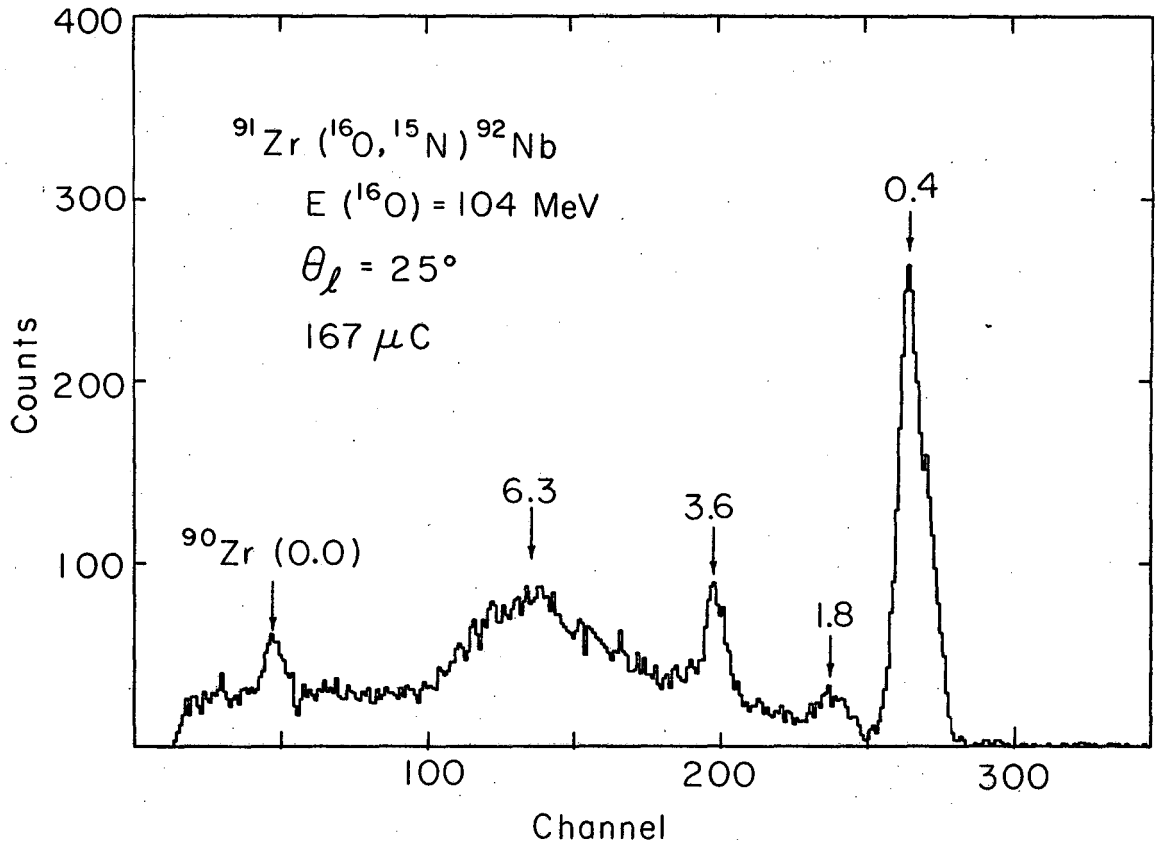

XBL 727-3441

Fig. 46. ^{15}N position spectrum from the ^{91}Zr(^{16}O,^{15}N)^{92}Nb reaction at θ_ℓ= 25°. The peak near channel 50 is due to leak-through of an intense ^{17}O peak from the ^{15}O(7+) gate (see Fig. 54).

Table XX. Levels Observed in the $^{91}Zr(^{16}O,^{15}N)^{92}Nb$ Reaction at 104 MeV.

Levels Observed[a] (MeV)	Peak Cross Section[b] (mb/sr)
0.4	7.22 ± 0.14
1.8	0.65 ± 0.04
3.6	1.38 ± 0.06
6.3	6.85 ± 0.14

[a]Excitation energy ± 200 keV.

[b]Differential cross section at $\theta_\ell = 25°$. The error shown is only that due to counting statistics. The cross sections have been corrected for charge state as described in the text (Sec. III-B).

multiplet based on the observed strong population of the 3.37 MeV $\pi d_{5/2}$ state in the $^{90}Zr(^{16}O,^{15}N)^{91}Nb$ reaction (Sec. IV-C2).

At higher excitation energy a very broad group appears with a centroid energy of 6.3 MeV. This group does not look like the 6 MeV groups observed in the spectra of the even-even targets (see, for example, Fig. 41), since it is not a double peak. The centroid energy of the group, however, still agrees well with the energy of the $p^{-1}_{3/2}$ excited state in ^{15}N. The difference in shape in this case may be due to the "valley" between the 5.9 and 6.6 MeV peaks in $^{90}Zr(^{16}O,^{15}N)$ being destroyed by averaging over the 500 keV wide ground state multiplet in ^{92}Nb. Also, since the level density of the odd-odd ^{92}Nb nucleus is undoubtedly greater than that of ^{91}Nb at the same excitation energy, there is probably more cross section in this region due to "real" ^{92}Nb states, which might have the effect of washing out the double peak structure.

6. $^{93}Nb(^{16}O,^{15}N)^{94}Mo$

The $^{93}Nb(^{16}O,^{15}N)^{94}Mo$ reaction was studied at $\theta_\ell = 20$ and 25°. The spectrum taken at $\theta_\ell = 20°$ is shown in Fig. 47. The ground state and low-lying levels are populated rather weakly and the spectrum is dominated by a doublet at 2.6 and 2.9 MeV. Based on the $^{93}Nb(^{3}He,d)$ results of Cates, Ball, and Newman,[4] there are many ^{94}Mo levels in the region near 2.6 MeV. Spin assignments to some of these have been made by Lederer, Jaklevic, and Hollander[115] in a study of in-beam γ-ray spectroscopy of the even molybdenum isotopes. The γ-decay data[115] indicate levels at 2.421 MeV (6^+), 2.608 MeV (5^-), 2.738 MeV (4^+), 2.870 MeV (6^+ or 6^-), and 2.953 MeV (8^+ or 8^-). These last two levels are connected by an E2 decay and thus must have the same parity. The

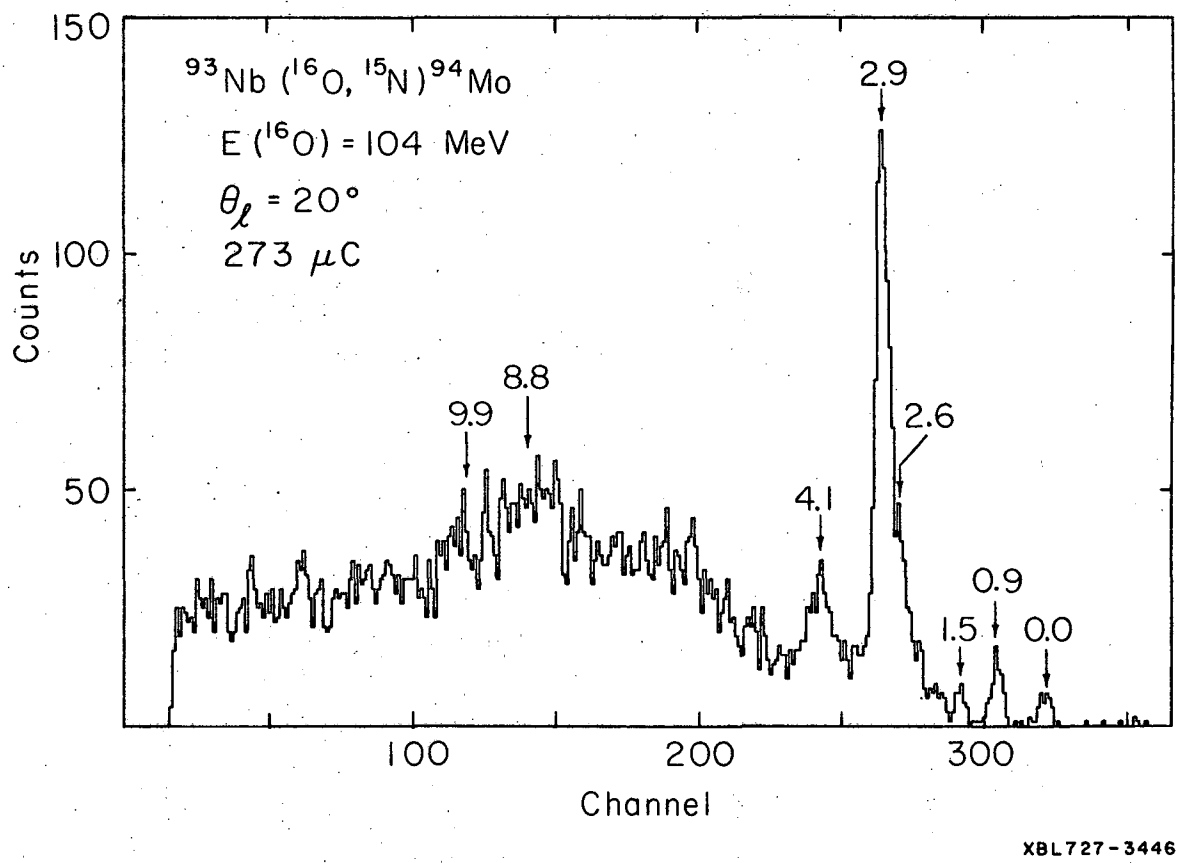

Fig. 47. ^{15}N position spectrum from the ^{93}Nb(^{16}O,^{15}N)^{94}Mo reaction at θ_ℓ= 20°.

^{93}Nb(^{3}He,d) reaction[4] assigns $\ell = 4$ to the 2.875 and 2.960 MeV states, which suggests that these levels are the 6^+ and 8^+ of the $(\pi g_{9/2})^2$ configuration. Similarly, the strong $\ell = 1$ transition to the 2.614 MeV level in (^{3}He,d) indicates a dominant $(\pi p_{1/2}^{-1}\, g_{9/2})_{5-}$ configuration for that state. A summary of the levels observed in the ^{93}Nb(^{16}O,^{15}N) reaction, as well as those seen in the (^{3}He,d) and γ-decay experiments, is given in Table XXI.

The highest state seen here, at 4.1 MeV, was not reported in Ref. 4. A number of levels in this region were seen in the γ spectroscopy experiment and given high-spin assignments ($J \geqslant 8$). Such high-spin states are likely to be multiparticle states. (The exceptions to this are the 9^- and 10^- states which arise from the $(\pi h_{11/2}\, g_{9/2})$ configuration. However, the $\pi h_{11/2}$ single-particle energy is quite high (> 6 MeV) in ^{93}Tc and is probably not too different in ^{94}Mo.) The probable 10^+ state at 3.894 MeV, for example, was tentatively associated with the $\left[(\pi g_{9/2})^2_{8^+}\ (\nu d_{5/2})^2_{2^+}\right]$ configuration. In a single-step stripping reaction, such a level could only be reached through an admixture of $\left[(\pi g_{9/2})\ (\nu d_{5/2})^2_{2^+}\right]_{9/2^+}$ in the ^{93}Nb ground state. Another possible explanation for states in this region would be levels with a dominant $\pi d_{5/2}$ configuration. Such states would be expected at about this excitation energy. The $\ell = 2$ admixtures determined for the low-lying levels seen in ^{93}Nb(^{3}He,d) were all quite small, indicating that the major $\pi d_{5/2}$ strength does lie at higher energies.

At very high energies in ^{94}Mo very broad structures appear in the spectrum. The excitation energies of these "levels", 8.8 and 9.9 MeV, could correspond to the double excitation which gives ^{94}Mo (2.9 MeV) and ^{15}N (6.33 MeV), in agreement with previous evidence.

Table XXI. Levels Observed in the $^{93}Nb(^{16}O,^{15}N)^{94}Mo$ Reaction at 104 MeV Compared with Previous Work.

This work		$^{93}Nb(^{3}He,d)^{94}Mo$[a]			In-beam γ spectroscopy[b]	
Levels Observed[c] (MeV)	Peak Cross Section[d] (mb/sr)	Levels Observed[e] (MeV)	ℓ_p	J^π	Levels Observed[f] (MeV)	J^π
0.0	0.18 ± 0.02	0.0	4	0^+	(0.0)	0^+
0.9	0.22 ± 0.03	0.873	2,4	2^+	0.870	2^+
1.5	0.10 ± 0.02	1.582	2,4	4^+	1.572	4^+
		1.868	2,4	2^+		
		2.08	4	$(0)^+$		
		2.295	2,4	$(\ )^+$	2.300	
		2.422	2,4	6^+	2.421	6^+
		2.527	1	$(3,4,5,6)^-$		
		2.566	2,4	$(\ )^+$		
2.6	1.22 ± 0.06	2.614	1	$(3,4,5,6)^-$	2.608	5^-
		2.773	2,4	$(\ )^+$	2.738	(4^+)
		2.837	1	$(3,4,5,6)^-$		
2.9	2.71 ± 0.09	2.875	4	$(8)^+$	2.870	$6^{(\pm)}$[g]
		2.960	4	$(8,1)^+$	2.953	$8^{(\pm)}$[g]

(continued)

Table XXI (continued)

This work		$^{93}Nb(^{3}He,d)^{94}Mo$[a]			In-beam γ spectroscopy[b]	
Levels Observed[c] (MeV)	Peak Cross Section[d] (mb/sr)	Levels Observed[e] (MeV)	ℓ_p	J^π	Levels Observed[f] (MeV)	J^π
		3.026	1	$(3,4,5,6)^-$		
					3.318	(8 to 10)
					3.357	(8^+)
					3.364	(7^-)
					3.803	(9 to 12)
					3.865	
					3.894	$10^{(\pm)}$[g]
					4.005	(8 to 10)
4.1	0.54 ± 0.04				4.187	(11,12)
					4.493	(8 to 10)
8.8[h]	1.53 ± 0.07					
9.9[h]	1.20 ± 0.06					

[a]Ref. 4. [b]Ref. 115. [c]Excitation energy ± 200 keV.

[d]Differential cross section at $\theta_\ell = 25°$. The error shown is only that due to counting statistics.

(continued)

Table XXI (continued)

The cross sections have been corrected for charge state as described in the text (Sec. III-B).

[e]Excitation energy ± 5 keV. [f]Excitation energy ± 1 keV.

[g]The 2.870, 2.953, and 3.894 MeV states are connected by E2 decay and must all have the same parity.

[h]Centroids and cross sections are for broad structures (see Fig. 47). Individual levels were not separated.

7. $^{90}Zr(^{16}O,^{15}O)^{91}Zr$

A spectrum of the $^{90}Zr(^{16}O,^{15}O)^{91}Zr$ reaction at $\theta_\ell = 25°$ is shown in Fig. 48. The resolution is about 250 keV (FWHM). To facilitate later comparison, a spectrum of the $^{90}Zr(\alpha,^{3}He)^{91}Zr$ reaction at 65 MeV is included in Fig. 48. As an example of the particle identification capabilities of the heavy ion focal plane detector, a spectrum of the $^{90}Zr(^{16}O,^{15}O)^{91}Zr$ reaction at a field setting corresponding to the $^{15}O(7+)$ magnetic rigidity is shown in Fig. 49. This spectrum is clearly identical to that shown in Fig. 48. The $^{15}O(7+)$ spectrum was separated from that of ^{15}N (see Fig. 41) by means of the two-dimensional arrays shown in Figs. 11-14. As can be seen from Figs. 48 and 49, only two levels are strongly populated, the ground and 2.16 MeV states. The angular distributions for these states, shown in Fig. 50, are quite similar to those from the $^{90}Zr(^{16}O,^{15}N)^{91}Nb$ reaction (Fig. 42). Both the ^{15}O and ^{15}N angular distributions peak at about the same angle, but the ^{15}O angular distributions fall off more rapidly at forward angles than do those of ^{15}N.

The expected Q-value dependence of heavy-ion induced transfer reactions has been discussed by Buttle and Goldfarb.[109] They find that for neutron transfer the favored Q-value is zero. This is a consequence of requiring that the distance of closest approach be approximately the same in both the initial and final channels. (In the case of the $(^{16}O,^{15}N)$ reaction this requirement favors a negative Q-value since there is a change in the outgoing Coulomb barrier.) For neutron transfer, a zero Q-value corresponds roughly to a momentum transfer of zero. In the present case, the ground state ($d_{5/2}$) transition requires L = 3 and the transition

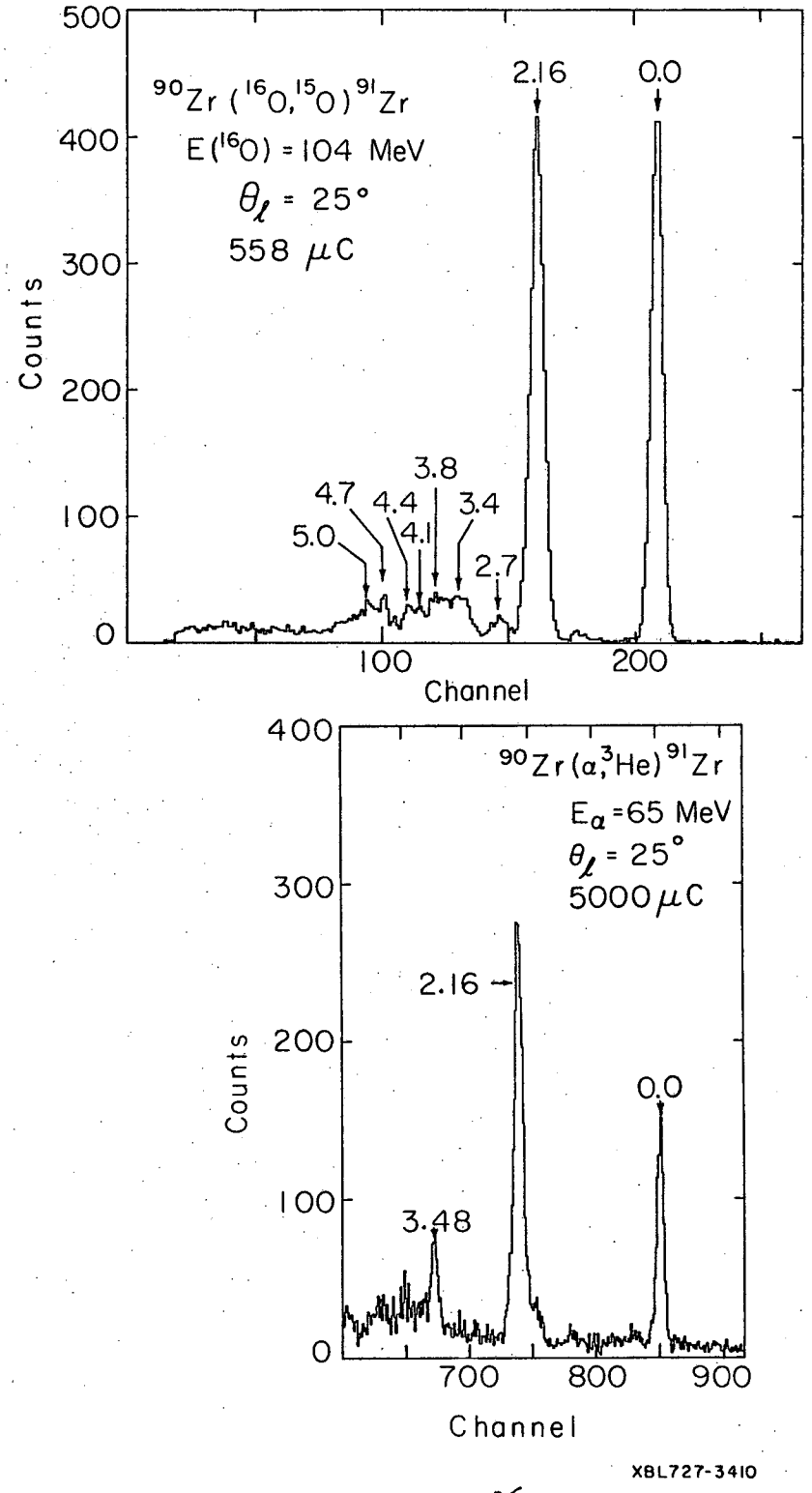

Fig. 48. ^{15}O position spectrum from the ^{90}Zr(^{16}O,^{15}O)^{91}Zr reaction at θ_ℓ= 25°. A ^{90}Zr(α,^{3}He)^{91}Zr spectrum at θ_ℓ= 25° is shown for comparison.

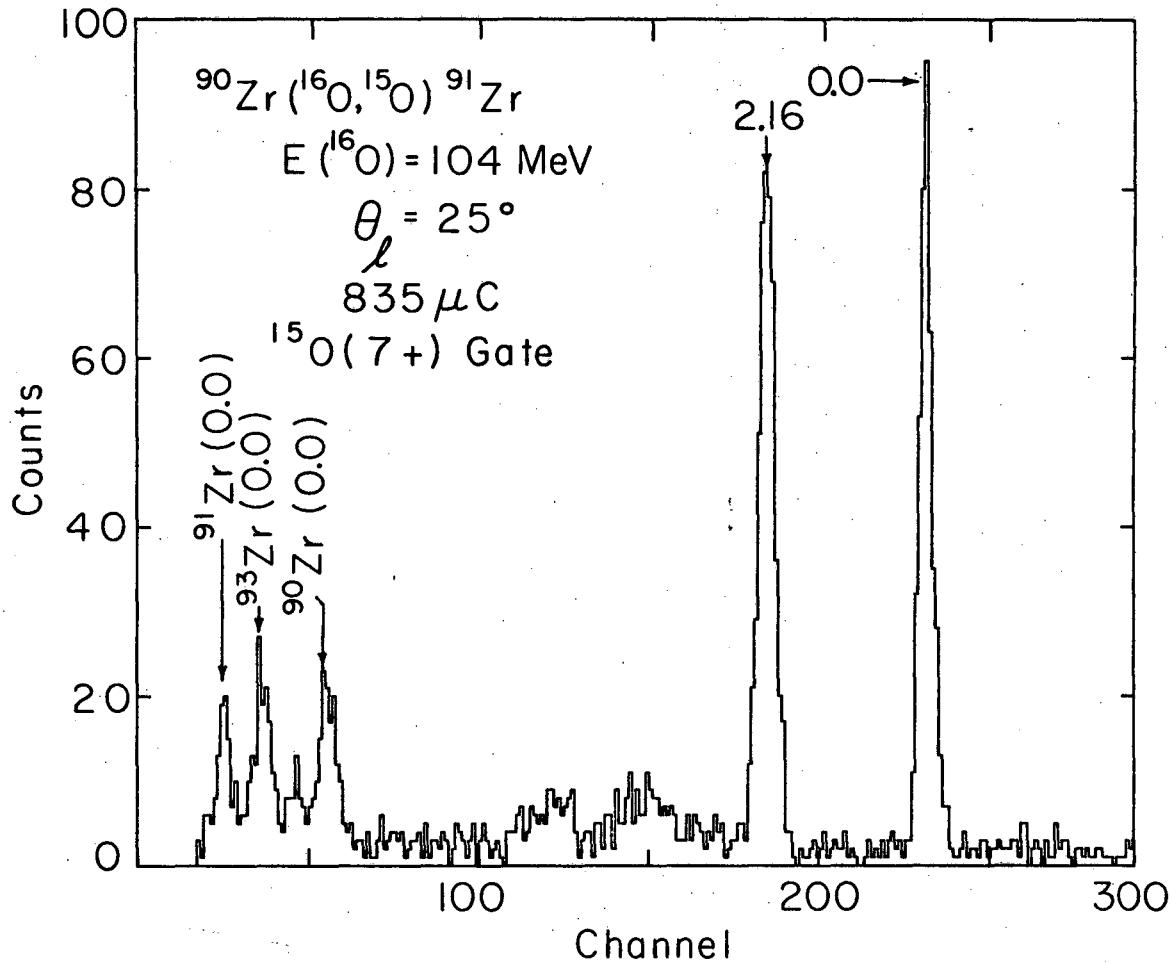

XBL 727-3411

Fig. 49. ^{15}O(7+) position spectrum from the ^{90}Zr(^{16}O,^{15}O)^{91}Zr reaction at θ_ℓ = 25°. The small peaks near channel 50 are due to the (^{16}O,^{17}O) reaction on isotopic impurities in the target leading to the final states indicated above the peaks.

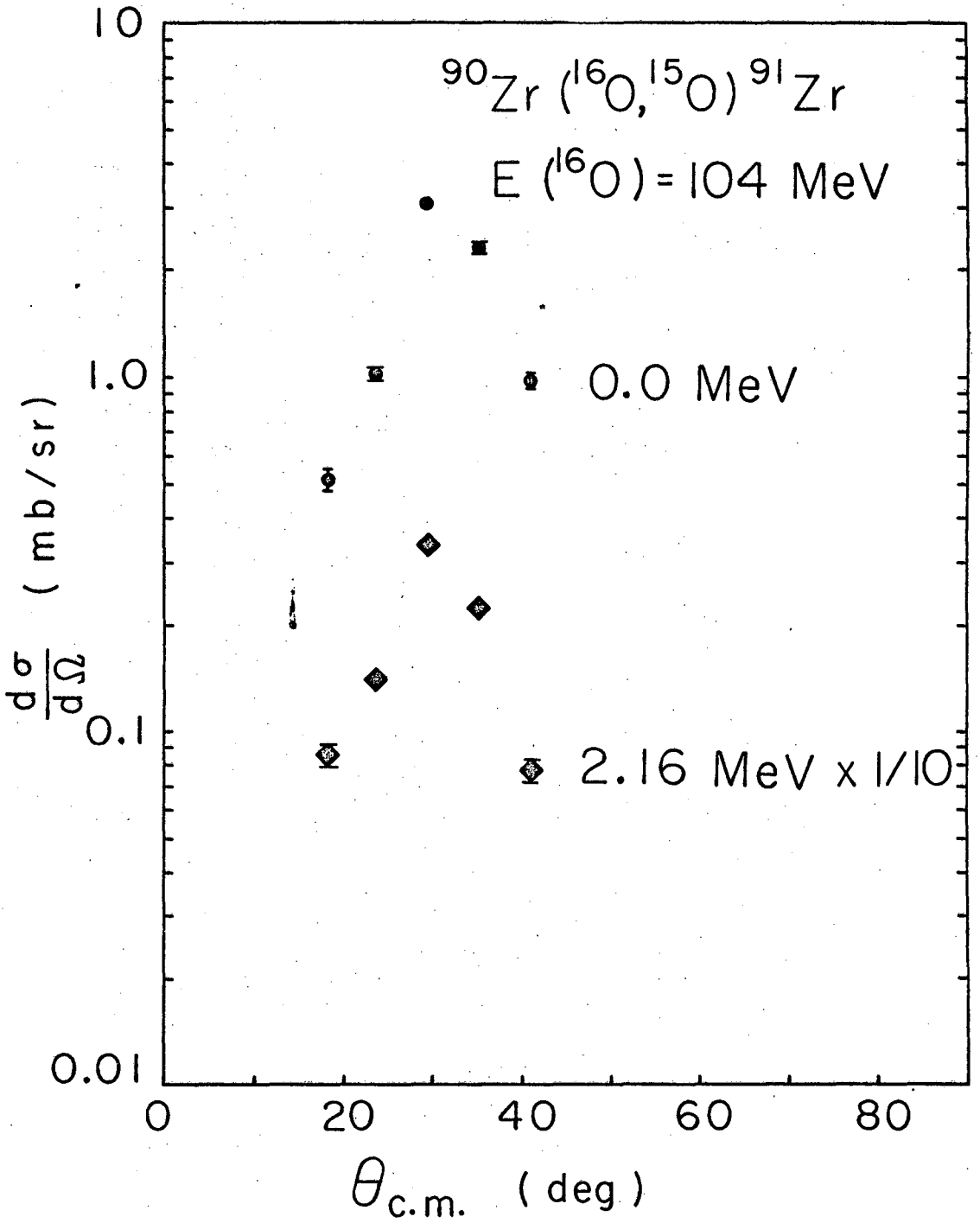

XBL727-3408

Fig. 50. ^{15}O angular distributions from the $^{90}Zr(^{16}O,^{15}O)^{91}Zr$ reaction leading to the 0.0 and 2.16 MeV states. According to the selection rules the ground state transition is L=3 and the 2.16 MeV transition is L=6.

to the 2.16 MeV state ($h_{11/2}$) requires L = 6 according to the selection rules (Sec. IV-C1). From the kinematic model described in Appendix A, an L = 3 transition corresponds to a Q-value of -1.5 MeV, while an L = 6 transition corresponds to a Q-value of -6 MeV. Thus, in this simple picture the ground state (L = 3) is about 7 MeV away from the favored Q-value and the 2.16 MeV state (L = 6) is off by about 4.5 MeV.

The Q-value dependence of heavy ion reaction cross sections is predicted to be quite steep. Von Oertzen[116] showed a factor of 10 decrease in cross section for a change from the optimum Q-value of 5 MeV for the $^{54}Fe(^{16}O,^{12}C)$ reaction. Similarly, Manko et al.[117] observed changes in cross section of about 1 order of magnitude for a Q-value change of 5 MeV in the $(^{16}O,^{15}N)$ reaction on the nickel isotopes leading to the $\pi g_{9/2}$ states in copper. According to the calculations of Buttle and Goldfarb,[109] the Q-value dependence for neutron transfer is even more pronounced than for proton transfer. In fact, both von Oertzen[108] and Buttle and Goldfarb[109] suggested that it would be necessary to select a reaction whose Q-value was near the optimum value in order to obtain "measurable" cross sections for single nucleon transfer reactions.

The data obtained here show cross sections for the ground and 2.16 MeV states (whose Q-values are -8.5 and -10.6 MeV, respectively) of 3 mb/sr at $\theta_\ell = 25°$. This indicates that measurable cross sections are obtainable with the $(^{16}O,^{15}O)$ reaction, at least for the higher angular momentum transfers, even at very negative Q-values. If the Q-value dependence suggested above were correct, then the cross section for the $(^{16}O,^{15}O)$ reaction near the optimum Q-value would be very large, perhaps as much as

100 times larger than the cross sections observed here. While this may be possible (peak cross sections of about 20 mb/sr were obtained for the $^{94}Zr(^{16}O,^{17}O)^{93}Zr$ reaction discussed below), it does seem improbable. Since conventional no-recoil DWBA calculations do predict correctly the magnitude of the cross sections measured here,[49] it seems apparent that the Q-value dependence at 104 MeV is less steep than suggested[108] by the lower energy results.

The levels of ^{91}Zr have been studied by means of the $^{90}Zr(d,p)^{91}Zr$ reaction.[118-120] The ground state is the $\nu d_{5/2}$ single-particle level and is observed with a spectroscopic factor of approximately unity in all cases. The situation for the doublet at 2.16 and 2.19 MeV is not so clearcut since they are assigned different ℓ values by the various groups. Cohen and Chubinsky[118] and Graue et al.[119] see only $\ell = 4$ strength, while Bingham and Halbert[120] and Booth et al.[63] assign the upper member as $\ell = 4$ ($g_{7/2}$) and the lower member as $\ell = 5$ ($h_{11/2}$). The $^{91}Zr(p,p')$ data of DuBard and Sheline[121] also give $J^{\pi} = 11/2^-$ for the 2.16 MeV state. Since the two levels were not resolved by Cohen and Chubinsky[118] and the data of Graue et al.[119] are fit equally well with either an $\ell = 4$ or an $\ell = 5$ curve, it will be assumed here that the $^{90}Zr(d,p)$ data establish the existence of an $h_{11/2}$ state at 2.16 MeV. A summary of the $^{90}Zr(^{16}O,^{15}O)$ results, compared with those from the $^{90}Zr(d,p)$ and $^{90}Zr(\alpha,^{3}He)$ reactions, is given in Table XXII.

The contribution to the 2.16 MeV peak from the unresolved $\nu g_{7/2}$ state at 2.19 MeV cannot be obtained from the data. However, it can be estimated with the help of the $^{92}Mo(^{16}O,^{15}O)^{93}Mo$ data presented below (Sec. IV-C8). In the $^{92}Mo(^{16}O,^{15}O)$ spectrum the $\nu g_{7/2}$ and $\nu h_{11/2}$ levels are no

Table XXII. Levels Observed in the $^{90}Zr(^{16}O,^{15}O)^{91}Zr$ Reaction at 104 MeV Compared with Previous Work.

This work		$^{90}Zr(d,p)^{91}Zr$[a]			$^{90}Zr(\alpha,^{3}He)^{91}Zr$[a]	
Levels Observed[b] (MeV)	Peak Cross Section[c] (mb/sr)	Levels Observed (MeV)	J^{π}	S	Levels Observed (MeV)	S
0.0[d]	3.07 ± 0.06	0.0	$5/2^{+}$	1.04	0.0	0.98
		1.201	$1/2^{+}$	0.93		
		1.459	$5/2^{+}$	0.03		
		1.871	$7/2^{+}$	0.08	1.874	0.09
		2.031	$3/2^{+}$	0.63	2.040	0.45
2.16[d]	3.38 ± 0.06	2.157	$11/2^{-}$	0.37	2.176	{0.41
		2.186	$7/2^{+}$	0.48		0.48}
		2.309	$11/2^{-}$	0.05	2.323	0.05
		2.541	$1/2^{+}$	0.34		
2.7	0.12 ± 0.01	2.681				
		2.792	$(3/2^{+}),5/2^{+}$[e]	0.07,0.03[e]		
		2.853	$3/2^{+}$	0.08	2.847	0.13
		2.902	$(1/2^{+})$	0.10		
		2.992				

(continued)

Table XXII (continued)

This work		$^{90}Zr(d,p)^{91}Zr$ [a]			$^{90}Zr(\alpha,{}^{3}He)^{91}Zr$ [a]	
Levels Observed [b] (MeV)	Peak Cross Section [c] (mb/sr)	Levels Observed (MeV)	J^{π}	S	Levels Observed (MeV)	S
		3.068	$3/2^{+}$	0.28	3.063	0.22
		3.270	$3/2^{+}$	0.17	3.277	0.19
3.4	0.31 ± 0.02	3.444	$7/2^{+}$	0.42	3.466	0.34
		3.533	$7/2^{+}$	0.09	3.575	0.08
		3.610				
		3.661	$(3/2^{+},11/2^{-})$	(0.11,0.03)	3.676	(0.11,0.03)
		3.721				
		3.824	$(3/2^{+})$	0.12	3.817	0.19
3.8	0.29 ± 0.02	3.880	$(3/2^{+},11/2^{-})$	(0.05,0.08)	3.904	(0.05,0.09)
4.1	0.11 ± 0.01		$11/2^{-}$		4.081	0.04
			$11/2^{-}$		4.254	0.06
4.4	0.12 ± 0.01					
4.7	0.12 ± 0.01					
5.0	0.15 ± 0.01					

(continued)

Table XXII (continued)

[a]Ref. 120.

[b]Excitation energy ± 200 keV.

[c]Differential cross section at $\theta_\ell = 25°$. The error shown is only that due to counting statistics.

[d]Used as a calibration point.

[e]Ref. 119.

0 0 0 0 3 8 0 7 0 2 9

longer degenerate but are separated by about 800 keV. The spectroscopic factors for the $g_{7/2}$ levels at 1.359 and 1.516 MeV, 0.26 and 0.14, respectively,[62] are about the same as that for the unresolved $g_{7/2}$ state at 2.19 MeV in ^{91}Zr, whose spectroscopic factor is 0.48.[120] Similarly, the $\ell = 5$ spectroscopic factors for the ^{91}Zr 2.16 MeV state and ^{93}Mo 2.32 MeV state are 0.37 and 0.33, respectively.[120,62] From the cross section ratio of the 1.5 and 2.3 MeV groups in ^{93}Mo, we can then estimate that about 20% of the 2.16 MeV peak in the $^{90}Zr(^{16}O,^{15}O)^{91}Zr$ reaction is due to the $\nu g_{7/2}$ state at 2.19 MeV. This is only a rough estimate but it does justify the assumption that the peak in the $^{90}Zr(^{16}O,^{15}O)$ data at 2.16 MeV is mainly $h_{11/2}$. An explanation for the dominance of the $h_{11/2}$ over the $g_{7/2}$ state can be found in the selection rules, which indicate L = 6 for the $h_{11/2}$ state and L = 3 for the $g_{7/2}$. In a situation of poor momentum matching (the favored $(^{16}O,^{15}O)$ L transfer at these Q-values is about 10) the high spin states will be closer to the favored conditions than the lower spin states and thus the high angular momentum transfers are preferred.

The higher states seen in the $^{90}Zr(^{16}O,^{15}O)^{91}Zr$ reaction are all quite weak. The 2.7 MeV state seen in the $(^{16}O,^{15}O)$ data with about 3% of the ground state cross section could correspond to the 2.8 MeV, $\ell = 2$ state in the $^{90}Zr(d,p)$ data[119] with a spectroscopic factor about 1/30 that of the ground state. The level in the ^{15}O spectrum at 3.4 MeV probably corresponds to the $g_{7/2}$ state observed at 3.47 MeV in the $^{90}Zr(d,p)$ reaction.[119,120] Similarly, $\ell = 5$ levels have been reported[120] near 4.1 MeV. Above this point the level density is too high to attempt to compare the $^{90}Zr(^{16}O,^{15}O)$ data with the light ion results.

8. $^{92}Mo(^{16}O,^{15}O)^{93}Mo$

The $^{92}Mo(^{16}O,^{15}O)^{93}Mo$ reaction was observed at θ_ℓ= 20 and 25°. A spectrum at θ_ℓ= 20° is shown in Fig. 51. The resolution is about 250 keV (FWHM). Included in Fig. 51 is a spectrum from the $^{92}Mo(\alpha,^3He)^{93}Mo$ reaction at 65 MeV. As was true for the $^{90}Zr(^{16}O,^{15}O)^{91}Zr$ data, very few levels are populated strongly. A summary of the levels observed in the $^{92}Mo(^{16}O,^{15}O)$ reaction and their intensities is given in Table XXIII.

The $^{92}Mo(d,p)^{93}Mo$ reaction has been studied by Moorhead and Moyer,[62] who assigned the 2.32 MeV level as ℓ = 5 ($h_{11/2}$). Booth et al.[63] also assigned ℓ = 5 to this level in the $^{92}Mo(d,p)$ reaction. The complementary $^{94}Mo(d,t)$ reaction has been studied by Diehl et al.[122] in order to confirm the assignments from (d,p) for the low-lying levels in ^{93}Mo. The 0.94 MeV state was found to be the strongest ℓ = 0 transition, with a spectroscopic factor of 0.64. Near 1.5 MeV several states are reported. From a comparison of the $^{92}Mo(d,p)$ and $^{94}Mo(d,t)$ data the levels are:[62,122] 1.359 MeV($7/2^+$), 1.489 MeV($9/2^+$), 1.502 MeV($3/2^+$), and 1.529 MeV($7/2^+$). Based on the ($^{16}O,^{15}O$) selection rules, the $9/2^+$ would be the most favorable transition (L = 5). However, this is a $\nu g_{9/2}^{-1}$ state, since it was populated strongly in the (d,t) experiment and not observed at all in the (d,p) data. Of the remaining states, it seems likely that the $g_{7/2}$ (L = 3) would be stronger than the $d_{3/2}$ (L = 1) in a situation where the momentum matching for low L transfers is poor. From Fig. 51 it is obvious that the relative intensities of the doublet at 1.5 MeV in the $^{92}Mo(^{16}O,^{15}O)$ reaction cannot be explained by populating only the $g_{7/2}$ states. The 1.36 MeV $7/2^+$ state has a larger spectroscopic factor than does the 1.53 MeV $7/2^+$ state,[62]

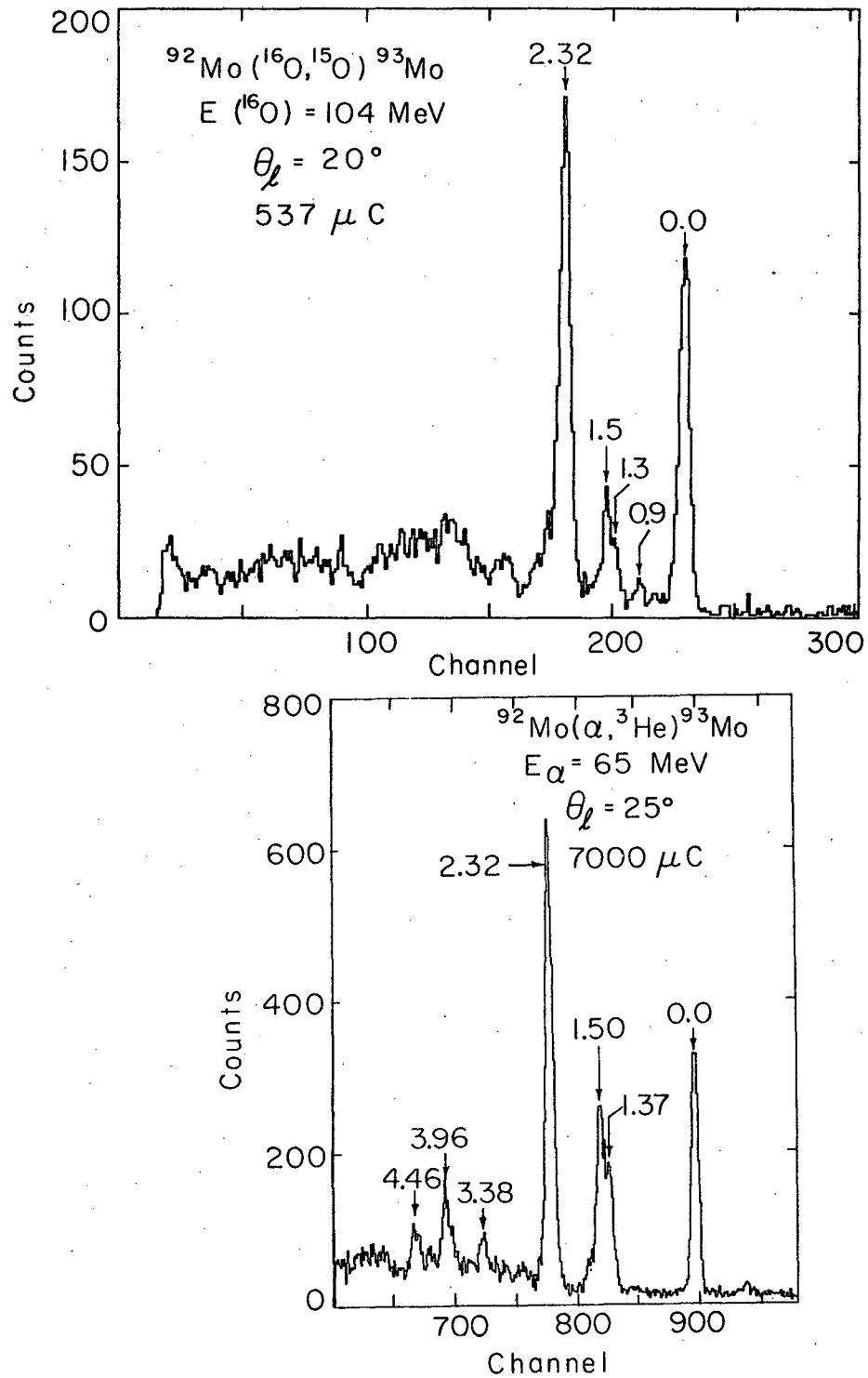

XBL727-3412

Fig. 51. ^{15}O position spectrum from the ^{92}Mo(^{16}O,^{15}O)^{93}Mo reaction at θ_ℓ= 20°. A ^{92}Mo(α,^{3}He)^{93}Mo spectrum at θ_ℓ= 25° is shown for comparison.

Table XXIII. Levels Observed in the $^{92}Mo(^{16}O,^{15}O)^{93}Mo$ Reaction Compared with Previous Work.

This work		$^{92}Mo(d,p)^{93}Mo$[a]		
Levels Observed[b] (MeV)	Peak Cross Section[c] (mb/sr)	Levels Observed[d] (MeV)	J^{π}	S
0.0[e]	2.64 ± 0.11	0.0	$5/2^+$	0.87
0.9	0.05 ± 0.02	0.950	$1/2^+$	0.64
1.3	0.22 ± 0.03	1.371	$7/2^+$	0.26
		1.486[f]	$9/2^+$	
1.5	0.48 ± 0.05	1.502	$3/2^+$	0.50
		1.529	$7/2^+$	0.14
		1.706	$3/2^+$	0.18
		2.157	$1/2^+$	0.007
		2.194	$3/2^+$	0.053
2.32[e]	2.50 ± 0.11	2.320	$11/2^-$	0.33

[a]Refs. 62 and 122.

[b]Excitation energy ± 200 keV.

[c]Differential cross section at $\theta_\ell = 25°$. The error shown is only that due to counting statistics.

[d]Only levels below 2.32 MeV are included here.

[e]Used as a calibration point.

[f]Observed only in the $^{94}Mo(d,t)$ data of Ref. 122.

while the $(^{16}O,^{15}O)$ data show more intensity to the upper level by roughly a factor of 2. (This is also true for the $^{92}Mo(\alpha,^{3}He)$ data in Fig. 51.) Whether the intensity of the 1.5 MeV state seen here is due to population of the $d_{3/2}$ state or to the appearance of the 1.49 MeV $g_{9/2}$ state cannot be determined without greatly improved experimental resolution. It should be remarked here that the estimate of the $\nu g_{7/2}$ contribution to the 2.16 MeV peak in the $^{90}Zr(^{16}O,^{15}O)^{91}Zr$ reaction (Sec. IV-C7) was based on the assumption that all of the observed intensity at 1.5 MeV in ^{93}Mo was due to the $\nu g_{7/2}$ states. Therefore, the estimate of 20% should be considered as roughly an upper limit to the expected contribution.

As in ^{91}Zr, the ground state of ^{93}Mo is the $\nu d_{5/2}$ single-particle state. Although the ground state Q-value for the $^{92}Mo(^{16}O,^{15}O)^{93}Mo$ reaction, -7.6 MeV, is 0.9 MeV less negative than that for the $^{90}Zr(^{16}O,^{15}O)^{91}Zr$ reaction, the latter reaction has a larger cross section at $\theta_\ell = 25°$ for the ground state transition. This runs counter to all arguments regarding optimum Q-values for neutron transfer. A tentative explanation for this is that the grazing angle for the $^{92}Mo(^{16}O,^{15}O)$ reaction should be about 2° larger than that for $^{90}Zr(^{16}O,^{15}O)$ due to the higher Coulomb barrier. Since the angular distributions of the $(^{16}O,^{15}O)$ reaction are sharply peaked at the grazing angle (see Fig. 50), a 2° shift could account for the 10% lower cross section at $\theta_\ell = 25°$ observed for the $^{92}Mo(^{16}O,^{15}O)^{93}Mo$ (g.s.) transition.

9. $^{93}Nb(^{16}O,^{15}O)^{94}Nb$

The $^{93}Nb(^{16}O,^{15}O)^{94}Nb$ reaction was observed at $\theta_\ell = 20$ and 25°. A spectrum at $\theta_\ell = 20°$ is shown in Fig. 52. The resolution was about 250

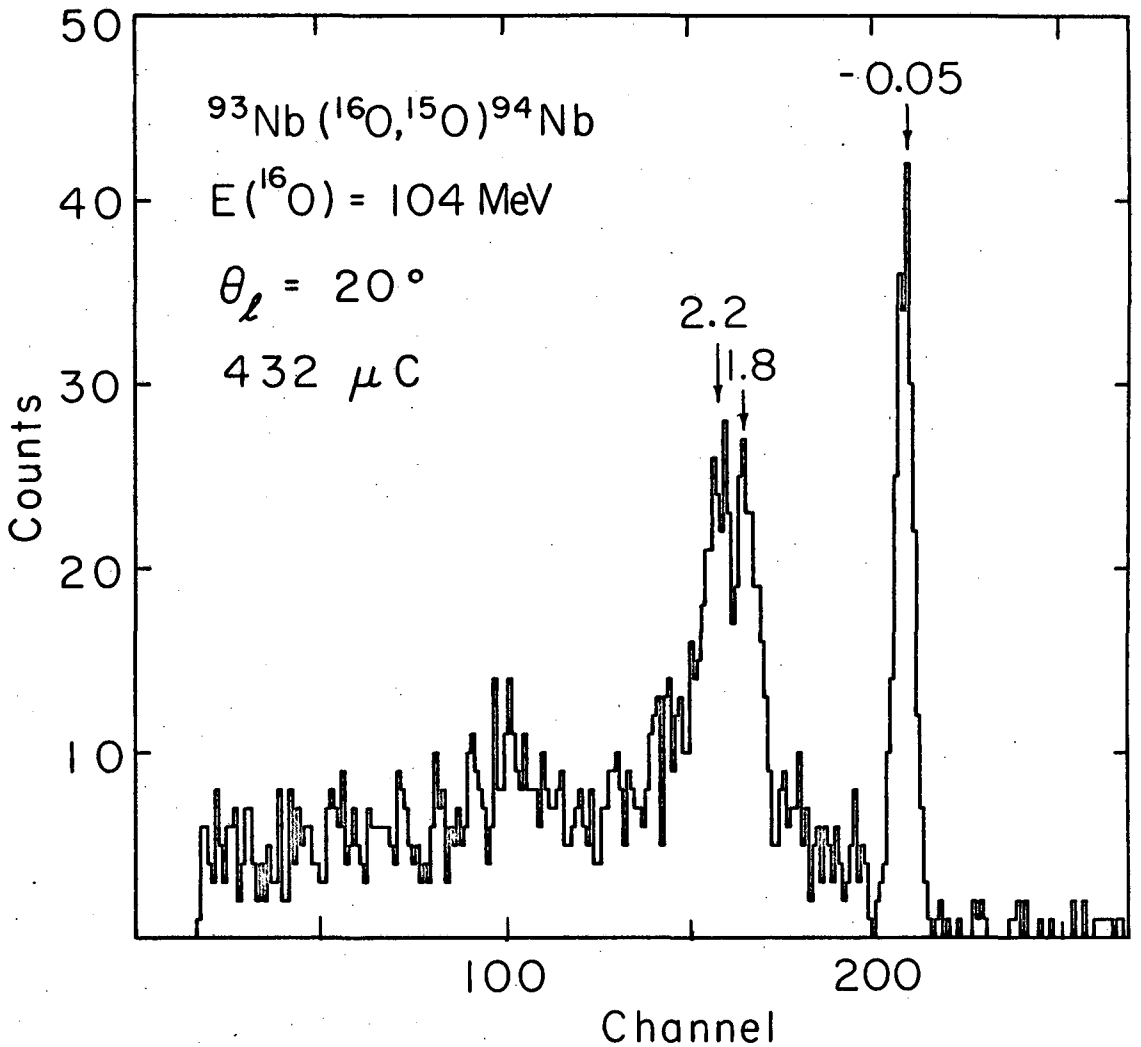

XBL727-3445

Fig. 52. ^{15}O position spectrum from the ^{93}Nb(^{16}O,^{15}O)^{94}Nb reaction at θ_ℓ= 20°. Due to difficulty with the calibration, the energy of the [$\pi g_{9/2}$,($\nu d_{5/2}$)$^3_{5/2}$] multiplet was found to be -0.05 MeV. The excitation energies for all three states are believed to be low by about 110 keV. (See text, Sec. IV-C9.)

keV (FWHM). Only three levels were populated strongly. Based on a calibration curve from the ^{93}Nb(^{16}O,^{15}N)^{94}Mo reaction, the excitation energies determined for the three strong levels are -0.05, 1.8, and 2.2 MeV. The peak cross sections for these levels are given in Table XXIV.

The ^{93}Nb(d,p)^{94}Nb reaction has been studied by Moorhead and Moyer[62] and by Sheline et al.[101] The low-lying levels are interpreted as being a multiplet whose main configuration is $\left[\pi g_{9/2},(\nu d_{5/2})^3_{5/2}\right]_{2^+\longrightarrow 7^+}$. These states are analogous to the low-lying multiplet seen in ^{92}Nb (see Sec. IV-A6). However, in ^{94}Nb the states are very close together. Five of the six states lie within 113 keV of the ground state in ^{94}Nb, while in ^{92}Nb the six levels span 500 keV of excitation energy. This explains why the peak in Fig. 52 looks narrow compared with the peak seen in the ^{91}Zr(^{16}O,^{15}N)^{92}Nb spectrum (Fig. 46). The cross section obtained for this multiplet in ^{94}Nb is only about half that found for the ^{90}Zr(^{16}O,^{15}O)^{91}Zr (g.s.) reaction, although the Q-values are the same in the two cases. In the ^{93}Nb(^{16}O,^{15}O) reaction, however, the presence of two $d_{5/2}$ neutrons in the target ground state will reduce the $\nu d_{5/2}$ cross section compared with that in the ^{90}Zr(^{16}O,^{15}O) reaction, since there are only 4 holes in the $d_{5/2}$ shell (in a simple picture) rather than 6. Moreover, there is expected[101] to be mixing between the $(\nu d_{5/2})^3_{5/2^+}$, $(\nu d_{5/2})^3_{3/2^+}$, and $(\nu d_{5/2})^3_{9/2^+}$ configurations which will remove some of the $\nu d_{5/2}$ strength from the ground state multiplet. (The ^{93}Nb(d,p) data indicate[100] $\ell = 2$ strength up to 1.5 MeV.)

The excitation energy obtained here for the $\nu d_{5/2}$ multiplet is clearly incorrect. The problem is due to there being no known states to include in the calibration curve. (In most other reactions at least the ground state was useful as a calibration point. While the overlap of known

Table XXIV. Levels Observed in the $^{93}Nb(^{16}O,^{15}O)^{94}Nb$ Reaction at 104 MeV.

Levels Observed[a] (MeV)	Adjusted Energy[b] (MeV)	Peak Cross Section[c] (mb/sr)
-0.05	0.06	1.68 ± 0.06
1.8	1.91	1.23 ± 0.05
2.2	2.31	0.96 ± 0.04

[a]Excitation energy ± 200 keV.

[b]Normalized to the expected excitation energy of the low-lying $\left[\pi g_{9/2},(\nu d_{5/2})^3_{5/2}\right]$ multiplet. (See text, Sec. IV-C9.)

[c]Differential cross section at $\theta_\ell = 25°$. The error shown is only that due to counting statistics.

points from various runs was never perfect, it was always possible to obtain reasonable excitation energy values when there were known points from each of the spectra being calibrated.) A first guess at the true excitation energy of the -0.05 MeV peak would be the centroid of the states seen in the ^{93}Nb(d,p) reaction. From Ref. 62 this is about 0.06 MeV. Thus, the excitation energies reported for the three states seen here are estimated to be low by about 110 keV.

The strength of the groups near 2 MeV in the (^{16}O,^{15}O) data argues strongly for a ($\pi g_{9/2}$,$\nu h_{11/2}$) multiplet at this energy in ^{94}Nb. As is clearly evident from the ^{92}Mo(^{16}O,^{15}O) data (Fig. 51) only the $\nu h_{11/2}$ transition is comparable in intensity to the $\nu d_{5/2}$ transition. The energy differences between the $\nu d_{5/2}$ and $\nu h_{11/2}$ groups in the ^{90}Zr(^{16}O,^{15}O) and ^{92}Mo(^{16}O,^{15}O) reactions, 2.2 and 2.3 MeV, respectively, agree quite well with the 2.1 MeV difference between the strong groups in the ^{93}Nb(^{16}O,^{15}O) data. No ℓ = 5 neutron transfers have been reported in the ^{93}Nb(d,p) reaction, but the cross sections for such transitions were estimated[62] to be less than 70 μb/sr at a deuteron energy of 12 MeV.

10. <u>^{94}Zr(^{16}O,^{15}O)^{95}Zr</u>

The ^{94}Zr(^{16}O,^{15}O)^{95}Zr reaction was observed only at θ_ℓ = 25°. The spectrum obtained from the ^{15}O(7+) charge state is shown in Fig. 53. Due to the fact that only the 7+ charge state was observed, the amount of data is rather small. Still, it was possible to identify the ground and 2.0 MeV states in ^{95}Zr.

The ^{94}Zr(d,p)^{95}Zr reaction was studied by Cohen and Chubinsky[118] some years ago. The ground state was found to be a $\nu d_{5/2}$ level with a spectroscopic factor S = 0.30. As would be expected from a simple picture

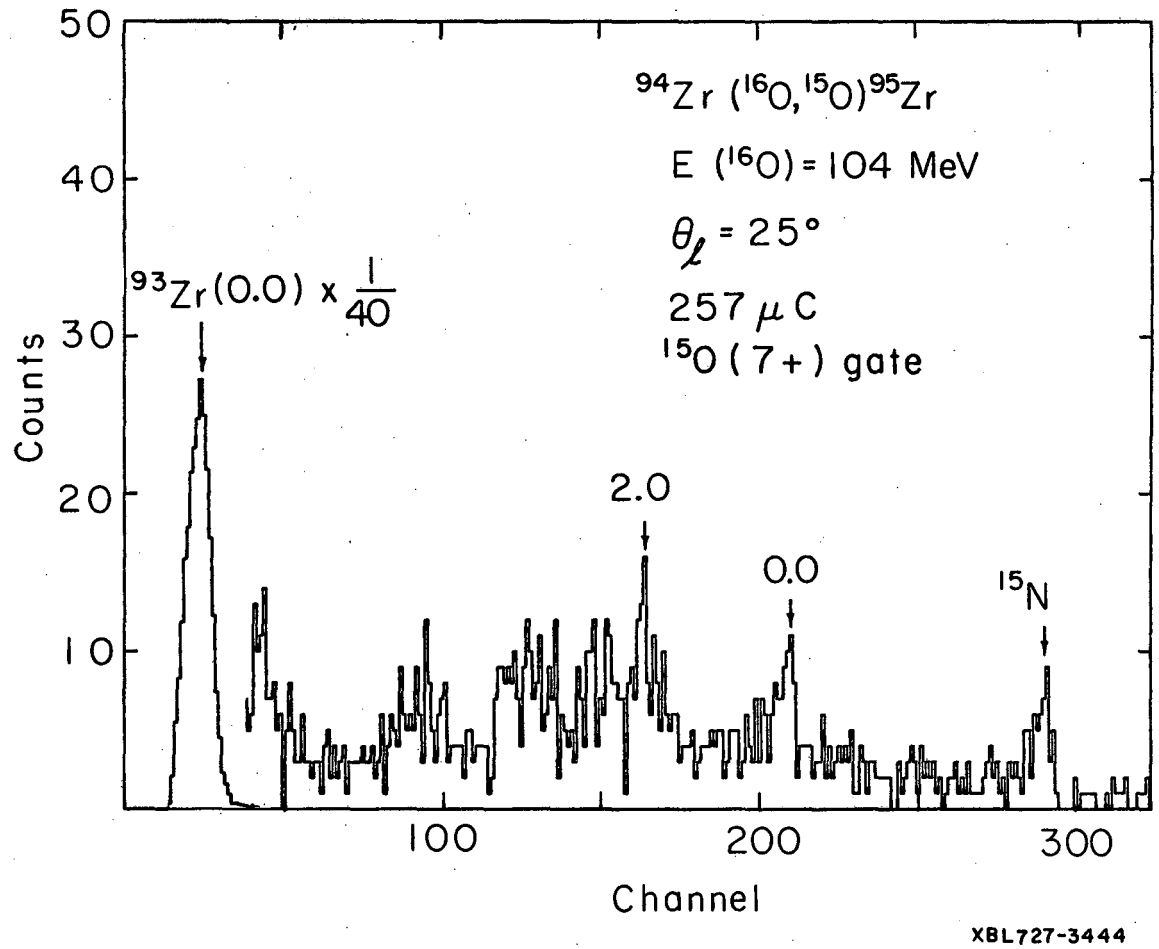

Fig. 53. ^{15}O(7+) position spectrum from the ^{94}Zr(^{16}O,^{15}O)^{95}Zr reaction at θ_ℓ = 25°. The large peak at the bottom of the spectrum is due to the ^{94}Zr(^{16}O,^{17}O)^{93}Zr (g.s.) reaction.

of the Zr isotopes, the spectroscopic factor of the $\nu d_{5/2}$ transition decreases about a factor of 3 in going from ^{90}Zr (6 holes in the $\nu d_{5/2}$ shell) to ^{94}Zr (2 holes in the $\nu d_{5/2}$ shell).

The 2.03 MeV state seen by Cohen and Chubinsky[118] was assigned $\ell = 4$ ($g_{7/2}$). From the "systematics" of the (^{16}O,^{15}O) reaction observed here, strong population of a $\nu g_{7/2}$ state would be unlikely. However, the 2.02 MeV state seen by Booth et al.[63] was assigned $\ell = 5$ ($h_{11/2}$), which agrees with the observed preference (see Secs. IV-C7 and IV-C8) for the (^{16}O,^{15}O) reaction to populate $\nu h_{11/2}$ states.

As discussed earlier, there are serious difficulties in attempting to obtain cross section information from data corresponding to ions which are not fully stripped (see Sec. III-B). However, in this case no data from the $^{15}O(8+)$ charge state were taken. In order to obtain at least an estimate of the cross sections for this reaction, the data were corrected with values of $R_{8/7}$ obtained from Sec. III-B, eq. (5b). Because of the possible error in this procedure, an arbitrary 50% error is given to these corrected values. Both the uncorrected and corrected cross sections are given in Table XXV.

11. $^{91}Zr(^{16}O,^{15}O)^{92}Zr$

The $^{91}Zr(^{16}O,^{15}O)^{92}Zr$ reaction was observed (with the $^{15}O(7+)$ charge state) only at $\theta_\ell = 25°$. The spectrum is shown in Fig. 54. Three states, at 0.9, 1.5, and 3.5 MeV, were identified. Their intensities, both uncorrected and corrected for charge state, are given in Table XXVI.

The $^{91}Zr(d,p)^{92}Zr$ reaction[118,120] indicates that the 0.0, 0.936, and 1.495 MeV levels are mainly $(\nu d_{5/2})^2$ states with spins of 0^+, 2^+,

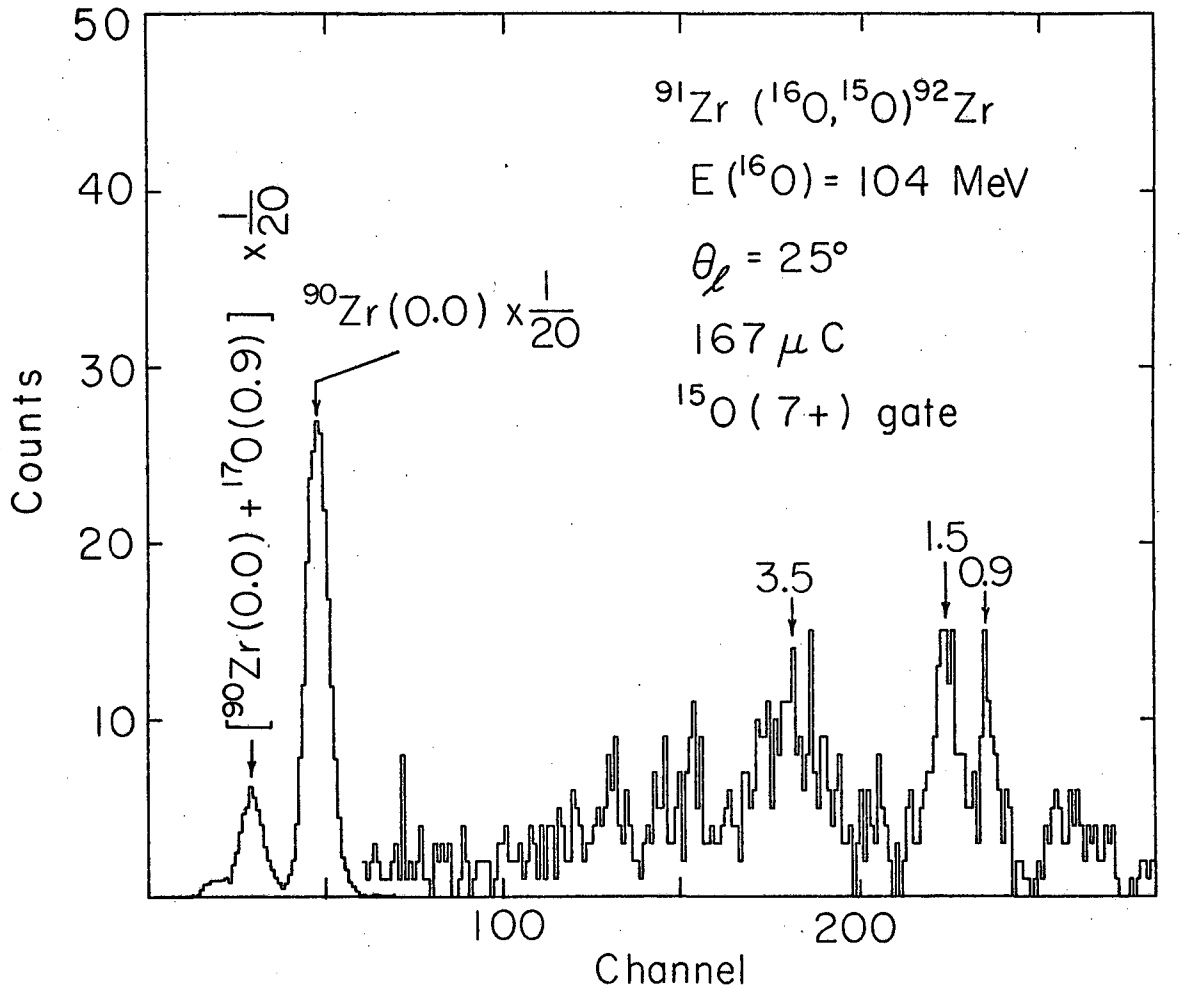

XBL727-3447

Fig. 54. ^{15}O(7+) position spectrum from the ^{91}Zr(^{16}O,^{15}O)^{92}Zr reaction at θ_ℓ= 25°. The peaks at the bottom of the spectrum are due to the ^{91}Zr(^{16}O,^{17}O)^{90}Zr(g.s.) reaction, with the larger one being due to ^{17}O in its ground state and the smaller one to ^{17}O in its 0.87 MeV ($s_{1/2}$) first excited state.

Table XXV. Levels Observed in the $^{94}Zr(^{16}O,^{15}O)^{95}Zr$ Reaction at 104 MeV.

Levels Observed[a] (MeV)	Peak Cross Section[b] (uncorrected) (mb/sr)	Peak Cross Section[c] (corrected) (mb/sr)
0.0	0.16 ± 0.02	0.87 ± 0.44
2.0	0.14 ± 0.02	0.72 ± 0.36

[a]Excitation energy ± 200 keV.

[b] $^{15}O(7+)$ differential cross section at $\theta_\ell = 25°$, but calculated as for $^{15}O(8+)$. See Sec. III-B, eq. (10b). The error shown is only that due to counting statistics.

[c] $^{15}O(7+)$ cross section from column 2 after correction by $R_{8/7}$ from Sec. III-B, eq. (5b). An arbitrary error of ± 50% is assumed for the correction.

Table XXVI. Levels Observed in the $^{91}Zr(^{16}O,^{15}O)^{92}Zr$ Reaction at 104 MeV.

Levels Observed[a] (MeV)	Peak Cross Section[b] (uncorrected) (mb/sr)	Peak Cross Section[c] (corrected) (mb/sr)
0.9	0.20 ± 0.02	1.13 ± 0.67
1.5	0.37 ± 0.03	2.03 ± 1.02
3.5	0.21 ± 0.02	1.11 ± 0.56

[a] Excitation energy ± 200 keV.

[b] $^{15}O(7+)$ differential cross section at $\theta_\ell = 25°$, but calculated as for $^{15}O(8+)$. See Sec. III-B, eq. (10b). The error shown is only that due to counting statistics.

[c] $^{15}O(7+)$ cross section from column 2 after correction by $R_{8/7}$ from Sec. III-B, eq. (5b). An arbitrary error of ± 50% is assumed for the correction.

and 4^+, respectively. The expected $(2J_f + 1)$ dependence of the stripping cross sections, which is followed rather well for these states in the (d,p) data, is the probable explanation for the lack of an identifiable ground state peak. (The $(^{16}O,^{15}O)$ cross sections of the 0.9 and 1.5 MeV peaks also follow the $(2J_f + 1)$ rule almost exactly.)

In the region near 3.5 MeV there were several $\ell = 5$ transitions observed by Bingham and Halbert.[120] The strongest of these was at 3.581 MeV. It seems reasonable to associate the 3.5 MeV level seen here with this $h_{11/2}$ state, based on the observed selectivity of the $(^{16}O,^{15}O)$ reaction in strongly populating only $\nu d_{5/2}$ and $\nu h_{11/2}$ states in the other targets studied.

12. $(^{16}O,^{17}O)$ Reactions

Due to the method of gating employed with the heavy ion focal plane detector (see Sec. III-B), there are certain ambiguities in the particle identification. An example of this is $^{17}O(8+)$ and $^{15}O(7+)$, which have the same Z and (within the resolution of the detector) the same value for M/q. If the Q-values for the $(^{16}O,^{15}O)$ and $(^{16}O,^{17}O)$ reactions are appropriate, they will fall in different regions of the focal plane and can therefore be observed simultaneously. Such is the case for the $(^{16}O,^{17}O)$ reaction on most of the Zr isotopes. Peaks corresponding to the $(^{16}O,^{17}O)$ reaction (leading to the ground state of the final nucleus) have been observed for ^{91}Zr, ^{92}Zr, ^{94}Zr, and possibly ^{96}Zr. These peaks were all observed in the $^{15}O(7+)$ gate set for the ^{90}Zr target at $\theta_\ell = 25°$. They are labelled in Fig. 49. (The small peak between the ^{90}Zr and ^{93}Zr ground state peaks has a position appropriate

for the $^{96}Zr(^{16}O,^{17}O)^{95}Zr$ ground state, although it corresponds to a very large cross section. Compared with the other $(^{16}O,^{17}O)$ cross sections determined here, however, it does not appear to be unreasonably large.)

Fortunately, it was possible to confirm the identity of some of the peaks seen in Fig. 49 by finding them in the $^{15}O(7+)$ gates of the other targets studied. Based on the isotopic abundances from Table I, cross sections for all of the ^{17}O peaks were calculated for the ^{90}Zr target. In the case of the $^{91}Zr(^{16}O,^{17}O)$ and $^{94}Zr(^{16}O,^{17}O)$ reactions (see Figs. 53 and 54), the cross sections calculated from the ^{90}Zr target agreed quite well with those from the ^{91}Zr and ^{94}Zr targets. No confirmation for the $^{92}Zr(^{16}O,^{17}O)$ or $^{96}Zr(^{16}O,^{17}O)$ cross section was possible since these targets were not used in the heavy ion experiments. The cross sections obtained for the $(^{16}O,^{17}O)$ reaction on the various targets are summarized in Table XXVII.

In the $^{91}Zr(^{16}O,^{17}O)$ reaction (Fig. 54), a peak corresponding to the ^{17}O first excited state at 0.87 MeV was also observed. For all of the other cases, the Q-value was such that the ^{17}O (0.87 MeV) peak was off the detector. Although the ^{17}O excited state was only observed once, its interpretation seems unambiguous. The intensity of the peak is roughly a factor of 20 higher than can be accounted for by an isotopic impurity, and the excitation energy, 0.9 MeV, cannot correspond to a state in the residual nucleus since the first excited state of ^{90}Zr is at 1.75 MeV. (Furthermore, the cross section for the 1.75 MeV 0^+ state in the $^{91}Zr(p,d)$ reaction[123] was less than 10^{-3} that of the ground state.) The cross section observed for the $^{91}Zr(^{16}O,^{17}O^*)^{90}Zr$ (g.s.) reaction was 22% of that for the $^{91}Zr(^{16}O,^{17}O)^{90}Zr$ (g.s.) reaction. From the selection rules, the latter reaction ($d_{5/2} \longrightarrow d_{5/2}$ transition) can have

Table XXVII. $Zr(^{16}O,^{17}O)$ Cross Sections at 104 MeV.

Reaction[b]	Target: ^{90}Zr	Peak Cross Section[a] (mb/sr) ^{91}Zr	^{94}Zr
$^{91}Zr(^{16}O,^{17}O)^{90}Zr(g.s.)$	12.6 ± 1.0	12.4 ± 0.2	—
$^{91}Zr(^{16}O,^{17}O^{*})^{90}Zr(g.s.)$	—	2.8 ± 0.1	—
$^{92}Zr(^{16}O,^{17}O)^{91}Zr(g.s.)$	12.1 ± 1.2	—	—
$^{94}Zr(^{16}O,^{17}O)^{93}Zr(g.s.)$	20.5 ± 1.8	—	21.8 ± 0.2
$^{96}Zr(^{16}O,^{17}O)^{95}Zr(g.s.)$	(51. ± 6)[c]	—	—

[a]Differential cross section at $\theta_{\ell} = 25°$. Isotopic abundances are taken from Table I. The error shown is only that due to counting statistics.

[b]The "$^{17}O^{*}$" refers to the outgoing ^{17}O being in its 0.87 MeV ($s_{1/2}$) first excited state.

[c]The amount of ^{96}Zr is given as < 0.1%, so only a lower limit to the cross section can be calculated.

contributions from L = 0, 2, and 4, while the former reaction ($d_{5/2} \longrightarrow s_{1/2}$ transition) is restricted to L = 2. The factor of 5 difference in cross section between the two reactions may be related to the preference for high L transfers ($\sigma_{L+2} \approx 10\sigma_L$) suggested by DWBA calculations.[110]

The trend in (^{16}O,^{17}O) cross sections with mass number can be qualitatively understood in terms of the filling of the $\nu d_{5/2}$ shell. In a simple picture the cross sections should be in the ratio 1:2:4:6 in going from ^{91}Zr to ^{96}Zr. With the exception of the ^{91}Zr to ^{92}Zr ratio, the experimental results (Table XXVII) are in reasonable agreement with this prediction. The states observed here were also seen in the (^{16}O,^{17}O) data of Christensen et al.[114] at 60 MeV. They report peak cross sections of 0.77, 2.13, and 8.4 mb/sr for the ^{92}Zr, ^{94}Zr, and ^{96}Zr targets, respectively. Since the $^{94}Zr(^{16}O,^{17}O)^{93}Zr$ (g.s.) cross section seen here is a factor of 10 larger than that reported at 60 MeV, a > 50 mb/sr cross section for the $^{96}Zr(^{16}O,^{17}O)^{95}Zr$ (g.s.) transition appears reasonable compared with the 8 mb/sr cross section observed in the lower energy experiment.

V. DISCUSSION

A. Single-nucleon Transfer

1. Comparison with Shell Model Predictions

As pointed out previously, there have been extensive shell model calculations performed in the Zr-Mo region.[7-9] These calculations have generally assumed that the low-lying levels can be described by configurations which include the "active" orbitals $\pi p_{1/2}$, $\pi g_{9/2}$, and $\nu d_{5/2}$, i.e., by the assumption of a closed shell at ^{88}Sr. (In some calculations a ^{90}Zr core, i.e., no $\pi p_{1/2}$ orbital, was assumed,[7] but the experimental evidence shows[4] that in the ground states of the Zr isotopes the $\pi p_{1/2}$ shell is only about half filled.) Within this model there are some low-lying states which can mix with the high-spin single particle orbitals. In this region the configurations which can mix are $(\pi g_{9/2})^n_{7/2^+}$ with the $\pi g_{7/2}$ single-particle orbital and $(\pi g_{9/2})^n_{9/2^+}$ with the $\pi g_{9/2}$ single-particle orbital.

For example, in the "unperturbed" picture of ^{91}Nb there are three $9/2^+$ states expected, two with seniority v = 1 and one with v = 3. (The seniority, v, is the number of particles which are unpaired, i.e., not coupled to $J^\pi = 0^+$.) The v = 1 states would be

$$(\pi p_{1/2})^2_{0^+} \quad (\pi g_{9/2}) \tag{1a}$$

and

$$(\pi g_{9/2})^2_{0^+} \quad (\pi g_{9/2}) \tag{1b}$$

In fact, however, the residual interaction mixes the $(\pi p_{1/2})^2_{0^+}$ and $(\pi g_{9/2})^2_{0^+}$ states in ^{90}Zr so that the ground and first excited states (both 0^+) are

g.s.: $$\alpha(\pi p_{1/2})^2_{0^+} + \beta(\pi g_{9/2})^2_{0^+} \quad (2a)$$

and 1.75 MeV: $$\beta(\pi p_{1/2})^2_{0^+} - \alpha(\pi g_{9/2})^2_{0^+} \quad (2b)$$

with[8] $\alpha^2 \approx 0.6$ and $\beta^2 \approx 0.4$. By analogy with configuration (1), the v = 1 $9/2^+$ states in ^{91}Nb become

$$\alpha'(\pi p_{1/2})^2_{0^+}\ (\pi g_{9/2}) + \beta'(\pi g_{9/2})^2_{0^+}\ (\pi g_{9/2}) \quad (3a)$$

and

$$\beta'(\pi p_{1/2})^2_{0^+}\ (\pi g_{9/2}) - \alpha'(\pi g_{9/2})^2_{0^+}\ (\pi g_{9/2}) \quad (3b)$$

If $\alpha' = \alpha$ and $\beta' = \beta$, we can describe configurations (3a) and (3b) as a $\pi g_{9/2}$ single particle coupled to the ground and first excited (1.75 MeV 0^+) states of ^{90}Zr. In this case, the state (3b) would have no overlap with the ^{90}Zr ground state and would have a spectroscopic factor for proton transfer in ^{90}Zr(^{3}He,d) or ^{90}Zr(α,t) of zero. However, if $\alpha' \neq \alpha$ and $\beta' \neq \beta$, a non-zero spectroscopic factor is allowed for the upper level as well, although generally it will be small.

In ^{91}Nb, the $9/2^+$ state corresponding to configuration (3b) (calculated to lie at 1.64 MeV) is expected[4] to have an intensity about 1/1800 that of the ground state. In this case the level would not be observed even in (α,t). The $(\pi g_{9/2})^3_{7/2^+}$ state was calculated[8] to lie at 1.62 MeV. Due to the nearby $p^{-1}_{3/2}$ state in the experimental spectrum, it is not clear whether or not this state is populated. At higher energy there is a calculated $(\pi g_{9/2})^3_{9/2^+}$ state with v = 3 at about 2.9 MeV.[8] This state might be associated with the observed[56] $9/2^+$ state at 2.63 MeV which is very weak in ^{90}Zr(^{3}He,d)[1] but is populated in ^{90}Zr(α,t) (Sec. IV-A2) with about 1% of the ground state intensity. A $7/2^+$ state at 2.792 MeV was

also observed by Rauch[56] and may correspond to the (α,t) state at 2.77 MeV. This state is not included in the shell model calculations since only one $7/2^+$ state can be formed from the $(\pi g_{9/2})^3$ configuration. At higher excitation energies, of course, it is unlikely that the few configurations used in the shell model calculations[7-9] will be adequate to describe the levels, since the presence of other single proton levels such as $\pi g_{7/2}$ and $\pi d_{5/2}$ becomes important.

In ^{93}Tc the low-lying levels are described in a manner similar to that for ^{91}Nb. The ground state is of the form

$$(\pi p_{1/2})^2_{0^+}\ (\pi g_{9/2})^2_{0^+}\ (\pi g_{9/2}) + (\pi g_{9/2})^4_{0^+}\ (\pi g_{9/2})$$

There is a very low-lying $(\pi g_{9/2})^3_{7/2^+}$ state calculated to be at 0.69 MeV,[8] which probably corresponds to the 0.68 MeV level seen in the ^{92}Mo(α,t) data. This state has about 1% of the ground state intensity in (α,t). The weak mixing with the $\pi g_{7/2}$ single particle state is not surprising. The single particle energy for $\pi g_{7/2}$ is quite high (about 5 MeV) in ^{91}Nb, and is probably similar in ^{93}Tc. It is unlikely that levels so far apart would strongly mix unless the off-diagonal matrix elements connecting them are extremely large. There are calculated[8] $9/2^+$ states at 1.9 and 2.4 MeV. For the upper level, the only candidate in ^{92}Mo(α,t) would be the 2.59 MeV state (possibly a doublet), which appears to be considerably stronger compared with the 3.36 MeV state than indicated by the (^{3}He,d) spectroscopic factors. The (α,t) strength of this state amounts to about 2% that of the ground state. A candidate for the lower $9/2^+$ level is less obvious. The 2.14 MeV state is relatively strong in (α,t) but was assigned $\ell = 3$ by Kozub and Youngblood.[5] The only low-lying (α,t) level unreported in (^{3}He,d) was that at 1.42 MeV, which has about 1% of the ground state intensity.

However, this level is rather far away from the calculated $9/2^+$ state (at 1.9 MeV) and may have been unobserved in (^{3}He,d) due to resolution problems rather than structure, since it is only about 90 keV away from the 1.51 MeV state.

The situation for ^{93}Nb is very complicated since there is appreciable mixing between the various states. Near 1 MeV both a $7/2^+$ and $9/2^+$ level are predicted.[7,9] Levels at this energy are populated in both the ^{92}Zr(α,t) and ^{92}Zr(^{3}He,d) reactions.[30,4] The 1.08 MeV state was assigned $\ell = 4$ by Cates, Ball, and Newman[4] and associated with the first calculated $9/2^+$ level. The calculated $9/2^+$ level was predicted[4] to have a spectroscopic factor about 12% that of the ground state, but the 1.08 MeV level has only 5% of the ground state intensity (in both (α,t) and (^{3}He,d)). Conflicting assignments for the 1.08 MeV level were obtained from Coulomb excitation measurements, one group[64] assigning $J^\pi = 9/2^+$, the other[12] $J^\pi = 7/2^+$. The level at 1.29 MeV seen in (α,t) is almost certainly a high-spin level based on its strength (12% that of the ground state). In fact, this ratio would be in better agreement with the predicted strength of the $9/2^+$ level than that from the 1.08 MeV level. The tentative assignments from Coulomb excitation of the 1.29 MeV level are $J^\pi = (7/2^+, 7/2^-, 9/2^-)$[64] and $J^\pi = (9/2^+)$.[12]

In view of the number of high-spin levels expected[7,9] in this region of ^{93}Nb, the strong (α,t) levels cannot be easily associated with unique states. One point seems worth making, however. The 1.29 MeV state in (α,t) is actually stronger than the $\pi g_{7/2}$ state observed at 4.8 MeV in ^{91}Nb (whose spectroscopic factor in (^{3}He,d) is[2] 0.34). Thus, if this

level is not associated with the $9/2^+$ state calculated in Ref. 4, there must be significant mixing with the $\pi g_{7/2}$ state even at a rather low excitation energy in ^{93}Nb. This seems somewhat surprising considering the situation in ^{91}Nb, but, if true, it would mean that wave functions computed by ignoring the $\pi g_{7/2}$ orbital cannot be compared with the experimentally observed states with any degree of confidence.

In ^{95}Nb the predicted $9/2^+$ state comes at 1.15 MeV and has about 1/30 of the ground state spectroscopic factor.[4] The 1.27 MeV state is assigned $\ell = 3,4$ in the ^{94}Zr(^{3}He,d) reaction.[4] The intensity ratio for the 1.27 MeV state seen in (α,t), about 8% of the ground state, is quite a bit larger than expected. The presence of strong $\pi g_{7/2}$ states may be important here too, so no association of the calculated and experimental levels seems possible.

2. Comparison Between α Particle and Heavy Ion Induced Reactions

The 60 MeV (^{16}O,^{15}N) data obtained by Nickles et al.[27] on the Zr isotopes were compared with the (^{3}He,d) data of Cates, Ball, and Newman[4] in order to find the single-particle states in the odd Nb isotopes. The (α,t) data (Sec. IV-A) on the same targets, however, showed many strong levels which were not reported in the (^{3}He,d) reaction. The reason for the difference in the (^{3}He,d) and (α,t) results is related to the different momentum matching in the two reactions, the (^{3}He,d) reaction preferentially populating low angular momentum ($\ell \leqslant 2$) states and the (α,t) reaction preferentially populating high angular momentum ($\ell \geqslant 3$) states. As was shown in Appendix A, the favored momentum transfer for the (^{16}O,^{15}N) reaction, L = 3, suggests that the (^{16}O,^{15}N) data should be compared with (α,t) as well as (^{3}He,d) data, in order to better reproduce the "momentum

matching" features of the heavy ion reaction. Table XXVIII lists the assumed core-excited levels reported by Nickles et al.[27] along with nearby strong states seen in the (α,t) reaction. As can be seen, essentially all of the levels reported in the (^{16}O,^{15}N) reaction also appear as strong (α,t) transitions. The levels at 2.18 and 2.75 MeV in $^{90}Zr(^{16}O,^{15}N)^{91}Nb$ may not have counterparts in the (α,t) data. However, neither of these states was observed in the present $^{90}Zr(^{16}O,^{15}N)$ experiment (see Fig. 41).

It is clear from the heavy ion data obtained in the experiments reported here that the preference for high angular momentum transfer is less pronounced than for the (α,t) reaction. As an example, consider the $^{90}Zr(^{16}O,^{15}N)^{91}Nb$ results. The intensity of the 3.37 MeV ($2d_{5/2}$) state is greater relative to that of the ground state ($1g_{9/2}$) than was true for the $^{90}Zr(\alpha,t)$ reaction. Moreover, the cross section for the 3.37 MeV ($2d_{5/2}$) state (L=3) is much larger compared with that of the 4.81 MeV ($1g_{7/2}$) state (L=3) in the heavy ion than in the light ion data. The apparent explanation for these observations is that heavy ion reactions, because they occur in a region well outside the nucleus, are even more sensitive to the "tail" of the nuclear wave function than are light ion reactions. The magnitude of the nuclear wave function at a give radius, however, depends on both the quantum numbers n and ℓ. For a given radial quantum number, n, the wave function peaks at a larger radius as ℓ increases. On the other hand, increasing the number of radial nodes of a wave function (i.e., increasing n) will also cause it to have a larger amplitude at large radius. Based on data from the $^{208}Pb(^{16}O,^{15}N)$ reaction,[110] it appears that the effect of an extra radial node is approximately the same as the effect of two additional units of transferred angular momentum.

Table XXVIII. Collective Levels Observed in $Zr(^{16}O,^{15}N)Nb$ Compared with the $Zr(\alpha,t)$ Results

	$(^{16}O,^{15}N)$[a]		(α,t)[b]		$(^{16}O,^{15}N)$[a]		(α,t)[b]	
Target	E_2[c] (MeV)	I_2[d]	E (MeV)	I[e]	E_3[f] (MeV)	I_3[d]	E (MeV)	I[e]
^{90}Zr	2.18	0.03	2.30	0.01	2.75	0.06	2.61	0.007
							2.77	0.003
							2.90	0.02
^{92}Zr	0.93	0.05	0.95	0.02	2.34	0.17	2.30, 2.36	0.03
^{94}Zr	0.92	--	0.82	0.04	2.05	0.36	2.10	0.08
			1.00	0.01				

[a]Taken from Ref. 27.

[b]Taken from Sec. IV-A.

[c]Assumed $[Zr(2^+) \otimes \pi g_{9/2}]$ configuration.

(continued)

Table XXVIII (continued)

[d] Ratio of differential cross section (at $\theta_\ell = 60°$) to that of ground state.

[e] Ratio of integrated cross section to that of ground state.

[f] Assumed $[Zr(3^-) \otimes \pi g_{9/2}]$ configuration.

In the case of the $^{90}Zr(^{16}O,^{15}N)^{91}Nb$ reaction, if we divide the observed cross sections for the ground and 3.37 MeV states by the values of $(2J_f + 1)\ C^2S$ from Ref. 2, we obtain reduced cross sections of $\sigma_R(1g_{9/2}) = 0.5$ and $\sigma_R(2d_{5/2}) = 0.7$. The same calculation using the $^{90}Zr(\alpha,t)$ cross sections yields $\sigma_R(1g_{9/2}) = 0.4$ and $\sigma_R(2d_{5/2}) = 0.1$. Thus, in (α,t) we would expect that the $1g_{9/2}$ cross section would be about 4 times larger than that for a $2d_{5/2}$ state with the same spectroscopic factor, while in $(^{16}O,^{15}N)$ the states would be populated about equally. (This argument is not meant to be quantitative, since Q-value effects have been ignored. However, for similar Q-values the estimates above are probably reasonable.) From the heavy ion selection rules, a $1g_{7/2}$ and $2d_{5/2}$ state require the <u>same</u> L transfer, and in this case the $2d_{5/2}$ state (with the extra radial node) is clearly favored. A nice example of this effect can be found in the $^{92}Mo(^{16}O,^{15}O)^{93}Mo$ spectrum (Fig. 51). (The $(^{16}O,^{15}O)$ and $(^{16}O,^{15}N)$ reactions have identical selection rules.) The ground state of ^{93}Mo is $2d_{5/2}$, the states near 1.5 MeV are $1g_{7/2}$, and the 2.32 MeV state is $1h_{11/2}$. Comparison with the $^{92}Mo(\alpha,^3He)$ spectrum (also in Fig. 51) shows that, relative to the $1h_{11/2}$ level, the $2d_{5/2}$ state is stronger in the heavy ion data, while the $1g_{7/2}$ states are considerably weaker compared with both the $2d_{5/2}$ and $1h_{11/2}$ levels.

The $^{94}Zr(^{16}O,^{15}N)^{95}Nb$ data obtained here show population of the same states observed by Nickles <u>et al</u>.[27] In $^{94}Zr(\alpha,t)$, the 0.74 - 0.82 MeV ($\ell = 1$) doublet had about twice the intensity of the 0.25 MeV ($\ell = 1$) state. Based on the results of fitting the ground state peak as a doublet, this ratio is essentially the same in the $^{94}Zr(^{16}O,^{15}N)$ data (see Table XIX).

Similarly, the 1.65 and 2.10 MeV states, which were strong in the (α,t) reaction, are also strong in the $(^{16}O,^{15}N)$ reaction. The 1.27 MeV level in $^{94}Zr(\alpha,t)$, which had about 8% of the ground state intensity, looks weaker in the heavy ion data (assuming it corresponds to the 1.1 MeV level). However, the intensity ratio of the 1.1 MeV state to the ground state, about 5%, does not differ greatly from the light ion ratio. The 2.0 MeV state appears relatively stronger in the heavy ion data, but this would occur even for $d_{5/2}$ states, for example, which would be expected to begin to appear at about this excitation energy. A strong $d_{5/2}$ state, of course, should have been observed in $^{94}Zr(^{3}He,d)$, but only levels up to 1.26 MeV were reported in Ref. 4.

The apparent absence of the 0.68 MeV level in the $^{92}Mo(^{16}O,^{15}N)$ data provides an argument against the importance of a multi-step reaction mechanism for this reaction. If this $7/2^+$ state is populated through a $\pi g_{7/2}$ admixture, its weakness (compared with the $1g_{9/2}$ and $2d_{5/2}$ states) in the $(^{16}O,^{15}N)$ reaction would be expected, based on the arguments given above. On the other hand, if a multi-step mechanism were important, the transition could proceed by a $\pi g_{9/2}$ transfer along with uncoupling the $(g_{9/2})^2_{0^+}$ protons. Fig. 44 indicates that the likelihood of such a process is small. Particularly in ^{93}Nb, there is good experimental evidence[64] that the low-lying states do have appreciable admixtures of the core-excited configuration $\left[^{92}Zr(2+) \otimes \pi g_{9/2}\right]$, but the (α,t) levels at 0.80 MeV $(5/2^+)$ and 0.95 MeV $(9/2^+)$ could account for the $(^{16}O,^{15}N)$ state reported by Nickles <u>et al.</u>[27] at 0.93 MeV.

An estimate of the importance of a multi-step reaction mechanism can also be made in the case of the $^{90}Zr(^{16}O,^{15}O)^{91}Zr$ reaction. From Fig. 48 it is obvious that only two levels are strongly populated - the same two levels which are strongly populated in the $^{90}Zr(\alpha,^{3}He)$ reaction. The locations of core-excited levels in ^{91}Zr have been determined by DuBard and Sheline[121] with the $^{91}Zr(p,p')$ reaction. They find that the 2.16 MeV level is indeed a member of the $\left[^{90}Zr(3^-) \otimes \nu d_{5/2}\right]$ multiplet, as are the states at 2.630 MeV ($1/2^-$), 2.683 MeV ($7/2^-$), 2.800 MeV ($9/2^-$), 2.821 MeV ($5/2^-$), and 3.022 MeV ($3/2^-$). As is evident from Fig. 48, only one member of this core-excited multiplet is populated with reasonable intensity. It seems extremely unlikely that <u>only</u> the $11/2^-$ state (which is known[63,120] to have an appreciable $\nu h_{11/2}$ single-particle amplitude) would be strongly populated in the $(^{16}O,^{15}O)$ reaction if core-excitation were an important part of the reaction mechanism. The $^{92}Mo(^{16}O,^{15}O)$ reaction (Fig. 51) also yields a spectrum very similar to that from the $(\alpha,^{3}He)$ reaction. Although it has not been experimentally verified, it is quite likely that the 2.32 MeV $11/2^-$ state in ^{93}Mo is also partly a $\left[^{92}Mo(3^-) \otimes \nu d_{5/2}\right]$ level. Here too, no other states except the known single-particle states are observed.

From the comparisons made above it must be concluded that, contrary to the suggestion of Nickles <u>et al.</u>,[27,114] there is no strong evidence for the population of states which do not have single-particle strength.

B. Two-nucleon Transfer

1. Q-value Dependence

As mentioned previously, the three criteria used for selecting (α,d) states of the same configuration are: (a) large cross section in (α,d), (b) similar angular distribution, and (c) regular dependence of the Q-value for forming the level, Q_f, on mass number. It has been shown that requirements (a) and (b) are met by the strong (α,d) levels seen in this work. A summary of the Q-values for formation of these levels in (α,d) is given in Table XXIX. Unfortunately, neither of the strong (α,d) groups seen here displays the regular Q_f vs. mass dependence observed previously.[15-17] It is clear that the lack of regularity in Q_f is not due to a failure of the reaction to selectively populate specific shell model configurations, since the 7^+ levels (which correspond to the energies labeled E_1 in Table XXIX) have been identified in all but one case by other reactions.[65,99,102] Since both groups of strong levels show the same Q-value behavior (i.e., the relative energy difference between the two groups remains nearly constant at about 2.4 MeV), it seems reasonable to associate the levels listed as E_2 in Table XXIX with a specific shell model state in spite of the irregular Q_f vs. A dependence.

One possible explanation for the anomalous behavior of the 7^+ levels is that both the $g_{9/2}$ proton and $d_{5/2}$ neutron are entering partially filled shells and thus the wave function is somewhat different in each case. For example, in ^{92}Nb the 7^+ is mainly a "simple" two-particle $(\pi g_{9/2}, \nu d_{5/2})_{7^+}$ state, while in ^{94}Tc the wave function is $\left[(\pi g_{9/2})^3_{9/2}, \nu d_{5/2}\right]_{7^+}$ and in ^{94}Nb it is $\left[\pi g_{9/2}, (\nu d_{5/2})^3_{5/2}\right]_{7^+}$. This was not the case for the

Table XXIX. Q-Values of Strong (α,d) States

Final Nucleus	E_1[a] (MeV)	Q_1[b] (MeV)	E_2 (MeV)	Q_2[b] (MeV)
^{90}Y	0.69[c]	-12.79	3.11[c]	-15.21
^{92}Nb	0.0	-13.03	2.58	-15.61
^{94}Tc	0.0	-13.37	2.68	-16.05
^{94}Nb	0.08	-12.89	2.42	-15.23
^{96}Nb	0.23	-12.60	2.38	-14.75

[a] $(\pi g_{9/2}, \nu d_{5/2})_{7^+}$ states. All levels except the ^{94}Tc ground state have been assigned 7^+ by other groups. See text, Sec. IV-B.

[b] Ground state Q-values taken from Ref. 51 except for ^{96}Nb, which is inferred from Ref. 104.

[c] Obtained from $^{88}Sr(\alpha,d)^{90}Y$ data, M. S. Zisman, E. A. McClatchie, and B. G. Harvey, University of California, Lawrence Radiation Laboratory Report UCRL-19530, p. 100 (1970), (unpublished).

levels observed in previous (α,d) studies[15-17] except for the 5^+ levels in ^{22}Na and ^{26}Al, which are in a deformed mass region. Consistent with this hypothesis is the fact that the Q_f vs. A dependence for the Zr isotopes alone is similar to that observed previously. From evidence presented below it seems likely that the higher group of levels also contains a $\pi g_{9/2}$ configuration, which would account for its behavior being similar to that of the 7^+ levels.

2. Shell Model Calculations

In this mass region there are a number of high-spin proton-neutron states which might be strongly populated in (α,d). One of these configurations, $(\pi g_{9/2},\nu d_{5/2})_{7^+}$, is already known in the nuclei studied here. As expected, this configuration is selectively populated in the (α,d) reaction in all cases. Other possible high-spin states, to which the higher (α,d) group might correspond, are $(\pi g_{9/2},\nu h_{11/2})_{10^-}$, $(\pi g_{9/2},\nu g_{7/2})_{8^+}$, $(d_{5/2})^2_{5^+}$, $(\pi g_{7/2},\nu d_{5/2})_{6^+}$, $(g_{7/2})^2_{7^+}$, and $(\pi g_{7/2},\nu h_{11/2})_{9^-}$.

In order to determine which possibilities are reasonable, simple shell model calculations have been performed using the code PHYLLIS.[124] The method of calculation is outlined by Brody and Moshinsky,[125] and is described in Appendix B. The calculations were done using a Gaussian potential employed by True in calculating the ^{14}N spectrum:[66]

$$V_{TE} = -52 \exp(-0.2922\ r^2)\ \text{(MeV)} \tag{1a}$$

$$V_{SE} = \frac{V_{TE}}{1.6} \tag{1b}$$

$$V_{SO} = V_{TO} = 0 \tag{1c}$$

where V_{TE}, V_{SE}, V_{TO}, V_{SO} refer to the triplet-even, singlet-even, triplet odd and singlet-odd potentials, respectively. The oscillator parameter, b,

was determined by requiring that the calculated residual interaction, V_{RES}, for the $(\pi g_{9/2},\nu d_{5/2})_{7^+}$ state be the same as the empirical value for the ^{92}Nb ground state, -0.679 MeV. This yielded a value of b = 0.156 fm^{-2}. In previous calculations[17] the oscillator parameter was calculated according to the formula

$$b = \frac{2n + \ell + 3/2}{R^2} = \frac{2n + \ell + 3/2}{(r_0 \cdot A^{1/3})^2} \qquad (2)$$

Our value of the oscillator parameter would correspond to a radius parameter r_0 = 1.32 fm.

Matrix elements and excitation energies obtained with this oscillator parameter are given in Table XXX. The single-particle energies required to calculate the excitation energies are taken from single-nucleon transfer data[2,120] and are listed in Table XXXI. Figure 55 illustrates the results of the calculation for the states belonging to the $(\pi g_{9/2},\nu d_{5/2})$ multiplet. The ordering and splitting of these levels are reproduced reasonably well by the calculations. Based on the results in Table XXX, it seems clear that the most likely configurations for the 2.58 MeV level in ^{92}Nb are $(\pi g_{9/2},\nu h_{11/2})_{10^-}$ and $(\pi g_{9/2},\nu g_{7/2})_{8^+}$. (The predicted excitation energies for states containing an $h_{11/2}$ neutron are lower limits because not all of the ℓ = 5 strength was observed in Ref. 120 and the remainder presumably lies at higher excitation energies in ^{91}Zr.) The large single-particle energies for excited proton states make it extremely unlikely that a state with other than a $g_{9/2}$ proton would appear at such a low excitation energy in ^{92}Nb. As can be seen from Table XXX, the calculated interaction energies are quite similar for all of the high-spin configurations considered here.

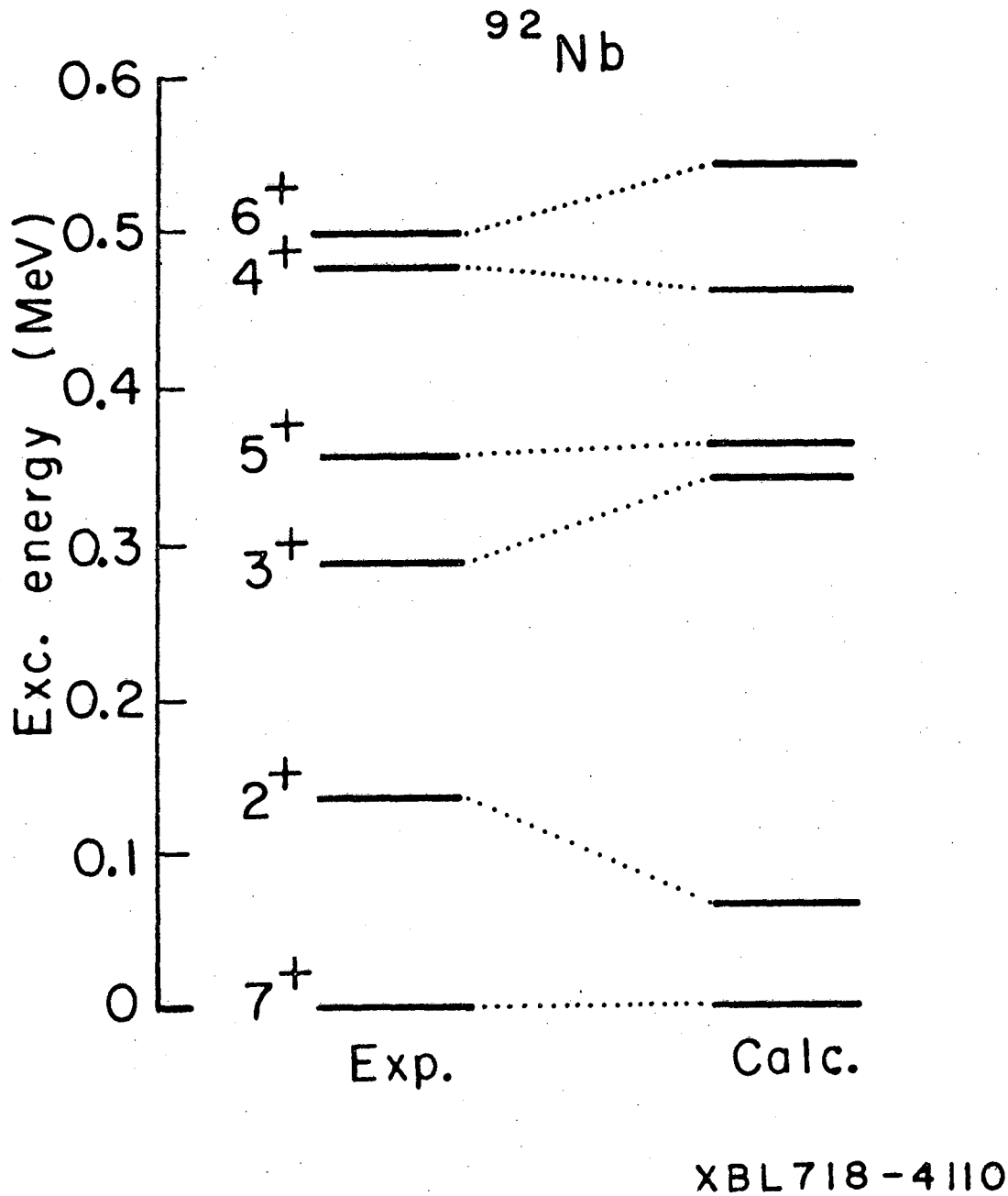

Fig. 55. Comparison between the calculated and experimental spectra for the $[\pi g_{9/2}, \nu d_{5/2}]$ multiplet in ^{92}Nb.

Table XXX. Summary of Shell Model Calculations for the Two-Particle States in ^{92}Nb.

Configuration	J^{π}	V_{RES}[a] (MeV)	E_x[b] (MeV)
$(\pi g_{9/2}, \nu d_{5/2})$	7^+	-0.678	0.0
$(\pi g_{9/2}, \nu h_{11/2})$	10^-	-1.263	> 2.10
		(-1.472)[c]	(> 1.89)[c]
$(\pi g_{9/2}, \nu g_{7/2})$	8^+	-1.098	2.35
$(d_{5/2})^2$	5^+	-1.129	3.75
$(\pi g_{7/2}, \nu d_{5/2})$	6^+	-0.543	5.66
$(g_{7/2})^2$	7^+	-1.268	7.70
$(\pi g_{7/2}, \nu h_{11/2})$	9^-	-0.975	> 7.90
		(-1.136)[c]	(> 7.74)[c]

[a]Calculated with a single oscillator parameter b = 0.156 fm^{-2} except as noted.

[b]Based on single-particle energies summarized in Table XXXI.

[c]Calculated with oscillator parameters 0.156 and 0.184 fm^{-2} for the proton and neutron, respectively.

Table XXXI. Single-Particle Energies for A = 91.

	^{91}Nb[a] (MeV)	^{91}Zr[b] (MeV)
$g_{9/2}$	0.0	---
$d_{5/2}$	4.20	0.04
$s_{1/2}$	5.27	1.66
$d_{3/2}$	6.43	2.76
$g_{7/2}$	5.52	2.77
$h_{11/2}$	---	> 2.68

[a]Taken from Ref. 2.

[b]Taken from Ref. 120.

Thus, the predicted excitation energies depend strongly on the single-particle energies but are not particularly sensitive to the choice of oscillator parameters.

One problem in doing these calculations arises because the $h_{11/2}$ level is in a different oscillator shell than the other levels. From eq. (2) above this should correspond to a different oscillator parameter. To see what effect this has on predicted interaction energies, a modified calculation (see Appendix B) with different oscillator parameters for the two particles was performed using the code NAOMI.[124] The generalized transformation brackets can be expanded in terms of products of standard Moshinsky brackets[125] using a formula derived by Gal.[126] The Talmi integrals must also be modified slightly because the transformation to relative coordinates requires a "redefined" oscillator parameter

$$b' = \frac{b_1 b_2}{b_1 + b_2} \quad , \tag{3}$$

where b_1 and b_2 are the oscillator parameters for particles 1 and 2. The oscillator parameter for the $h_{11/2}$ neutron was obtained by assuming the shell dependence indicated in eq. (2):

$$b_2 = \frac{2n_2 + \ell_2 + 3/2}{2n_1 + \ell_1 + 3/2} \times b_1$$

$$= \frac{6.5}{5.5} \times 0.156$$

$$= 0.184 \text{ fm}^{-2}$$

The results of this calculation are included in Table XXX. The larger $h_{11/2}$ oscillator parameter has the effect of increasing the residual interaction matrix elements by about 15%. The predicted excitation energies are, therefore, decreased by about 200 keV.

3. (α,d) Structure Factors

Shell model calculations (Sec. V-B2) suggest that the best candidates for the higher level observed in the (α,d) data are $(\pi g_{9/2},\nu h_{11/2})_{10^-}$ and $(\pi g_{9/2},\nu g_{7/2})_{8^+}$. Such high-spin states are kinematically favored in (α,d), because the momentum matching (see Appendix A) for the reaction is best for large L transfers. [The semi-classical angular momentum transfer is $\vec{q} \times \vec{R} \approx 8$.] The structure of these high-spin states is also favorable for the (α,d) reaction, since they contain relatively large amounts of the [target core + deuteron] configuration required for strong population in (α,d). Structure factors for these levels have been tabulated by Glendenning[92] and are listed in Table XXXII. The probability of finding the favored ^3S correlation for the transferred pair (with center of mass angular momentum L) is given by

$$P_L = \sum_N G^2_{NL} \qquad (4)$$

This probability, weighted by 2J + 1, is also given in Table XXXII. Since no kinematic effects are included in this probability, the ratios in Table XXXII cannot be interpreted as relative cross sections even if the wave functions are adequately described by these simple configurations. However, the relative probabilities do serve to indicate, for example, that the $(\pi g_{9/2},\nu g_{7/2})_{8^+}$ would probably be weaker than the $(\pi g_{9/2},\nu h_{11/2})_{10^-}$ (assuming the L = 8 and L = 9 kinematics are similar) and that either of these states would be comparable in strength to the $(\pi g_{9/2},\nu d_{5/2})_{7^+}$ level.

Table XXXII. Structure Factors for (α,d) States.

Configuration	G_{NL} [a]	P_L [b]	$(2J + 1)P_L$ [c]
$(\pi g_{9/2}, \nu d_{5/2})_{7^+}$	$G_{16} = -0.0221$, $G_{26} = 0.3140$	0.099	1.0
$(\pi g_{9/2}, \nu h_{11/2})_{10^-}$	$G_{19} = 0.4396$	0.193	2.7
$(\pi g_{9/2}, \nu g_{7/2})_{8^+}$	$G_{18} = 0.3277$	0.107	1.2
$(\pi d_{5/2}, \nu d_{5/2})_{5^+}$	$G_{14} = 0.0447$, $G_{24} = 0.0351$, $G_{34} = 0.3278$	0.111	0.8

[a] Taken from Ref. 92.

[b] $P_L = \sum_N G_{NL}^2$. P_L represents the probability of finding the appropriate ^3S correlations in the wave function.

[c] Relative to the $(\pi g_{9/2}, \nu d_{5/2})_{7^+}$ state. This ratio does not include any kinematic effects, which are also important in determining which states will be strongly populated.

4. Other Evidence

The (α,d) structure factors (Sec. V-B3) indicate that the $(\pi g_{9/2},\nu h_{11/2})_{10^-}$ state should be stronger than the $(\pi g_{9/2},\nu g_{7/2})_{8^+}$ state. The shell model calculations (Sec. V-B2) predict these states to be close together in ^{92}Nb, because the residual interaction matrix elements are similar for the two configurations and the $\nu g_{7/2}$ and $\nu h_{11/2}$ single-particle energies in ^{91}Zr (see Table XXXI) are almost identical. In ^{93}Mo the situation may be different. The ^{92}Mo(d,p)^{93}Mo reaction[62] indicates single-particle energies for the $\nu g_{7/2}$ and $\nu h_{11/2}$ configurations of 1.6 and 2.3 MeV, respectively. This would argue for a 10^- assignment for the ^{94}Tc 2.68 MeV level, since the observed $\nu g_{7/2}$ centroid (1.6 MeV) corresponds to a repulsive residual interaction if the 2.68 MeV level is associated with the $(\pi g_{9/2},\nu g_{7/2})_{8^+}$ configuration. Unfortunately, large fractions of both the $\nu g_{7/2}$ and $\nu h_{11/2}$ spectroscopic strengths have not been observed, so it is not yet possible to reach any firm conclusions.

One consequence of the assumed configurations for the strong (α,d) state is that the level should be observable in a reaction where a neutron is transferred to ^{93}Nb, i.e., ^{93}Nb(d,p), ^{93}Nb(α,^{3}He), or ^{93}Nb(^{16}O,^{15}O), since the ^{93}Nb ground state is a $\pi g_{9/2}$ level. As mentioned previously, the ^{93}Nb(d,p)^{94}Nb reaction[62,101] did not locate any $\nu h_{11/2}$ transfers. No ^{93}Nb(α,^{3}He) data were obtained in these experiments and the reaction has not been reported in the literature. However, from the results obtained here with the (^{16}O,^{15}O) reaction (Sec. IV-C), this may be the best of the three reactions for looking

at $\nu h_{11/2}$ transfers, since these are significantly stronger than $\nu g_{7/2}$ transfers (see Sec. V-A2). In spite of the calibration problem, the ^{93}Nb(^{16}O,^{15}O)^{94}Nb data (Sec. IV-C9 and Fig. 52) indicate clearly that the ($\pi g_{9/2}$,$\nu h_{11/2}$) levels are located near the energy of the strong ^{92}Zr(α,d)^{94}Nb state (2.42 MeV). This does not prove that ($\pi g_{9/2}$,$\nu g_{7/2}$) states are not also located in this region, but three $\nu g_{7/2}$ states were reported[62] in ^{93}Nb(d,p) below 2 MeV, none of which correspond to strong (α,d) transitions. In any case the ^{93}Nb(^{16}O,^{15}O)^{94}Nb data do demonstrate experimentally that at least one of the configurations suggested here for the strong (α,d) state appears plausible.

VI. CONCLUSIONS

A. (α,t) Reactions

A search for high-spin proton levels in ^{91,92,93,95}Nb and ^{93}Tc has been made with the (α,t) reaction. Based on relative strengths compared with (^{3}He,d) data, the following levels are believed to be populated with $\ell > 2$ transitions: ^{91}Nb [2.39, 2.53, 2.61, 2.77, 2.90, 3.01, 4.18, 4.77, 4.89, and (5.14) MeV], ^{93}Tc [0.68, (3.58), 3.91, 4.37, (4.47), (4.67), 4.77, 4.90, 6.01 (multiplet), 6.17 and 6.44 MeV], ^{92}Nb [≈ 5 MeV multiplet], ^{93}Nb [1.08, 1.29, and ≈ 4.5 MeV], and ^{95}Nb [1.27, 1.65, (2.10), and ≈ 4.5 MeV]. The states near 5 MeV in these nuclei are in a region where $\ell = 5$ proton strength has been tentatively identified in the ^{92}Mo(^{3}He,d)^{93}Tc reaction.[5] The 4.18 MeV level in ^{91}Nb and the 3.91 MeV level in ^{93}Tc have been assigned $\ell = 2$ in (^{3}He,d),[4,1] but both states are populated too strongly in (α,t) to be consistent with the measured spectroscopic factors. In the case of the ^{91}Nb 4.18 MeV level, additional evidence for a high-spin assignment is obtained from the fact that it is fed by the β decay of ^{91}Mo($9/2^+$).[10] Comparison with published shell-model calculations[7-9] suggests that the ^{91}Nb 2.63 and 2.77 MeV states, the ^{93}Tc 0.68 MeV state, the ^{93}Nb 1.08 or 1.29 MeV states, and the ^{95}Nb 1.27 MeV state may be populated through small admixtures of $\pi g_{9/2}$ and $\pi g_{7/2}$ single-particle strength in the calculated $(\pi g_{9/2})^n_{9/2^+}$ and $(\pi g_{9/2})^n_{7/2^+}$ levels. The $(2J_f + 1)$ dependence of the $(\pi g_{9/2}, \nu d_{5/2})$ multiplet in ^{92}Nb was investigated with the ^{91}Zr(α,t) reaction. The results are in good agreement with recent spin determinations for these states.[65] Finally, a new Q-value for the ^{90}Zr(α,t)^{91}Nb reaction,

-14.643 ± 0.027 MeV, was determined from this work. This value corresponds to a change in the ^{91}Nb mass excess of +98 keV, and is consistent with several other recent determinations of the ^{91}Nb mass.[53,54,56]

B. (α,d) Reactions

The $^{14}N(\alpha,d)^{16}O$ reaction has been investigated with improved resolution. The excitation energies and widths for the previously observed[15] triplet whose proposed configuration is $\left[^{14}N(1^+) + (d_{5/2})^2_{5^+}\right] 4^+, 5^+, 6^+$ are: 14.40 ± 0.03 MeV ($\Gamma_{c.m.}$ = 30 ± 30 keV), 14.82 ± 0.03 MeV ($\Gamma_{c.m.}$ = 69 ± 30 keV), and 16.24 ± 0.04 MeV ($\Gamma_{c.m.}$ = 125 ± 50 keV). From other evidence, the 14.82 MeV state has been assigned[82,83] $J^\pi = 6^+$, and the 14.40 MeV state has been shown[84] to have unnatural parity. A comparison of this work and the $^{12}C(^6Li,d)$ measurements of Bassani et al.[76] indicates that the 16.24 MeV state seen here is different from the 4p-4h 6^+ state near this energy. Two excited states, at 15.80 ± 0.04 and 17.17 ± 0.04 MeV can be assigned T=0 by this work. Compared with the population of the known 1p-1h and 2p-2h states, the 4p-4h states in ^{16}O are populated extremely weakly in the $^{14}N(\alpha,d)^{16}O$ reaction.

It has been demonstrated that the tendency of the (α,d) reaction to selectively populate high-spin states continues in the Zr-Mo region. The $(\pi g_{9/2},\nu d_{5/2})_{7^+}$ transfer is strong in all of the Nb isotopes studied here. The ground state of ^{94}Tc has been shown to be a 7^+ by this work, based on its strength and angular distribution, and the ^{94}Tc 0.21 MeV level is a probable 5^+ state. Levels of the $\left[\pi g_{9/2},(\nu d_{5/2})^2\right]$ configuration have been observed in ^{93}Nb. In particular, the $17/2^+$ assignment[12] for the 1.337 MeV level is in agreement with these results and a candidate for the $15/2^+$ level has been observed at 1.48 MeV in ^{93}Nb. A second strong (α,d) state was observed in all the nuclei studied here at about 2.4 MeV higher excitation energy than the 7^+ level. (See table XXIX for

a summary of the preferentially populated (α,d) states.) Simple shell model calculations suggest that $(\pi g_{9/2},\nu g_{7/2})_{8^+}$ and $(\pi g_{9/2},\nu h_{11/2})_{10^-}$ are the most likely high-spin configurations expected in this energy region. The structure factors for $(\alpha,d)^{92}$ indicate that either of these levels would be strong in the (α,d) reaction. The $^{93}Nb(^{16}O,^{15}O)^{94}Nb$ reaction has given experimental evidence for the existence of $(\pi g_{9/2},\nu h_{11/2})$ levels near the energy of the strong state in the $^{92}Zr(\alpha,d)^{94}Nb$ reaction (2.42 MeV). This fact, as well as the apparently low value for the $\nu g_{7/2}$ centroid in ^{93}Mo, make the $(\pi g_{9/2},\nu h_{11/2})_{10^-}$ assignment appear more probable at present, although a $(\pi g_{9/2},\nu g_{7/2})_{8^+}$ assignment cannot be conclusively eliminated.

C. Heavy Ion Reactions

The heavy ion data obtained here provide a good example of the resolution and particle-identification capabilities offered by a magnetic spectrometer and position-sensitive focal plane detector.[47] The present $Zr(^{16}O,^{15}N)$ results, when compared with the 60 MeV results of Nickles *et al.*,[27] generally show population of the same states. The cross sections measured at 104 MeV, however, are much larger than those reported at 60 MeV. As expected, the $(^{16}O,^{15}N)$ reaction shows a preference for high angular momentum transfers similar to (but not as pronounced as) that shown by the (α,t) reaction. There also appears to be a preference for populating levels with high radial quantum numbers which is roughly as important as the preference for high angular momentum transfer.

The $(^{16}O,^{15}O)$ reaction was also observed on the targets studied here. Although the Q-values for this reaction are supposed to be very unfavorable,[108,109] measurable cross sections (about 3 mb/sr) were observed in all cases. The data from the $^{90}Zr(^{16}O,^{15}O)$ and $^{92}Mo(^{16}O,^{15}O)$ reactions are very similar to those from the $(\alpha,^{3}He)$ reaction on the same targets. The $(^{16}O,^{15}O)$ reaction, at least in this mass region, appears to be an excellent way of observing $\nu h_{11/2}$ levels. The $\nu h_{11/2}$ levels are about 5 to 10 times stronger than $\nu g_{7/2}$ levels in the $(^{16}O,^{15}O)$ reaction, while in the $(\alpha,^{3}He)$ reaction the $\nu h_{11/2}$ and $\nu g_{7/2}$ transitions have nearly comparable intensities.

The $(^{16}O,^{17}O)$ reaction on ^{91}Zr and ^{94}Zr, (and possibly on ^{92}Zr and ^{96}Zr, which are present as isotopic impurities in the targets used here) has also been observed. Only the ground state transition was seen in all cases.

Outgoing $^{17}O^*$ (0.87 MeV) particles were identified in the $^{91}Zr(^{16}O,^{17}O)$ data, with an intensity about 22% that of the ^{17}O ground state. The cross sections for this reaction are quite large, more than 20 mb/sr in the case of $^{94}Zr(^{16}O,^{17}O)$. Some evidence for the existence of excited outgoing particles was also obtained in the $(^{16}O,^{15}N)$ and $(^{16}O,^{16}O')$ reactions. In these cases the peaks were very broad, as would be expected for particles which γ decay in flight. However, there was no indication of excited outgoing particles in the $(^{16}O,^{15}O)$ data.

Notably absent in the present data are the proposed core-excited states in ^{91}Nb at 2.18 and 2.75 MeV reported by Nickles et al.[27] Similarly, the 0.68 MeV $(g_{9/2})^3_{7/2^+}$ state in ^{93}Tc was unobserved in the $^{92}Mo(^{16}O,^{15}N)$ data. In the $(^{16}O,^{15}O)$ data on ^{90}Zr and ^{92}Mo, only the $11/2^-$ member of the core-excited multiplet was populated. These $11/2^-$ states have been seen in both (d,p) and $(\alpha,^3He)$ and have significant $\nu h_{11/2}$ single-particle strength.[120,62] Insofar as the other possible core-excited states seen by Nickles et al.[27] all appear as strong (α,t) transitions, it is concluded here that there is no strong evidence for the multi-step mechanism implied by the 60 MeV results.

ACKNOWLEDGMENTS

I wish to express my appreciation to:

My research director, Dr. Bernard G. Harvey, for his assistance and advice during the course of this project and, perhaps more important, for providing a continuing example of the enjoyment of nuclear chemistry research;

Dr. David L. Hendrie and Prof. Joseph Cerny for their interest and encouragement during my work as a graduate student;

Dr. Edward McClatchie, Dr. Andrew Bacher, Dr. John Meriwether, Dr. Chi Chang Lu, Dr. Joel Moss, and Dr. Charles Glashausser for their help in teaching a new graduate student how to do experiments;

Dr. Dennis Kovar for advice and assistance in using the new magnetic spectrometer and for assistance with the heavy ion experiments, Dr. Fredrick Becchetti for assistance with the heavy ion experiments and for numerous discussions of heavy ion theory, and Dr. Falk Pühlhofer for his help with the heavy ion experiments;

My fellow graduate students, Dr. Nolan Mangelson, Dr. Mary Reed, Dr. Donald Fleming, Dr. Gilbert Butler, Dr. Gordon Ball, Dr. Heinz Brunnader, Dr. George Goth, Dr. John Esterl, Mr. Gordon Wozniak, Mr. Richard Sextro, Mr. John Macdonald, Mr. Kenneth Wilcox, and Mr. Robert Weisenmiller, for help with experiments, numerous discussions, and for generally making Building 88 a pleasant place in which to work;

Mr. Joseph Sherman, who provided the major part of the assistance on almost all of the experiments reported here;

Dr. Creve Maples, who provided numerous computer programs which helped to make the data analysis faster and easier;

Miss Jeannette Mahoney for her part in fabricating the heavy ion focal plane detector and for writing and modifying many of the data taking and data analysis programs used here - often on very short notice;

Mr. Don Landis and Dr. Frederick Goulding for designing the electronics used in this work;

Mr. Robert Lothrop, Mr. Jack Walton, and Dr. Richard Pehl for fabrication of the excellent solid state detectors used in these experiments;

Mr. Claude Ellsworth for providing the targets;

Mr. Roy Burton and Mr. Tom Chan for designing much of the equipment used in this work;

The numerous support groups at the 88-inch cyclotron, particularly Mr. John Bowen and the cyclotron crew, and Mr. Frank Hart and Mr. Wayne Olthoff and the Accelerator Technicians;

My parents and the Wollins family for their encouragement and confidence in my ability to complete this work;

My wife, Phyllis, for an excellent job of typing the rough draft of this thesis, for her support during the difficult times in a graduate student's life, and, most of all, for sharing her optimism in the future.

Work done under the auspices of the U.S. Atomic Energy Commission.

APPENDIX A

CALCULATION OF THE FAVORED MOMENTUM TRANSFER

1. "Plane Wave" Picture

In the plane wave theory of nuclear reactions,[127] the Coulomb interaction is ignored. If, in addition, the reaction is pictured as being localized near the nuclear surface, i.e., being a grazing collision between the projectile and target nucleus, it is possible to estimate the favored momentum transfer semi-classically. The appropriate vector diagram is shown in Fig. 56. The momentum transfer to the core in a stripping reaction is

$$\vec{q} = \vec{k}_i - \frac{M_{tgt}}{M_{final}} \vec{k}_o \qquad \text{(A-1a)}$$

$$= \vec{k}_i - \vec{K} \qquad \text{(A-1b)}$$

where k_i and k_0 are the incoming and outgoing momenta. As a function of scattering angle this can be written (see Fig. 56(b))

$$|\vec{q}| = \left[k_i^{\,2} + K^2 - 2k_i K \cos\theta\right]^{1/2} \qquad \text{(A-2)}$$

The transferred angular momentum is then

$$L = |\vec{q} \times \vec{R}| = |\vec{q}| \cdot |\vec{R}| \sin\gamma \qquad \text{(A-3)}$$

If we additionally assume a tangential collision ($k_i \perp R$), we can obtain from the geometry that

$$L = |\vec{q}| \cdot |\vec{R}| \cdot \left[1 - \frac{K^2}{q^2} \sin^2\theta\right]^{1/2} \qquad \text{(A-4)}$$

The value for "$\vec{q} \times \vec{R}$" normally quoted[29,30] is at 0° and, from eq. (A-3), corresponds to

$$L = |\vec{q}| \cdot |\vec{R}| \qquad \text{(A-5)}$$

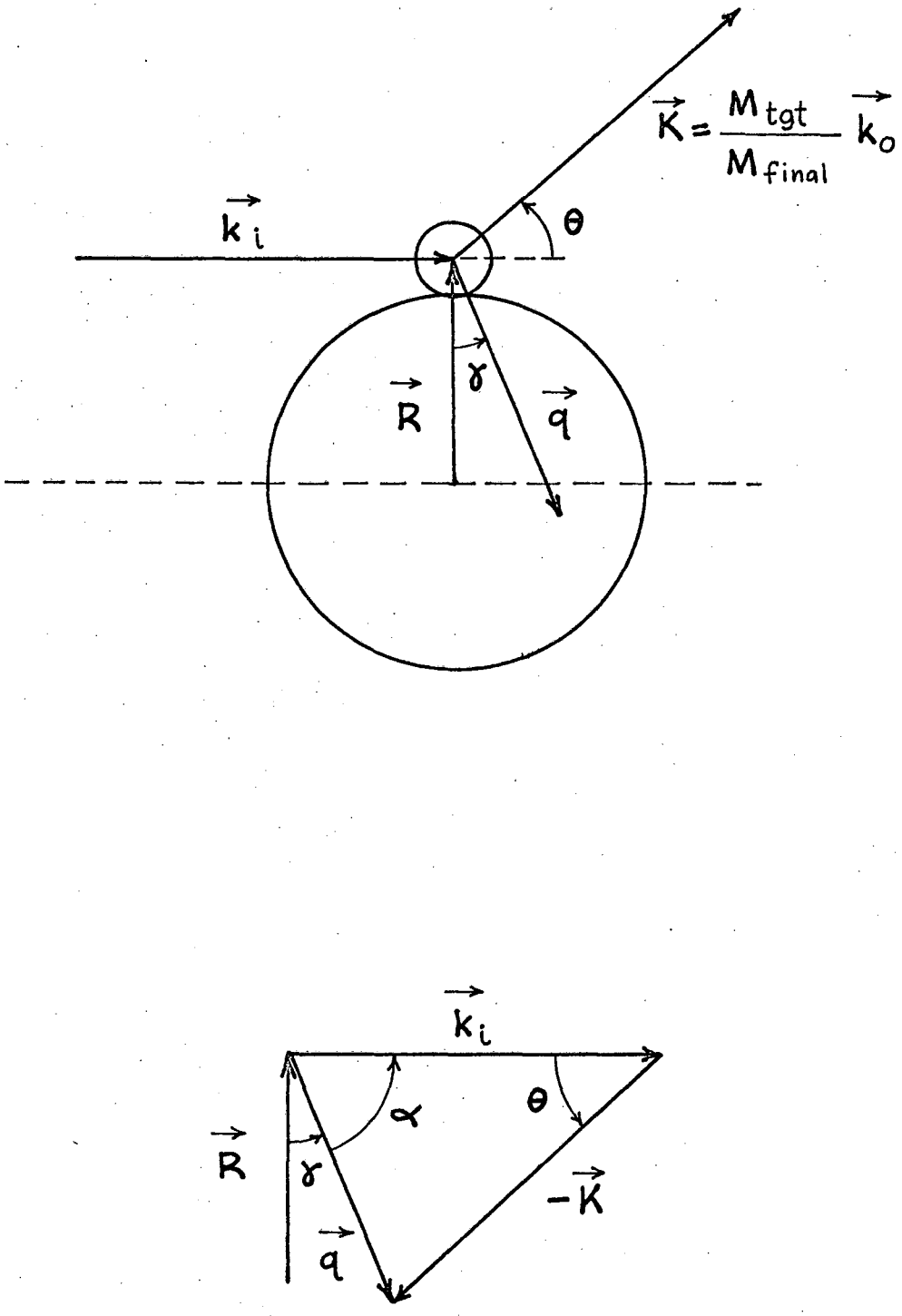

XBL 726-1078

Fig. 56. (a) Momentum vector diagram illustrating the angular momentum transfer in the plane wave picture of a nuclear reaction. (b) Momentum vector triangle corresponding to the reaction shown in (a).

where R is generally parameterized as

$$R = 1.3\ [A_1^{1/3} + A_2^{1/3}]\ \text{fm} \tag{A-6}$$

For numerical calculations the following (non-relativistic) expressions are employed:

$$E_{c.m.} = \frac{M_{tgt}}{M_{tgt} + M_i} \cdot E_{lab} \tag{A-7a}$$

$$\mu_i = \frac{M_{tgt}}{M_{tgt} + M_i} \cdot M_i \tag{A-7b}$$

$$k_i = \frac{[2 \cdot \mu_i \cdot E_{c.m.}]^{1/2}}{\hbar} \tag{A-7c}$$

$$\mu_o = \frac{M_{final}}{M_{final} + M_o} \cdot M_o \tag{A-7d}$$

and

$$k_o = \frac{[2 \cdot \mu_o \cdot (E_{c.m.} + Q)]^{1/2}}{\hbar} \tag{A-7e}$$

where Q is the reaction Q-value.

For the $^{90}Zr(^3He,d)^{91}Nb(g.s.)$ reaction at 31 MeV,[4] we obtain (at 0°) $L \approx 2$, while for the $^{90}Zr(\alpha,t)^{91}Nb(g.s.)$ reaction reported here, $L \approx 6$. The large difference between the two results can be traced to the very negative Q-value which characterizes the (α,t) reaction on essentially all targets. For the two reactions considered here, the decrease in μ_o relative to μ_i is very similar, but the $(^3He,d)$ reaction generally has a Q-value of approximately zero, compared with an average (α,t) Q-value of -13 MeV. The negative Q-value for (α,t) causes k_o to be much smaller than

k_i and therefore a large momentum transfer is required even at 0°. A comparison of eqs. (A-7c) and (A-7e) clearly shows that, for stripping reactions ($\mu_o < \mu_i$), a large <u>negative</u> Q-value increases the favored momentum transfer while, for pick-up reactions ($\mu_o > \mu_i$), a large <u>positive</u> Q-value makes L larger. For this reason a large momentum transfer is characteristic of most reactions involving an incoming or outgoing α particle, e.g., (α,t), (α,d), (α,^{3}He), (^{3}He,α), etc.

2. <u>Coulomb Effects</u>

If the Coulomb potential is included in the description of the reaction, it is necessary to consider hyperbolic orbits. The formalism of Sec. 1 overestimates the preferred angular momentum transfer. The effect is clearly seen for heavy ion reactions. For example, at 104 MeV the value of $\vec{q} \times \vec{R}$ for the $^{90}Zr(^{16}O,^{15}N)^{91}Nb$ (g.s.) reaction at 0° is about 7, and it increases to 17 at 25°. This would suggest an extreme momentum mismatch for all nuclear states and presumably, therefore, very low transfer cross sections. This is in contradiction with the sizable cross sections for heavy ion induced transfer reactions which are actually observed (see, e.g., Ref. 27).

The description chosen here is to assume that the transfer occurs at the classical "distance of closest approach" of the hyperbolic orbits of both the incoming and outgoing particles. From Rutherford scattering theory we have

$$D = \frac{Z_1 Z_2 \, e^2}{2E_{c.m.}} \cdot (1 + \csc \theta/2) \qquad \text{(A-8)}$$

where $E_{c.m.}$ is the incident particle energy and θ is the center of mass scattering angle. It has been found empirically, however, that if D is parameterized by

$$D = d_o \cdot (A_1^{1/3} + A_2^{1/3}) \qquad \text{(A-9)}$$

the maximum of the heavy ion induced transfer reaction cross section corresponds quite generally to a radius parameter $d_o = 1.65$ fm.[108] In what follows we will use this value of d_o and eq. (A-9) in predicting the favored angular momentum transfer at the maximum in the angular distribution. Figure 57 shows the trajectories assumed in the model. Note that the actual scattering angle observed in the reaction does not correspond to either of the scattering angles which would be obtained from eq. (A-8) for a single Coulomb orbit.

To obtain the momentum transfer we replace eqs. (A-7c) and (A-7e) by their "local" values at the distance of closest approach:

$$k_i' = \frac{[2 \cdot \mu_i \cdot (E_{c.m.} - V_c)]^{1/2}}{\hbar} \qquad \text{(A-10a)}$$

and

$$k_o' = \frac{[2 \cdot \mu_o \cdot (E_{c.m.} + Q - V_c')]^{1/2}}{\hbar} \qquad \text{(A-10b)}$$

where V_c and V_c' are the heights of the initial and final Coulomb barriers, respectively. The favored angular momentum transfer is then

$$\Delta L = L_i - L_o = k_i' D - k_o' D \qquad \text{(A-11)}$$

A summary of the results of calculations using this equation for the $^{90}Zr \longrightarrow {}^{91}Nb(g.s.)$ transition with $(^{16}O,{}^{15}N)$, (α,t), and $(^{3}He,d)$ is given in Table XXXIII. The results are in qualitative agreement with the

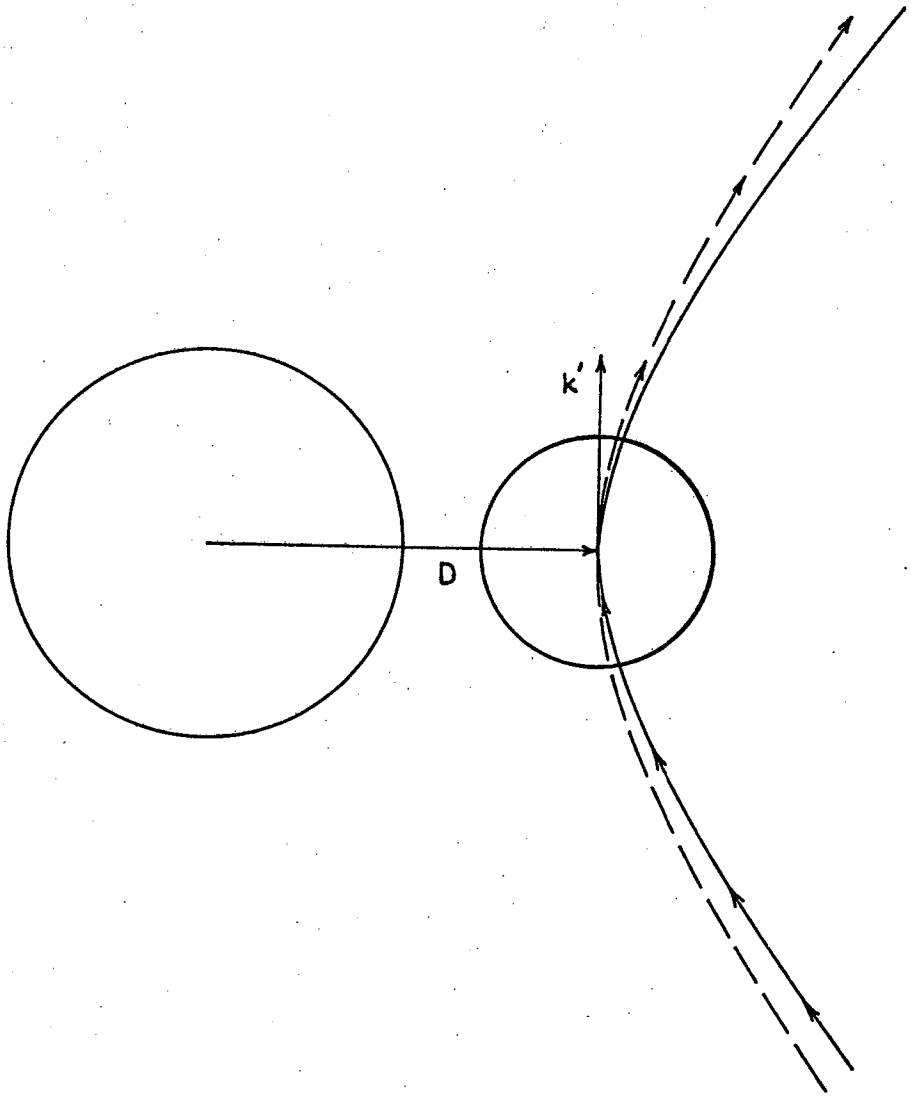

XBL 726-1077

Fig. 57. Trajectories for a nuclear reaction in the presence of the Coulomb force. The reaction is assumed to occur at the distance of closest approach, D, of both the incoming (solid curve) and outgoing (dashed curve) Coulomb orbits. The actual path of the particles is indicated by the arrows. Note that in this picture the observed scattering angle does not correspond to the scattering angles associated with the individual Coulomb orbits.

Table XXXIII. Calculation of the Favored L-Transfer for the $^{90}Zr \longrightarrow {}^{91}Nb(g.s.)$ Transition Using Coulomb Trajectories.

Reaction	E_{lab} (MeV)	$E_{c.m.}$ (MeV)	D^a (fm)	V_c (MeV)	V'_c (MeV)	Q (MeV)	k'_i (fm^{-1})	k'_f (fm^{-1})	L_i	L_f	ΔL
$(^{16}O,^{15}N)$	104	88.3	11.6	39	34	-6.96	5.7	5.4	66	63	3
"	60	50.9	"	"	"	"	2.8	2.5	32	29	3
(α,t)	50	47.9	7.9	16	8	-14.64	2.4	1.9	19	15	4
$(^3He,d)$	31	30.0	7.7	"	"	-0.32	1.4	1.4	11	11	0

[a] $D = d_o\,(A_1^{1/3} + A_2^{1/3})$. For heavy ions $d_o = 1.65$ fm, for light ions $d_o = 1.3$ fm.

observed preference of the reactions to populate high-spin states. If we use the relative population of the ground state ($g_{9/2}$) and 3.37 MeV state ($d_{5/2}$) as a measure of this preference, we obtain values of 1/2, 4/1, and 15/1 for the (^{3}He,d), (^{16}O,^{15}N), and (α,t) reactions, respectively, while the corresponding favored momentum transfers are 0, 3, and 4.

3. Recoil Effects

For the heavy ion induced transfer reaction

$$(C_1 + t) + C_2 \longrightarrow (C_2 + t) + C_1 \quad ,$$

where C_1 and C_2 refer to the heavy "cores" and t is the transferred particle, the DWBA transition amplitude can be written[106]

$$t_{fi} = \int dr\, dr_1\, \chi_f^{(-)*}(\vec{k}_f,\vec{r}_f)\, \psi^*_{\ell_2\lambda_2}(\vec{r}_2)$$

$$\times\, V_{C_1 t}(\vec{r}_1)\, \psi_{\ell_1\lambda_1}(\vec{r}_1)\, \chi_i^{(+)}(\vec{k}_i,\vec{r}_i) \qquad \text{(A-12)}$$

Referring to Fig. 58, the relationships between the various vectors in eq. (A-12) are:

$$\vec{r}_2 = \vec{r}_1 - \vec{r} \qquad \text{(A-13a)}$$

$$\vec{r}_1 = \vec{r} - \frac{M_t}{M_{C_1} + M_t}\, \vec{r}_1 \qquad \text{(A-13b)}$$

and

$$\vec{r}_f = \vec{r} + \frac{M_t}{M_{C_2} + M_t}\, \vec{r}_2$$

$$= \frac{M_{C_2}}{M_{C_2} + M_t}\, \vec{r} + \frac{M_t}{M_{C_2} + M_t}\, \vec{r}_1 \qquad \text{(A-13c)}$$

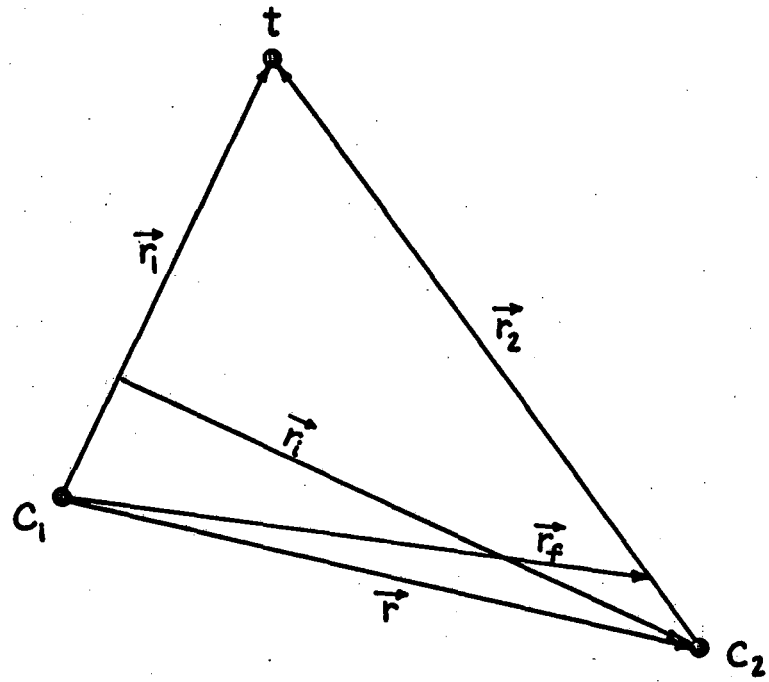

$$\vec{r}_2 = \vec{r}_1 - \vec{r}$$

$$\vec{r}_i = \vec{r} - \frac{M_t}{M_{c_1}+M_t}\vec{r}_1$$

$$\vec{r}_f = \vec{r} + \frac{M_t}{M_{c_2}+M_t}\vec{r}_2$$

$$= \frac{M_{c_2}}{M_{c_2}+M_t}\vec{r} + \frac{M_t}{M_{c_2}+M_t}\vec{r}_1$$

XBL 727-1288

Fig. 58. Diagram of the coordinate system for heavy ion induced transfer reactions. The relationships between the various vectors are indicated below the diagram.

where M_{C_1}, M_{C_2}, and M_t are the masses of the various nuclei.

Equation (A-12) is a six-dimensional integral which, since it is very difficult to perform, is seldom attempted. Instead the "no recoil" approximation, which corresponds to ignoring the terms $(M_t/M_{C_1} + M_t)$ and $(M_t/M_{C_2} + M_t)$ in eqs. (A-13b) and (A-13c), is made. In this approximation the distorted waves χ_i and χ_f depend only on $\vec{r}$. By expanding $\psi^*_{\ell_2\lambda_2}(\vec{r}_2)$ in terms of $\vec{r}$ and $\vec{r}_1$ (see eq. (A-13a)) the resulting expression for the transition amplitude can be reduced to two 3-dimensional integrals[106] which can be handled by a conventional DWBA code. Making the no recoil approximation implies that the transfer occurs when the particle t lies along the vector $\vec{r}$, i.e., (see Fig. 58) when t is between the cores C_1 and C_2. However, replacing the vectors $\vec{r}_i$ and $\vec{r}_f$ by $\vec{r}$ means that the new vector has neither the correct length nor the correct direction.

In an effort to overcome these defects, Buttle and Goldfarb have proposed[109] a partial solution, namely, to make $\vec{r}_1$ proportional to $\vec{r}$. They argue that the $\vec{r}_1$ integral in eq. (A-12), which is a product of the bound state wave functions $\psi_{\ell_1\lambda_1}(\vec{r}_1)$ and $\psi_{\ell_2\lambda_2}(\vec{r}_2)$ with the interaction potential $V_{C_1t}(\vec{r}_1)$, will have its major contribution near nucleus C_1, since $V_{C_1t}(\vec{r}_1)$ decreases rapidly outside the nucleus. Therefore, they replace $\vec{r}_1$ with $(R_1/|\vec{r}|)\,\vec{r}$, where R_1 is the radius of C_1. Furthermore, since the $\vec{r}$ integral will be largest at a distance corresponding roughly to the distance of closest approach of the semi-classical orbits, a valid approximation for $\vec{r}_1$ is

$$\vec{r}_1 \approx \frac{R_1}{D}\,\vec{r} \qquad \text{(A-14)}$$

where D is the (average) distance of closest approach. With this estimate of the recoil term the corrected values for $\vec{r}_i$ and $\vec{r}_f$ become (cf. eqs. (A-13b) and (A-13c))

$$\vec{r}_i = \left[1 - \frac{M_t}{(M_{C_1} + M_t)} \quad \frac{R_1}{D}\right] \vec{r} \tag{A-15a}$$

and

$$\vec{r}_f = \left[\frac{M_{C_2}}{(M_{C_2} + M_t)} + \frac{M_t}{(M_{C_2} + M_t)} \quad \frac{R_1}{D}\right] \vec{r} \tag{A-15b}$$

For Coulomb wave functions the radius enters only as the product $\vec{k} \cdot \vec{r}$ and eqs. (A-15a) and (A-15b) are equivalent to using the "recoil corrected" wave numbers

$$k_i' = \left[1 - \frac{M_t}{(M_{C_1} + M_t)} \quad \frac{R_1}{D}\right] k_i \tag{A-16a}$$

and

$$k_f' = \left[\frac{M_{C_2}}{(M_{C_2} + M_t)} + \frac{M_t}{(M_{C_2} + M_t)} \quad \frac{R_1}{D}\right] k_f \tag{A-16b}$$

With this modification the integral in eq. (A-12) is still separable but the Q-value dependence of the resulting calculations is much improved. In particular, the results of the post treatment (described here) now agree with those of the formally equivalent prior treatment of the DWBA transition amplitude.

An important effect of the recoil term is to change the favored Q-value. The largest cross sections are predicted to occur for a Q-value such that the distances of closest approach in the initial and final channels are approximately equal. Since the distances of closest approach

are related to k_i and k_f (or E_i and $E_f = E_i + Q$) by eq. (A-8), the result of using k_i' and k_f' from eq. (A-16) is to change the predicted Q-value for which the initial and final distances of closest approach coincide. In the case of the $^{90}Zr(^{16}O,^{15}N)^{91}Nb$ reaction considered here, this change in Q-value is about 2.5 MeV.

A second consequence of the recoil term is that the parity rule no longer holds.[108] The introduction of the parity rule is based on the separation of the $\vec{r}$ and $\vec{r}_1$ integrals in eq. (A-12) and no longer appears if the full integral is calculated. Alternatively, if $\vec{r}_i$ and $\vec{r}_f$ are not parallel, an additional source of angular momentum transfer becomes available which allows angular momentum transfers of the "wrong" parity to occur.

Based on the mass ratio in eq. (A-13b), it would appear that recoil corrections are very important in light ion reactions. For example in (d,p) we are ignoring a term 1/2 r_1, as opposed to 1/16 r_1 in the case of the $(^{16}O,^{15}O)$ reaction. However, most light ion reactions are calculated with the zero-range approximation, which corresponds to replacing V_{C_1t} in eq. (A-12) with a delta function. In this case $r_1 \longrightarrow 0$ and the zero-range integral is identical to that obtained in the heavy ion "no recoil" approximation. For relative s-state particles full finite-range calculations are possible in some cases, because the fact that $\ell_1 = 0$ greatly restricts the number of terms which must be calculated.[128] The effect of the finite-range calculation (i.e., including recoil) for light ions is to predict the same angular distribution (and give the same selection rules[108,128]) as would be obtained from a zero-range calculation. Since only the magnitude of the cross section is affected, it is possible to incorporate a

correction term ("Local Energy Approximation") into the zero-range form factor which simulates the results of the finite-range calculation almost exactly.[129] Thus, for light ions it is possible to do a pseudo finite-range calculation rather easily, and there is no need to consider "recoil effects" separately. In contrast, the calculations for heavy ion reactions are generally prohibitively lengthy and some approximate method, for example the treatment of Buttle and Goldfarb[109] described above or a series expansion as proposed by Austern et al.,[128] is required.

APPENDIX B

CALCULATION OF SHELL MODEL DIAGONAL MATRIX ELEMENTS

The calculation of shell model matrix elements using harmonic oscillator wave functions has been described in detail by Brody and Moshinsky.[125] For completeness this derivation will be reproduced here. This appendix will be concerned only with the case of the diagonal matrix element of a central potential, although Brody and Moshinsky also consider off-diagonal matrix elements and matrix elements of spin-orbit and tensor forces. For simplicity, the conventions used here will conform to those of Ref. 125. In particular, the radial quantum number, n, will be 1 less than that generally used to label shell model states, e.g., the lowest oscillator shell will be 0s rather than 1s, etc. The derivation in Part 1 describes the calculation carried out by the program PHYLLIS,[124] with the exception that the program includes the straightforward generalization to off-diagonal matrix elements of a central force. In Part 2, the generalization to the case of two different oscillator parameters (which was not considered by Brody and Moshinsky) is described. This derivation forms the basis for the program NAOMI.[124]

1. Diagonal Matrix Elements - Single Oscillator Parameter

The single-particle wave function in a harmonic oscillator potential is

$$|n\ell m\rangle = R_{n\ell}(\vec{r})\, Y_{\ell}^{m}(\hat{r}) \qquad \text{(B-1)}$$

The two-particle wave function is

$$|n_1\ell_1, n_2\ell_2, \lambda\mu\rangle =$$

$$\sum_{m_1 m_2} \langle \ell_1\ell_2\, m_1 m_2 | \lambda\mu\rangle\, R_{n_1\ell_1}(\vec{r}_1)\, R_{n_2\ell_2}(\vec{r}_2)$$

$$\times\, Y_{\ell_1}^{m_1}(\hat{r}_1)\, Y_{\ell_2}^{m_2}(\hat{r}_2) \qquad \text{(B-2)}$$

This wave function can also be written in the relative-center of mass (RCM) coordinate system, which is defined by

$$\vec{r} = \frac{1}{\sqrt{2}}\,(\vec{r}_1 - \vec{r}_2) \qquad \text{(B-3a)}$$

$$\vec{R} = \frac{1}{\sqrt{2}}\,(\vec{r}_1 + \vec{r}_2) \qquad \text{(B-3b)}$$

This is not the usual definition of this coordinate system. However, it has the advantage that the harmonic oscillator wave functions are the same as those referred to the center of the well coordinate system, i.e., those using $\vec{r}_1$ and $\vec{r}_2$, since with the definition in eq. (B-3) we have

$$V = \frac{1}{2}\, m\omega^2\, (r_1{}^2 + r_2{}^2) = \frac{1}{2}\, m\omega^2\, (R^2 + r^2) \qquad \text{(B-4)}$$

In the RCM system the two-particle wave function is written

$$|n\ell, NL, \lambda\mu\rangle =$$

$$\sum_{mM} \langle \ell LmM|\lambda\mu\rangle\, R_{n\ell}(\vec{r})\, R_{NL}(\vec{R})\, Y_\ell^m(\hat{r})\, Y_L^M(\hat{R}) \qquad \text{(B-5)}$$

Since the RCM system forms a complete set, we can expand the wave function (B-2) in terms of wave functions (B-5):

$$|n_1\ell_1, n_2\ell_2, \lambda\mu\rangle$$

$$= \sum_{n\ell NL} |n\ell, NL, \lambda\mu\rangle\, \langle n\ell, NL, \lambda|n_1\ell_1, n_2\ell_2, \lambda\rangle \qquad \text{(B-6)}$$

The transformation coefficient in eq. (B-6) is the "Moshinsky bracket" and is tabulated in Ref. 125. Since the value of the Moshinsky bracket is independent of μ, this quantum number is not included in eq. (B-6). The summation in eq. (B-6) is restricted by energy and angular momentum conservation:

$$2n + \ell + 2N + L = 2n_1 + \ell_1 + 2n_2 + \ell_2 \tag{B-7}$$

and

$$\vec{\ell} + \vec{L} = \vec{\lambda} = \vec{\ell}_1 + \vec{\ell}_2 \tag{B-8}$$

The reason for the transformation (B-6) is that the two-particle residual interaction, $V(r)$, depends only on the relative coordinate $\vec{r}$ (defined by eq. (B-3a)). Thus, by calculating residual interaction matrix elements in the RCM system, only a single integral must be evaluated.

We wish to calculate the diagonal matrix element

$$\langle n_1\ell_1, n_2\ell_2, \lambda\mu | V(r) | n_1\ell_1, n_2\ell_2, \lambda\mu \rangle \tag{B-9}$$

Transforming (B-9) to the RCM coordinate system by means of eq. (B-6) we get

$$\begin{aligned}
&\langle n_1\ell_1, n_2\ell_2, \lambda\mu | V(r) | n_1\ell_1, n_2\ell_2, \lambda\mu \rangle \\
&= \sum_{n\ell NL} \langle n\ell, NL, \lambda | n_1\ell_1, n_2\ell_2, \lambda \rangle^2 \\
&\qquad \times \langle n\ell, NL, \lambda\mu | V(r) | n\ell, NL, \lambda\mu \rangle
\end{aligned} \tag{B-10a}$$

$$\begin{aligned}
&= \sum_{n\ell NL} \langle n\ell, NL, \lambda | n_1\ell_1, n_2\ell_2, \lambda \rangle^2 \\
&\qquad \times \sum_{mM} \langle \ell LmM | \lambda\mu \rangle^2 \ \langle NLM | NLM \rangle \\
&\qquad \times \int d\hat{r}\ Y_\ell^{m*}(\hat{r})\ Y_\ell^{m}(\hat{r}) \\
&\qquad \times \langle n\ell \| V(r) \| n\ell \rangle
\end{aligned} \tag{B-10b}$$

where the wave function $|NLM\rangle$ is defined in eq. (B-1). Due to the properties of the Clebsch-Gordan coefficient, and the orthonormality of the harmonic oscillator wave functions and the spherical harmonics, eq. (B-10b) becomes

$$\langle n_1\ell_1, n_2\ell_2, \lambda\mu | V(r) | n_1\ell_1, n_2\ell_2, \lambda\mu \rangle$$

$$= \sum_{n\ell NL} \langle n\ell, NL, \lambda | n_1\ell_1, n_2\ell_2, \lambda \rangle^2 \langle n\ell \| V(r) \| n\ell \rangle \qquad \text{(B-11)}$$

In both eqs. (B-10b) and (B-11) the reduced matrix element is defined by

$$\langle n\ell \| V(r) \| n\ell \rangle \equiv \int_0^\infty R^*_{n\ell}(r)\, V(r)\, R_{n\ell}(r)\, r^2\, dr \qquad \text{(B-12)}$$

From eq. (B-11) we see that the calculation of the diagonal matrix element (B-9) has been simplified to a sum of reduced matrix elements (B-12). We must now obtain an explicit expression for these reduced matrix elements. To do so we write the harmonic oscillator radial wave function as

$$R_{n\ell}(r) = r^\ell\, e^{-r^2/2} \sum_{k=0}^{n} a_{n\ell k}\, r^{2k} \qquad \text{(B-13a)}$$

where

$$a_{n\ell k} = \left[\frac{2\,(n!)}{\Gamma(n + \ell + 3/2)}\right]^{1/2} \binom{n+\ell+1/2}{n-k} \frac{(-)^k}{k!} \qquad \text{(B-13b)}$$

$$\binom{n+\ell+1/2}{n-k} = \frac{\Gamma\,(n+\ell+3/2)}{\Gamma\,(n-k+1)\;\Gamma\,(\ell+k+3/2)} \qquad \text{(B-13c)}$$

$$\Gamma(i + 3/2) = \frac{(2i + 1)!!}{2^{i+1}} \sqrt{\pi} \qquad \text{(B-13d)}$$

and

$$\Gamma(i) = (i - 1)! \qquad \text{(B-13e)}$$

Inserting eq. (B-13a) into eq. (B-12) gives

$$\langle n\ell \| V(r) \| n\ell \rangle$$

$$= \sum_{k=0}^{n} a^2_{n\ell k} \int_0^\infty r^{4k+2\ell} \; e^{-r^2} \; V(r) \; r^2 \; dr \tag{B-14}$$

We now define a new summation variable

$$p \equiv 2k + \ell \tag{B-15}$$

The reduced matrix element then becomes

$$\langle n\ell \| V(r) \| n\ell \rangle$$

$$= \sum_{p=\ell}^{2n+\ell} a^2_{n\ell(p-\ell)/2} \quad \frac{\Gamma(p+3/2)}{2}$$

$$\times \int_0^\infty \frac{2}{\Gamma(p+3/2)} \; r^{2p} \; e^{-r^2} \; V(r) \; r^2 \; dr \tag{B-16a}$$

$$= \sum_{p=\ell}^{2n+\ell} a^2_{n\ell(p-\ell)/2} \quad \frac{\Gamma(p+3/2)}{2} \quad I_p \tag{B-16b}$$

where I_p, the "Talmi integral" is defined in eq. (B-16a).

In the notation of Brody and Moshinsky,

$$a^2_{n\ell(p-\ell)/2} \quad \frac{\Gamma(p+3/2)}{2} \equiv B(n\ell, n\ell, p) \tag{B-17}$$

and we can write eq. (B-16b) as

$$\langle n\ell \| V(r) \| n\ell \rangle = \sum_{p=\ell}^{2n+\ell} B(n\ell, n\ell, p) \; I_p \tag{B-18}$$

Referring to eq. (B-11), the residual interaction matrix element becomes

$$\langle n_1\ell_1,\ n_2\ell_2,\ \lambda\mu | V(r) | n_1\ell_1,\ n_2\ell_2,\ \lambda\mu \rangle$$

$$= \sum_{n\ell NL} \langle n\ell,\ NL,\ \lambda | n_1\ell_1,\ n_2\ell_2,\ \lambda \rangle^2 \sum_{p=\ell}^{2n+\ell} B(n\ell,n\ell,p)\ I_p \tag{B-19}$$

Generally the two-particle wave functions are jj coupled, i.e.,

$$| n_1\ell_1 j_1,\ n_2\ell_2 j_2,\ JM \rangle$$

$$= \sum_{\lambda S} \begin{bmatrix} \ell_1 & 1/2 & j_i \\ \ell_2 & 1/2 & j_2 \\ \lambda & S & J \end{bmatrix} \left\{ | n_1\ell_1,\ n_2\ell_2,\ \lambda\mu \rangle\ \chi_S^{m_S} \right\} \tag{B-20}$$

where the curly bracket denotes vector coupling and the square bracket is a jj-LS transformation coefficient.

In this coupling scheme the residual interaction matrix element becomes

$$\langle n_1\ell_1 j_1,\ n_2\ell_2 j_2,\ JM | V(r) | n_1\ell_1 j_1,\ n_2\ell_2 j_2,\ JM \rangle$$

$$= \sum_{\lambda S} \begin{bmatrix} \ell_1 & 1/2 & j_1 \\ \ell_2 & 1/2 & j_2 \\ \lambda & S & J \end{bmatrix}^2 \langle n_1\ell_1,\ n_2\ell_2,\ \lambda\mu | V(r) | n_1\ell_1,\ n_2\ell_2,\ \lambda\mu \rangle \tag{B-21}$$

where the "LS" matrix element is given by eq. (B-19).

In order to evaluate eqs. (B-21) and (B-19) we choose a Gaussian form for V(r):

$$V(r) = -V_o \quad \exp[-\beta r'^2] \tag{B-22}$$

The use of r' on the right hand side of eq. (B-22) is because the potential is written in terms of the <u>actual</u> separation distance

$$\vec{r}' = \vec{r}_1' - \vec{r}_2' \tag{B-23}$$

This differs from the variable "r" used above in two respects. First of all, we have made the radius a dimensionless quantity by writing it in units of the oscillator parameter $b^{1/2} = (M\omega/\hbar)^{1/2}$, and second we have defined the relative coordinate as in eq. (B-3a) rather than the proper definition (B-23). To make r' consistent with the other definition we let

$$\vec{r}' \longrightarrow \sqrt{2}\,\frac{\vec{r}}{\sqrt{b}} \tag{B-24}$$

and eq. (B-22) becomes

$$V(r) = -V_o \exp[-2\beta r^2/b] \tag{B-25}$$

Now, if we use this expression for V(r) in the Talmi integral defined by eq. (B-16) we obtain the simple analytic expression

$$I_p = \frac{-V_o}{(1+2\beta/b)^{p+3/2}} \tag{B-26}$$

Finally, the program PHYLLIS[124] calculates the matrix element (B-21) using eqs. (B-19) and (B-26).

2. <u>Diagonal Matrix Elements - Two Oscillator Parameters</u>

This calculation follows a derivation by Gal.[126] We define the relative and center of mass coordinates for particles 1 and 2, having oscillator parameters b_1 and b_2 as follows:

$$\vec{r} = \vec{r}_1 - \vec{r}_2 \tag{B-27a}$$

$$\vec{R} = \frac{b_1\vec{r}_1 + b_2\vec{r}_2}{b_1 + b_2} \tag{B-27b}$$

$$b' = \frac{b_1 b_2}{b_1 + b_2} \tag{B-27c}$$

$$B' = b_1 + b_2 \tag{B-27d}$$

Using these definitions we can make an expansion similar to eq. (B-6):

$$|n_1\ell_1, n_2\ell_2, \lambda\mu\rangle$$

$$= \sum_{n\ell NL} |n\ell, NL, \lambda\mu\rangle \langle n\ell, NL, \lambda | n_1\ell_1, n_2\ell_2, \lambda\rangle_\beta \tag{B-28}$$

where the transformation bracket (with index β) is now a generalized Moshinsky bracket. The transformation (B-28) connects the eigenfunctions of the center of the well coordinates $\vec{r}_1$ and $\vec{r}_2$ to those of a proper relative coordinate (B-27a) and a "fake" center of mass coordinate (B-27b). As demonstrated in Part 1, the residual interaction matrix element does not depend on $\vec{R}$, so the "reality" of this coordinate is unimportant.

The generalized Moshinsky bracket can be expanded in terms of standard Moshinsky brackets:

$$\langle n\ell, NL, \lambda | n_1\ell_1, n_2\ell_2, \lambda\rangle_\beta$$

$$= i^{m'-m} \sum_{n_3\ell_3 n_4\ell_4} e^{-im''\beta} \langle n\ell, NL, \lambda | n_3\ell_3, n_4\ell_4, \lambda\rangle$$

$$\times \langle n_1\ell_1, n_2\ell_2, \lambda | n_3\ell_3, n_4\ell_4, \lambda\rangle \tag{B-29a}$$

where

$$m = \frac{1}{2}(2n + \ell - 2N - L) \tag{B-29b}$$

$$m' = \frac{1}{2}(2n_1 + \ell_1 - 2n_2 - \ell_2) \tag{B-29c}$$

and

$$m'' = \frac{1}{2}(2n_3 + \ell_3 - 2n_4 - \ell_4) \tag{B-29d}$$

The summation in eq. (B-29a) is restricted by energy and angular momentum as in eqs. (B-7) and (B-8). The bracket index β depends on the two oscillator parameters:

$$\beta = \arccos\left[\frac{b_2 - b_1}{b_2 + b_1}\right] \qquad 0 \leqslant \beta \leqslant \pi \tag{B-30}$$

The "standard" Moshinsky bracket, where $b_1 = b_2$, corresponds to the phase $\beta = \pi/2$.

Using the transformation (B-28) we obtain, analogous to eq. (B-11),

$$\langle n_1\ell_1, n_2\ell_2, \lambda\mu \mid V(r) \mid n_1\ell_1, n_2\ell_2, \lambda\mu \rangle$$

$$= \sum_{n\ell NL} \langle n\ell, NL, \lambda | n_1\ell_1, n_2\ell_2, \lambda \rangle_\beta^2 \langle n\ell \| V(r) \| n\ell \rangle \tag{B-31}$$

The calculation of the reduced matrix element proceeds as before and yields

$$\langle n_1\ell_1, n_2\ell_2, \lambda\mu \mid V(r) \mid n_1\ell_1, n_2\ell_2, \lambda\mu \rangle$$

$$= \sum_{n\ell NL} \langle n\ell, NL, \lambda | n_1\ell_1, n_2\ell_2, \lambda \rangle_\beta^2 \sum_{p=\ell}^{2n+\ell} B(n\ell, n\ell, p) I_p \tag{B-32}$$

Again, however, we must be careful in evaluating I_p. The argument of the Gaussian force (B-22) is now properly defined but must still be put in the dimensionless form

$$\vec{r}' \longrightarrow \frac{\vec{r}}{\sqrt{b'}} \tag{B-33}$$

where b' is defined in eq. (B-27c). This results in an expression for the Talmi integral similar to eq. (B-26):

$$I_p = \frac{-V_o}{(1 + \beta/b')^{p + 3/2}} \tag{B-34}$$

The program NAOMI[124] calculates the matrix element (B-21) from Part 1, making use of eqs. (B-32), (B-34), and (B-29). This calculation is rather lengthy due to the summation in eq. (B-29), since the calculation of the standard Moshinsky bracket is already the most time consuming part of the calculation outlined in Part 1. For this reason no attempt to calculate off-diagonal matrix elements was made. The output of the program NAOMI was verified by repeating some of the calculations in Part 1 with $b_1 = b_2$.

REFERENCES

1. J. Picard and G. Bassani, Nucl. Phys. A131, 636 (1969).
2. G. Vourvopoulos, R. Shoup, J. C. Fox, and J. B. Ball, in Nuclear Isospin, edited by J. D. Anderson, S. D. Bloom, J. Cerny, and W. W. True, (Academic Press, Inc., New York, 1969), p. 205.
3. H. Ohnuma and J. L. Yntema, Phys. Rev. 176, 1416 (1968).
4. M. R. Cates, J. B. Ball, and E. Newman, Phys. Rev. 187, 1682 (1969).
5. R. L. Kozub and D. H. Youngblood, Phys. Rev. C 4, 535 (1971).
6. K. T. Knöpfle, M. Rogge, C. Mayer-Böricke, J. Pederson, and D. Burch, Nucl. Phys. A159, 642 (1970).
7. K. H. Bhatt and J. B. Ball, Nucl. Phys. 63, 286 (1965).
8. N. Auerbach and I. Talmi, Nucl. Phys. 64, 458 (1965).
9. J. Vervier, Nucl. Phys. 75, 17 (1966).
10. K. Hesse and E. Finckh, Nucl. Phys. A141, 417 (1970).
11. S. M. Brahmavar and J. H. Hamilton, Phys. Rev. 187, 1487 (1969).
12. V. C. Rogers, L. E. Beghian, F. M. Clikeman, F. Hofman, and S. Wilensky, Nucl. Phys. A142, 100 (1970).
13. J. Cerny, B. G. Harvey, and R. H. Pehl, Nucl. Phys. 29, 120 (1962).
14. R. H. Pehl, E. Rivet, J. Cerny, and B. G. Harvey, Phys. Rev. 137, B114 (1965).
15. E. Rivet, R. H. Pehl, J. Cerny, and B. G. Harvey, Phys. Rev. 141, 1021 (1966).
16. C. C. Lu, M. S. Zisman, and B. G. Harvey, Phys. Letters 27B, 217 (1968).
17. C. C. Lu, M. S. Zisman, and B. G. Harvey, Phys. Rev. 186, 1086 (1969).

18. M. S. Zisman, E. A. McClatchie, and B. G. Harvey, Phys. Rev. C 2, 1271 (1970).

19. N. K. Glendenning, Ann. Rev. Nucl. Sci. 13, 191 (1963); N. K. Glendenning, Phys. Rev. 137, B102 (1965).

20. A. Gallmann, F. Haas, and B. Heusch, Phys. Rev. 164, 1257 (1967).

21. E. K. Warburton, Phys. Rev. 163, 1032 (1967).

22. A. R. Poletti, E. K. Warburton, and J. W. Olness, Phys. Rev. 164, 1479 (1967).

23. P. C. Rogers and G. E. Gordon, Phys. Rev. 129, 2653 (1962).

24. R. E. Hintz, F. B. Selph, W. S. Flood, B. G. Harvey, F. G. Resmini, and E. A. McClatchie, Nucl. Instr. Methods 72, 61 (1969).

25. E. B. Carter, G. E. Mitchell, and R. H. Davis, Phys. Rev. 133, B1421 (1964); G. E. Mitchell, E. B. Carter, and R. H. Davis, Phys. Rev. 133, B1434 (1964).

26. Nuclear Reactions Induced by Heavy Ions, edited by R. Bock and W. R. Hering (North Holland Publishing Company, Amsterdam, 1970).

27. R. J. Nickles, V. I. Manko, P. R. Christensen, and F. D. Becchetti, Phys. Rev. Letters 26, 1267 (1971).

28. F. D. Becchetti, N. Baron, P. R. Christensen, V. I. Manko, and R. J. Nickles, in Proc. of the International Conf. on Heavy Ion Physics, Dubna, 1971, p. 361.

29. M. S. Zisman and B. G. Harvey, Phys. Rev. C 4, 1809 (1971).

30. M. S. Zisman and B. G. Harvey, Phys. Rev. C 5, 1031 (1972).

31. A. D. Bacher, E. A. McClatchie, M. S. Zisman, T. A. Weaver, and T. A. Tombrello, Nucl. Phys. A181, 453 (1972).

32. N. F. Mangelson, UCRL-17732 (Ph.D. Thesis), 1967 (unpublished).

33. E. A. McClatchie, M. S. Zisman, A. D. Bacher, C. Glashausser, R. H. Pehl, E. Rivet, and F. S. Goulding, UCRL-18667 (1968 Annual Report), 1969, p. 332.

34. C. C. Maples, LBL-253 (Ph.D. Thesis), 1971 (unpublished).

35. F. S. Goulding, D. A. Landis, and R. H. Pehl, UCRL-17989 (1967 Annual Report), 1968, p. 278.

36. F. S. Goulding, D. A. Landis, J. Cerny, and R. H. Pehl, Nucl. Instr. Methods 31, 1 (1964).

37. D. L. Hendrie, J. R. Meriwether, F. B. Selph, D. W. Morris, W. S. Flood, and B. G. Harvey, UCRL-20426 (1970 Annual Report), 1971, p. 280.

38. H. A. Enge, in Focusing of Charged Particles, Vol. II, edited by A. Septier, (Academic Press, New York, 1967), p. 203.

39. F. B. Selph, Lawrence Berkeley Laboratory Engineering Note UCID-3388, 1969 (unpublished).

40. H. A. Enge, Rev. Sci. Instr. 29, 885 (1958).

41. K. L. Brown, Stanford Linear Accelerator Report No. SLAC-75, 1967 (unpublished).

42. D. L. Hendrie, in Nuclear Reactions and Spectroscopy, edited by J. Cerny, (Academic Press, New York), to be published.

43. C. J. Borkowski and M. K. Kopp, Rev. Sci. Instr. 39, 1515 (1968); C. J. Borkowski and M. K. Kopp, IEEE Trans. on Nucl. Sci. NS17, 340 (1970).

44. Available from the General Electric Company, (Valley Forge, Pa.).

45. M. P. Baker, J. R. Calarco, N. S. Chant, J. G. Cramer, and S. Hendrickson, Univ. of Washington Nuclear Physics Laboratory Annual Report (1971), p. 49, (unpublished).

46. J. L. C. Ford, Jr., P. H. Stelson, and R. L. Robinson, Nucl Instr. Methods 98, 199 (1972).

47. B. G. Harvey, J. Mahoney, F. G. Pühlhofer, F. S. Goulding, D. A. Landis, J-C. Faivre, D. G. Kovar, M. S. Zisman, J. R. Meriwether, S. W. Cosper, and D. L. Hendrie, LBL-651, submitted to Nucl. Instr. Methods.

48. F. Pühlhofer, H. L. Harney, and R. Weisenmiller, private communication.

49. F. D. Becchetti, private communication.

50. L. C. Northcliffe, Ann. Rev. Nucl. Sci. 13, 67 (1963).

51. C. C. Maples, G. W. Goth, and J. Cerny, Nucl. Data A2, 429 (1966).

52. J. H. E. Mattauch, W. Thiele, and A. H. Wapstra, Nucl. Phys. 67, 1 (1965).

53. H. J. Kim, R. L. Robinson, C. H. Johnson, and S. Raman, Nucl. Phys. A142, 35 (1970).

54. S. Matsuki, Y. Yoshida, M. Hyakutake, M. Matoba, S. Nakamura, and I. Kumabe, Nucl. Phys. A174, 343 (1971).

55. J. B. Ball and M. R. Cates, Phys. Letters 25B, 126 (1967).

56. F. Rauch, Z. Physik 243, 105 (1971).

57. D. L. Matthews, T. P. Lindsay, M. Koike, and C. F. Moore, Phys. Rev. C 4, 1876 (1971).

58. P. Roussel, G. Bruge, A. Bussiere, H. Faraggi, and J. E. Testoni, Nucl. Phys. A155, 306 (1970).

59. B. M. Preedom, E. Newman, and J. C. Hiebert, Phys. Rev. 166, 1156 (1968).

60. J. Bommer, H. Fuchs, K. Grabisch, H. Kluge, and G. Röschert, Nucl. Phys. A173, 383 (1971).

61. P. J. Riley, J. L. Horton, C. L. Hollas, S. A. Zaidi, C. M. Jones, and J. L. C. Ford, Jr., Phys. Rev. C 4, 1864 (1971).

62. J. B. Moorhead and R. A. Moyer, Phys. Rev. 184, 1205 (1969).

63. W. Booth, S. M. Dalgliesh, K. C. McLean, R. N. Glover, and F. R. Hudson, Phys. Letters 30B, 335 (1969).

64. P. H. Stelson, R. L. Robinson, W. T. Milner, F. K. McGowan, and M. A. Ludington, Bull. Am. Phys. Soc. 16, 619 (1971).

65. T. S. Bhatia, W. W. Daehnick, and T. R. Canada, Phys. Rev. C 3, 1361 (1971).

66. W. W. True, Phys. Rev. 130, 1530 (1963).

67. J. D. Larson and R. H. Spear, Nucl. Phys. 56, 497 (1964).

68. W. H. Bassichis and G. Ripka, Phys. Letters 15, 320 (1965).

69. I. Kelson, Phys. Letters 16, 143 (1965).

70. G. E. Brown and A. M. Green, Nucl. Phys. 75, 401 (1966).

71. L. S. Celenza, R. M. Dreizler, A. Klein, and G. J. Driess, Phys. Letters 23, 241 (1966).

72. J. D. Larson and T. A. Tombrello, Phys. Rev. 147, 760 (1966).

73. E. B. Carter, private communication.

74. C. P. Browne and I. Michael, Phys. Rev. 134, B133 (1964).

75. K. Meier-Ewert, K. Bethge, and K-O. Pfeiffer, Nucl. Phys. A110, 142 (1968)

76. G. Bassani, G. Pappalardo, N. Saunier, and B. M. Traore, Phys. Letters 34B, 612 (1971).

77. K. Bethge, K. Meier-Ewert, K. Pfeiffer, and R. Bock, Phys. Letters 24B, 663 (1967).

78. J. R. Comfort, G. C. Morrison, B. Zeidman, and H. T. Fortune, Phys. Letters 32B, 685 (1970).

79. V. I. Chuev, V. V. Davidov, A. A. Ogloblin, and S. B. Sakuta, Arkiv Fysik 36, 263 (1967).

80. G. J. Wozniak, H. L. Harney, K. H. Wilcox, and J. Cerny, Phys. Rev. Letters 28, 1278 (1972).

81. J. Lowe and A. R. Barnett, Nucl. Phys. A187, 323 (1972).

82. T. R. Ophel, Ph. Martin, S. D. Cloud, and J. M. Morris, Nucl. Phys. A173, 609 (1971).

83. J. J. Ramirez and E. M. Bernstein, Nucl. Phys. A173, 207 (1971).

84. K. P. Artemov, V. Z. Goldberg, I. P. Petrov, V. P. Rudakov, I. N. Serikov, and V. A. Timofeev, Phys. Letters 37B, 61 (1971).

85. A. P. Zuker, B. Buck, and J. B. McGrory, Phys. Rev. Letters 21, 39 (1968); A. P. Zuker, B. Buck, and J. B. McGrory, Brookhaven National Laboratory Report No. BNL-14085 (unpublished).

86. D. A. Bromley, H. E. Gove, J. A. Kuehner, A. E. Litherland, and E. Almqvist, Phys. Rev. 114, 758 (1959); J. A. Kuehner, A. E. Litherland, E. Almqvist, D. A. Bromley, and H. E. Gove, Phys. Rev. 114, 775 (1959).

87. W. Bohne, H. Homeyer, H. Lettau, H. Morgenstern, J. Scheer, and F. Sichelschmidt, Nucl. Phys. A128, 537 (1969).

88. C. C. Lu, UCRL-18470 (Ph. D. Thesis), 1968 (unpublished).

89. R. Weibezahn, H. Freiesleben, F. Pühlhofer, and R. Bock, Nucl. Phys. A176, 645 (1971).

90. G. Bassani, T. H. Kruse, N. Saunier, and G. Souchere, Phys. Letters, 30B, 621 (1969).

91. F. Pühlhofer, H. G. Ritter, R. Bock, G. Brommundt, H. Schmidt, and K. Bethge, Nucl. Phys. A147, 258 (1970).

92. N. K. Glendenning, UCRL-18270, 1968 (unpublished).

93. J. P. Elliot and B. H. Flowers, Proc. Roy. Soc. (London) 242, 57 (1957).

94. H. W. Fulbright, J. A. Robbins, M. Blann, D. G. Fleming and H. S. Plendl, Phys. Rev. 184, 1068 (1969).

95. J. R. Comfort, J. E. E. Baglin, and M. N. Thompson, Bull. Am. Phys. Soc. 13, 608 (1968).

96. A. R. Barnett, Nucl. Phys. A120, 342 (1968).

97. N. K. Aras, E. Eichler, and G. G. Chilosi, Nucl. Phys. A112, 609 (1968).

98. A. S. M. de Jesus and W. L. Rautenbach, Nucl. Phys. A138, 626 (1969).

99. U. Gruber, R. Koch, B. P. Maier, O. W. B. Schult, J. B. Ball, K. H. Bhatt, and R. K. Sheline, Nucl. Phys. 67, 433 (1965).

100. E. T. Jurney, H. T. Motz, R. K. Sheline, E. B. Shera, and J. Vervier, Nucl. Phys. A111, 105 (1968).

101. R. K. Sheline, R. T. Jernigan, J. B. Ball, K. H. Bhatt, Y. E. Kim, and J. Vervier, Nucl. Phys. 61, 342 (1965).

102. J. R. Comfort, J. V. Maher, G. C. Morrison, and J. P. Schiffer, Phys. Rev. Letters 25, 383 (1970).

103. S. Cochavi and D. B. Fossan, Phys. Rev. C 5, 164 (1972).

104. S. Antman, H. Pettersson, and Y. Grunditz, Nucl. Phys. A110, 289 (1968); S. Antman, Y. Grunditz, A. Johansson, B. Nyman, H. Pettersson, and B. Svahn, Z. Physik 233, 275 (1970).

105. H. W. Taylor, B. Singh, R. J. Cox, and A. H. Kukoc, Z. Physik 239, 42 (1970).

106. P. J. A. Buttle and L. J. B. Goldfarb, Nucl. Phys. 78, 409 (1966).

107. F. Schmittroth, W. Tobocman, and A. A. Golestaneh, Phys. Rev. C 1, 377 (1970).

108. W. von Oertzen, in Nuclear Reactions and Spectroscopy, edited by J. Cerny, (Academic Press, New York), to be published.

109. P. J. A. Buttle and L. J. B. Goldfarb, Nucl. Phys. A176, 299 (1971).

110. D. G. Kovar, F. D. Becchetti, B. G. Harvey, F. G. Pühlhofer, J. Mahoney, D. W. Miller, and M. S. Zisman, submitted to Phys. Rev. Letters.

111. G. C. Morrison, H. J. Körner, L. R. Greenwood, and R. H. Siemssen, Phys. Rev. Letters 28, 1662 (1972).

112. D. K. Scott, P. N. Hudson, P. S. Fisher, C. U. Cardinal, N. Anyas-Weiss, A. D. Panagiotou, P. J. Ellis, and B. Buck, Phys. Rev. Letters 28, 1659 (1972).

113. H. Doubre, D. Royer, M. Arditi, L. Bimbot, N. Frascaria, J. P. Garron, and M. Riou, Phys. Letters 29B, 355 (1969).

114. P. R. Christensen, V. I. Manko, F. D. Becchetti, and R. J. Nickles, to be published.

115. C. M. Lederer, J. M. Jaklevic, and J. M. Hollander, Nucl. Phys. A169, 449 (1971).

116. W. von Oertzen, J. de Physique 32, C6-233 (1971).

117. V. I. Manko, F. D. Becchetti, P. R. Christensen, and R. J. Nickles, J. de Physique 32, C6-225 (1971).

118. B. L. Cohen and O. V. Chubinsky, Phys. Rev. 131, 2184 (1963).

119. A. Graue, L. H. Herland, K. J. Lervik, J. T. Nesse and E. R. Cosman, Nucl. Phys. A187, 141 (1972).

120. C. R. Bingham and M. L. Halbert, Phys. Rev. C 2, 2297 (1970).

121. J. L. DuBard and R. K. Sheline, Phys. Rev. 182, 1320 (1969).

122. R. C. Diehl, B. L. Cohen, R. A. Moyer, and H. L. Goldman, Phys, Rev. C 1, 2132 (1970).

123. J. B. Ball and C. B. Fulmer, Phys. Rev. 172, 1199 (1968).

124. Shell-model matrix element code written by M. S. Zisman (unpublished).

125. T. A. Brody and M. Moshinsky, Tables of Transformation Brackets, (Gordon and Breach Science Publishers, Inc. New York, 1967).

126. A. Gal, Ann. Phys. (N. Y.) 49, 341 (1968).

127. S. T. Butler, Nuclear Stripping Reactions, (John Wiley & Sons, Inc., New York, 1957).

128 N. Austern, R. M. Drisko, E. C. Halbert, and G. R. Satchler, Phys. Rev. 133, B3 (1964).

129. J. K. Dickens, R. M. Drisko, F. G. Perey, and G. R. Satchler, Phys. Letters 15, 337 (1965).

LEGAL NOTICE

This report was prepared as an account of work sponsored by the United States Government. Neither the United States nor the United States Atomic Energy Commission, nor any of their employees, nor any of their contractors, subcontractors, or their employees, makes any warranty, express or implied, or assumes any legal liability or responsibility for the accuracy, completeness or usefulness of any information, apparatus, product or process disclosed, or represents that its use would not infringe privately owned rights.

TECHNICAL INFORMATION DIVISION
LAWRENCE BERKELEY LABORATORY
UNIVERSITY OF CALIFORNIA
BERKELEY, CALIFORNIA 94720